Journal of Engineering

ISSN 1726-4073

A Scientific Refereed Journal Published by College of Engineering University of Baghdad

June

2014

Number 6

Volume 20

مجلـــة الهندســـــة

ISSN 1726-4073

مجلة علمية محكمة تصدرها
كلية الهندسة ـ جامعة بغداد

حزيران
2014

العدد 6
المجلد 20

List of Contents

Assessment of Modified - Asphalt Cement Properties

Prof. Saad Issa Sarsam
Department of Civil Engineering
College of Engineering
University of Baghdad
Email: saadisasarsam3@hotmail.com

Ibtihal Mouiad Lafta
Department of Civil Engineering
College of Engineering
University of Baghdad

ABSTRACT

The Asphalt cement is produced as a by-product from the oil industry; the asphalt must practice further processing to control the percentage of its different ingredients so that it will be suitable for paving process. The objective of this work is to prepare different types of modified Asphalt cement using locally available additives, and subjecting the prepared modified Asphalt cement to testing procedures usually adopted for Asphalt cement, and compare the test results with the specification requirements for the modified Asphalt cement to fulfill the paving process requirements. An attempt was made to prepare the modified Asphalt cement for pavement construction in the laboratory by digesting each of the two penetration grade Asphalt cement (40-50 and 60-70) with sulfur, fly ash, silica fumes. Three different percentages of each of the above mentioned additives have been tried using continuous stirring and heating at 150 ºC for 30 minutes .

The prepared modified Asphalt specimens were subjected to physical properties determination; the penetration, softening point, ductility before and after laboratory aging. It was concluded that all percentage of additives has reduced the penetration value of asphalt cement, an exception to that could be noticed when using asphalt cement (40-50) and when adding sulfur. Softening point was increased with the addition of all percentage of additives except that with 7% sulfur by wt. of asphalt cement (40-50) it decreased by 8%.

After aging in general, the penetration decreased by about 37% for control specimens and the softening point increased by about 8% for control specimens.

For asphalt cement 40-50 after aging, Sulfur has the least impact on ductility since it reduces it by 20%. Silica fumes have moderate effect on ductility when it reduces it by 35%, while fly ash shows the highest impact of 36%.

For asphalt cement 60-70 after aging, sulfur was able to almost retain its ductility, while fly ash shows moderate reduction in ductility within a range of 20-36% and silica fumes shows high impact on ductility in the range of 30-50%.

Keywords: Ductility, Fly ash, Silica Fumes, Modified asphalt cement, sulfur, softening point, penetration.

دراسة لخصائص الاسفلت الاسمنتي المحسن

أ. سعد عيسى سرسم
قسم الهندسة المدنية
كلية الهندسة / جامعة بغداد

ابتهال مؤيد لفتة
قسم الهندسة المدنية
كلية الهندسة / جامعة بغداد

الخلاصة

يتم إنتاج الاسفلت السمنتي كمنتج ثانوي من قبل صناعة النفط، ويجب ان يخضع للعديد من العمليات من اجل السيطرة على النسب المئويه من مكوناته المختلفة بحيث تكون مناسبة لعملية الرصف.والهدف من هذا العمل هو إعداد أنواع مختلفة من الاسفلت السمنتي وتعديلها باستخدام المضافات المتوفرة محليا، وإخضاع الاسفلت السمنتي المعدل لعديد من إجراءات الاختبار.وبذلت محاولات لتحضير الاسفلت السمنتي المعدل في المختبر حيث تم استخدام نوعين من الاسفلت السمنتي ذو اختراق درجة (40-50 و 60-70) مع المضافات (الكبريت ,الرماد المتطاير و غبار السيليكا).وتم استخدام ثلاثة نسب مختلفة من كل من المواد المضافة المذكورة أعلاه وخضعت عينات الأسفلت المعدل للخلط مع التسخين بدرجة 150 مئوية ولمدة نصف ساعة. اجريت العديد من. الفحوصات لتحديد الخصائص الفيزيائية؛. اختراق، نقطة الليونة،القدره على السحب قبل وبعد التقادم المختبري .

تم الاستنتاج بان المضافات قامت بتقليل قيم الاختراق بصورة عامة باستثناء الاسفلت السمنتي نوع 40-50 بعد اضافة الكبريت بينما ازدادت درجة حرارة الليونة عند استخدام المضافات مع استثناء حالة اضافة الكبريت بنسبة 7% حيث قلت بمقدار 8% للاسفلت ذي نوع 40-50.

بعد التقادم تقلصت قيمة الاختراق بصورة عامة بمقدار 37% وازدادت قيم درجة الليونة بمقدار 8% عنها في النماذج المرجعية.

للاسفلت السمنتي 40-50 بعد التقادم يظهر الكبريت اقل تاثير على السحبية حيث تقل بمقدار 20% بينما يبين تاثير ابخرة السليكا بصورة متوسطة على السحبية حيث تقل بنسبة 35% اما الرماد المتطاير فيعطي اكبر تاثير وبقيمة 36%.

للاسفلت السمنتي 60-70 بعد التقادم يظهر الكبريت امكانية المحافظة على قيم السحبية بصورة عامة بينما يظهر الرماد المتطاير تاثير متوسط على السحبية حيث تناقصت بمقدار 20-36% اما ابخرة السليكا فتظهر اكبر تاثير على السحبية بمقدار 30-50%

كلمات رئيسية: السحبية، رماد متطاير،ابخرة السليكا، اسفلت سمنتي محسن، كبريت، درجة اليونة، نفاذية

1. INTRODUCTION

Highways play an important role in the economic and social development of societies; therefore, many studies are directed towards modifying pavement properties. In Iraq as well as other countries, pavement surface cracks and rutting are considered as major problems in roads. Asphaltic material with aggregate is usually used as a pavement mixture which is designed considering flexibility, durability and stability. Asphalt binder physical properties are critical to road performance. If an asphalt binder is too soft, rutting may occur soon after completion of the road due to traffic loads. On the other hand, if the binder is too hard or brittle, thermal cracking will occur during periods of cold weather. In addition, oxidative aging causes the binder to harden, thereby compounding its thermal cracking susceptibility over the life of the pavement, **Domke , 1999.**

The quality and grade of the asphalt binder varied due to the crude oil sources and the refining processes which often caused considerable distress to the pavement. Over the past few years, road networks have been subjected to more severe traffic conditions characterized by an increase in the number of vehicles, the load limits and by tire inflation pressures, **Sarsam , 2008**. Despite the use of asphalt mixes poor in binder quality and the enforcement of stricter specifications for materials – especially asphalt, the limits of mechanical stability of road surfacing have often been exceeded and this has resulted in damage such as cracking

and deformation. To control these phenomena, road surfacing must have better resistance to fatigue, increased resistance to permanent deformation, greater flexibility at low temperatures, higher resistance to raveling and stripping, and adequate resistance to ageing.
The use of modified asphalt makes it possible to improve these properties especially for some types of surfacing under particularly severe conditions of services, **Sarsam , 2012**.
Improvements made by adding modifiers to asphalt include increasing the viscosity of the binder, reducing the thermal susceptibility of the binder, and increasing the cohesion of the bitumen, **Sarsam , 2011**.
Increasing the resistance to permanent deformation and improving the resistance to fatigue at low temperatures could mark a good start, on the other hand, improving binder-aggregate adhesion (higher viscosity of the binder), Slowing down the ageing process (thicker film of binder around the aggregate) are considered to be vital for long term service of the pavement, **Vonck and Van , 1989.**
Collins and Bouldin , 1992. stated that the handling properties of the modified asphalt depend on the following factors: Asphalt type, modifier type and content and methods of modification. The effect of silica fumes and Phospho - gypsum as additives have been studied by **Sarsam , 2012,** and its positive impact on asphalt rheological and physical properties were pointed out.

2. MATERIAL

2.1 Asphalt Cement

For the purpose of this work, two type of asphalt cement penetration grade were considered, (40-50) and (60-70). Both types are obtained from the Duraa refinery, south-west of Baghdad. The asphalt cement properties based on the conventional penetration grading system.

2.2 Fly Ash

Fly ash, a by-product of coal combustion, is widely used as a cementation and pozzolanic ingredient in Portland cement concrete and asphalt concrete. Fly ash is available in local markets with low cost. This fly ash has low specific gravity (2.0) as compared with ordinary Portland cement (3.15), and specific surface area ranged to (500-750) m^2/kg. Chemical components of fly ash are tested in the laboratories of General Directorate of Geological survey and Mining and given in **Table.** while **Fig.1** present a sample of the fly ash used.

2.3 Sulfur

It was obtained from Al-Meshrak state company (30 km north of Mosul). The physiochemical properties of these materials are shown in **Table 2. Table 3.** present physical properties of sulfur. While **Fig2** present sample of the sulfur used.

2.4 Silica Fumes

Silica fumes are produced by a vapor phase hydrolysis process using chlorosilanes such as: silicon tetrachloride in a flame of hydrogen and oxygen. silica fumes is supplied as a white, fluffy powder, **ACI 234R, 1996.** Chemical compositions were tested in the laboratories of

General Directorate of Geological survey and Mining and given in **Table 4.,** The physical properties are given in **Table 5.** ,while **Fig3.** present the silica Fumes sample used.

3. PREPARATION OF MODIFIED ASPHALT CEMENT

3.1 Fly ash-Asphalt cement mix

Asphalt cement has been heated to 160 C for asphalt cement (40-50), 150°C for asphalt cement (60-70), and the fly ash was added gradually with continuous stirring on the hot plate for 30 minutes as blending time. Three percentage of the fly ash (5%, 10%, and 15%) by weight of asphalt cement (40-50) and (60-70) have been implemented. Samples were subjected to physical properties determination before and after aging process using thin film oven test.

3.2 Sulfur-Asphalt cement mix

Asphalt cement has been heated to 160 C for asphalt cement (40-50), 150°C for asphalt cement (60-70), and sulfur was introduced in a powder form to it and mixed using manual mixing and constant stirring on the hot plate for 30 minutes as blending time. Three percentage of the sulfur (3%, 5%, and 7%) by weight of asphalt cement (40-50) and (60-70) have been implemented based on work by **Sarsam , 2006**. Samples were subjected to physical properties determination before and after aging process using thin film oven test.

3.3 Silica Fumes -Asphalt cement mix Asphalt cement has been heated to160 C for asphalt cement (40-50), 150°C for asphalt cement (60-70), and then silica fume was added with mixing using manual stirring on the hot plate for 45 minutes as a constant blending time. Three percentage of the silica Fumes (1%, 2%, and 3%) by weight of asphalt cement (40-50) and (60-70) have been introduced based on previous work by **Sarsam (2012)**. Samples were subjected to physical properties determination before and after aging process using thin film oven test.

4. TESTING PROGRAM

4.1 Penetration Test

The penetration test, **ASTM D-5 (2002)** is an empirical measure of asphalt consistency. In this test, a container of asphalt cement is placed at the standard test temperature (25°C) in a temperature-controlled water bath. A prescribed needle, weighted to 100 grams, is placed on the surface of the asphalt cement for 5 seconds. The depth of penetration, expressed in units of 0.1mm, is considered the “penetration” of the asphalt cement.

4.2 Softening point test

The softening point test, **ASTM D36 (2002)** is also used to measure asphalt consistency. The test is performed by confining asphalt samples in brass rings and loading the samples with steel balls. The samples are placed in a beaker of water at a specified height above a metal plate. They are then heated at a specified rate. As the asphalt heats, the weight of the steel ball pulls the sample down toward the plate. When the sample and ball touch the plate, the water temperature is measured and designated as the ring and ball softening point of the asphalt.

4.3 Ductility Test

The ductility of a asphalt cement can be defined as the “distance to which it will elongate before breaking when two ends of a briquette specimen of the material, are pulled apart at a specified speed (5cm/min ±5.0%) and at a specified temperature (25±0.50C) **ASTM D113-99 (2002).** This test method provides measure of tensile properties of bituminous materials and may be used to measure ductility for specific requirements. Ductility is an indicator of flexible behavior of asphalt under various temperatures.

4.4Thin film oven test

Physical properties of asphalt cement changes with respect to time and temperature. Consequently, the performance of pavement will also witness some changes. To take into account the effects of mixing and compaction temperatures as well as the storage time on the behavior of asphalt cement and asphalt mixture. All the asphalt samples have been exposed to accelerated aging by heating the samples in an oven for 5 hours at 163°C .The **ASTM D - 1754 (2002)** has the satisfied information about this test. Ductility, Penetration and softening point after thin film oven test have been determined for asphalt cement for all percentage of modifiers that will be used.

5. DISCUSSIONS ON TEST RESULTS

5.1 Impact of additives on physical properties

Fly ash was added to the asphalt cement by the percentage of (5, 10 and 15%) by weight of asphalt cement (40-50) and (60-70). For asphalt cement (40-50), increasing the percentage to (15%) the penetration was decreased about 68.18%. **Figure 4** presents such behavior. The softening point was (50°C) at (5%fly ash). Increasing the percentage to (15%), the softening point was increased about 6%. **Figure 5** shows the impact. The ductility was (53) at (5% fly ash).Increasing the percentage to (15%), the ductility was decreased to (28). **Figure 6** illustrates such behavior.

For asphalt cement (60-70), increasing the percentage to (15%), the penetration was decreased about 18.18%. **Figure 7** shows such details. At (5% fly ash) the softening point was (45°C).Increasing the percentage to (15%), the softening point was increased about 6.25%. **Figure 8** discusses such behavior. The ductility was (60) at (5% fly ash) .Increasing the percentage to (15%) the ductility was decreased to (30). **Figure 9** demonstrates the impact on ductility.

Sulfur was added to the asphalt cement by the percentage of (3, 5, and 7%) by weight of asphalt cement (40-50) and (60-70). For asphalt cement (40-50), increasing the percentage to (7%), the penetration was decreased by (27.27%). The softening point was decreased to (44°C) at (3% sulfur).Increasing the percentage to (7%), the softening point was decreased by 8%. The ductility was (+100) at (3% sulfur) .Increasing the percentage to (7%), the ductility was decreased to (95).

At asphalt cement (60-70) it was noticed that at (3% sulfur) the penetration was increased to (80).Increasing the percentage over (7%) the penetration was increased by 48.48%. The softening point was decreased to (45°C) at (3% sulfur) .Increasing the percentage over (7%) the softening point was decreased about 16.66%. The ductility was (+100) at (3% sulfur).

Silica Fumes was added to the asphalt cement by the percentage of (1, 2 and 3%) by weight of asphalt cement (40-50) and (60-70). It was noticed that:
At asphalt cement (40-50) increasing the silica fumes percentage to (3%) the penetration was decreased by 4.5%. The softening point was increased to (55°C) at (1% silica fumes) and decreased to (52°C) at (3% silica fumes).The ductility was decreased to (19) at (1% silica fumes) and increased to (25) when using (3%) silica fumes.
At asphalt cement (60-70), increasing the silica fumes percentage to (3%), the penetration was decreased by 33.3%.
The softening point was increased to (52°C) when a (3%) silica fume was introduced. The ductility was decreased to (27) at (1% silica fumes) and decreased to (19) when (3%) silica fumes was adopted.
Table 6 demonstrates the impact of additives on asphalt cement (40-50) properties. While **Table 8** shows the impact of additives on asphalt cement (60-70) properties.

5.2 Impact of additives on aging behavior

The impacts of additives on physical properties of asphalt cement after aging are illustrated in **table 7**. The asphalt cement of grade 40-50 has retained 40% of its ductility after aging; the softening point was increased by 8%, and the penetration was decreased by 36%. When additives were introduced, their impact was variable; the ductility was reduced by a range of 10-60 % based on additive type and percentage. Sulfur has the least impact on ductility since it reduces it by 20%. Silica fumes have moderate effect on ductility when it reduces it by 35%, while fly ash shows the highest impact of 36%. The softening point increases after aging by a range of 6-8% when different percentages and type of additives were introduced. The penetration value shows variations by a range of 20-60% based on additive type and percentage.
On the other hand, the asphalt cement of grade 60-70 exhibit 22% reduction in penetration, 6% increment in softening point and 25% reduction in ductility due to aging. When additives were introduced, sulfur was able to retain its ductility, while fly ash shows moderate reduction in ductility within a range of 20-36% and silica fumes shows high impact on ductility in the range of 30-50%.
The impact of additives on softening point was in a range of 3-6% for various percentages and type of additives. Sulfur shows the lowest impact on penetration in a range of 5-15%, while fly ash and silica fumes shows higher impact within a range of 17-30%.
Such behavior of additives may be attributed to the increase in viscosity due to high specific surface area of silica fumes, and to possible chemical reaction took place in case of sulfur and fly ash.

6. CONCLUSIONS

Based on the testing program, the following conclusions may be drawn:
1. All percentage of additives has reduced the penetration value of asphalt cement, an exception to that could be noticed when using asphalt cement (40-50) and when adding sulfur.
2. Softening point was increased with the addition of all percentage of additives except that with 7% sulfur by wt. of asphalt cement (40-50) it decreased by 8%.

3. Ductility was decreased with the addition of all percentages of additives.
4. For asphalt cement 40-50 after aging, Sulfur has the least impact on ductility since it reduces it by 20%. Silica fumes have moderate effect on ductility when it reduces it by 35%, while fly ash shows the highest impact of 36%.
5. The softening point increases after aging by a range of 6-8% when different percentages and type of additives were introduced. The penetration value shows variations by a range of 20-60% based on additive type and percentage.
6. For asphalt cement 60-70 after aging, sulfur was able to almost retain its ductility, while fly ash shows moderate reduction in ductility within a range of 20-36% and silica fumes shows high impact on ductility in the range of 30-50%.
7. The impact of additives on softening point was in a range of 3-6% for various percentages and type of additives. Sulfur shows the lowest impact on penetration in a range of 5-15%, while fly ash and silica fumes shows higher impact within a range of 17-30%.

REFERENCES

ASTM D-5, 2002 , *Standard Test Method for Penetration of Bituminous Materials*, American Society of Testing and Materials.

ASTM D-113, 2002 , *Standard Test Method for Ductility of Bituminous Materials*, American Society of Testing and Materials.

ASTM D-1754, 2002 , *Standard Test Method for Effects of Heat and Air on Asphaltic Materials (Thin-Film Oven Test*; American Society of Testing and Materials.

ASTM D-36, 2002 “Standard Test Method for Softening Point of Bitumen”, American Society of Testing and Materials.

Collins, J. H. and Bouldin, M., 1992, "Stability of Straight and Polymer Modified Asphalt", TRB No. 1342, pp (92-100).

Domke, C.H., 1999, *Asphalt Compositional Effects on Physical and Chemical Properties*,Ph.D. Dissertation, Texas A&M University.

Sarsam S. *Assessing rheological and physical characteristics of modified asphalt cemen*t Proceedings, 8th International Conference on Material Sciences (CSM8-ISM5), Beirut–Lebanon, May 28-30, 2012.

Sarsam S., 2012 , *Effect of Silica fumes and Phospho -gypsum on rheological and physical characteristics of Asphalt cement*, Proceedings, Eight International Conference on Material Sciences (CSM8-ISM5), Beirut–Lebanon, May 28-30, 2012.

Sarsam S., 2008 , *Evaluating and testing rheological and physical properties of Mastic Asphalt*, Indian Highways IRC Vol. 36 No.5-2008, India.

Sarsam S., 2006 , *Evaluating and testing rheological and physical properties of Mastic Asphalt*, proceeding, IRC Seminar on Innovation in construction and maintenance of flexible pavement-Agra-India, 2nd -4th September 2006.

Sarsam S., 2011 , *Assessing rheological and physical characteristics of modified Asphalt cement*, Proceeding, Scientific and Engineering Conference, Ministry of Construction and Housing, 20-5-2011, Baghdad.

Vonck, W. C. and Van G., G., 1989 ,*Improvement of Paving Grade Bitumen with SBS polymers*", Forth Eurobitume Symposium, Vol. I, Summaries and papers, pp (299-303), Madrid (Spain).

Figure 1. Fly ash.

Figure 2. Sulfur.

Figure 3. Silica fumes.

Table 1. Chemical Components of Fly Ash as tested by the laboratories of General Directorate of Geological survey and Mining.

Oxide	Percent	ASTM Requirement C618 (%)
SiO2	61.95	---------
Fe2O3	2.67	---------
Al2O3	28.82	---------
SiO2+Fe2O3+Al2O3	93.44	70.0 min.
Na2O	0.26	1.5 max.
CaO	0.88	----------
MgO	0.34	5.0 max
SO3	< 0.07	5.0 max
L.O.I	0.86	6.0 max

Table 2. Physiochemical properties of sulfur waste Element (% by weight).

Material	% Content
Sulfur	88-90
Carbon	10-12
Ash	0.1
sp. gr.	2.03

Table 3. physical properties of sulfur.

Physical properties	
Phase	solid
Density	2.07 $g \cdot cm^{-3}$
Liquid density	1.819 $g \cdot cm^{-3}$
Melting point	115.21 °C, 239.38 °F

Table 4. Chemical Components of silica Fumes tested in the laboratories of General Directorate of Geological survey and Mining.

Oxide	Percent
SiO2	99.1
Fe2O3	35.0 p.p.m
Al2O3	< 0.035
TiO2	< 0.006
CaO	0.03
MgO	52.0 p.p.m
SO3	< 0.07
L.O.I	0.7

Table 5. Physical properties of silica Fumes as supplied by the Manufacturing Company (Weaker Company 47).

Physical Properties	Test result
surface area m^2/g	50-600
Density kg/m^3	160-190
Loss of weight% when drying at 1000˚c for 2hrs	< 2
Loss of weight% when drying at 105˚c for 2 hrs	< 1.5
PH	3.9-4.3
% retained on 40 µm sieve	< 0.04
Moisture %	0.82

Table 6. Physical properties of Modified Asphalt cement Grade (40-50) before aging.

Asphalt cement (40-50)	Penetration	Softening point	Ductility
Control	44	50	>100
5%fly ash	25	50	53
10%fly ash	15	50	30
15%fly ash	14	53	28
3% sulfur	68	44	>100
5%sulfur	63	45	97
7%sulfur	50	46	95
1% silica fumes	25	53	19.5
2% silica fumes	32	53.5	21
3% silica fumes	41	51	22

Table 7. Physical properties of Modified Asphalt cement Grade (40-50) after aging.

Asphalt cement (40-50)	Penetration	Softening point	Ductility
Control	28	54	60
5%fly ash	15	52	33
10%fly ash	11	53	19
15%fly ash	9	55	11
3% sulfur	22	48	81
5%sulfur	50	46	79
7%sulfur	51	46	77
1% silica fumes	33	56	8
2% silica fumes	25	58	19
3% silica fumes	15	57	16

Figure 4. Effect of additive type and percentages on penetration value before aging for asphalt cement (40-50).

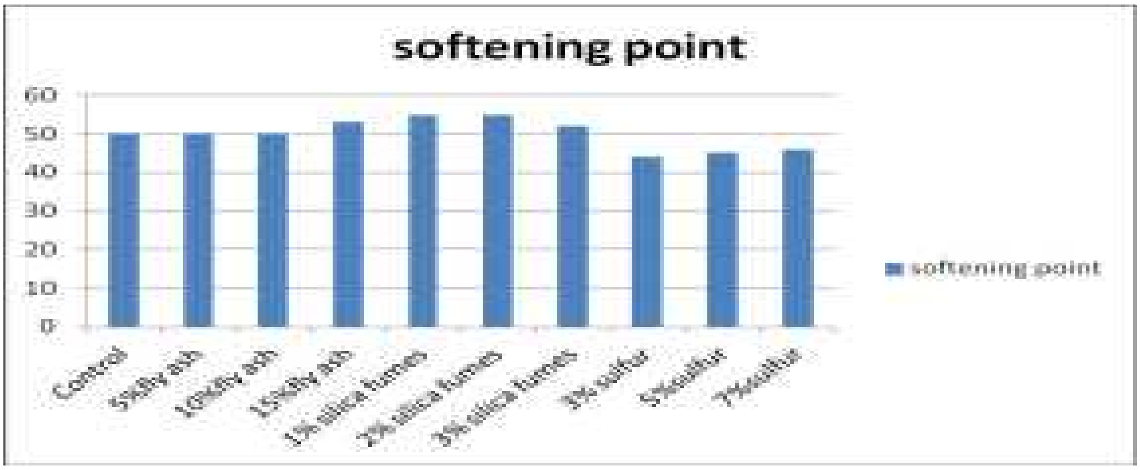

Figure 5. Effect of additive type and percentages on softening point value before aging for asphalt cement (40-50).

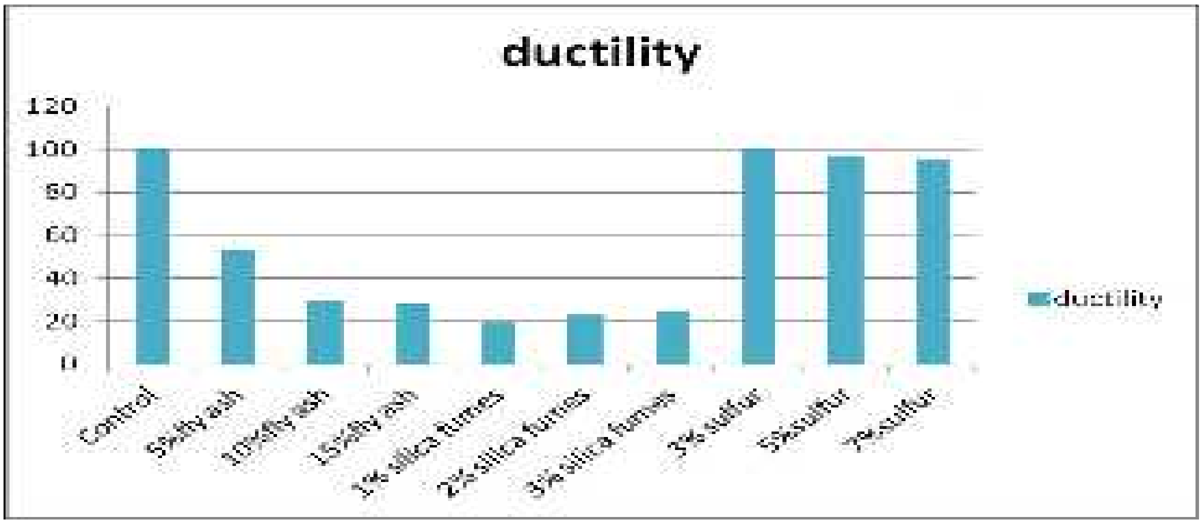

Figure 6. Effect of additive type and percentages on ductility value before aging for asphalt Cement (40-50).

Table 8. Physical properties of Modified Asphalt cement Grade (60-70) before aging

Asphalt cement (60-70)	Penetration	Softening point	Ductility
Control	66	48	>100
5%fly ash	52	45	60
10%fly ash	47	46	40
15%fly ash	54	51	30
3% sulfur	80	45	>100
5%sulfur	93	42	>100
7%sulfur	98	40	>100
1% silica fumes	63	48	27
2% silica fumes	57	54	25
3% silica fumes	44	52	19

Table 9. Physical properties of Modified Asphalt cement Grade (60-70) after aging.

Asphalt cement (60-70)	Penetration	Softening point	Ductility
Control	51	51	75
5%fly ash	41	46	48
10%fly ash	32	48	27
15%fly ash	42	53	19
3% sulfur	67	48	>100
5%sulfur	88	45	>100
7%sulfur	85	43	>100
1% silica fumes	52	50	19
2% silica fumes	41	55	16
3% silica fumes	32	54	9

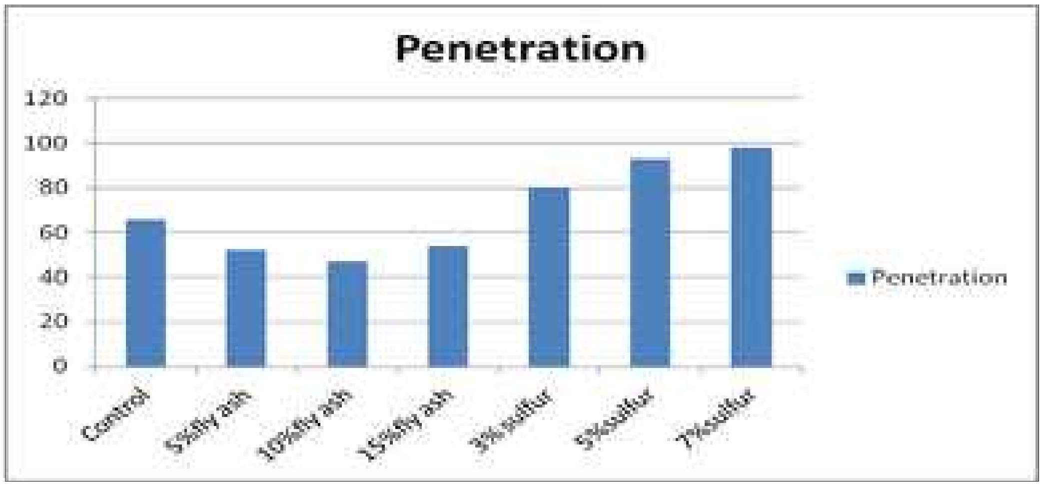

Figure 7. Effect of additive type and percentages on penetration value before aging for asphalt cement (60-70).

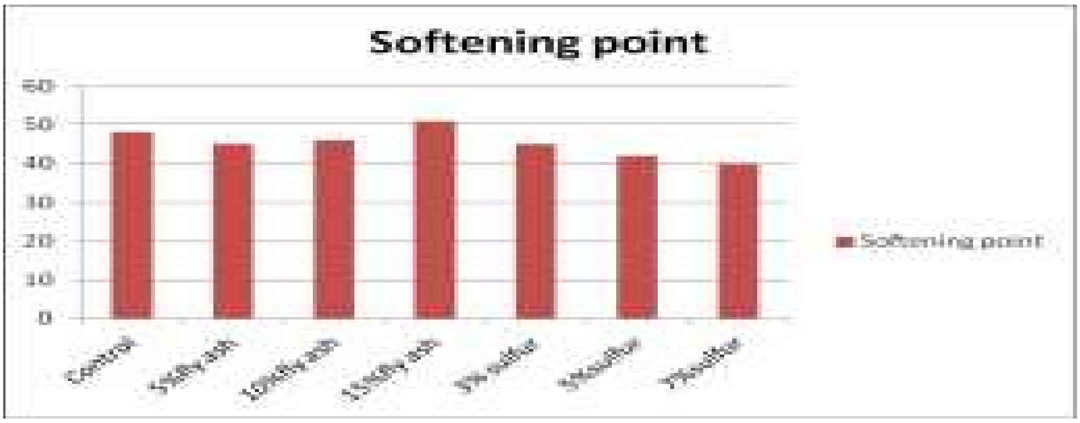

Figure 8. Effect of additive type and percentages on softening point value before aging for asphalt cement (60-70).

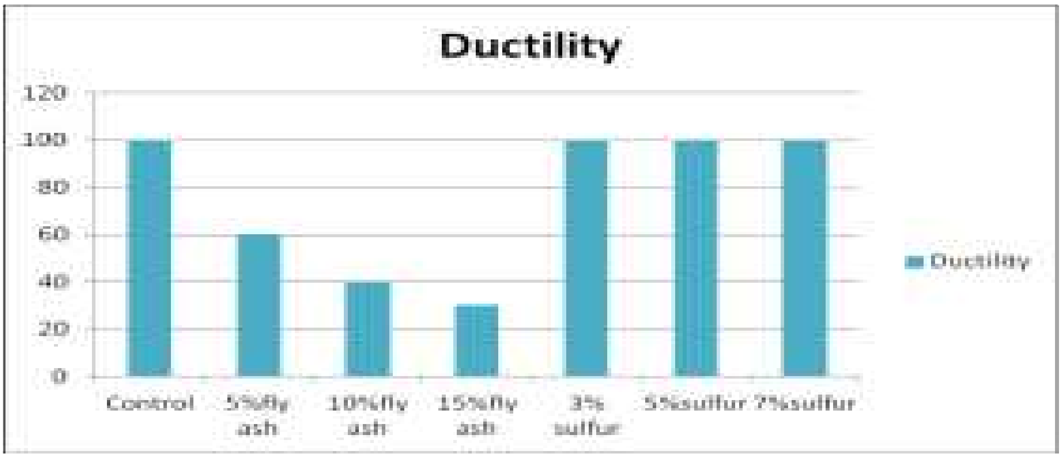

Figure 9. Effect of additive type and percentages on ductility before aging , asphalt cement (60-70).

Finite Element Analysis of Reinforced Concrete T-Beams with Multiple Web Openings under Impact Loading

Dr.Nazar Kamel Oukaili
Professor
College of Engineering- University of Baghdad
E-mail: dr_nazar12000@yahoo.com

Abeer Hussein Al-Shammari
Lecturer
College of Engineering-University of Al-Mustansiriya
E-mail: abeeralshammari83_2010@yahoo.com

ABSTRACT

In this study, a three-dimensional finite element analysis using ANSYS 12.1 program had been employed to simulate simply supported reinforced concrete (RC) T-beams with multiple web circular openings subjected to an impact loading. Three design parameters were considered, including size, location and number of the web openings. Twelve models of simply supported RC T-beams were subjected to one point of transient (impact) loading at mid span. Beams were simulated and analysis results were obtained in terms of mid span deflection-time histories and compared with the results of the solid reference one. The maximum mid span deflection is an important index for evaluating damage levels of the RC beams subjected to impact loading. Three experimental T-beams were considered in this study for calibration of the program. All models had an identical cross-section and span similar to those of the experimental beams. The diameter of the openings of the experimental beams was 110 mm. Three other diameters were varied (50, 80 and 130) mm. The location of the face of the opening with respect to the location of impact loading was investigated (the face of the opening at distance varied 0d, 0.5d, 1d and 1.5d from the location of loading, where d is the effective depth) and the number of web openings was varied (2,4 and 6) openings. All modeled beams subjected to dropping mass of 24.5 kg with height of drop of 250 mm (as for the experimental beams). Results obtained from this study showed that the behavior of beams with circular openings of diameter equal to 22% the web depth has a small effect on the response of the RC T-beams. On the other hand, introducing circular openings with a diameter equal to 35% and 57% of the web depth (80 and 130 mm) increases the maximum mid span deflection by 23% and 43% respectively. Results also showed that, openings with a distance greater than or equal to 1.5 d from the location of impact loading have no effect on the deflection of the RC beams.

Key words: beams, web openings, impact loading.

التحليل بإستخدام العناصر المحدده لعتبات خرسانيه مسلحه ذات مقطع (T) حاويه على فتحات وتره متعدده تحت تأثير الحمل الصدمي

د. نزار كامل العقيلي
أستاذ
كلية الهندسه / جامعة بغداد

عبير حسين الشمري
مدرس
كلية الهندسه / الجامعة المستنصريه

الخلاصه

في هذه الدراسه تم عمل تحليل ثلاثي الأبعاد بإستخدام طريقة العناصر المحدده عن طريق البرنامج التحليلي ANSYS وذلك لتمثيل عتبات خرسانيه مسلحه ذات مقطع (T) تحتوي على فتحات وتره متعدده دائريه الشكل خاضعه لحمل صدمي. تم إعتماد ثلاث متغيرات تصميميه تضم: حجم وموقع و عدد الفتحات. تم تسليط الحمل الصدمي على 12 نموذج من العتبات الخرسانيه المسلحه بسيطة الإسناد في نقطه واحده تقع منتصف الفضاء. النتائج التي تم الحصول عليها والتي هي بدلالة مخططات هطول منتصف الفضاء مع الزمن تم مقارنتها مع نتائج النموذج المرجعي الغير حاوي على فتحات حيث إن الهطول الأقصى هو

مؤشر مهم لتحديد مستوى الضرر للعتبات الخاضعه للحمل الصدمي. تم اعتماد نتائج ثلاث عتبات مفحوصه عمليا من أجل معايرة البرنامج. جميع النماذج لها مقطع وفضاء مماثل للعتبات المفحوصه عمليا. قطر فتحات العتبات المفحوصه عمليا يساوي 110ملم. ثلاثة أقطار أخرى تم دراستها (50، 80، 130 ملم) وكذلك تم دراسة موقع الفتحات نسبة الى موقع الحمل الصدمي (بداية الفتحه تتغير بمسافة d0، d0.5، d1، d1.5 من موقع الحمل) وكذلك عدد الفتحات متغير (2، 4، 6 فتحات). النتائج المستحصله بينت أن العتبات ذات فتحات دائريه بقطر 22% من عمق الوتره لها تأثير قليل على هطولها. من ناحيه أخرى فإن عمل فتحات دائريه بقطر 35% و 57% من عمق الوتره يزيد من الهطول الأقصى لمنتصف الفضاء بنسبة 23% و 43% على التوالي. كذلك بينت النتائج بأن الفتحات ذات مسافه اكبر أو تساوي d1.5 من موقع الحمل الصدمي ليس لها تأثير على هطول العتبات الحاويه على تلك الفتحات.

1. INTRODUCTION

Web openings in beams are essential to provide a convenient passage of service ducts and pipes. As a result, story height of buildings can be reduces and slight reduction in concrete beams weight would improve the demand on the supporting frame both under gravity loading and seismic excitation which resulting in major cost saving.

Size of opening did affect strength, but an unreinforced web containing a square opening of one-quarter the web depth, or a circular opening of three-eighths the web depth, did not reduce the strength of the specimen **,ASCE-ACI Committee 426**. According to **Somes and Corley, 1974**, a circular opening may be considered as large when its diameter exceeds 0.25 times the depth of the web because introduction of such openings reduces the strength of the beam. **Mansur, et al., 1991** made an investigation on eight reinforced concrete continuous beams, each containing a large transverse opening. Their study showed that an increase in the depth of opening from 140 mm to 220 mm led to a reduction in collapse load from 240 kN to 180 kN.

In practice, there are many incidents in which the structures undergo impact or dynamic loading, such as during an explosion, transportation structures subjected to vehicle crash impact, impact of ice load on marine and offshore structures, accidental falling loads, etc. The behavior of concrete beams subjected to impact loads, is different compared to the behavior under static loading. Due to the short duration of loading, the strain rate of material is significantly higher than that under static loading conditions.

At the present time, many methods for analyzing RC members are available. One of the most powerful methods is the finite element technique which spares much time and efforts. Even though many experimental studies have been reported, limited research studies have been done on reinforced concrete T-beam with multiple web openings under impact loading by simulation. In order to verify the finite element model, three experimental beams (a solid beam without openings and two other beams with four and six un-strengthened circular openings provided in the study of **Oukaili,** and **Shammari, 2013** were considered in this study.

2. OBJECTIVES AND SCOPES

The purpose of this study is to investigate the effect of size, location and number of circular web openings on the impact response of RC T-beams without strengthening of the openings by additional reinforcement. This research study focuses on three variables:

1. Diameter of openings (50, 80, 110 and 130 mm).
2. Location of openings with respect to the location of impact loading (clear distance between the impact load and the beginning of opening = 0d, 0.5d, d and 1.5d)
3. Number of web openings (2, 4 and 6 openings).

The scope of this study is to simulate simply supported RC T-beams with the mentioned variables under transient (impact) loading using **ANSYS 12.1** program to obtain mid span deflection-time histories and compare them with the solid reference beam.

All T-beams have identical dimensions and reinforcement based on Oukaili and Shammari (2013) experimental beams. Thickness of flange =60mm, width of flange =300mm, depth of web =230mm and width of web =120mm. Beam length =2000mm with an effective span of 1800mm. All beams were reinforced with 2 20mm longitudinal bars as tension reinforcement, four 6 mm longitudinal bars as compression reinforcement and 4 mm at 130 mm center to center as stirrups. The dimensions and details of reinforcement are shown in **Fig. 1a.**

Fig. 1b-1d shows the details of the experimental beams which were considered in this study for calibration of the program. The distance between the end of the first opening (near the support) and the support equals 130 mm; this is about half the effective depth. The centers of the circular openings were located at 145 mm along the y-direction from soffit of the beam. Diameter of openings is 110mm (0.48 the web depth).

3. MODELS SPECIFICATIONS

3.1 Material Properties

3.1.1 **Concrete**

Concrete is a quasi-brittle material and has different behavior in compression and in tension. Solid65 element was used to model this material. This element has eight nodes with three degrees of freedom at each node - translation in the nodal x, y, and z directions. This element is capable of plastic deformation, cracking in three orthogonal directions, and crushing. A schematic of the element is shown in **Fig. 2 ANSYS Manual, Version 12.1**. Smeared cracking approach has been used in modeling the concrete in the present study **William,** and **Wranke, 1975**. Poisson's ratio ( ) for concrete was assumed to be 0.2 ,**Bangash, 1989**. Self-weight of the beams was considered.

3.1.2 Reinforcement

Modeling of reinforcing steel in finite elements is much simpler than the modeling of concrete. A Link 8 element was used to model steel reinforcement. This element is a three dimensional spar element and it has two nodes with three degrees of freedom -translations in the nodal x, y, and z directions. This element is also capable of plastic deformation. This element is shown in **Fig. 3**. A perfect bond between the concrete and steel reinforcement is considered. However, in the present study the steel reinforcing was connected between nodes of each adjacent concrete solid element, so the two materials shared the same nodes. The steel for the finite element models is assumed to be an elastic-perfectly plastic material and identical in tension and compression. A Poisson's ratio of 0.3 is used for the steel reinforcement.

3.2 Boundary Conditions and Loading

Taking advantages of the symmetry, only quarter of the beam was modeled. Rollers were used to show the symmetry condition at internal faces, whereas the nodes at the support were restrained against vertical displacement.

Transient dynamic analysis (sometimes called time-history analysis) is a technique used to determine the dynamic response of a structure under the action of any general time-dependent loads. This type of analysis can be used to determine the time-varying displacements, strains, stresses, and forces. Three methods are available in ANSYS program to do a transient dynamic analysis: full, mode superposition, and reduced. ANSYS analysis was done using the reduced method; this method condenses the problem size by using master degrees of freedom and reduced matrices. After the displacements at the master DOF have been calculated, ANSYS expands the solution to the original full DOF set. Multiple load steps are usually required to specify the load history in a transient analysis. The first load step is used to establish initial

conditions, and second and subsequent load steps are used for the transient loading. **Fig. 4** shows FE mesh, boundary conditions and load step.
Damping has much less importance in controlling the maximum response of a structure to impact loads than for periodic or harmonic loads because the maximum response to a particular impulsive load will be reached in a very short time, before the damping forces can absorb much energy from the structure, **Clough, 2003**, for this reason only the undamped response to impact loads will be considered in this study.

4. VERIFICATION STUDY

The finite element analysis calibration study includes modeling of RC T-beams with dimensions and properties corresponding to solid beam and two other beams with four and six circular web openings of diameter equals 110mm tested by **Oukaili**, and **Shammari, 2013**. The aim of the comparison is to ensure that the elements, material properties and convergence criteria are adequate to model the response of the beams and to be sure that the simulation process is correct, the test setup of the experimental beams is shown in **Fig.5**.
Transient analyses were made for dropping mass of 24.5 kg and height of drop of 250 mm for the three experimental beams. Finite element analysis results in terms of mid span deflection-time histories are shown in **Fig. 6**. In general, the agreement is good and the plots have similar trends.

5. PARAMETRIC STUDY

Results and discussion can be presented in three sections according to the parametric study. In the first section, the finite element modeling of the reinforced concrete beams with circular openings in varying diameters (50, 80, 110 and 130 mm) will be discussed. In the second section, the discussion will be made about the effective location of the opening with respect to the location of the impact loading. In the third section, the effect of different number of openings (2, 4 and 6) will be presented. These modeled beams have the same dimensions as the experimental beams tested by **Oukaili**, and **Shammari, 2013**. Twelve models were needed for this study; details of these models were presented in **Table 1**.

6. RESULTS AND DISCUSSION

6.1 Effect of Size of Web Openings

The transient (impact) response of four RC modeled beams with six openings of distance between the point of applied load and the beginning of first opening equals 0.5d and with variable diameter, 50, 80, 110 and 130 mm, was studied. From the analysis results, it was found that the maximum mid span deflection of the modeled beam with six openings, each of 50 mm diameter was 2.44 mm while that for the solid one was 2.24 mm. The increase in the maximum mid span deflection was 8%. Hence, introducing openings with a diameter equal to 22% the web depth of the beam has a small effect on the deflection of the beam.
On the other hand, it was found that the maximum mid span deflections of the modeled beams of six openings with 80, 110 and 130 mm diameter six openings were 2.74, 3 and 3.2 mm. The increase in the maximum mid span deflection was 23%, 34% and 43% compared to the solid beam. **Fig. 7** shows the effect of the size of openings.

6.2 Effect of Location of Web Openings

In this section, the effective location of the opening with respect to the location of the impact loading that affect the response of the RC beam can be found. Four different locations of two symmetrical openings were studied, 0d, 0.5d, d and 1.5d from the point of impact loading to the beginning of the opening. It was found that as the distance of the opening from the point of impact loading increases, the effect of opening on the response of the RC beams in terms of mid span deflection-time history decreases till this distance reach 1.5 d ;at this distance, the opening has no effect on the mid span deflection-time history of the beam. **Fig. 8** shows the effect of the location of openings.

6.3 Effect of Number of Web Openings

In this section, the effect of number of web openings with different locations along the span of the modeled beams on the impact response of RC beams was presented. From the analysis results it can be found that the maximum mid span deflections for the modeled beams are of approximately equal values when the distance of the opening is 0.5d from the applied load location, regardless the number of web openings (2, 4 or 6 openings). Modeled beam with six openings which were distributed one close to the other in the middle part of the beam web showed maximum mid span deflection of 56% greater than that of the solid beam. **Fig. 9** shows the effect of number of openings of different locations on the mid span deflection-time history.

7. CONCLUSIONS

The following conclusions can be obtained from the analysis results. The conclusions are based on transient analyses which made by dropping mass of 24.5 kg and height of drop of 250 mm as in the experimental beams:

1. Introducing openings with a diameter equal to 22% the web depth of the beam causes an increase in the maximum mid span deflection by 8%.
2. The increase in the maximum mid span deflection is 23%, 34% and 43% for beams with six openings with 80, 110 and 130 mm diameter respectively, compared to the solid beam.
3. As the distance of the opening from the point of impact loading increases, the effect of opening on the response of the RC beams in terms of mid span deflection-time history decreases till this distance reaches 1.5 d; at this distance, the opening has no effect on the mid span deflection-time history of the beam
4. The maximum mid span deflections for the modeled beams are of approximately equal values when the distance of the opening is 0.5d from the applied load location, regardless the number of web openings.
5. Modeled beam with six openings which were distributed one close to the other in the middle part of the beam web showed maximum mid span deflection of 56% greater than that of the solid beam.

REFERENCES

ACI-ASCE Committee 426, 1974., *Shear Strength of Reinforced Concrete Members (ACI 426R-74) (Reapproved 1980),* Proceeding, ASCE, V.99, No.ST6, June, pp.1148-1157.

ANSYS, ANSYS User?s Manual Release 12.1, ANSYS, Inc.

Bangash, M.Y. H., 1989, *Concrete and Concrete Structures: Numerical Modeling and Applications*, Elsevier Science Publishers Ltd., London, England, 1989.

Clough, R. W., and, Penzien, J., 2003, *Dynamics of Structures*, Book, Third Edition, USA, 730p.

Mansur, M.A., Lee, Y.F., Tan, K.H. and Lee, S.L., 1991, *Test on RC Continuous Beams with Openings*, Journal of Structural Engineering, Vol. 117, No. 6, pp. 1593-1605.

Oukaili, N. K., and Shammari, A. H., 2013, *Response of Reinforced Concrete Beams with Multiple Web Openings to Static and Impact Loads*, Ph.D. Thesis, University of Baghdad.

Somes, N.F., and Corley, W.G., 1974, *Circular Openings in Webs of Continuous Beams*, American Concrete Institute, Detroit, MI, pp. 359-398.

William, K. J. and Warnke, E. P., 1975, *Constitutive Model for the Triaxial Behavior of Concrete*, Proceedings, International Association for Bridge and Structural Engineering, Vol. 19, ISMES, Bergamo, Italy, 174 p.

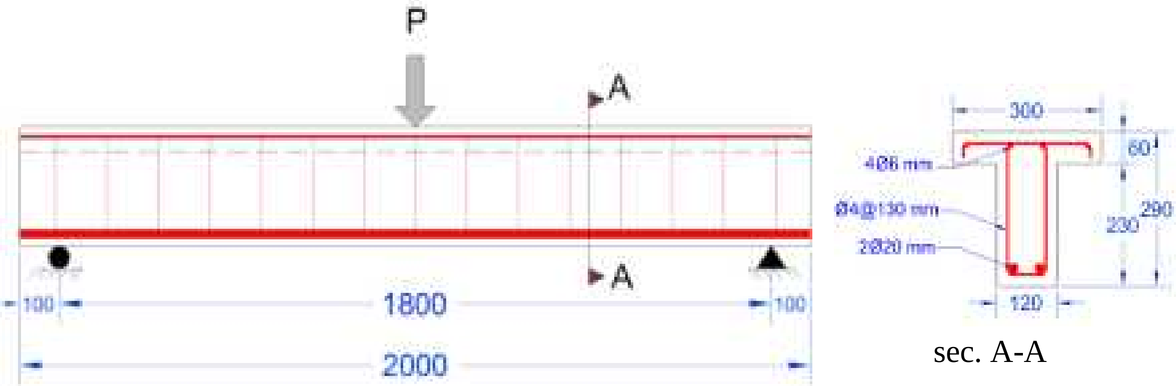

sec. A-A

a. Dimensions and reinforcement details of experimental beams.

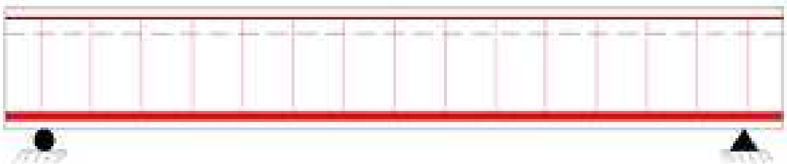

b. Solid beam (first experimental beam).

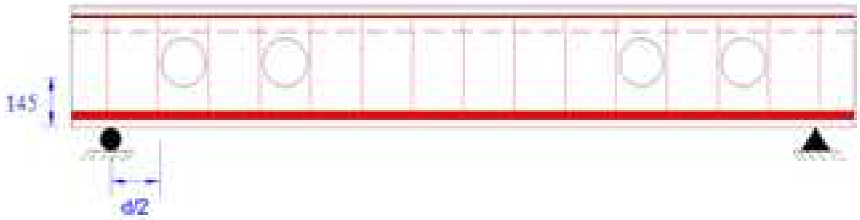

c. Beam with four circular openings (second experimental beam).

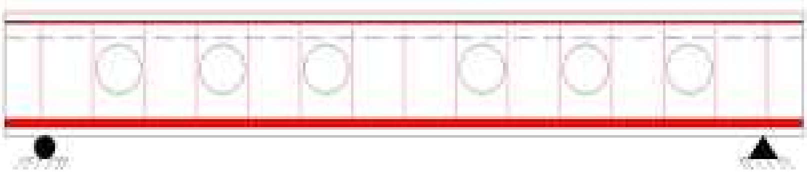

d. Beam with six circular openings (third experimental beam).

Figure 1. Details of the experimental b.

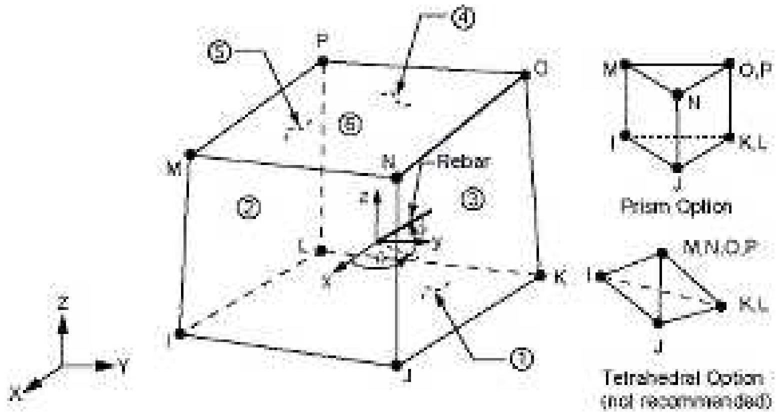

Figure 2. Solid 65 element geometry.

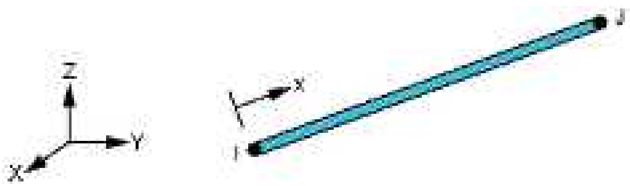

Figure 3. Link 8 element geometry.

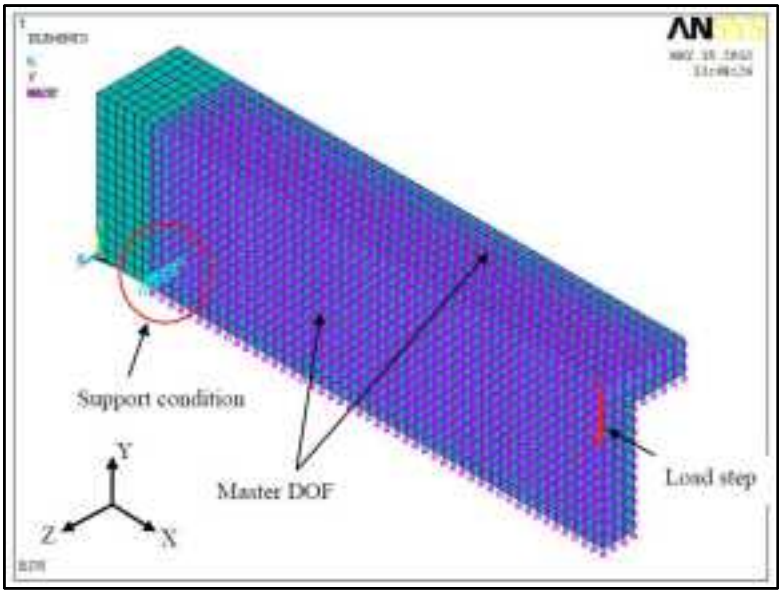

Figure 4. FE mesh, boundary conditions and load step.

Figure 5. Test setup of experimental beams.

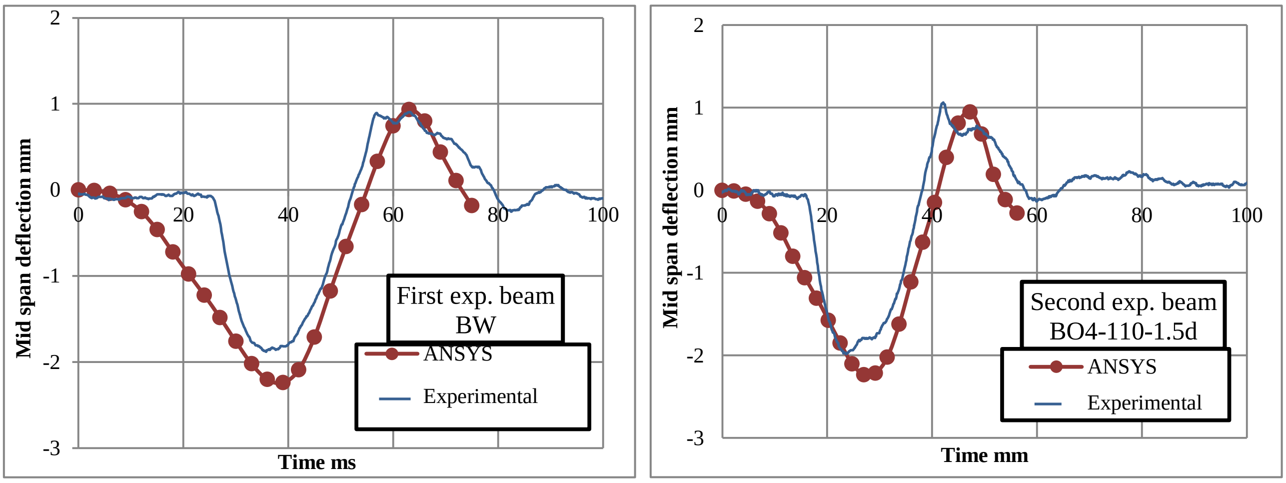

Figure 6. Comparison of predicted results to test results for mid span deflection-time histories for the calibration beams.

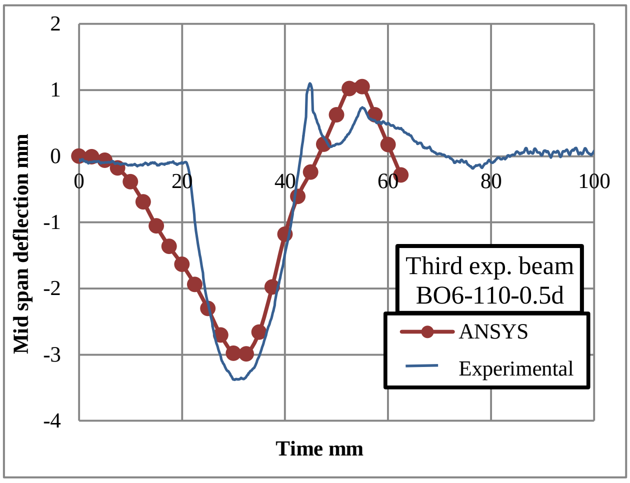

Figure 6. Continue, Comparison of predicted results to test results for mid span deflection-time histories for the calibration beams.

Table 1. Details of the modeled beams.

Modeled beam symbol	**Details**	**Quarter modeled beam in ANSYS**
*BW	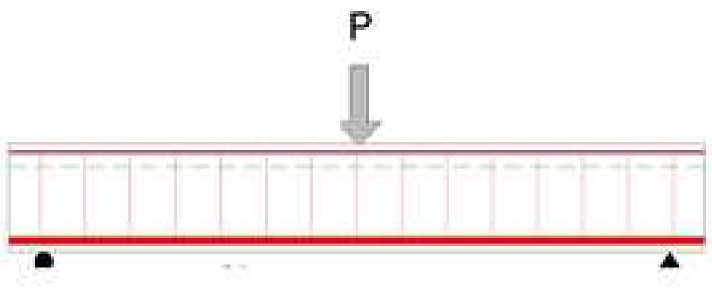	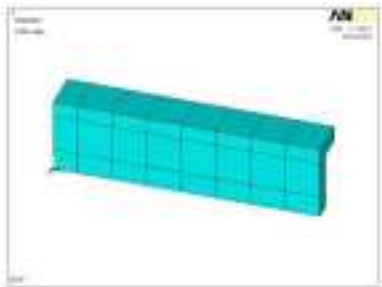
*BO4-110-1.5d	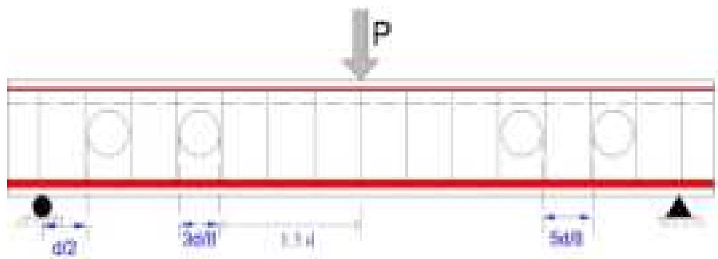	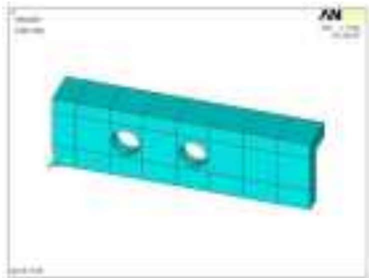
*BO6-110-0.5d	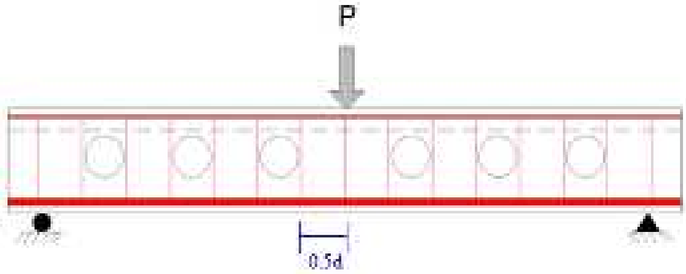	

**BO6-50-0.5d	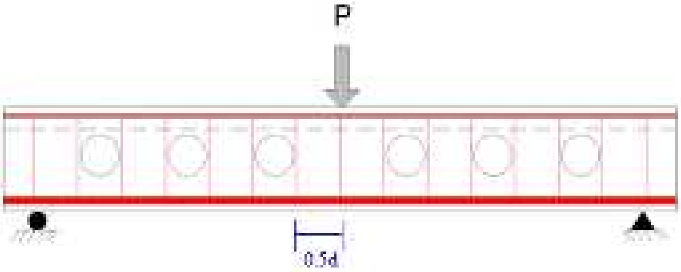	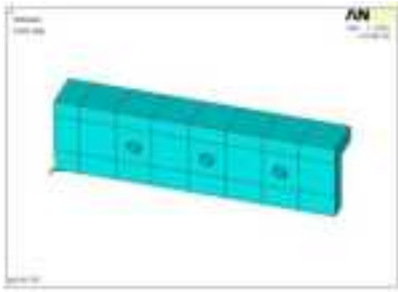
BO6-80-0.5d	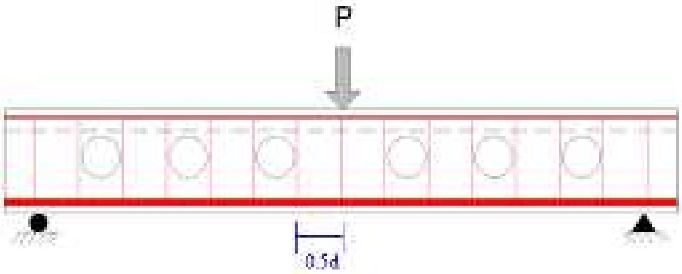	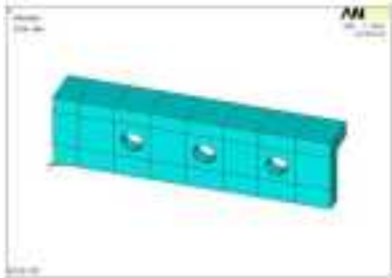
BO6-130-0.5d	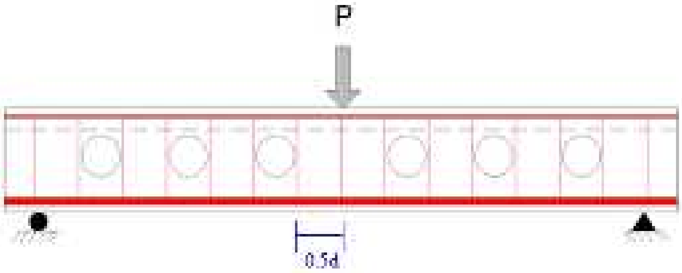	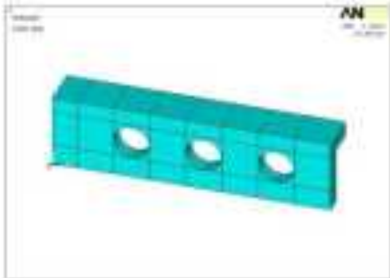
BO2-110-0d	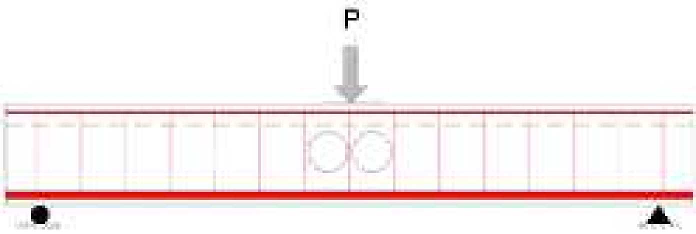	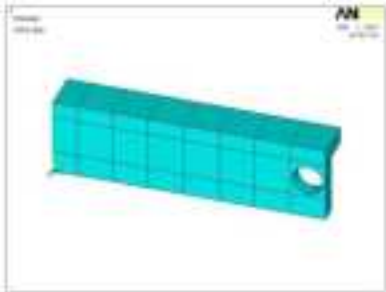
BO2-110-0.5d	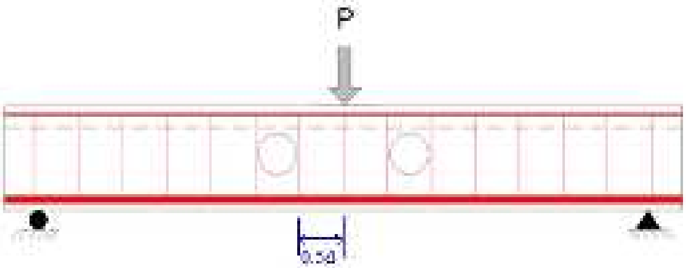	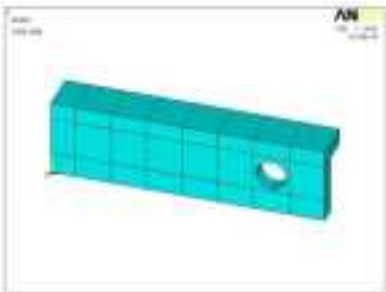

BO2-110-d	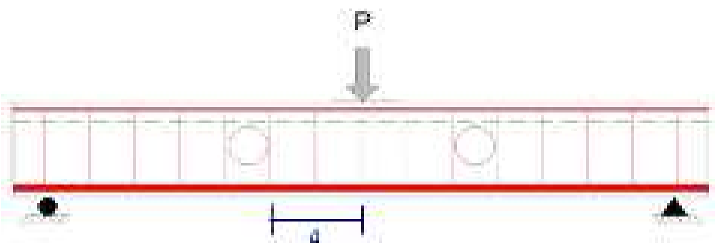	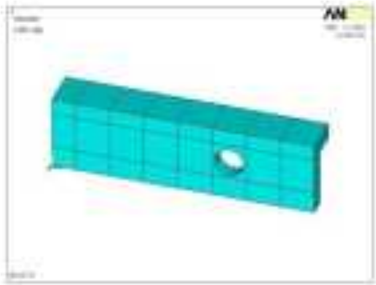
BO2-110-1.5d	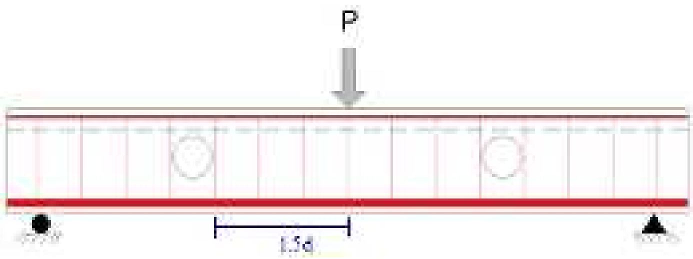	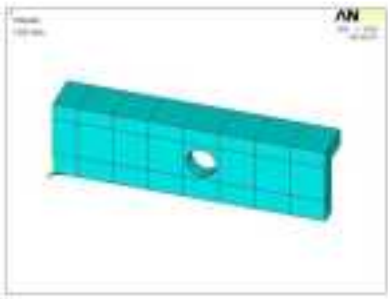
BO4-110-0.5d	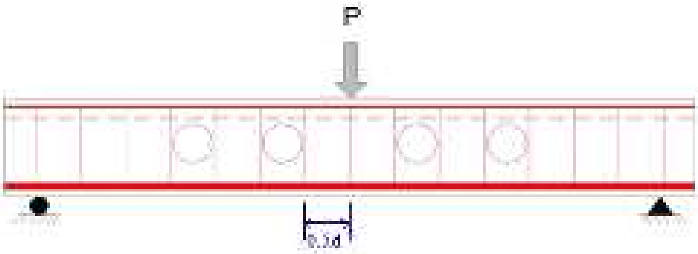	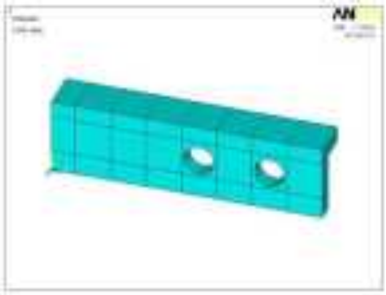
BO6-110-Mid	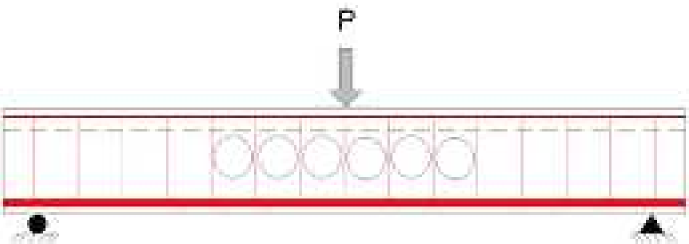	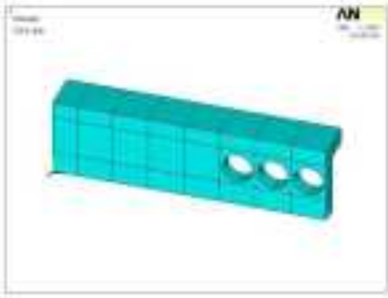

*Experimental beams.

Designation **BO6-50-0.5d (for example): **B**eam with **6 O**penings, opening diameter = **50** mm and the distance between the point of applied load and the beginning of first opening is **0.5d**.

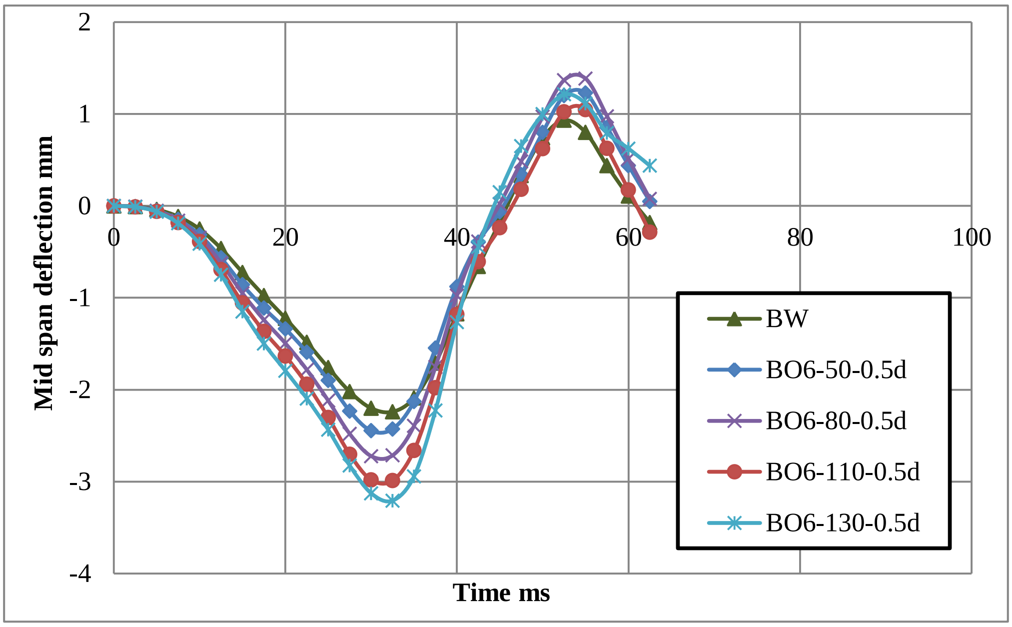

Figure 7. Effect of size of circular web openings on mid span deflection-time histories from ANSYS analyses.

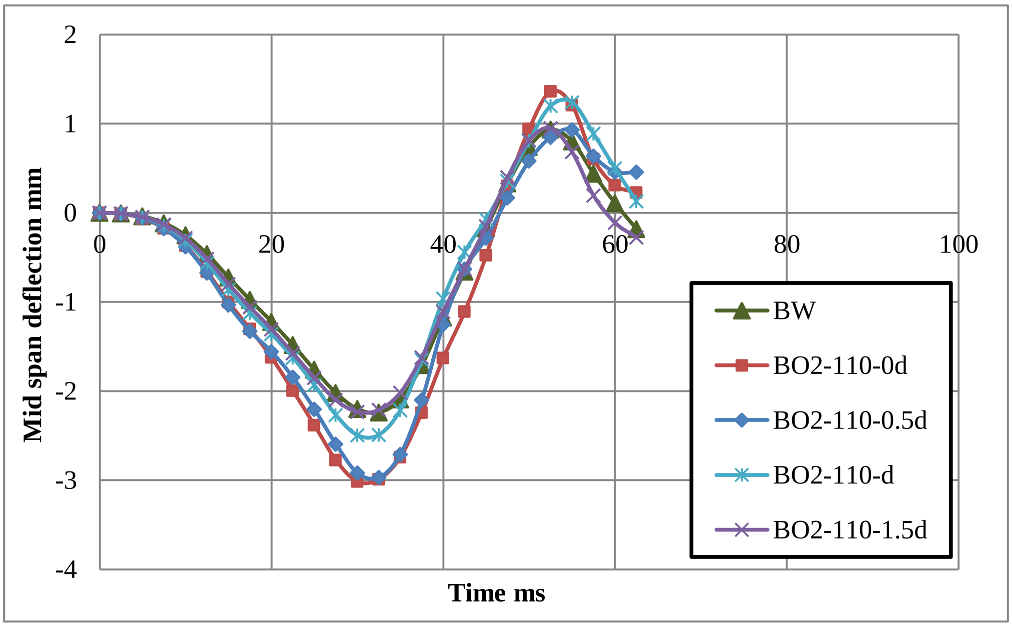

Figure 8. Effect of location of web openings on mid span deflection-time histories from ANSYS analyses.

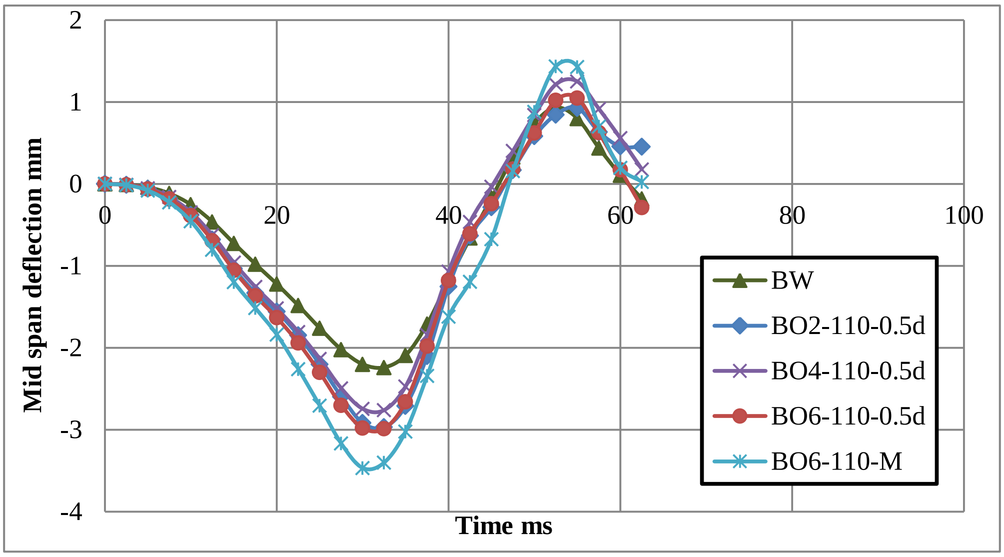

Figue 9. Effect of number of web openings on mid span deflection-time histories from ANSYS analyses.

Performance Analysis of Four Conceptual Designs for the Air Based Photovoltaic / Thermal Collectors

Karima Esmail Amori **Mustafa Adil Al-Damook**
Assistant Professor
Univ. of Baghdad/ Mech. Eng. Dept. , Aljaderiya - Baghdad-Iraq
drkarimaa@yahoo.com ma_eng80@yahoo.com

ABSTRACT

The thermal and electrical performance of different designs of air based hybrid photovoltaic/thermal collectors is investigated experimentally and theoretically. The circulating air is used to cool PV panels and to collect the absorbed energy to improve their performance. Four different collectors have been designed, manufactured and instrumented namely; double PV panels without cooling (model I), single duct double pass collector (model II), double duct single pass (model III), and single duct single pass (model IV) . Each collector consists of: channel duct, glass cover, axial fan to circulate air and two PV panel in parallel connection. The temperature of the upper and lower surfaces of PV panels, air temperature, air flow rate, air pressure drop, wind speed, solar radiation and ambient temperature were measured. The power produced by solar cells is measured also. A theoretical model has been developed for the collector model IV based on energy balance principle. The prediction of the thermal and hydraulic performance was obtained for the fourth model of PV/T collector by developing a Matlab computer program to solve the numerical model. The experimental results show that the combined efficiency of model III is higher than that of models II and IV. The pressure drop of model III is less than that of models I and IV, by (43.67% and 49%). The average percentage error between the theoretical and experimental results was 9.67%.

Keywords: solar energy; hybrid collector; PV/T; thermal; electrical; performance; air based collector.

تحليل الأداء لتصاميم مختلفة لمجمعات شمسية هوائية حرارية/ فوتوفولطائية

كريمة اسماعيل عموري **مصطفى عادل عبد الرحيم**
أستاذ مساعد
جامعة بغداد- كلية الهندسة – قسم الميكانيك

الخلاصة

تم التحقيق عمليا من الأداء الحراري والكهربائي لتصاميم مختلفة لمجمعات شمسية هوائية مهجنة (فوتوفولتائية/ حرارية). استخدم الهواء لتبريد الألواح الشمسية وتجميع الطاقة الممتصة لتحسين اداء الالواح. تم تصميم وتصنيع وتجهيز اربعة مجمعات شمسية مختلفة بأجهزة القياس ، المجمعات كانت لوحين شمسيين مربوطين بدون تبريد (نموذج I) ، مجمع ذومجرى منفرد ومرور مزدوج للمائع (نموذج II) ، مجريين مع مرور منفرد للمائع(نموذج III) ، و مجرى منفرد ومرور منفرد(نموذج IV). يتكون كل مجمع شمسي من: مجرى، غطاء زجاجي، مروحة محورية لتدوير الهواء ولوحين شمسيين مربوطان على التوازي. قيست درجة حرارة السطح العلوي والسفلي للألواح ، درجة حرارة الهواء، معدل جريان الهواء، وهبوط الضغط له، سرعة الرياح، الأشعاع الشمسي، ودرجة حرارة الجو والقدرة المنتجة من قبل الألواح الشمسية. تم بناء نموذج نظري للمجمع الشمسي الرابع بأعتماد مبدأ الأتزان الحراري. تم التوصل الى تخمين الأداء الحراري والهيدروليكي للنموذج الرابع ببناء برنامج حاسوبي بلغة ماتلاب لحل النموذج الرياضي. بينت النتائج العملية ان الكفاءة المركبة للنموذج الثالث كانت اكبر من تلك الخاصة بالنموذج الثاني والرابع. ان هبوط الضغط للنموذج الثالث كان اقل من ذلك المسجل للنموذج الثاني والرابع بمقدار (43.67% و 49%). أن متوسط نسبة الخطأ المئوية بين النتائج العملية والنظرية كانت 9.67%.

الكلمات الرئيسية: طاقة شمسية، مجمع هجين ، حراري، كهربائي ، اداء ، مجمع هوائي.

1. INTRODUCTION

Photovoltaic thermal hybrid solar collectors (hybrid PV/T systems), are systems that convert solar radiation into thermal and electrical energy. These systems combine a photovoltaic cell, with a solar thermal collector which converts part of the solar radiation (electromagnetic radiation (photons)) into electricity, and the other part is an energy absorbed by the black surface which heats a flowing fluid. Photovoltaic (PV) cells suffer from a drop in efficiency with the rise in their temperature.

Many experimental studies have been reported on the photovoltaic-thermal (PV/T) system, **Kern and Russell 1978.** presented the concept of PV/T collector using water or air as a fluid for removing the absorbed energy. **Raghuraman 1981.** developed two separate one-dimensional models for the prediction of the thermal and electrical performance of both liquid and air flat plate (photovoltaic/ thermal) collectors. **Garg and Adhikari 1997.**analyzed a PV/T air heating system of a single and double glass covers. **Sopian et.al. 2000.** developed and tested a double pass photovoltaic thermal solar collector suitable for solar drying applications. **Chow et al. 2003.** investigated the BIPVT options of a hotel building in South China at (22.2^o N). The PV/T face was attached to a full day air conditioned service room to investigate its cooling by means of natural flow of air behind the PV models. **Othman et al. 2005.**studied theoretically and experimentally the PV/T solar air collector with concentrating reflectors. **Shahsavar et al. 2010.** designed, built and tested a PV/T air collector in Kerman, Iran under natural and forced convection with two, four and eight fans operating together to circulate air. **Prashant et al. 2011.**presented a new design of a parallel flow solar air heater with packed material in its upper channel to be capable of providing a higher heat flux compared to the conventional non-porous bed double flow systems. The collector efficiency of upward-type double-pass flat plate solar air heaters with fins attached and external recycle is investigated theoretically by **Chii et al. 2011,** and , **Ma et al. 2011**. They proposed a design of a solar collector that is able to provide both hot water and hot air to increase the annual thermal conversion ratio of solar energy.

The objective of the present work is to identify experimentally the electrical and thermal performance of PV/T collectors under Iraq climate conditions considering the effect of air flow rate.

2. EXPERIMENTAL WORK

Four different models of hybrid PV/T collectors are designed manufactured and instrumented. These models are shown in **Figs. 1, 2 and 3**. In these models two PV modules in parallel connection are mounted in wooden structure. The air duct was perfectly sealed to avoid air leakage. Air has been passed through the duct by using a single DC fan of (6 W) power at the duct outlet. The PV/T system has been mounted on a steel frame with the feasibility to change the inclination angle. The specifications for PV module and PV/T collector used in this work are given in Tables 1 and 2 respectively. In model II, air flows in a single duct for one pass over and under the absorber as shown in **Fig**.**1a**. In model III air flows in two ducts over and under the PV module in the same direction with single pass, while in model IV air passes in a single duct below the absorber only, as shown in **Fig**. **3**.

Twenty two calibrated thermocouples of type k are used to measure the temperatures in this work. Ten of them are distributed at equal distances at back surface of the panels with three thermocouples are fixed on the upper surface along the PV panel at distances of (0.1m , 0.3m , 2.2m) from the inlet. Eight thermocouples are distributed along the air duct of models II, III, and IV including the inlet and outlet air temperature, and one thermocouple is fixed on the collector glass cover, as shown in **Fig**.**4**. The ambient temperature was measured at 1.5m above ground. All thermocouples are connected to a selector switch type K. The air velocity was measured using a multifunctional anemometer device (model (EM-9000). The air pressure drop is measured using inclined differential manometer between two points namely ducts' inlet and outlet as shown in **Fig**.**1a**. The pressure drop is calculated from manometers reading (H) as

$$\mathbf{\Delta p = \gamma H.\sin\theta} \tag{1}$$

where θ is manometer inclination angle.

The solar radiation is measured by using south facing Solar meter (TES-1333R Data logging) at the same collector tilt angle.

The power generated by the PV panels was calculated according to the equation:

$$\mathbf{P_{pv} = V * I} \tag{2}$$

where V is the voltage and I is the current produced by PV panels. These parameters are measured by multimeter model (3500/3600) made in England especially for AC or DC applications.

2.1 Experimental Procedure

The test of the PV/T collectors and PV array for eight months from December 2010 to July 2011 includes.

1. Testing model I without load for ten clear days and with different flow rate ranging from [36.2-83.1] l/s. This test was carried out during December, 2010 and January, 2011.
2. The data of model I & model II were taken at the same time for ten clear days with different flow rate ranging from [66.62-126.5] l/s during February & March, 2011.
3. Model III is tested at flow rate [66.62-126.5] l/s with the same manner in 1 and 2 above during April & May 2011.
4. Model IV is tested during July 2011.

3. THEORETICAL MODEL

The fourth model used in this work is composed of a single glass cover, a PV modules and a well insolated back plate as shown in **Fig.5**. The energy balance principle is applied on each element with the following assumptions: The system is in a quasi-steady state condition, There is no air leakage from the hydraulically smooth flow channel, Heat capacity of the glass cover, enclosed air, PV modules absorber and bottom plates are negligible at steady state, The temperatures of the PV modules, glass, absorber and bottom plates vary only along the x-direction of the air flow, and heat loss from the sides of the duct is very small and hence neglected **, Duffie, and Beckman 1990**. **Fig.5** shows the various heat transfer coefficient along the surface of the system.

- Absorber PV/T (**Fig. 6**)

$$(\qquad)\qquad(\qquad)\qquad(\qquad) \tag{3}$$

- Bottom Plate (**Fig**. **7**) **(Al-Damook 2011)**

$$(\qquad)\qquad(\qquad)\qquad(\qquad) \tag{4}$$

3.1 Calculation of Heat Transfer Coefficients

3.1.1 Heat Loss Coefficients

The overall heat loss factor consists of top, bottom, and edge heat loss coefficients.

The bottom loss coefficient (Ub) is evaluated by considering conduction and convection losses from the absorber PV/T in the downward direction through the bottom of the collector. It can be evaluated as: **(Sumeet 2010)**

$$\mathbf{U_b} = \left[\frac{\mathbf{L_c}}{\mathbf{K_c}} + \frac{\mathbf{L_w}}{\mathbf{K_w}} + \frac{1}{\mathbf{h_w}}\right]^{-1} \tag{5}$$

where $\mathbf{h_w}$ is the wind heat transfer coefficient, which is calculated from: McAdams model **, Francis 2002**.

h . . ind (6)

The top heat loss is given by: **, Duffie, and Beckman 1990.**

$$\mathbf{U_t} = \left[\frac{1}{\mathbf{h_w} + \mathbf{h_{rw}}} + \frac{1}{\mathbf{h_{pc}} + \mathbf{h_{rpc}}} \right]^{-1} \tag{7}$$

where,

$\mathbf{h_{rw}}$ = radiation heat transfer coefficient between cover glass and the sky given as:

hr g (c s)(c s) (8)

$\boldsymbol{\varepsilon_g}$ = glass emittance

σ = Stefan-Boltzmanns' constant equals to $5.67*10^{-8}$ $W/m^2.K^4$

$\mathbf{T_s}$ = sky temperature is usually calculated from:

(9)

$\mathbf{h_{rpc}}$ = radiant heat transfer coefficient from absorber PV/T to cover is given as:

$$\mathbf{h_{rpc}} = \frac{\boldsymbol{\sigma}(\mathbf{T_{pm}^2} + \mathbf{T_c^2})(\mathbf{T_{pm}} + \mathbf{T_c})}{\frac{1}{\boldsymbol{\varepsilon_p}} + \frac{1}{\boldsymbol{\varepsilon_g}} - 1} \tag{10}$$

where $\boldsymbol{\varepsilon_p}, \boldsymbol{\varepsilon_g}$ = plate and glass emittance.

3.1.2 Heat Transfer Coefficient in the Upper Channel

The natural convection heat transfer coefficient ($\mathbf{h_{pc}}$) between the absorber plate and glass cover of the collector model IV is estimated by the equation proposed by **Meyer et al. (Hussam 2011)** as:

u c r n (11)

where, c and n are constants affected by the tilt angle. These constants are listed in table (3).
The Grashof No. (Gr) is defined as

$$\mathbf{Gr} = \frac{\mathbf{g}\boldsymbol{\beta}_v(\mathbf{T_p} - \mathbf{T_a})\mathbf{L_m^3}}{\boldsymbol{\nu}^2} \tag{12}$$

where: g=Gravitational acceleration (m/s^2). β_v=volumetric expansion coefficient (K-1) given as:

$$\boldsymbol{\beta}_v = \frac{1}{\mathbf{T}} \tag{13}$$

$\mathbf{L_m}$ = Mean space between absorber plate and glass cover (m).

$\boldsymbol{\nu}$ = Kinematic air viscosity (m^2/s).

The convective heat transfer coefficient is then calculated as:

$$h_{pc} = \frac{NuK_a}{L_m} \tag{14}$$

where K_a is air thermal conductivity (W/m.K)

3.1.3 Heat Transfer Coefficient in Lower Channel

The forced convection heat transfer coefficient between air stream and absorber plate (h_f) of collector model IV and the properties of air are calculated at local fluid temperature (T_f) by: ,**Duffie, and Beckman1990.**

$$u_f \quad e \quad r \tag{15}$$

where:

$$e \quad \text{——} \quad \frac{\dot{}}{(\quad)} \tag{16}$$

D_h = The hydraulic diameter of the air passage is calculated as:

$$D_h = \frac{2L_2 h}{L_2 + h} \tag{17}$$

where L_2 = collector width, h is duct inlet height, $\dot{m}$ = air flow rate (kg/s.).

μ air dynamic viscosity (kg/m.s)

Thus, the convective heat transfer coefficient can be obtained as:

$$h_f \quad \frac{a}{h} \quad u_f \tag{18}$$

A Matlab computer program is developed to solve the numerical model. **Fig 8.** illustrates the flow chart of this program.

4. RESULTS AND DISCUSSION

Fig.(**9** shows the ambient conditions in Fallujah city for selected clear days during the test period namely; (28/12/2010, 28/4/2011 and 2/7/2011. The ambient temperature follows the incident solar radiation from sunrise to solar noon, after which a considerable deviation in its behavior is indicated in April and July.

Fig.**10** demonstrates the effect of PV panel temperature on electrical power generated at different flow rates for models (I , II and III) . It is obvious that the electrical power increases when the panel temperature decreases.

Fig.**11** presents the hourly distribution of combined efficiency, thermal efficiency and electrical efficiency for models I, II and III. Table (4) illustrates a comparison between the electrical and combined efficiencies of models II, and III with model I higher efficiency was recorded for model III.

Fig.**12** shows the effect of air flow rate on average PV panel temperature. The heat transfer coefficient increases with increasing of mass flow rate which leads to absorb more heat and decrease the temperature difference between the surface panel and flowing air. This result agrees with that obtained by **(Jin et al. 2010)**.

Fig. **13** demonstrates the effect of Reynolds number on pressure drop for models II & III. It is clear that the pressure drop increases with increasing of Reynolds number according to:

$$\textbf{pressure loss} = f_f\left(\frac{L\mu^2}{D_h^5}\rho\right)Re^2 \tag{19}$$

Fig. 14a shows a comparison between the electrical power produced by models I and II on 29/3/2011. Lower values are indicated for model I than that for model II due to: optical losses, edge losses, difficulty of cleaning the panel, which leads to dust accumulation on the panels.

Fig.14b demonstrates hourly temperature distribution of the upper and lower PV panel surfaces on (29/3/2011) for models I & II. The maximum temperature differences between model I and II for the upper and lower surfaces were 14.94 ^{o}C and 15.2^{o}C, respectively and the minimum temperature differences were 2.11^{o}C and 6.7^{o}C, respectively.

4.1 Comparison with Previous Published Results

A quantitative comparison between the present results and previously reported results is difficult due to the differences in local ambient conditions such as; solar radiation, ambient temperature, wind speed, humidity and the type of the solar panel used. So a qualitative comparison have been adopted as shown in **Fig.15**, which illustrates a very good agreement between the present work and the previously published results.

4.2 Comparison between Theoretical and Experimental Values for Model IV

Fig.16 presents good agreement between theoretical and experimental results of air temperature in the lower channel for model IV. The maximum percentage deviation is 3.41%.

Fig.17 demonstrates a comparison between theoretical and experimental values of heat gain for model IV. The deviation between them is due to the optical losses because of dust accumulation. The percentage error was 13.2%.

Fig.18 illustrates a comparison between theoretical and experimental values for thermal efficiency. The deviation between them is due to several factor namely:

- Fluctuated wind speed values.
- Over all heat transfer coefficient.
- Variation in real ambient temperature.
- Optical losses.

The maximum percentage deviation was 7.6%.

4.3 Comparison between the Four Models for Multi Parameters

The maximum average parameter values for all measured days (thermal efficiency, electrical efficiency, pressure drop, power consumed (p_c) due to air mass flow rate, power of fan, temperature rise and Reynolds number are given in Table (5) . This table also demonstrates the percentage enhancement for any parameter which is calculated as:

$$\frac{\quad}{\quad} \tag{20}$$

5. CONCLUSIONS

From the experimental investigation of the models I, II, III and IV in Iraq climate conditions, the following conclusions can be concluded. The electric efficiency was a function of PV panel temperature; the increase of temperature above the design temperature decreases the efficiency of the panel. It is found that the acceptable range of temperature and solar radiation were (22^{o}C-38^{o}C) and (550 – 850) W/m^2 respectively, and depending on the grade of PV panel used (A, B, C). The thermal efficiency of model III was 102.7 % greater than that of model IV. The thermal efficiency of model III is 26.9 % greater than that of model I. The combined efficiency of model III was 90.4 % greater than that of model IV. The combined efficiency of model III is 5.91 times the efficiency of model I. The total efficiency (combined efficiency) of model III was 9.45 times that of model II in the measured days. The combined efficiency of model (I) is 7.29 times greater than that of model

II in the measured days. The pressure drop inside the duct of model III was 43.67 % less than that of model I in the measured during days despite the fact that mass flow rate for model III was greater than that of model I. The thermal behavior was improved by increasing the flow rate above 130 L/s when the range of solar radiation was above 530 W/m^2. The average percentage error between theoretical and experimental results was 9.67%.

REFERENCES

- Alghareeb, A. A.,1992, *The effect of thermal radiation and heat transfer area on the performance of a solar air heater*, M.Sc. thesis, univ. of Basrah, Chemical Engineering.

- ASHRAE Applications Handbook, 1999. *Chapter 32 by American Society of Heating, Solar Energy Use* (ASHRAE). Atlanta, GA.

- Baa, Y. and Adam, N. 2008, *Performance analysis for flat plate collector with and without porous media*, Journal of Energy in Southern Africa, V.19, No 4.

- Chii, D. H., HoMing, Y., Tsung, C. C., 2011, *Collector efficiency of upward-type double pass solar air heaters with fins attached*, International Communications in Heat and Mass Transfer, V.38, pp. 49–56.

- Chow, T. T., Hand, J. W., Strachan, P. A., 2003, *Building-integrated photovoltaic and thermal applications in a subtropical hotel building, Applied Thermal Engineering*, V.23(16),pp.2035-2049.

- Duffie, J.A., Beckman, W. A., 1990, *Solar Engineering of Thermal Processes , John Wiley & Sons, Inc.*

- Francis, W., 2002, *Heat transfer loss or gain*) coefficients from bare flat plate solar heat collectors, The Zomeworks Program Office of the Double Play System: Summer Cooling and Winter Heating.

- Garg, H. P., Adhikari, R. S., 1997, *Conventional hybrid Photovoltaic/Thermal* (PV/T) air heating collectors: steady-state simulation, Renewable Energy, V.11, No.3, PP.363-385.

- Hussam, H. J., 2011, *Evaluation of a solar assisted desiccant cooling system for a small meeting hall*, M.Sc thesis, university of Baghdad in Mechanical Engineering.

- Jin, L.G., Ibrahim, A., Chean, Y.K., Daghigh, R., Ruslan, H., Mat, S., Othman, M.Y., Sopian, K., 2010, *Evaluation of Single-Pass Photovoltaic-Thermal Air Collector with Rectangle Tunnel Absorber*, American Journal of Applied Sciences, V.7 (2), pp.277-282.

- Kern Jr. EC, Russell Mc., 1978, *Combined Photovoltaic and Thermal Hybrid Collector System*, Proceedings of 13th IEEE Photovoltaic Specialist pp.1153–7.

- Ma J., Sun, W., Ji J., Zhang, Y., Zhang, A., Fan, W., 2011, *Experimental and theoretical study of the efficiency of a dual-function solar collector*, App. Thermal Eng., V.31, pp.1751– 1756.

- Mustafa Adil AlDamook, 2011, *Performance analysis of various conceptual design for the air based Photovoltaic*/Thermal collectors, M.Sc. thesis, Univ. of Baghdad, Dept. of Mech. Eng.

- Otham, M. H., Yatim, B., Sopian, K., AbuBakar, M. N., 2005, *Performance analysis of a double-pass photovoltaic/thermal* (PV/T) solar Collector with CPC and Fins, Renewable Energy V.30,pp .2005-2017.

- Othman YM, Yatim B, Sopian K, AbuBakar M.N., 2007, *Performance studies on a finned double-pass photovoltaic-thermal* (PV/T) solar collector, Desalination V209, pp.43-49.

- Prashant, D., Thakur, N. S., Kumar, A., Singh,S., 2011, *An analytical model to predict the thermal performance of a novel parallel flow packed bed solar air heater,* Applied Energy,V.88 , pp. 2157-2167.

- Raghuraman, P., 1981, *Analytical predictions of liquid and air photovoltaic/Thermal flat plate collect performance,* J. of solar energy eng., V. 103, Nov., PP. 291-298.

- Shahsavar, A., Ameri, M., 2010, *Experimental investigation and modeling of a direct coupled PV/T air collector*, Solar Energy, V.84, pp.1938-1958.

- Sopian, K., Liu, H. T., Kakac, S., Veziroglu, T. N., 2000, *Performance of a double pass photovoltaic thermal solar collector suitable for solar drying systems,* Energy Conversion and Management, V.41, pp.353-365.

- Sopian K., Alghoul M. A., Alfegi E. M., Sulaiman M. Y. and Musa E A., 2009, *Evaluation of thermal efficiency of double-pass solar collector with porous–non porous media*, Renewable Energy, V.34, pp.640–645.

- Sumeet, S., 2010, *Mathematical modeling of solar air heater with different geometries*, M.Sc. thesis, Thapar University, Patiala Mechanical Eng. Dept.

NOMENCLATURE

Latin Symbols		Re	Reynolds No.
A_c	area of PV cell m^2	S	Solar radiation (W/m^2)
A_p	area of absorber plate m^2	S_g	energy absorbed by the glass cover (W/m^2)
Cp	air specific heat (J/kg.K)	S_p	energy absorbed by the absorber plate (W/m^2)
CFD	Computational fluid dynamics	t_c	thickness of PV cells (m)
D	depth of air duct (m)	t_g	thickness of glass cover (m)
D_h	hydraulic diameter of the air duct (m)	t_{in}	thickness of insulation (m)
dx	length of Elemental duct division (m)	T_a	Ambient air temperature (K).
e	root mean square of percentage deviation	T_{bm}	bottom plate temperature (K)
F	Packing factor	T_f	fluid (air) temperature (K)
g	gravitational acceleration (m/s^2)	T_g	Collector glass cover temperature (K).
G	incident solar radiation (W/m^2)	T_{pm}	absorber (PV module) temperature (K).
H	manometer reading (m)	T_{ref}	reference temperature (K).
h_f	fluid convection heat transfer coefficient (W/m^2K)	T_s	sky temperature (K).

h_p	forced convection heat transfer coefficient (W/m^{2}K)	V_{pv}	PV voltage (volt)
h_{p-g}	free heat transfer coefficient in the air gap (W/m^2)	V_w	wind velocity (m/s)
$h_{r,g-sky}$	radiation heat transfer coefficient between absorber PV/T and sky (W/m^{2}K)	W	width of the air duct (m)
$h_{r,pb}$	radiation heat transfer coefficient between absorber PV/T and bottom plate (W/m^{2}K)	U_t	Overall top heat loss coefficient (W/m2.K)
$h_{r,pg}$	radiation heat transfer coefficient between absorber PV/T and glass cover (W/m^{2}K)	V	PV voltage (Volt)
h_w	wind heat transfer coefficient (W/m^2.K),	x	distance along the duct
I	PV current (Amp.)		**Greek Symbols**
K_c	thermal conductivity of bottom plate (W/m.K)	α_c	absorptivity of cells
K_{in}	thermal conductivity of insulation (m)		
K_w	thermal conductivity of wood (m)	α_p	absorptivity of the plate
L	length of absorber plate (m)	β	collector tilt angle (deg)
L_1	Collector Length (m)	ε_g	glass emittance
L_2	Collector width (m)	ε_p	Plate emittance
L_c	thickness of bottom plate (m)	η_c	conversion efficiency of PV module
L_w	thickness of wood (m)	μ	dynamic viscosity (kg/m.s)
$\dot{m}$	air mass flow rate, (kg/s)	ρ	density of manometer fluid (kg/m^3)
Δp	pressure drop (Pa)	σ	Stephen-Boltzmann constant
P_{pv}	power produced by PV (W)	θ	manometer tilt angle (deg)
r	linear coefficient of correlation	τ_g	transmissivity of glass
Ra	air gap Rayleigh No.	τ_{po}	transmissivity of pottant

Table 1. Specification of PV/T collectors.

Collector tilt angle (degree)	44^o(II), 23^o (III), 5^o (VI) **(ASHRAE Handbook 1999)**
Collector length (mm)	3310
Collector width (mm)	580
Overall height (mm)	60
Upper duct height (mm)	35
Lower duct height (mm)	24
Inlet area(mm^2)	70×540 model II 10.2×540 model III
outlet area(mm^2)	70×540 model II, model III
Plate type	Flat plate
Cover material	Ordinary clear glass, τ . 6 [Sopain et al. (2009)]
Number of covers	1
Thermal conductivity of Insulation material (Wood panel)	k= 0.059 **(Hussam 2011)**
Back insulation thickness (mm)	20

Table 2. Specification of PV panel.

ELECTRICAL DATA	
Maximum Power at STC	60 W
Maximum Power voltage at STC	17.6 V
Maximum Power Current at STC	3.4 Amp
Open Circuit Voltage (V_{oc})	21.6
Short Circuit Current (I_{sc})	3.74
Operating Temperature	25(^{o}C)
Operating Radiation	1000W/m^2
MECHANICAL DATA	
Cell Type	Poly-crystalline
No. of cells and cells Arrangement	60 (6 x 10)
Dimensions(mm)	1200 x 540 x 32mm
Weight	20kg (44.1 lbs)
Front Cover	Tempered glass
Frame Material	Anodized Aluminum Alloy
Standard Packaging (Modules per Pallet)	20 pcs

Table 3. Constants for Eq.(10).

Tilt angle	c	n
0	0.060	0.410
10	0.065	0.400
20	0.070	0.390
30	0.075	0.380
40	0.080	0.367

Table (4): Comparison between PV/T collectors.
(Values are taken at solar noon)

Compare between Models	Combined Efficiency%	Electrical Efficiency	Ratio B/A
I and II	A=9.55 (model I)	9.55 (model I)	7.2
	B=44 (model II)	9.3 (model II)	
III and II	A= 44 (model II)	9.3 (model II)	1.32
	B= 58 (model III)	6 (model III)	

Table (5): Comparison between daily performance parameters for models II, III, IV.

Parameter	Model II	Model III	Model IV	Enhancement ratio% for (model)
Combined efficiency	65.4	78.7	41.35	90.4%(III)
Thermal efficiency	57.1	72.5	35.8	102.7%(III)
( )	73.5	41.4	77.44	49%(III)
Pc(mW)	67	57.8	95.75	39.7%(III)
Temp. rise(^{o}C)	7.2	6.23	8.1	30%(IV)
Power fan( )	33	47	47	21.2(I)

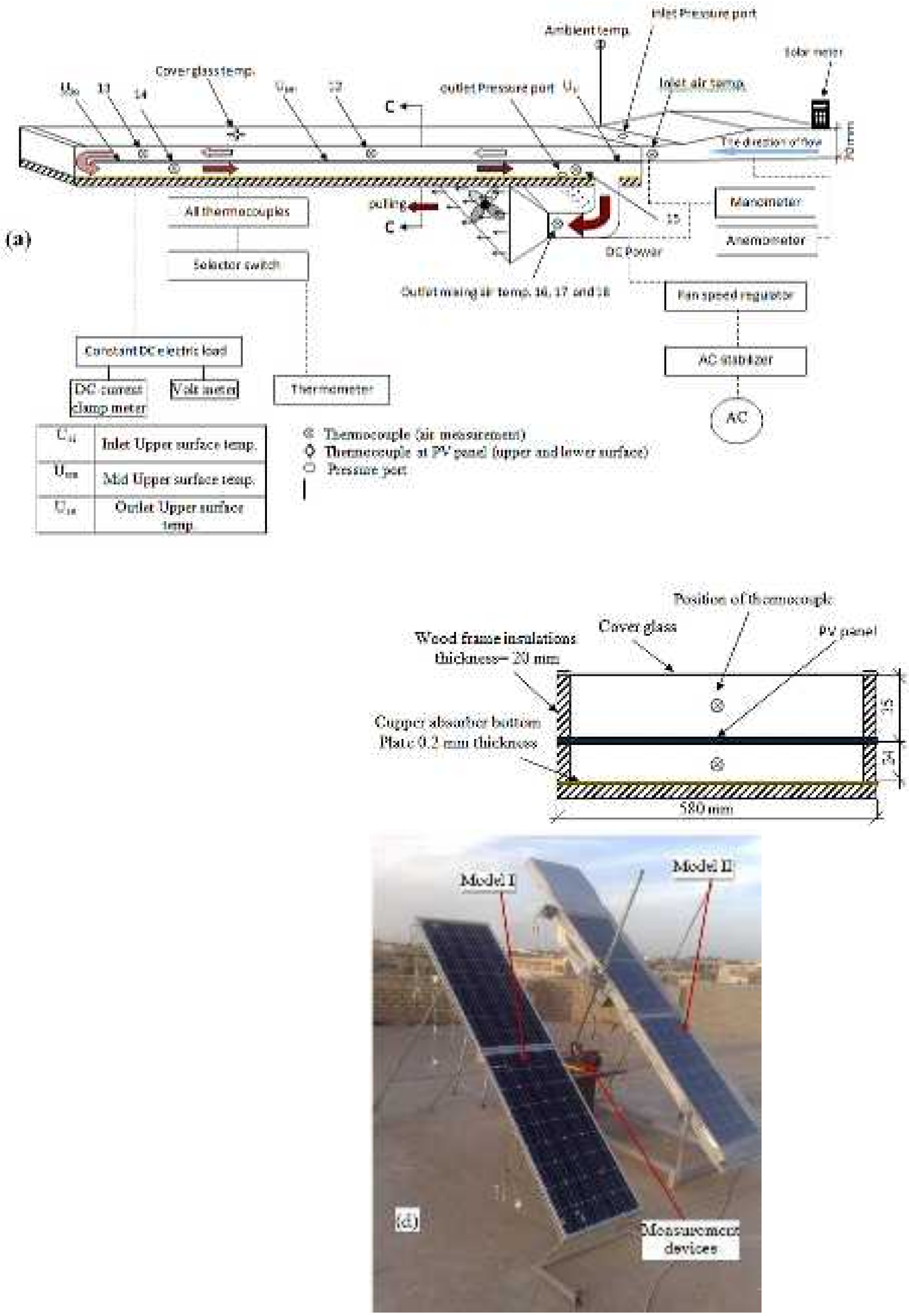

Figure 1. (a) Schematic diagram of experimental setup for model II; (b) Top view of PV panels; (b) Cross section view of C-C, (d) Outdoor test of model I and model II

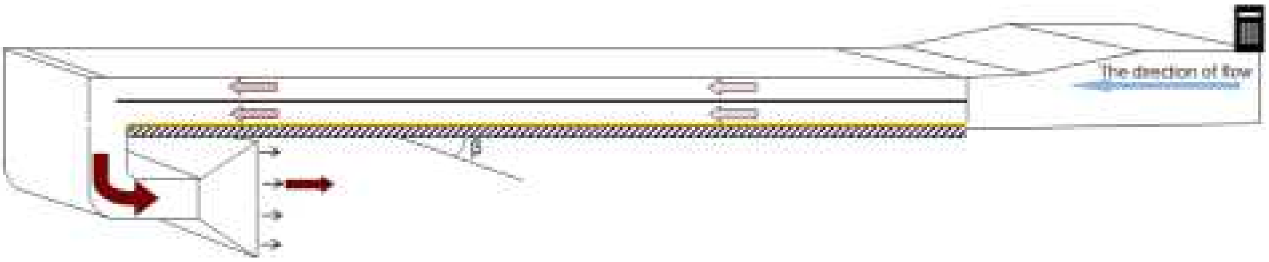

Figure 2. Schematic Diagram of Experimental Setup for Model III.

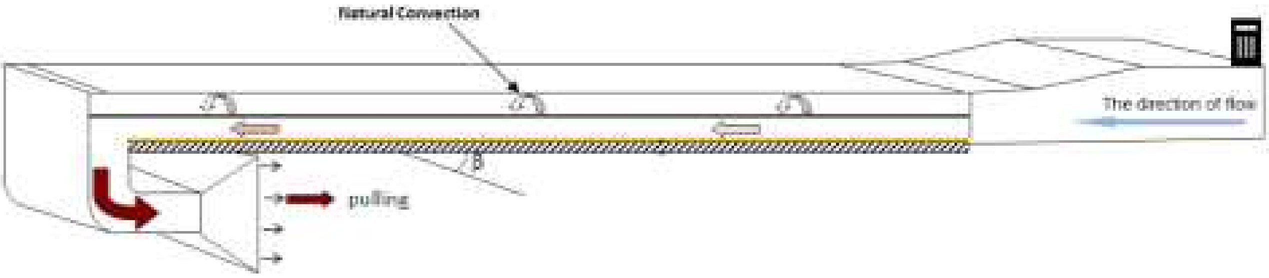

Figure 3. Schematic Diagram of Experimental Setup for Model IV

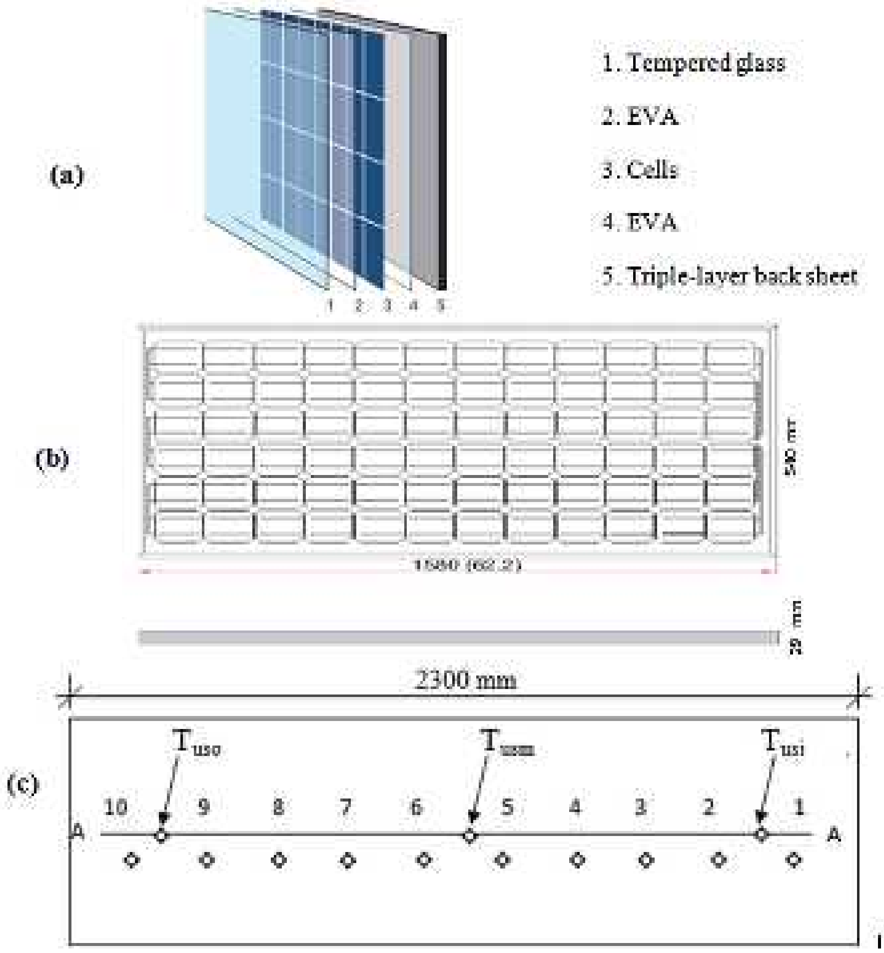

Figure 4. (a) Cross section of the layers for model I,
(b) Top view of PV panel, (c) Thermocouples positions.

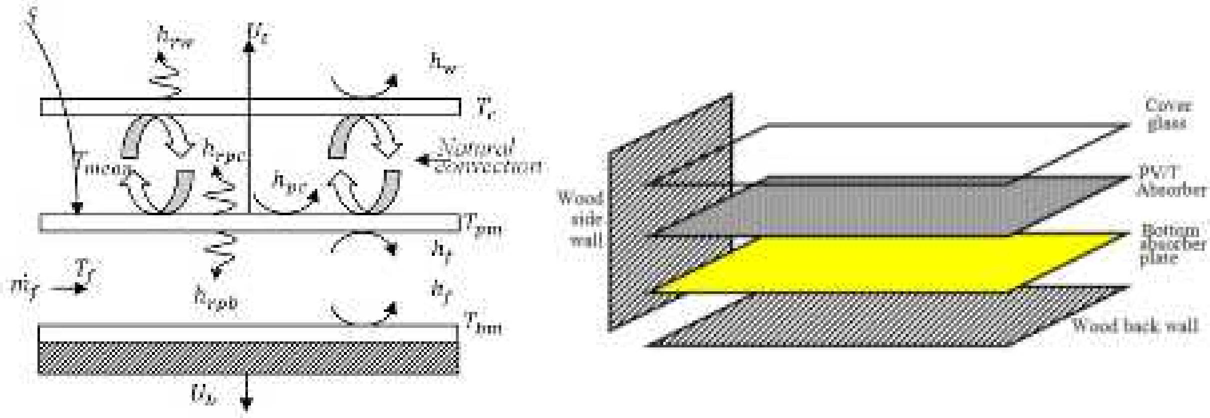

(a) (b)

Figure 5. (a) Various Heat transfer coefficient along the surface of the system. (b)schematic diagram of the studied PV/T air system (Model IV).

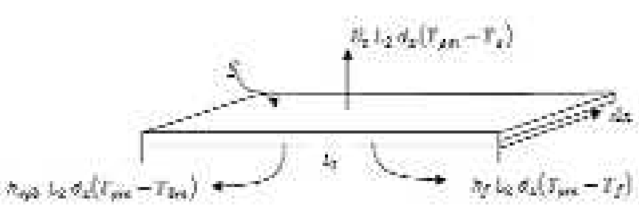

Figure 6. Energy equations for absorber PV/T for model iv

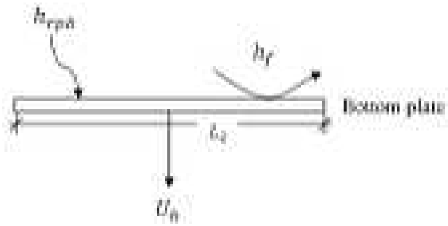

Figure 7. Energy equations for absorber bottom plate for model IV

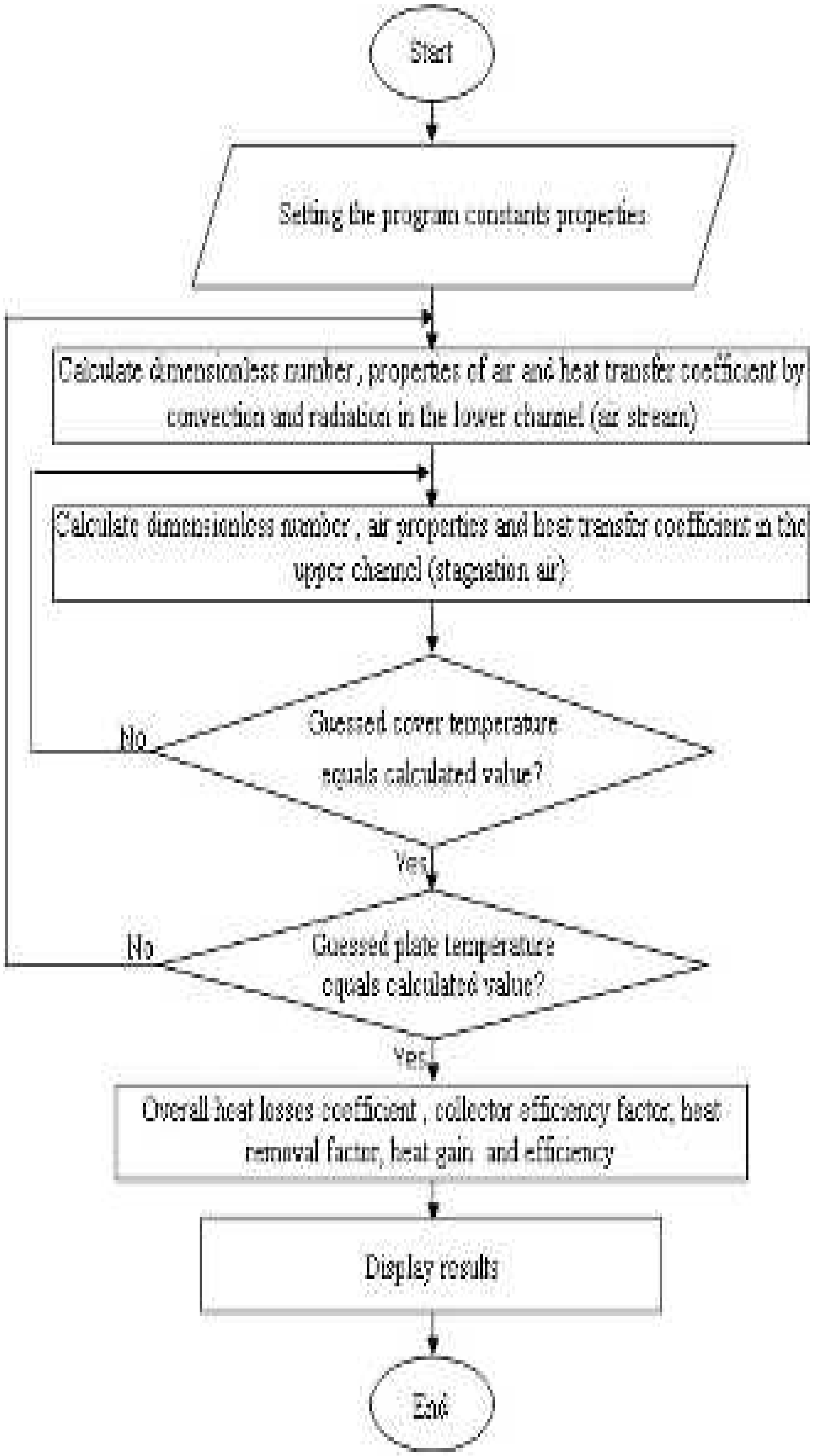

Figure 8. Flow chart of the computer program

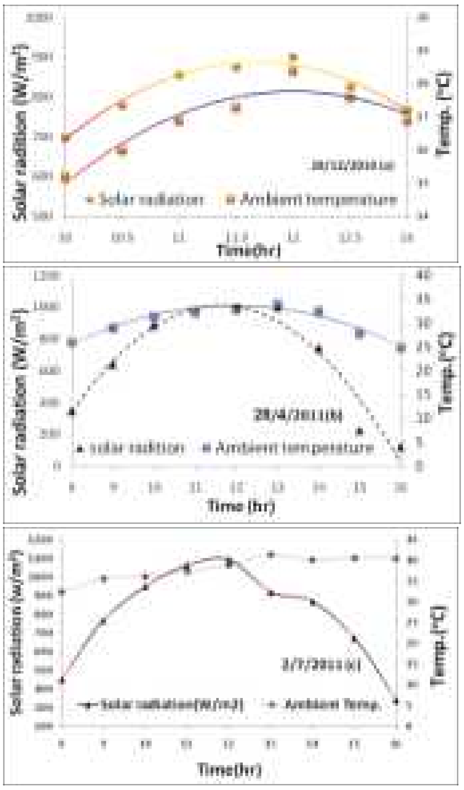

Figure 9. Hourly variation of solar radiation and ambient temperature for selected days from December 2010 to July 2011

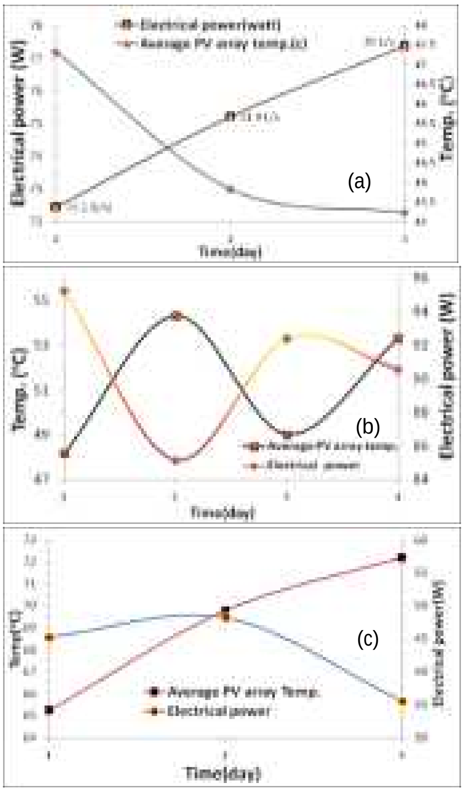

Figure 10. Effect of PV panel temp. on electric power for three models (a) model II (b) model III (c) model IV

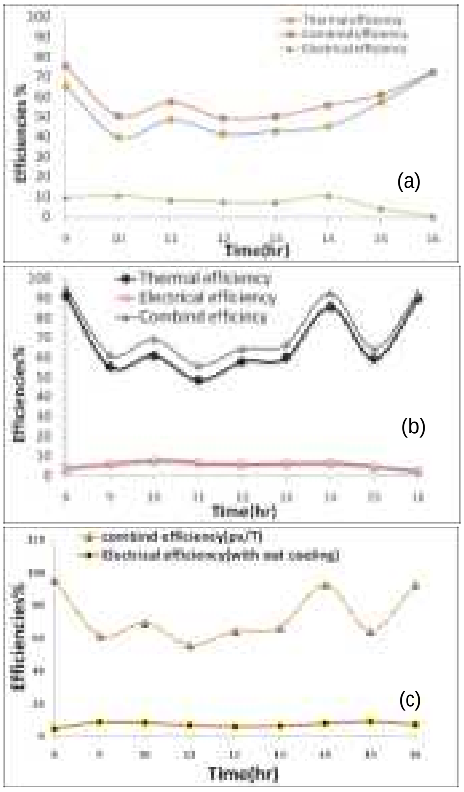

Figure 11. Hourly total efficiency, thermal efficiency and electrical efficiency for a) model II, b) model III, c) models I and III

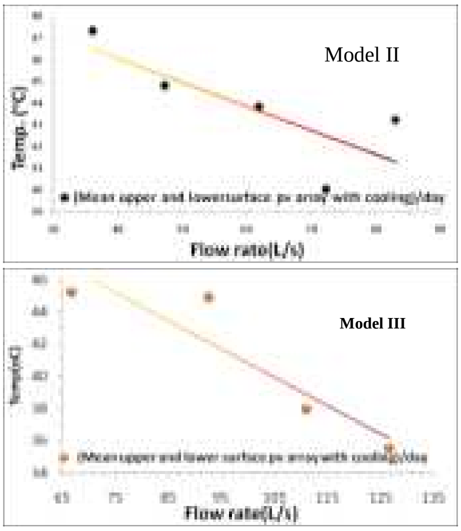

Figure 12. Effect of daily air flow rate on PV panel temp. for models II & III

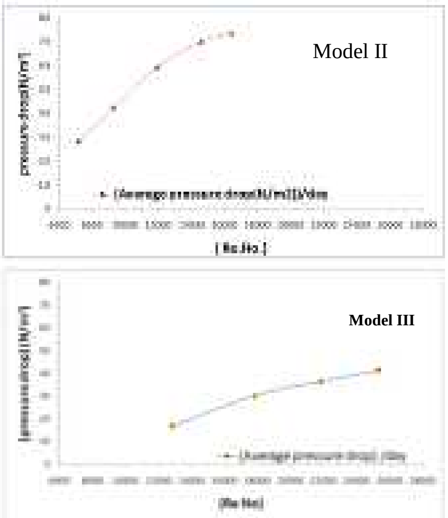

Figure 13. Effect of Reynolds number on pressure drop for models II & III

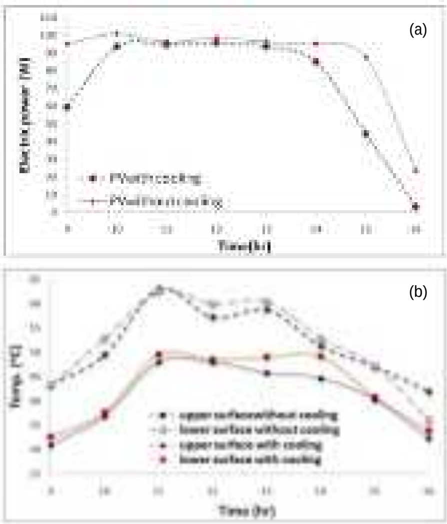

Figure 14. (a) Hourly electrical power produced by models I& II on (29/3/2011) (b) Hourly temperature distribution of the upper and lower PV panel on (29/3/2011) for models I&II

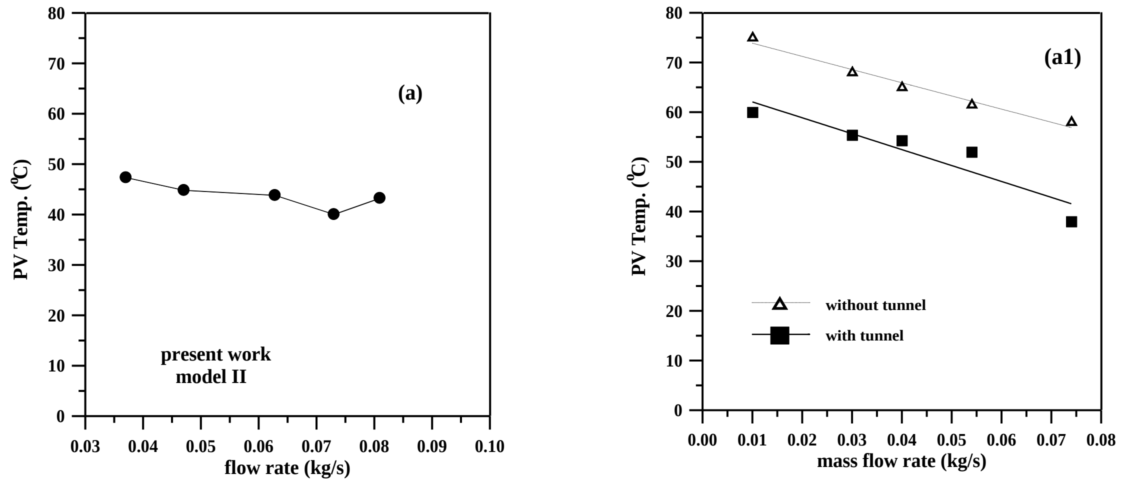

Effect of air mass flow rate on temperature of PV module for collector model II,
(a) present results, (a1) results of **(**Jin et al. 2010)

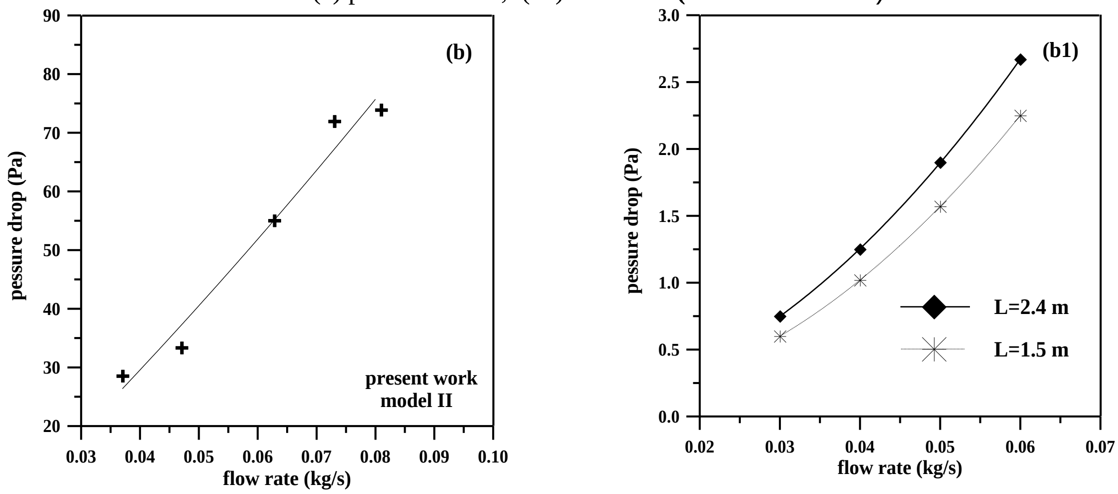

Effect of air mass flow rate on pressure drop for collector model II,
(b) present results, (b1) results of **(Baa** 2008)

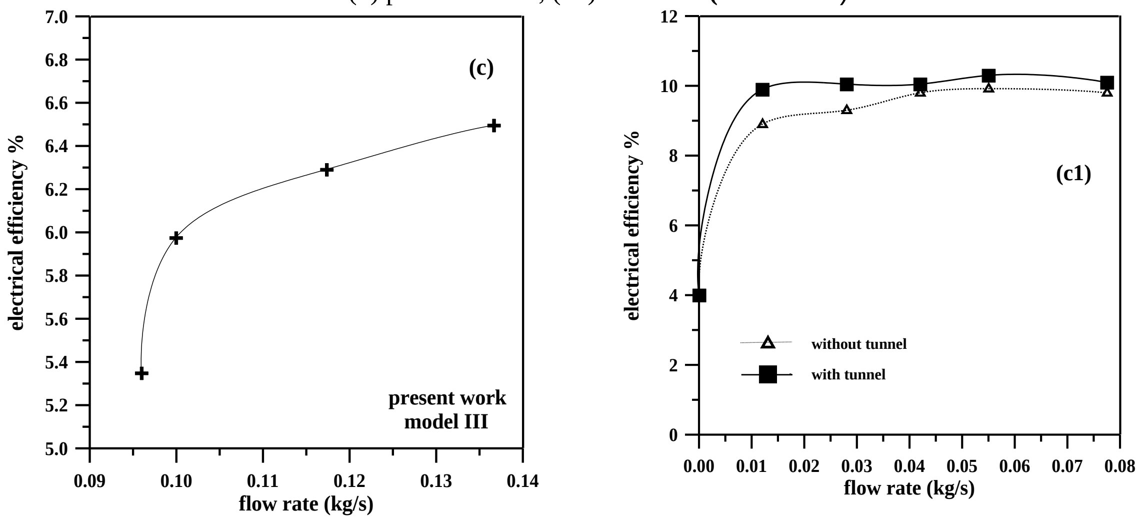

Effect of mass flow rate on electrical efficiency PV module for collector model III,
(c) present results, (c1) results of **(**Jin et al. 2010)

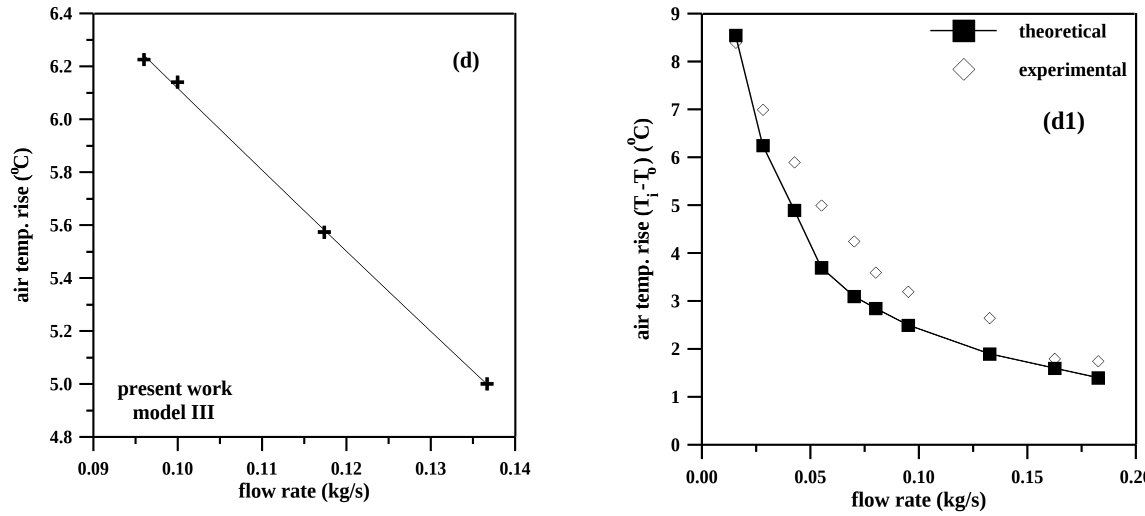

Effect of mass flow rate on air temperature rise for collector model III,
(d) present results, (d1) results of (Othman et al.2007)

Figure 15. Comparison of the present results with previously published results.

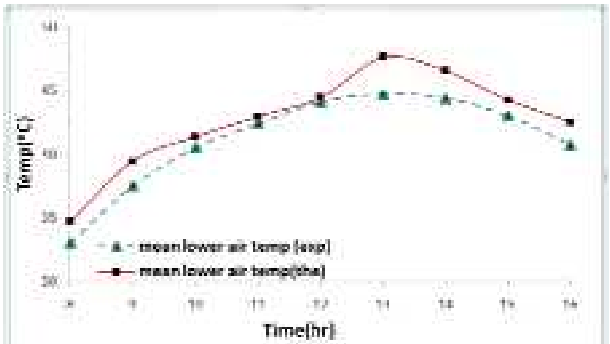

Figure 16. Comparison between theoretical and experimental values of hourly air temperature on (2/7/2011) for model IV

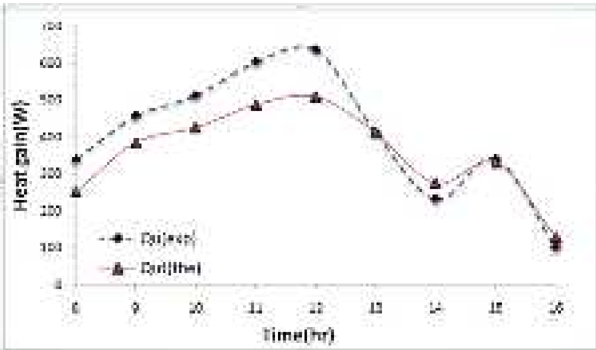

Figure 17. hourly comparison between theoretical and experimental values of hourly heat gain on (2/7/2011) for model IV

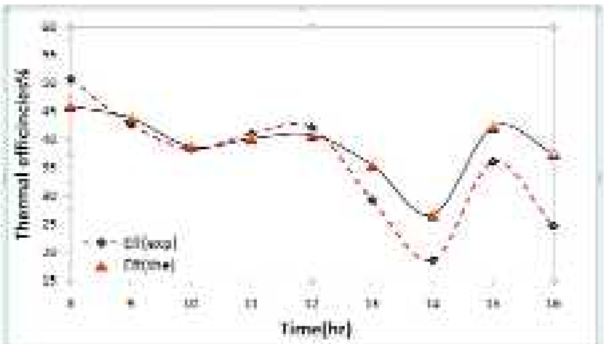

Figure 18. Comparison between theoretical and experimental values of hourly thermal efficiency on (2/7/2011) for model IV

Modeling of Electron and Lattice Temperature Distribution Through Lifetime of Plasma Plume

Chief of Engineers: Ali Hamza Alwan Al-taee
Gas Filling Company
Ministry of Oil
Email: alihaltaee@yahoo.com

ABSTRACT

When employing shorter (sub picosecond) laser pulses, in ablation kinetics the features appear which can no longer be described in the context of the conventional thermal model. Meanwhile, the ablation of materials with the aid of ultra-short (sub picosecond) laser pulses is applied for micromechanical processing.

Physical mechanisms and theoretical models of laser ablation are discussed. Typical associated phenomena are qualitatively regarded and methods for studying them quantitatively are considered. Calculated results relevant to ablation kinetics for a number of substances are presented and compared with experimental data. Ultra short laser ablation with two-temperature model was quantitatively investigated. A two-temperature model for the description of transition phenomena in a non-equilibrium electron gas and a lattice under picosecond laser irradiation is proposed. Some characteristics are hard to measure directly at all. That is why the analysis of physical mechanisms involved in the ablation process by ultra-short laser pulses has to be performed on the basis of a theoretical consideration of `indirect' experimental data.

For Copper and Nickel metal targets, the two-temperature model calculations explain that the temperature of the electron subsystem increased suddenly and approached a peak value at the end of laser pulse. In addition, the temperature profile of lattice temperature subsystem evolution slowly, and still increasing after the end of laser pulse. A good agreement prevails when a comparison between the present results and published results.

Key words: pulsed laser, heat ablation by laser, two-temperature model, plasma plume.

نمذجة توزيع درجة حرارة الالكترونات و الشبكة خلال فترة تكون غيمة البلازما

رئيس مهندسين: **علي حمزة علوان الطائي**
شركة تعبئة الغاز
وزارة النفط

الخلاصة

عند استخدام نبضات الليزر ألقصيرة (اقل من 10^{-12} Sec.)، في حركية التذرية تظهر خصائص لا يمكن وصفها في سياق النماذج الحرارية التقليدية. لذا فان تشغيل المعادن الميكانيكي (بمقاييس مايكروية) يتم انجازه بتذرية المواد بدعم نبضات الليزر فائقة القصر (اقل من بيكو ثانية).

في البحث الحالي تم مناقشة الآليات الفيزيائية والنماذج النظرية للتذرية بواسطة المصادر الليزرية المنبضة. الظواهر النموذجية المرافقة تعتبر نوعية و تم بحثها بطرق كمية. لعدد من المواد, النتائج ذات الصلة بحركية التذرية تم عرضها ومقارنتها مع البيانات التجريبية المنشورة سابقا واظهرت توافق جيد. التذرية بواسطة المصادر الليزرية المنبضة فائقة القصر تمت دراستها باستخدام نموذج ثنائي درجة الحرارة وكان التحليل كمي. لبيان الظواهر غير المتوازنة و الانتقالية لخليط " غاز الالكترونات-الايون" بسبب الإشعاع الساقط من مصادر ليزرية منبضة فائقة القصر قد تم اقتراح استخدام النموذج ثنائي درجة الحرارة. بعض الخواص يصعب قياسها بشكل مباشر. لذا فان دراسة آلية عمل التذرية بواسطة المصادر الليزرية المنبضة قد تم انجازها بمراعاة الاعتبارات النظرية غير المباشرة التي تم الحصول عليها من تجارب عملية سابقة.

الحسابات النظرية باستخدام نموذج ثنائي درجة الحرارة بينت ان درجة حرارة الالكترونات تزداد بشكل سريع و مفرط وتصل لاقصى قيمة عند نهاية نبضة الليزر عند استخدام النحاس او النيكل كمعدن هدف. تزداد درجة حرارة الشبكة في نهاية زمن نبضة الليزر, وتستمر بالتنامي بعد انتهاء النبضة. قيمة درجة حرارة الشبكة دائما اقل من درجة حرارة الالكترونات. ضعف الترابط بين الالكترونات و الشبكة يؤدي الى انخفاض معدل التذرية خلال زمن نبضة الليزر.

الكلمات الرئيسية: ليزر منبض, تذرية بالليزر, نموذج ثنائي درجة الحرارة, غيمة البلازما.

1. INTRODUCTION

Ablation occurred when solid surface exposure to an intense laser irradiation. As a result atoms or clusters may emit from the target surface. For the ultra-short laser pulse duration, there is a variation in the temperature between electrons and lattice sub-systems. Two temperature model one of the approaches can be applied to investigate the temperature profiles throughout the laser target.

Schäfer, et al., 2002, investigated picosecond laser ablation of metals by using a hybrid simulation scheme. Laser energy input into the electron system and heat conduction within it are modeled using a finite-difference scheme for solving the heat conduction equation. Energy transfer between the electronic and atomic subsystems due to electron-phonon coupling is taken into account. **Zhigilei, et al., 2002,**discussed two computational schemes developed for simulation of laser coupling to organic materials and metals and present a multi-scale model for laser ablation and cluster deposition of nano-structured materials. For metals, the two temperature model coupled to the atomistic (molecular dynamics) MD model provides an adequate description of the laser energy absorption into the electronic system and fast electron heat conduction. **Korte, et al., 2000,** investigated the production sub-diffraction limited structures in thin metal films and bulk dielectric materials using femtosecond laser pulses. The physics of ultrashort pulse laser ablation of solids is outlined. They reported the results on the fabrication of sub-micrometer structures in 100-200 nm chrome-coated surfaces by direct ablation.

Anisimov, et al., 1996, performed the ablation of Cu and Al targets with 170 fs laser pulses in the intensity range of 1012-1014 W/cm^2. They compare the measured removal depth with 1D hydrodynamic simulations. The electron-ion temperature decoupling is taken into account using the standard two-temperature model.

Bulgakova, et al., 2007, presented a number of numerical models, which have been developed to describe the processes taking place at different time and length scales in different classes of materials under the irradiation by ultra-short laser pulses. The two-temperature model is used to follow heating dynamics of irradiated matter and to analyze its phase transformations on the basis of thermodynamic concepts.

Chimmalgi, et al., 2005, simulated a numerical calculations insight into the spatial distribution of the enhanced field intensity underneath the tip and associated physical phenomena. Calculate the temperature distribution in the microprobe tip and possible tip expansion. **Hermann, et al., 2005,** investigated micromachining of CuInSe2 (CIS)-based photovoltaic devices with short and ultra-short laser pulses. Therefore, ablation thresholds and ablation rates of ZnO, Mo and CuInSe2 thin films have been measured for irradiation with nanosecond laser pulses of ultraviolet and visible light and sub-picosecond laser pulses of a Ti:sapphire laser. The experimental results were compared to the theoretical evaluation of the samples heat regime.

Leitz, et al., 2011, presented contribution a comparative study of the ablation of metal with micro-, nano-, pico and femtosecond laser pulses. In ultra-short pulse laser ablation extreme pressures, densities and temperatures build up and accelerate the ionized material to enormous velocities. Due to the short interaction time the material cannot evaporate continuously but is transferred into a state of overheated liquid. This merges into a high pressure mixture of liquid droplets and vapor expanding rapidly.

Ultra-short laser pulses provide unique possibilities for high-precision material processing. Due to rapid energy delivery, localized heat-affected zone, and minimal residual damage. As a result, numbers of numerical models are presented which have been developed to describe the processes taking place at different time and length scales in different classes of materials under the irradiation by ultra-short laser pulses.

Pulsed laser ablation is the process of material removal, after the target irradiated by intensive laser pulses. The short pulse duration confines heat diffusion, which leads to high-quality machining. Sharp-edged, clean and highly reproducible machining results have obtained using a femtosecond laser.

When the laser irradiation strike the metal targets. There are three energy transfer stages during femtosecond laser ablation, **Harrach, 1977.** These stages are:

1. The free electrons absorb the energy from the laser. This stage characterized by a lack of thermal equilibrium among the electrons.
2. The electrons reach thermal equilibrium and the density of states can now represented by the Fermi distribution. However, electrons and the lattice are still at two different temperatures.
3. Electron and lattice reach thermal equilibrium and thermal diffusion carries the energy into the bulk.

This mechanism can be represented geometrically by a large block of material subjected to short pulse of laser beam radiation. The power of the laser beam is incidents on the surface of the material, over a circular area $(r_{ab}^2\pi)$. Then the material absorbs the energy. The absorbed energy will interacts with the material as above. Where, the energy diffuses through the material in all dimensions. Through the material, the temperature profile rises from the room temperature to a very high value. A phase transition process will occurred.

The effects of the absorbed laser energy by material were represented by a source term in the energy equation analysis, **Schäfer, et al., 2002. Fig. 1.b,** showed the cylindrical coordinates system for semi-infinite medium.

In the present study the two-temperature model with nonlinear change in physical properties is modeled. A comparison study is carried out. This study explain the effect of every physical quantity "property" in the performance of temperature evolution for every sub-system "free electron and lattice".

2. MATHEMATICAL MODEL

Laser ablation cannot be described within a single computational model **Zhigilei, et al., 2002.** The two-temperature models used to predict the non-equilibrium. **Anisimov, et al., 1996.** and, **Qiu,** and **Tien, 1993.** First described the temperature distribution between electrons and, lattice during femtosecond laser irradiation of metals. The two-temperature model looks at the heating mechanism as; initially due to inverse- Bremsstrahlung the laser energy is absorbed by free electrons. The absorption followed by a fast energy relaxation within the electronic subsystem, thermal diffusion and an energy transfer to the lattice due to electron-phonon coupling. Under the following assumptions:

1. When the laser beam incident vertically on the material surface i.e. axi-symmetric the material will be isotropic $\frac{\partial}{\partial\theta} = 0$, **Al-moosawy, 2002.** As indicated in **Fig. 1.a.**
2. Neglecting the material thermal expansion completely and declaring that one needs a definite amount of energy to initiate ablation, **Alan, and David, 1973.**
3. The present investigation achieved per pulse.
4. The time scale is less than the time for energy transfer from the electrons to the lattice, **Schäfer, et al., 2002.** Therefore there is a temperature shift between electron and lattice sub-systems.
5. For calculation, the laser beam is considered as uniform in space with temporal Gaussian distribution, **Cheng, and Xu, 2005.**
6. Near the critical point, the temperature dependent properties nor available always, therefore some of the material properties is considered as not temperature dependent. Moreover, the uncertainties in the properties will not affect this study since the focus is on the mechanism of laser ablation.
7. The laser beam is incident vertically on the surface of the target material. In other words, the angle of incident equals zero.

Through the cylindrical coordinates system; the following three-dimensional equations are described spatial and temporal evolution of the electron and lattice temperature in a material. They treat electrons and lattice as two separate sub-systems with different temperatures.

1. For electron sub-system:

$$C_e\left(\frac{\partial T_e}{\partial t}\right) = K_e\left(\frac{\partial^2 T_e}{\partial r^2} + \frac{1}{r}\frac{\partial T_e}{\partial r} + \frac{1}{r^2}\frac{\partial^2 T_e}{\partial \theta^2} + \frac{\partial^2 T_e}{\partial z^2}\right) - \gamma(T_e - T_l) + S_{ab} \tag{1.a}$$

2. For lattice sub-system:

$$C_l\left(\frac{\partial T_l}{\partial t}\right) = K_l\left(\frac{\partial^2 T_l}{\partial r^2} + \frac{1}{r}\frac{\partial T_l}{\partial r} + \frac{1}{r^2}\frac{\partial^2 T_l}{\partial \theta^2} + \frac{\partial^2 T_l}{\partial z^2}\right) + \gamma(T_e - T_l) \tag{1.b}$$

The last term into Eq. (1.a) represents the laser energy absorbed by the material target. The second term in the right hand side (R.H.S) of Eq. (1) represents the rate at which energy exchanges between the two subsystems. The above governing equations are right only with ultrashort laser pulses. Where, in the case of material processing with long laser pulses the electronic and atomic subsystems are in equilibrium i.e. $T_l = T_e$.

2. 1. Further Calculations

1. Fermi temperature is function of material i.e. different for each material. It is calculated as: $T_F = \frac{E_F}{k_B}$ (2)

where the Fermi energy equals$\left[E_F = \frac{1}{2}mv_F^2\right]$ see **Korte, et al., 2002.**

2. The thermal conductivity of the electron and lattice is temperature dependent. **Colombier, et al., 2006. Schäfer, et al., 2002.** and, **Anisimov, et al., 1997.** the electron thermal conductivity commonly expressed as:

$$K_e = \alpha\frac{(\theta_e^2+0.16)^{4/5}(\theta_e^2+0.44)}{(\theta_e^2+0.092)^{1/2}(\theta_e^2+\beta\theta_i)}\theta_e \tag{3}$$

where, θ_e and, θ_l are electron and ion temperature normalized to Fermi temperature ($\theta e = T_e/T_F$, $\theta_l = T_l/T_F$). α and, β are material dependent parameters. When (k_BT_e) remains smaller than the Fermi energy, another equation used to evaluate electronic thermal conductivity **Ashcroft, and Mermin, 1976.** as:

$$K_e = \frac{1}{3} C_e v_F^2 \tau \tag{4}$$

Moreover, the lattice thermal conductivity is dependent on electron and, lattice temperature as follows:

$$K_l = 0.01 \times K_e \tag{5}$$

3. The electronic heat capacity is much less than the lattice heat capacity. Therefore, the electrons can heat to very high transient temperatures. Many equations used to calculate the electronic heat capacity. **Mannion, et al., 2002,** considered it as a function of electron number density: $\left[C_e \approx \frac{3}{2} n_e k_B\right]$ **.Colombier, et al., 2006.** ,and **Korte, et al., 2000** used another equation considers it as a function of electronic temperature and, number density: $\left[C_e \approx \frac{\pi^2}{2}\left(\frac{k_B T_e}{E_F}\right) n_e k_B\right]$ The condition to use this relation is as the condition for use Eq. (5). In the present study, take the electronic heat capacity as a material property.

4. At high fluences and short pulse width, rapid solid-vapor phase change controlled by nucleation dynamics rather than by heat transfer at the phase change interface **Xianfan, 2004.** At the solid-vapor interface, i.e. "superheating/under cooling " , the interface velocity (V_{sv}) can represent as:

$$V_{sv} = \frac{(1-R) \times (J_f/t_P)}{[\rho L_{sv} + \rho C_l (T_b - T_o)]} \tag{6}$$

5. The ablated crater diameter is related to the peak fluence, **Mannion et al., 2001,** as:

$$D_{ab}^2 = 2 \times r_b^2 \times \ln\left(\frac{\emptyset_o}{\emptyset_{th}}\right) \tag{7}$$

where, $\emptyset_o = \frac{2 \times J_f}{\pi \times r_b^2}$ and $r_{ab} = \frac{D_{ab}}{2}$

6. The laser-heating source S: This term in Eq. (1.a) represents the laser energy deposition into the electron subsystem, "heat generation term in the governing equation". Several equations suggested evaluating this effect **Zhigilei, et al., 2002.** , **Alan, and David, 1973.** , **Cheng, and Xu, 2005.** , **Xianfan, 2004.** , and **Mannion et al., 2001.** In the present study, one of them selected. This selected equation has the largest number of the parameters affects the incident laser beam. The standard form for the laser pulse with a Gaussian temporal and, spatial distribution , **Alan, and David, 1973.** , **Cheng, and Xu, 2005.** and **Xianfan, 2004.** In the present work the source term equation is:

$$S_{(t,r,z)} = \frac{1}{\sqrt{\pi}} \frac{(1-R) J_f}{t_P \times \delta} \times Exp\left\{-\left[\left(\frac{t-t_o}{t_p}\right)^2 + \left(\frac{\sqrt{r^2+z^2}}{\delta}\right)\right]\right\} \tag{8}$$

As indicated before, **Alan, and David, 1973,** showed that when the cylinder is solid rather than hollow. The third term in the R.H.S of Eq. (1) becomes:

$$\lim_{r\to 0}\left(\frac{1}{r^2}\right)\left(\frac{\partial^2 T}{\partial \phi^2}\right) = \lim_{r\to 0}\left(\frac{\partial}{\partial r}\right)\left(\frac{\partial^2 T}{\partial \phi^2}\right)/2r = \lim_{r\to 0}\left(\frac{\partial^2}{\partial r^2}\right)\left(\frac{\partial^2 T}{\partial \phi^2}\right)/2 = 0 \qquad (9)$$

Therefore, Eq. (1) can be written as:

$$C_e\left(\frac{\partial T_e}{\partial t}\right) = K_e\left(\frac{\partial^2 T_e}{\partial r^2} + \frac{1}{r}\frac{\partial T_e}{\partial r} + \frac{\partial^2 T_e}{\partial z^2}\right) - \gamma(T_e - T_l) + S_{ab} \qquad (10.a)$$

$$C_l\left(\frac{\partial T_l}{\partial t}\right) = K_l\left(\frac{\partial^2 T_l}{\partial r^2} + \frac{1}{r}\frac{\partial T_l}{\partial r} + \frac{\partial^2 T_l}{\partial z^2}\right) + \gamma(T_e - T_l) \qquad (10.b)$$

Where z is measured along the axis of ejection of the plasma and r radial outwards from the axis. A special consideration must be given to the central node at $r = 0$. At $r = 0$ the first term in the R.H.S of Eq. (10),$\left(\frac{1}{r}\right)\left(\frac{\partial T}{\partial r}\right)$ is indeterminate. This term can be evaluated by suing L'Hopital's rule.

$$\lim_{r\to 0}\left(\frac{1}{r}\right)\left(\frac{\partial T}{\partial r}\right) = \lim_{r\to 0}\left\{\left(\frac{\partial}{\partial r}\right)\left(\frac{\partial T}{\partial r}\right)/\left(\frac{\partial}{\partial r}\right)(r)\right\} = \left(\frac{\partial^2 T}{\partial r^2}\right) \qquad (11)$$

Thus the governing Eq. (10) can be re-formulated as:

$$C_e\left(\frac{\partial T_e}{\partial t}\right) = K_e\left(\frac{\partial^2 T_e}{\partial r^2} + \frac{\partial^2 T_e}{\partial r^2} + \frac{\partial^2 T_e}{\partial z^2}\right) - \gamma(T_e - T_l) + S_{ab} \qquad (12.a)$$

$$C_l\left(\frac{\partial T_l}{\partial t}\right) = K_l\left(\frac{\partial^2 T_l}{\partial r^2} + \frac{\partial^2 T_l}{\partial r^2} + \frac{\partial^2 T_l}{\partial z^2}\right) + \gamma(T_e - T_l) \qquad (12.b)$$

2. 2. Initial and Boundary conditions

Applying initial and boundary conditions to solves Eq. (12). The electron and lattice initial temperature of the material target equal the ambient temperature. Yet there is no laser beam incident on the material surface **Schäfer, et al., 2002.**

At $t = 0,$ $$T_e(0, r, z) = T_o \qquad (13.a)$$

$$T_l(0, r, z) = T_o \qquad (13.b)$$

The mechanism for machining with femtosecond laser pulse is very different from the conventional laser machining. Where the pulse duration small and, there is no enough time for convection and radiation losses. In other words, no heat will release from the upper boundary of the target, see **Fig. 1.a.**

At $z = 0,$ $$\left.\frac{\partial T_e(t,r,0)}{\partial z}\right|_{z=0} = 0 \qquad (14.a)$$

$$K_l\left.\frac{\partial T_l(t,r,0)}{\partial z}\right|_{z=0} = \rho L V_{sv} \qquad (14.b)$$

Select the origin point of the domain into, the center of the upper surface of the target, from symmetry of the cylindrical geometry. The boundary conditions obtained as follows:

At $r = 0,$ $$\left.\frac{\partial T_e(t,0,z)}{\partial r}\right|_{r=0} = 0 \quad (15.a)$$

$$\left.\frac{\partial T_l(t,0,z)}{\partial r}\right|_{r=0} = 0 \quad (15.b)$$

The nature of the femtosecond laser ablation is different. Therefore, diffusion effect is very little in comparison with the conventional mechanisms. As a result, that the bottom surface of the material target considered insulated **Alan, and David, 1973.** These words also right for the distance far in the radial direction.

At $z = L_{ab}$, $$\left.\frac{\partial T_e(t,r,L_{ab})}{\partial z}\right|_{z=L} = 0 \quad (16.a)$$

$$\left.\frac{\partial T_l(t,r,L_{ab})}{\partial z}\right|_{z=L} = 0 \quad (16.b)$$

At $r = L_{ab}$, $$\left.\frac{\partial T_e(t,L_{ab},z)}{\partial r}\right|_{r=L} = 0 \quad (17.a)$$

$$\left.\frac{\partial T_l(t,L_{ab},z)}{\partial r}\right|_{r=L} = 0 \quad (17.b)$$

3. NUMERICAL SOLUTION

A numerical solution of Eq. (12) depends upon the explicit finite difference technique to calculate the electron and lattice temperature distribution of plume through r and z axes. The scripts T and F used for the electron and lattice temperatures respectively, then the indices i and j will be used for indicating the points along the r and z directions respectively, and the index n will be used for indicating the points over the time layers. We shall use the approximation of the first order of accuracy for time, and of the second order of accuracy for space. The distances between the points in the established grid are $\Delta r, \Delta z, and \Delta t$ .The grid is represented by **Fig. 1.c.** The finite difference form of Eq.(12) with explicit formulation, **Anderson, et al., 1984.** :

For electron subsystem:

$$T_{i,j}^{n+1} = T_{i,j}^{n}\left(1 - \frac{4K_e\Delta t}{C_e\Delta r^2} - \frac{\gamma\Delta t}{C_e}\right) + T_{i+1,j}^{n}\left(\frac{K_e\Delta t}{C_e\Delta r^2} + \frac{K_e\Delta t}{2C_e r_i\Delta r}\right) + \frac{K_e\Delta t}{C_e\Delta r^2}\left(T_{i,j+1}^{n} + T_{i,j-1}^{n}\right) + \frac{\Delta t\gamma}{C_e}F_{i,j}^{n} + \frac{\Delta t}{C_e}S_{ab} \quad (18.a)$$

For lattice subsystem

$$F_{i,j}^{n+1} = F_{i,j}^{n}\left(1 - \frac{4K_l\Delta t}{C_l\Delta r^2} - \frac{\gamma\Delta t}{C_l}\right) + F_{i+1,j}^{n}\left(\frac{K_l\Delta t}{C_l\Delta r^2} + \frac{K_l\Delta t}{2C_l r_i\Delta r}\right) + F_{i-1,j}^{n}\left(\frac{K_l\Delta t}{C_l\Delta r^2} - \frac{K_l\Delta t}{2C_l r_i\Delta r}\right) + F_{i,j+1}^{n}\left(\frac{K_l\Delta t}{C_l\Delta r^2} - \frac{V_{sv}\Delta t}{2\Delta z}\right) + F_{i,j-1}^{n}\left(\frac{K_l\Delta t}{C_l\Delta r^2} + \frac{V_{sv}\Delta t}{2\Delta z}\right) + \frac{\Delta t\gamma}{C_l}T_{i,j}^{n} \quad (18.b)$$

The Eq. (18) is so-called explicit formulation of Eq. (12). Then after applying the boundary conditions, the governing equation for every zone in the solution domain is:

1. At $r=0$ and $z=0$. $T^n_{i-1,j}=T^n_{i+1,j}$ and $F^n_{i-1,j}=F^n_{i+1,j}$ and $T^n_{i,j-1}=T^n_{i,j+1}$ and $F^n_{i,j-1}=F^n_{i,j+1}$ Eq. (18) can be re-written in the central difference form as:

$$T^{n+1}_{i,j}=T^n_{i,j}\left(1-\frac{4K_e\Delta t}{C_e\Delta r^2}-\frac{\gamma\Delta t}{C_e}\right)+T^n_{i+1,j}\left(\frac{2K_e\Delta t}{C_e\Delta r^2}\right)+\frac{2K_e\Delta t}{C_e\Delta r^2}\left(T^n_{i,j+1}\right)+\frac{\Delta t\gamma}{C_e}F^n_{i,j}+\frac{\Delta t}{C_e}S_{ab} \tag{19.a}$$

$$F^{n+1}_{i,j}=F^n_{i,j}\left(1-\frac{4K_l\Delta t}{C_l\Delta r^2}-\frac{\gamma\Delta t}{C_l}\right)+F^n_{i+1,j}\left(\frac{2K_l\Delta t}{C_l\Delta r^2}\right)+F^n_{i,j+1}\left(\frac{2K_l\Delta t}{C_l\Delta r^2}\right)+\frac{\Delta t\gamma}{C_l}T^n_{i,j} \tag{19.b}$$

2. At $0\langle r\langle L$ and $z=0$. $T^n_{i,j-1}=T^n_{i,j+1}$ and $F^n_{i,j-1}=F^n_{i,j+1}$ Eqns. (18) can be re-written in the central difference form as:

$$T^{n+1}_{i,j}=T^n_{i,j}\left(1-\frac{4K_e\Delta t}{C_e\Delta r^2}-\frac{\gamma\Delta t}{C_e}\right)+T^n_{i+1,j}\left(\frac{K_e\Delta t}{C_e\Delta r^2}+\frac{K_e\Delta t}{2C_er_i\Delta r}\right)+T^n_{i-1,j}\left(\frac{K_e\Delta t}{C_e\Delta r^2}-\frac{K_e\Delta t}{2C_er_i\Delta r}\right)+ +T^n_{i,j+1}\left(\frac{2K_e\Delta t}{C_e\Delta r^2}\right)+\frac{\Delta t\gamma}{C_e}F^n_{i,j}+\frac{\Delta t}{C_e}S_{ab} \tag{20.a}$$

$$F^{n+1}_{i,j}=F^n_{i,j}\left(1-\frac{4K_l\Delta t}{C_l\Delta r^2}-\frac{\gamma\Delta t}{C_l}\right)+F^n_{i+1,j}\left(\frac{K_l\Delta t}{C_l\Delta r^2}+\frac{K_l\Delta t}{2C_lr_i\Delta r}\right)+F^n_{i-1,j}\left(\frac{K_l\Delta t}{C_l\Delta r^2}-\frac{K_l\Delta t}{2C_lr_i\Delta r}\right)+ F^n_{i,j+1}\left(\frac{2K_l\Delta t}{C_l\Delta r^2}\right)+\frac{\Delta t\gamma}{C_l}T^n_{i,j} \tag{20.b}$$

3. At $r=0$ and $0\langle z\langle L$. $T^n_{i-1,j}=T^n_{i+1,j}$ and $F^n_{i-1,j}=F^n_{i+1,j}$ Eq. (18) can be re-written in the central difference form as:

$$T^{n+1}_{i,j}=T^n_{i,j}\left(1-\frac{4K_e\Delta t}{C_e\Delta r^2}-\frac{\gamma\Delta t}{C_e}\right)+T^n_{i+1,j}\left(\frac{2K_e\Delta t}{C_e\Delta r^2}\right)+\frac{K_e\Delta t}{C_e\Delta r^2}\left(T^n_{i,j+1}+T^n_{i,j-1}\right)+\frac{\Delta t\gamma}{C_e}F^n_{i,j}+ \frac{\Delta t}{C_e}S_{ab} \tag{21.a}$$

$$F^{n+1}_{i,j}=F^n_{i,j}\left(1-\frac{4K_l\Delta t}{C_l\Delta r^2}-\frac{\gamma\Delta t}{C_l}\right)+F^n_{i+1,j}\left(\frac{2K_l\Delta t}{C_l\Delta r^2}\right)+F^n_{i,j+1}\left(\frac{K_l\Delta t}{C_l\Delta r^2}-\frac{V_{sv}\Delta t}{2\Delta z}\right)+ F^n_{i,j-1}\left(\frac{K_l\Delta t}{C_l\Delta r^2}+\frac{V_{sv}\Delta t}{2\Delta z}\right)+\frac{\Delta t\gamma}{C_l}T^n_{i,j} \tag{21.b}$$

4. Apply Eqns. (18) when
$0<r<L \; and \; 0<z<L.$

$\left(1-\frac{4K_e\Delta t}{C_e\Delta r^2}-\frac{\gamma\Delta t}{C_e}\right)$ Is the convergence term as described by references, **Alan, and David, 1973.** , and **Anderson, et al., 1984.** Where the convergence criteria mentioned that the value of the convergence term must be greater than or equal zero, to avoid solution fluctuation:

The electron and lattice temperature distribution through r-z plane, where $r=2$ to $L-1$ and $z=2$ to $L-1$ is represented as shown in **Fig. 1.b**. A special consideration is carried out for the exterior nods, with aid of factious points to mesh. The computer program was built in Visual FORTRAN language and run on pentium4 PC, using operating system Microsoft XP. Run time of about several minutes was needed to achieve the required convergence.

4. REULTES AND DISCUSSION

Figs. 2 to 5 explain the electron and lattice subsystem reduced temperature temporal distribution through the time with respect to laser pulse duration. Form these figures can be conclude that the temperature of the electron subsystem raised rapidly and approached to peak value at the end of laser pulse duration because of that the electron heat capacity is less than the lattice heat capacity. Electrons absorb the laser energy i.e., where the free electrons absorb the incident energy of the laser pulse due to invers-Bremsstrahlnug **Grojo, et al., 2003** and **Zeng,** and **Xianzhong, 2004.** In addition the electron heat capacity is low in comparison with the lattice-subsystem heat capacity, **Mannion, et al., 2001.** At the end of the pulse duration the temperature of the electron subsystem will decrease rapidly sometimes suddenly due to the electron-phonon (lattice) coupling and energy transfer to the lattice subsystem, as shown in **Figs. 4 and 5**.

In accordance with the different in the heat capacities of electron and lattice subsystems, the lattice temperature subsystem not much increase in compared with the electron subsystem. Briefly the behavior of electron and lattice can be expressed as the electron temperature will be increased rapidly until the end of laser pulse, then decreased rapidly. Moreover for the lattice subsystem, the temperature profile increased slowly form the beginning of laser pulse and remain increased after the end of pulse duration (for several pulse duration times), due to large heat capacity for the lattice subsystem, **Cheng, and Xu, 2005.**

The electron temperature reaches peak value at the end of laser pulse. It can also be seen that till this time the lattice remains virtually cold. Subsequently, the initial laser energy is totally absorbed by the electrons within the optical penetration depth. These energetic electrons move at very high speeds on the order of ~ 106 m/s. Subsequently, the electrons reach thermal equilibrium and diffuse deeper into the material at reduced speeds. It is only at a much longer time scale that energy transfer to the lattice occurs. Thereafter, both the electrons and the lattice reach the same temperature, and at long time scales > 40 ps they behave as a single system. Beyond this time, heat transfer occurs by conduction at much lower speeds, **Chimmalgi, et al., 2005.** Therefore, it can be stated that the calculations consistence with the published results.

In comparison between **Figs. 2, 3** for nickel and **Figs. 4, 5** for copper, it can be noticed that the reduced temperature profile for electron subsystem of copper metal is suddenly decreased after pulse duration due to electron-phonon relaxation coupling.

Figs. 6 and **7** show the electron and lattice subsystems reduced temperature profiles (T/T_C) versus the reduced radius (r/R) at time (1 tp), "the end of laser pulse". These figures indicate that the electron and lattice temperatures reach the peak value at the center of the laser crater because of Gaussian distribution of the laser beam. In addition, the value of the electron temperature is much higher than the lattice temperature for the same reasons as in **Figs. 2** to **5**.

Figs. 8 and **9** explain the electron and lattice subsystems reduced temperature (T/T_C) versus the reduced depth (z/R) at the end of pulse. These figures show that in spite of that the free electrons in the surface layer of target metal absorbs the laser beam energy, that the free electrons in the depth of metal target are also absorbs the energy of the transmitted part of the irradiated beam. Finally, the energy of the electron subsystem is transferred to lattice subsystem; after several times of pulse duration. In addition, that the reduced temperature profile will be decreased gradually with depth. Finally the temperature profile for the electron and lattice subsystems will be approached the same value at the distance far from the surface of the metal target.

At different pulse duration times, **Figs. 10** and **12** indicate the spatial temperature distribution for electron subsystem. The temperature curve for every figure show that the temperature increased with time and reached the maximum value at time equals 1 tp, and then the temperature will be decreased rapidly and approached initial value after several tp. It can be noticed that the temperature profile in the radial and depth direction approximately the same.

Figs. 11 and **13** show the distribution of reduced lattice temperature spatially for different pulse duration times in the radial and depth directions. From these figures, it can be noticed that the reduced temperature levels is less than the reduced temperature values in **Figs. 10** and **12** respectively, where the heat capacity of lattice subsystem is greater than that of electron subsystem, **Qiu, & Tien, 1993.** The reduced lattice temperature approaches the peak value at time equals 5 tp. In comparison with **Figs. 10** and **12,** it can be concluded that the lattice subsystem gain the heat slowly, but the free electrons absorb heat rapidly and radiant it at high rate.

Figs. 14 and **15** plot the isothermal contour map for reduced electron and lattice temperature in the rz-plane for copper. These two figures indicate the big difference in the temperature levels between the free electron and lattice subsystem, for the same conditions.

5. CONCLUSION

The time evolution for temperature of electron subsystem is faster than the temperature of lattice subsystem. Where, the heat capacity of the lattice was higher than the heat capacity of the free electrons. The metal target treated as two subsystems, in the ultra-short pulsed laser irradiation. The plasma plume existence in the ultra-short pulsed laser where, the temperatures of the electron and lattice subsystems exceed the critical temperature.

The weaker non-equilibrium between the electron and lattice (phonon) during the laser pulse reduce the ablation rate, and vies versa especially for Nickel. Nickel has a shorter lattice response time than for the copper. As explained in **Figs. 2** to **5**.

As a rule, the models employed in the theory of laser ablation are reliant on complex nonlinear systems of partial differential equations whose solution calls for the use of numerical methods.

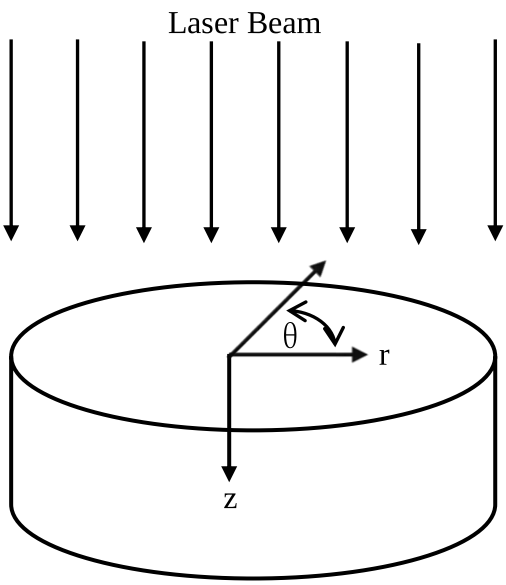

(a) Schematic of the computational domain

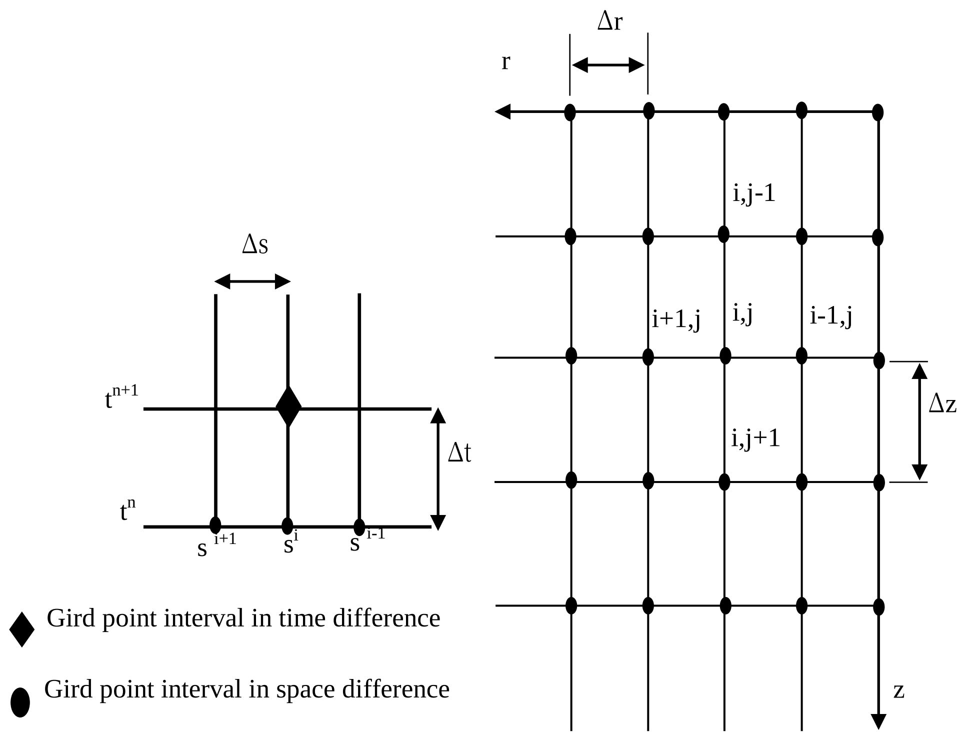

(c) (b)

Figure 1. Type of fixed boundary conditions for electron and lattice temperature distributions.

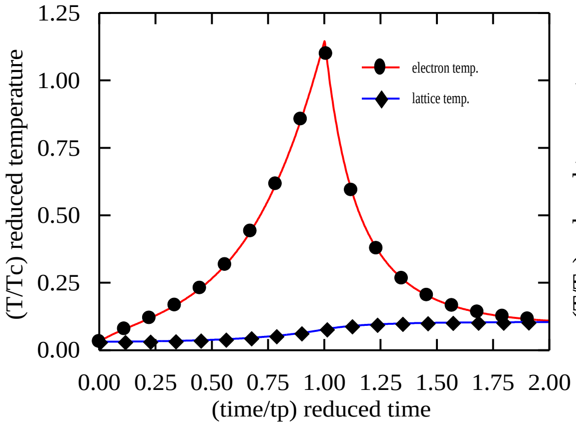

Figure 2. Reduced Lattice & Electron Temp. vs. the Pulse Duration Time for tp=0.5E-12 S, J_f=0.27 J/cm^2 Metal:Nickel

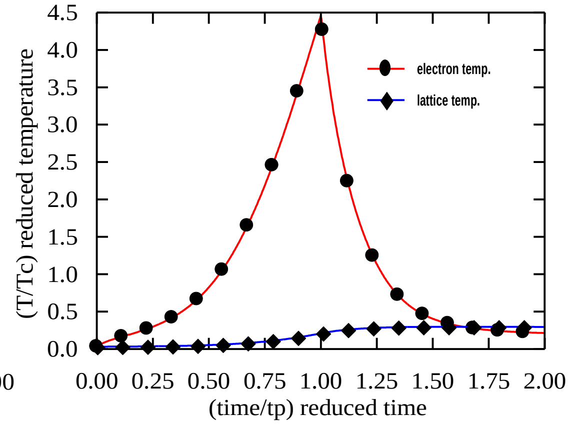

Figure 3. Reduced Lattice & Electron Temp. vs. the Pulse Duration Time for tp=0.5E-12 S, J_f=1.0 J/cm^2 Metal:Nickel

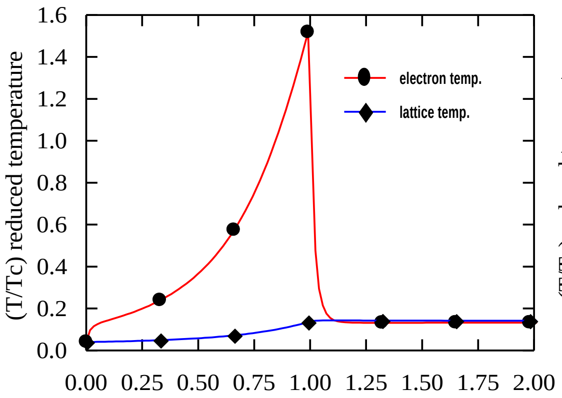

Figure 4. Reduced Lattice & Electron Temp. vs. the Pulse Duration Time for tp=0.5E-12 S, J_f=0.3529 J/cm^2 Metal:Copper

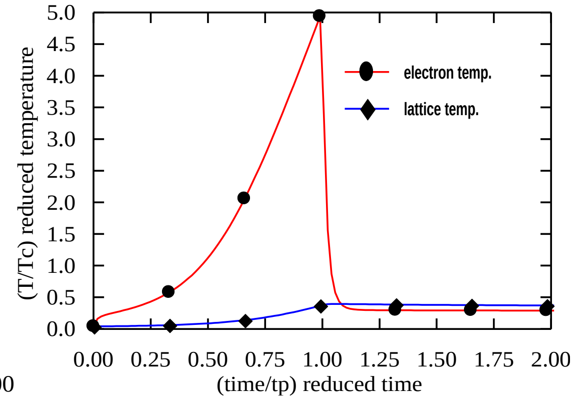

Figure 5. Reduced Lattice & Electron Temp. vs. the Pulse Duration Time for tp=0.5E-12 S, J_f=1.0 J/cm^2 Metal:Copper

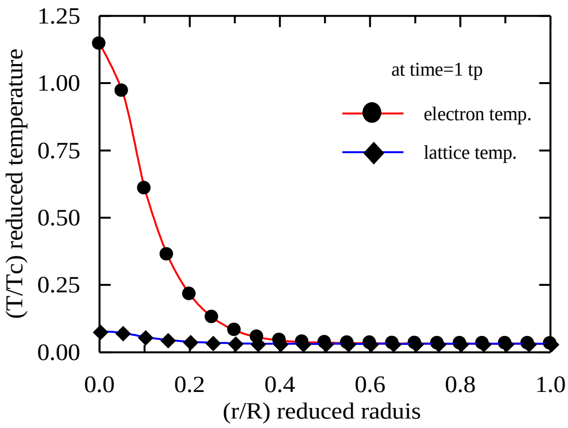

Figure 6. Reduced Lattice & Electron Temp. vs. Radial Dist for tp=0.5E-12 S, J_f=0.27 J/cm^2 Metal:Nickel

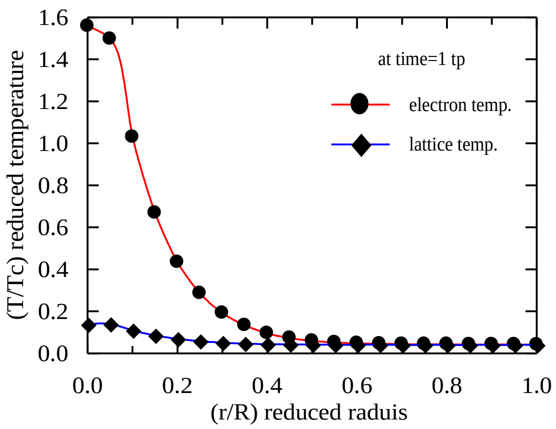

Figure 7. Reduced Lattice & Electron Temp. vs. Radial Dist. for tp=0.5E-12 S, J_f=0.3529 J/cm^2 Metal:Copper

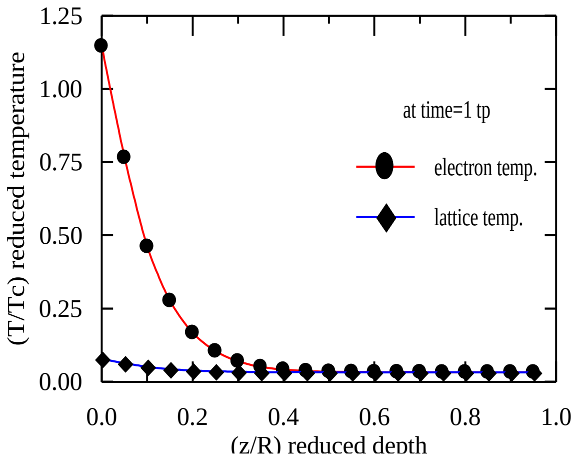

Figure 8. Reduced Lattice & Electron Temp. vs. Reduced Depth Dist. for tp=0.5E-12 S, J_f=0.27 J/cm^2 Metal:Nickel

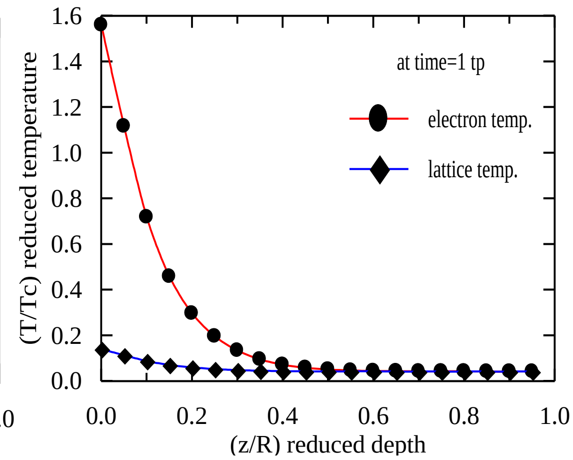

Figure 9. Reduced Lattice & Electron Temp. vs. Reduced Depth Dist. for tp=0.5E-12 S, J_f=0.3529 J/cm^2 Metal:Copper

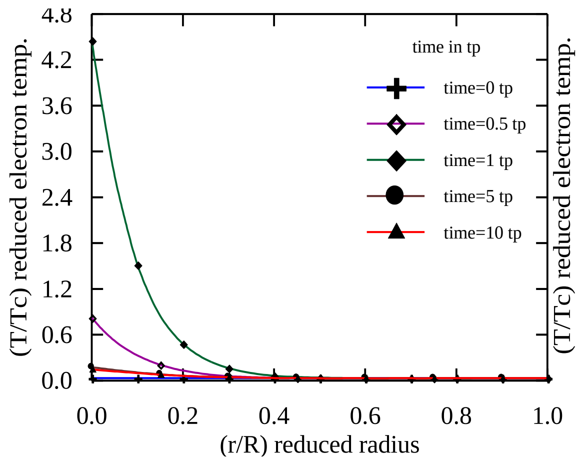

Figure 10. Reduced Electron Temp. for Different Pulse Duration Times vs. Reduced Raduis for tp=0.5E-12 S, J_f=0.3529 J/cm^2 Metal:Nickel

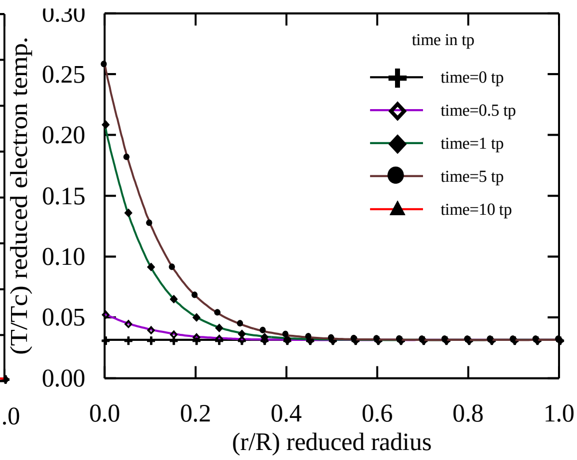

Figure 11. Reduced Lattice Temp. for Different Pulse Duration Times vs. Reduced Raduis for tp=0.5E-12 S, J_f=1.0 J/cm^2 Metal:Nickel

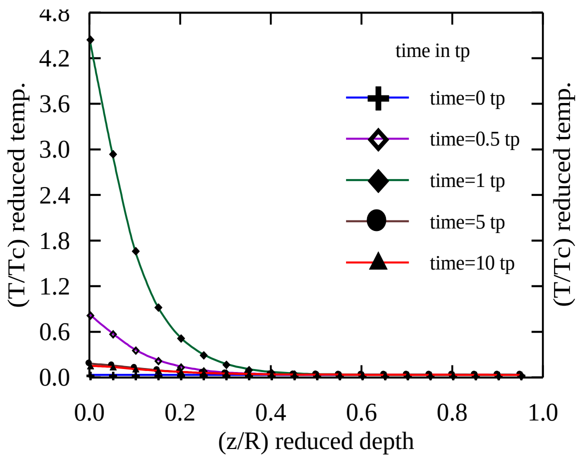

Figure 12. Reduced Electron Temp. for Different Pulse Duration Times vs. Reduced Depth for tp=0.5E-12 S, J_f=1.0 J/cm^2 Metal:Nickel

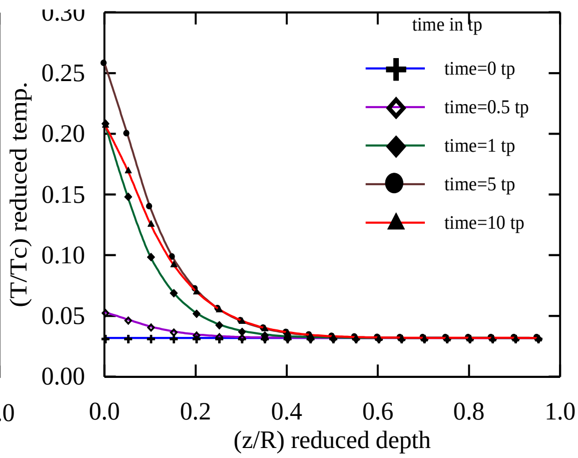

Figure 13. Reduced Lattice Temp. for Different Pulse Duration Times vs. Reduced Depth for tp=0.5E-12 S, J_f=1.0 J/cm^2 Metal:Nickel

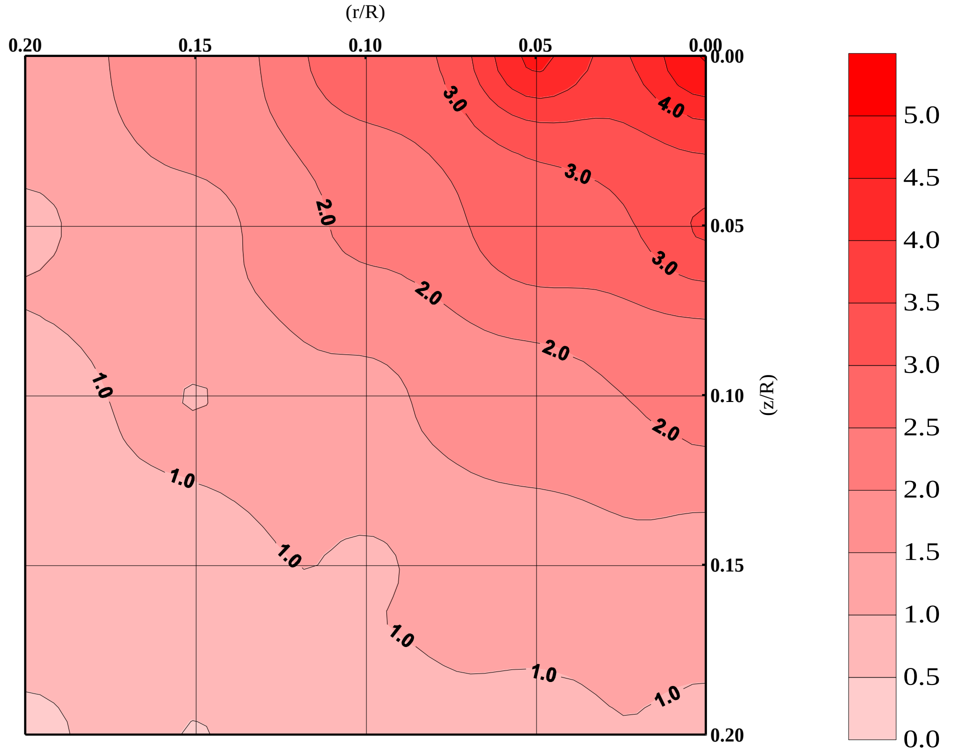

Figure(14):Isothermal contour map of reduced electron temp.vs. the normlized r-z palne for tp=0.5E-12 sec Jf=1.0 J/cm² metal:Copper

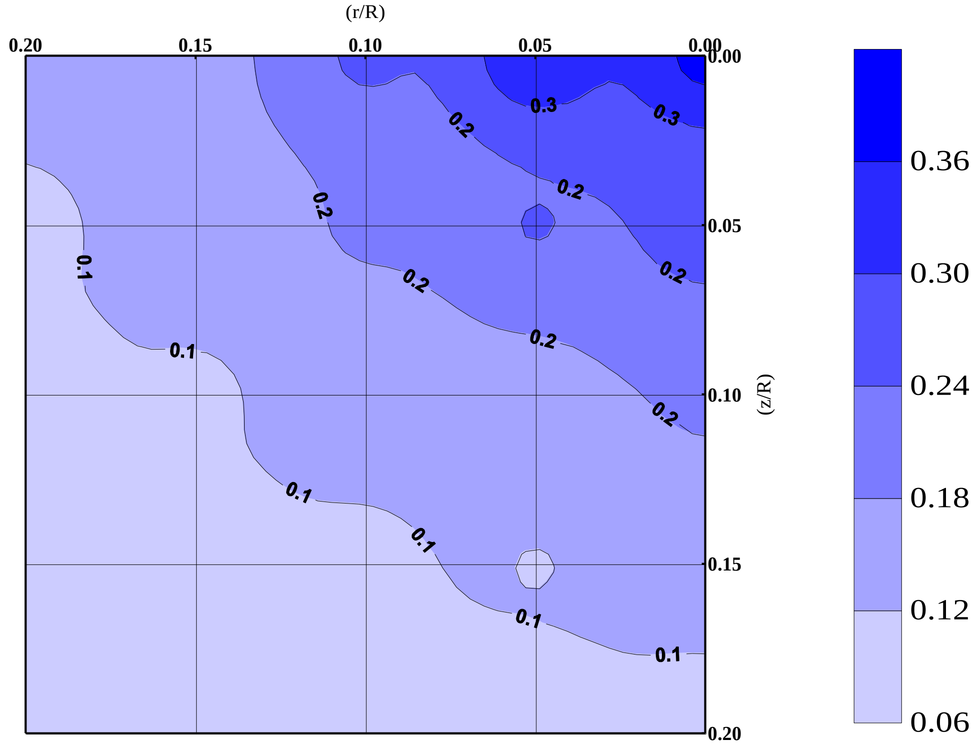

Figure(15): Isothermal contour map of reduced lattice temp.vs. the normlized r-z palne for tp=0.5E-12 sec Jf=1.0 J/cm² metal:Copper

NOMENCLATURES

Sample	*Description*	*Unite*
C_e	specific heat of electron subsystem	$J/m^3.K$
C_l	specific heat of lattice subsystem	$J/m^3.K$
D_e	electron diffusion coefficient	m^2/S
E	energy transferred	J
E_f	fermi energy	J
e	subscript denotes the electron subsystem	--
l	subscript denotes the lattice subsystem	--
I	laser power intensity	W/cm^2
i, j	The indexes increase along the r, z	--
J_f	incident laser fluence	W/m^2
K_e	electron thermal conductivity coefficient	$W/m.K$
K_l	lattice thermal conductivity coefficient	$W/m.K$
k_B	Boltzmann constant	
L_{sv}	enthalpy of sublimation per atom	J/kg
m	electron mass	kg
n_e	electron density	m^{-3}
n	index increases along the time	--
R	material reflectivity	--
r	radial distance	m
r_{ab}	radius of ablation crater	m
S_{ab}	source in the governing equation	S
t	time	S
t_p	laser pulse duration time	S
T_e	electron temperature	K
$T_{i,j}^n$	electron temperature in numerical form	K
T_l	lattice temperature	K
$F_{i,j}^n$	lattice temperature in numerical form	K
T_F	Fermi temperature	K
T_o	ambient temperature	K
T_b	boiling temperature	K
T_c	critical temperature	K
V_{sv}	solid-vapor interface velocity	m/S
α	material dependent parameter	--
ρ	material density	Kg/m^3
τ	electron relaxation time which is determined by electron-electron and electron-phonon collisions.	S
γ	coefficient of electron-lattice relaxation rate	$W/m^3.K$
ν_F	electron velocity	m/S
δ_{ab}	absorption ablation depth	m

REFERENCES

Al-moosawy, Adil, A., 2002, *Modeling of Thermal History of Solid Material Processed by Laser* , Ph.D. Thesis, University of Technology, Mech. Dept.,.

Alan Adams, J., and David, F., Rogers., 1973, *Computer-Aided Heat Transfer Analysis*, McGraw-Hill,.

Anderson, D. A., Tannehill, J. C., and Pletcher, R. H., 1984, *Computational Fluid Mechanics and Heat Transfer*, McGraw-Hill,.

Bulgakova, M., Nadezhda, M., Igor, Burakov, Meshcherykov, Yuri, P., Stoian, Razvan, Rosenfeld, Arkadi, and Hertel, Ingolf, V., 2007,*Theoretical Models and Qualitative Interpretations of Fs Laser Material Processing*, JLMN-Journal of Laser Micro/Nanoengineering Vol. 2, No. 1,.

Chimmalgi, A., Grigoropoulos, C., P., and Komvopoulos, K., 2005, *Surface Nanostructuring by Nano-femtosecond Laser-assisted Scanning Force Microscopy,* Journal of Applied Physics, 97, 104319.

Cheng, Changrui, and Xu, Xianfan, 2005, *Mechanisms of Decomposition of Metal during Femtosecond Laser Ablation,* Physical Review B,72,165415,.

Grojo, D., Hermann, J., Bruneau, S., and Itina, T., 2003, Analyses of Femtosecond Laser Ablation of Ti, Zr and Hf, LP3-FRE 2165 CNRS,Faculté des Sciences de Luminy,Case 917,13288 Marseille Cedex 9,France.

Hermann, J., Benfarah, M., Coustillier, G., Bruneau, S., Axente, E., Guillemoles, J.,-F., Sentis, M., Alloncle, P., Itina, T., 2005, *Selective Ablation of Thin Films with Short and Ultrashort Laser Pulses*, Applied Surface Science.

Harrach, R. J., Dec. 1977, *Analytic Solutions for Laser Heating and Burn-through of Opaque Slabs,* J. Appl. Phys., Vol. 48, pp. 2370-2375.

J.P. Colombier, P. Combis, F. Bonneau, R. Le Harzic, and E. Audouard., 2006, *Hydrodynamic Simulations of Metal Ablation by Femtosecond Laser Irradiation*, Dept. de Physique Th´eorique et Appliqu´ee ,France.

Korte, F. Adams S., Egbert, A. Fallnich, C. Ostendorf, A., 17July, 2000, *Sub-diffraction Limited Structuring of Solid Targets with Femtosecond Laser Pulses,* Institute of Applied Physics, Friedrich-Schiller-University Jena, Vol.7, No.2/Optics Express,Jena,Germany.

Leitz, Karl-Heinz, Redlingshöfer, Benjamin, Reg, Yvonne, Otto, Andreas, Schmidt, Michael, 2011, *Metal Ablation with Short and Ultrashort Laser Pulses*, Physics Procedia 12, 230−238.

Mannion, P. T., Favre, S., Mullan, C., Ivanov, D. S., O'Connor, G. M., Glynn, T. J., Doggett, B., and, Lunney, J. G., 2002, *Langmuir Probe Investigation of Plasma*

Expansion in Femto and Picosecond Laser Ablation of Selected Metals ,National Centre for Laser Applications, NUI Galway, Ireland.

Mannion, Paul, Magee, Jonathan, Coyne, Edward, and M., O'Connor, Gerard, 2001, *Ablation Thresholds in Ultrafast Laser Micro-machining of Common Metals in Air,* National Centre for Laser Applications, National University of Ireland, Galway, Ireland, Proc. of SPIE Vol. 4876.

N.W. Ashcroft and N.D. Mermin, *Solid State Physics* ,Saunders College Publishing, New York,1976.

Qiu, T. Q., and Tien, C. L., 1993, *Heat Transfer Mechanisms During Short-pulse Laser Heating of Metals* ASME J. Heat Transfer, 115, pp. 835−841.

Schäfer, C.; Urbassek, H.M.; Zhigilei, L.V., 2002,*Metal Ablation by Picosecond Laser Pulses: A hybrid simulation*. Phys. Rev. B, in press.

S.I. Anisimov, B.S. Luk'yanchuk, A. Luches, 1996, *An Analytical Model for Three-dimensional Laser Plume Expansion into Vacuum in Hydrodynamic Regime*, Appl. Surface Science 96-98, pp 24-32.

S.I. Anisimov and B. Rethfeld, Izv. Ross. Akad. Nauk, Ser. Fiz. 61, 1642, 1997.

Xianfan Xu , 2004, *Molecular Dynamics Study of Phase Change Mechanisms During Femtosecond Laser Ablation,* Journal of Heat Transfer (ASME).

Zhigilei, Leonid, V., and Dongare, Avinash, M., 2002, *Multi-scale Modeling of Laser Ablation: Applications to Nanotechnology*, CMES, vol.3, no.5, pp.539-555,

Zeng, Xianzhong, 2004,*Laser Ablation of Electronic Materials Including the Effects of Energy Coupling and Plasma Interactions,* Ph.D. Thesis, University of California, Berkeley.

Energy Savings in Thermal Insulations for Sustainable Buildings

Prof.Dr. Angham Alsaffar
Department of Civil Engineering
Collage of Engineering
Baghdad University
Email: anghamalsaffar@yahoo.com

Qusay Adnan Alwan
Department of Civil Engineering
Collage of Engineering
Baghdad University
Email: kosayadnan@yahoo.com

ABSTRACT

Energy use is second to staffing in building operating costs. Sustainable technology in the energy sector is based on utilizing renewable sources of energy such as solar, wind, glazing systems, insulation. Other areas of focus include heating, ventilation and air conditioning; novel materials and construction methods; improved sensors and monitoring systems; and advanced simulation tools that can help building designers make more energy efficient choices.

The objective of this research is studying the effect of insulations on energy consumption of buildings in Iraq and identifying the amount of energy savings from application the insulations in buildings. HAP (Hourly Analysis Program) is used to calculate the thermal loads and the amount of energy needed. It is concluded that the use of the thermal insulation in the roof, walls, floors, and double glazing system for windows in building effectively reduces the energy required for air conditioning.

Keywords: sustainable buildings design, energy efficiency technologies, insulations, double glazing system.

وفورات الطاقة في العزل الحراري للابنية المستدامة

أ.د. أنغام الصفار
قسم الهندسة المدنية
كلية الهندسة /جامعة بغداد

قصي عدنان علوان
قسم الهندسة المدنية
كلية الهندسة/جامعة بغداد

الخلاصة

ياتي استخدام الطاقة في المرتبة الثانية في تكاليف تشغيل المبنى. تستند التكنولوجيا المستدامة في قطاع الطاقة الى استخدام مصادر الطاقة المتجددة مثل الطاقة الشمسية، طاقة الرياح، أنظمة الزجاج، والعزل. هناك مجالات أخرى تتضمن التدفئة، التهوية وتكييف الهواء، أساليب البناء واستخدام مواد جديدة ، وتحسين أجهزة الاستشعار ونظم الرصد، وأدوات المحاكاة المتطورة يمكن أن تساعد مصممي المبنى في اختيار الطاقة الاكثر كفاءة.

يهدف هذا البحث الى دراسة تاثير العوازل في الجدران والسقوف والارضيات والنوافذ على استهلاك الطاقة في الابنية في العراق وتحديد كمية الوفورات في الطاقة الناتجه من تطبيق العوازل في الابنية. تم استخدام برنامج Hourly Analysis Program لحساب الاحمال الحرارية وكمية الطاقة اللازمة. حيث تبين ان استخدام العازل في الجدران والارضيات والسقوف واستخدام النوافذ ذات الزجاج المزدزج في الابنية يقلل بشكل فعال من كمية الطاقة اللازمة للتكييف .

كلمات رئيسية: تصميم الابنية المستدام، تقنيات كفاءة الطاقة، العوازل، نظام الزجاج المزدوج.

1. INTRODUCTION

Sustainable design, green architecture, sustainable constructions, and green buildings these are all new way and method for designing and constructing. The environmental and economical challenges of this era are affecting many sectors. New buildings are being designed, executed and operated by modern technologies which reduces the environmental impact and at the same time leads to reduction in cost especially running costs.

Buildings are large consumers of energy in all countries. In regions with harsh climatic conditions, a substantial share of energy goes to heat and cool buildings. This heating and air-conditioning load can be reduced through many means; notable among them is the proper design and selection of building envelope and its components.

The proper use of thermal insulation in buildings does not only contribute in reducing the required air-conditioning system size but also in reducing the annual energy cost. Additionally, it helps in extending the periods of thermal comfort without reliance on mechanical air-conditioning especially during inter-seasons periods. The magnitude of energy savings as a result of using thermal insulation vary according to the building type, the climatic conditions at which the building is located as well as the type of the insulating material used. The question now in the minds of many building owners is no longer should insulation be used but rather which type, how, and how much.

2. RESEARCH OBJECTIVE

The objective of this research is to identify the potential savings in energy for Building by using insulations in walls, floors, roof, and windows. In order to calculate the energy savings in building, HAP 4.7 (Hourly Analysis Program) from Carrier is used to calculate the thermal loads on two stages:

1. Building without insulations.
2. Building with insulations.

The main objectives of this research are:

1. Identifying the potential quantitative savings in energy from the application of insulations in green house.
2. Studying the effect of sustainable energy technologies systems in Buildings.

3. SUSTAINABILITY

The concept of sustainability in building and construction has evolved over many years. The initial focus was on how to deal with the issue of limited resources. More recently, an appreciation of the significance of non-technical issues has grown. It is now recognized that economic and social sustainability are important, as are the cultural heritage aspects of the built environment. Sustainable design concept can be divided into following aspects, **Jain et al., 2013**:

1. Sustainable site planning, preservation of site character, erosion, and sedimentation.
   Buildings envelop design, optimum design as per climate conditions and energy conservation building codes.
2. Ecologically sustainable material which is based on zero or low toxicity reduces adverse environmental impact.
3. Indoor Ambience, ventilation system to meet minimum indoor air ventilation rates.

.

4. Water and waste management, facilitate efficiency in use of water resources.
5. Integration of renewable energy use of energy efficient fixture, materials and integration of energy sources.

4. ENERGY EFFICIENCY TECHNOLOGIES

Energy needs can be reduced in several ways. Improving the performance of a building's envelope means less heating and cooling energy will be required, so the Heating, Ventilation, and Air Conditioning (HVAC) system can be smaller. High efficiency motors should be specified for all heating, ventilation, and air Conditioning components and heat recovery systems. More efficient lighting designs will reduce both lighting and cooling energy costs ,**Perkins and Stantec, 2003**.

4.1 Glazing System

Double glazing window system is commonly used in buildings of today. There have been many attempts to improve the insulation performance of this system such as low-e coating of glass surface, gas-filling between the glass panes, inserting a thermal breaker made of polyurethane or polyamide in frame, etc.. ,**Song et al., 2005**.

The performance of glazing is dependent on the overall rate of heat flow (U-value or thermal transmittance), Solar Heat Gain Coefficient, and visible transmittance. The U-Factor is a measure of how easily heat is transferred through a material and therefore a lower U-Factor indicates the lower amount of heat transfer through a window (from the interior to the exterior). The Solar Heat Gain Coefficient (SHGC) is the fraction of solar heat that enters through a glazing system and becomes heat. Visible transmittance (VT) is the percentage of the visible spectrum that is transmitted through glazing. For example, when daylight is a desired goal, glazing with a high VT is preferable ,**Perkins and Stantec, 2003**.

Double-glazing can substantially reduce the U-value of the glazed area of a building and as such it has become popular. However, double-glazing units are composed of a number of components as opposed to single sheets of glass. Double-glazing units are composed of a number of different materials, including glass, spacer bar, desiccant and sealant. The ultimate properties, qualities and Life time of any double-glazing units depends to a large extent on the type and quality of the individual components and the excellence of their manufacture, **Garvin and Wilson, 1998**.

In the UK the majority of PVC-U and aluminum frames are drained and ventilated. However, timber and steel windows are more commonly fully bedded. Examples of both types of system are shown in **Fig. 1** and **Fig. 2**, **Garvin and Wilson, 1998**.

4.2 Insulation

Well-insulated building envelopes are primary considerations in comfort and sustainability. Insulation helps to protect a building's occupants from heat, cold, and noise; in addition, it reduces pollution while conserving the energy needed to heat and cool a building. The comfort and energy efficiency of a home and, to a lesser degree, an office depend on the thermal resistance (R value) of the entire wall, roof, or floor (i.e., whole-wall R value), not just the R-value of the insulation. Techniques such as advanced framing increase the wall area covered by insulation, thereby increasing the whole wall's effectiveness. Framing conducts far more heat than insulation, in the same manner that most window frames conduct more heat than double-paned glass. An additional layer of rigid insulation between framing and exterior sheathing can help improve the whole-wall R-value by insulating the entire wall, and not just the clear space,**Kubba, 2009**.

According to **Mohsen and Akash,2001**, the heating load was calculated for a typical single house using different insulation materials. It was shown that the energy saving up to 77% can be achieved when polystyrene is used for both wall and roof insulation.

Al-Homoud, 2004, summarized the benefits for using thermal insulation in buildings, as follows:

1. A matter of principle: Using thermal insulation in buildings helps in reducing the reliance on mechanical/electrical systems to operate buildings comfortably and, therefore, conserves energy and the associated natural resources.
2. Economic benefits: An energy cost is an operating cost, and great energy savings can be achieved by using thermal insulation.
3. Environmental benefits: The use of thermal insulation.
4. Thermally comfortable buildings: The use of thermal insulation in buildings extends the periods of indoor thermal comfort especially in between seasons.
5. Reduced noise levels.
6. Building structural integrity.
7. Vapor condensation prevention: Proper design and installation of thermal insulation helps in preventing vapor condensation on building surfaces.
8. Fire protection.

American Society of Heating, Refrigerating and Air Conditioning Engineers (2001) mentioned building thermal insulation, which fall under the following basic materials and composites:

1. Inorganic Materials
   - Fibrous materials such as glass, rock, and slag wool.
   - Cellular materials such as calcium silicate, bonded perlite, vermiculite, and ceramic products.
2. Organic Materials
   - Fibrous materials such as cellulose, cotton, wood, pulp, cane, or synthetic fibers.
   - Cellular materials such as cork, foamed rubber, polystyrene, polyethylene, polyurethane, polyisocy-anurate and other polymers.
3. Metallic or metalized reflective membranes: These must face an air-filled, gas-filled, or evacuated space to be effective.

Fig. 3 shows a graphical comparison of the thermal resistances of 5 cm thickness for common building insulation materials. Concrete block is not considered as an insulating material. However, it was included in the figure as a reference (no insulation case) for comparison purposes only.

5. CASE STUDY

The case study evaluates the impacts of high quality insulation in energy consumption in single-family home. In this study a typical Iraqi house layout is considered for a single family. The consists of two floors ground and first floor with a total plot area about 200 square meters having four rooms and two bathrooms one in each floor.

Assumptions:
Air conditioning system consists of package unit and all house walls, roofs and floors without insulations in home.

1. Glass considered single layer with 4 mm thick for windows and doors.
2. The Air Conditioning (AC) plans layout shown in **Fig. 4.**
3. Air Conditioning work 7 months from (April to October).
4. Ordinary bricks used for non-insulated house and insulated concrete block used for insulated house.

5.1 Energy Baseline Usage for Non-insulated House

In order to calculate the efficiency of the new technologies used for sustainable house design, the baseline energy consumption of air conditioning use should be calculated.

Baseline energy consumption of the air condition of the house in the case that the house has not used insulation in the walls, roofs and floors, and windows HAP 4.7 (Hourly Analysis Program) from Carrier is used to calculate the thermal loads. So, What Is HAP?

Carrier's Hourly Analysis Program is two powerful tools in one package. HAP provides versatile features for designing HVAC systems for commercial buildings. It also offers powerful energy analysis capabilities for comparing energy consumption and operating costs of design alternatives. By combining both tools in one package significant time savings are achieved. Input data and results from system design calculations can be used directly in energy studies.

HAP is used to calculate the thermal loads and the amount of energy needed through the introduction of country specific information such as climate, latitude and longitude, spaces dimensions and materials used in walls, floors and roofs. Hap calculated thermal loads and provides the equivalent of the amount of cooling by type of cooling plants used.

Enter the information for each space in the house such as the name of the space, floor area, room lighting, the number of people, walls and windows areas of space exposed to sun radiation, roof area if exposed to sun radiation as shown in **Fig.5**.

After completing the introduction of all information about spaces of house then choosing the AC plant type and specifications required. HAP program analyzes and calculates the thermal loads and the monthly amount of energy required for a period of 7 months in kilowatt. hour (kw.h) as shown in **Table 1.** The results show that the total amount of energy for non-insulated house =24989 kw. h/year.

5.2 Application of Insulation

Majority of insulation in buildings is for thermal purposes, the term also applies to acoustic insulation, fire insulation, and impact insulation. Thermal insulation in buildings is an important factor to achieving thermal comfort for its occupants. Insulation reduces unwanted heat loss or gain and can decrease the energy demands of heating and cooling systems. It does not necessarily deal with issues of adequate ventilation and may or may not affect the level of sound insulation. In a narrow sense insulation can just refer to the insulation materials employed to slow heat loss, such as: cellulose, glass wool, rock wool, polystyrene, urethane foam, vermiculite, perlite, wood fiber, plant fiber (cannabis, flax, cotton, cork, etc.).

For the purpose of insulation the home, insulated concrete block with polystyrene thick 10 inches used instead of ordinary bricks for walls with 0.5 inch gypsum plaster and 0.5 inch cement plaster so the overall thermal transmittance (U-Value) become 0.085 British temperature units / Fahrenheit x foot square x hour (Btu/ F ft^2 h). roofs consist of 0.5 inch gypsum plaster, 8 inches concrete, 0.5 inch asphalt sheathing, 2 inches R7 board insulation, 4 inches sand and 1.5 inches cement tiles so the overall U-Value become 0.06 Btu/ F ft^2 h. Double glazing 1/4 inch grey reflective outer glaze and 1/4 inch clear with 1/2 inch air space used for windows. **Fig.6** shows the roof, wall, floor, and windows layers.

When insulated the walls, roofs, floors and windows the thermal transmittance U-value become less than from non-insulated be. **Fig. 7** shows the U-Value for non-insulated wall and **Table 2** shows the U-Values calculated by HAP. After completing the introduction of all information about insulated spaces of House then choose the Air Conditioning plant type and specifications required. HAP program analyzes and calculates the thermal loads and the monthly amount of energy required for a period of 7 months in (kW.h) (see **Table 3**).

The results show the total amount of energy for insulated house =16874 kW.h/year Yearly Savings of air conditioning will be 24989 – 16874 = 8115 kW.hr/year

6. CONCLUSION

The following points have been identified as the overall conclusions of the research:

1. The Sustainable design should seek to reduce negative impacts on the environment, and the health and comfort of building occupants, thereby improving building performance. Integration of architecture and technology can alleviate sustainability in a great way.
2. The cost of such green buildings may be higher by 5-10% than that of conventional building, it will result in 30-40% energy saving and the excess cost can be recovered within 3-4 years. The incorporation of sustainable features should be made mandatory through separate Bye laws for energy efficient buildings to conserve depleting resources and to reduce the overall negative impact of development on the environment.
3. Wall and roof insulation are recommended for buildings in all climates for more thermally comfortable space and, therefore, less energy requirements. Insulation helps in reducing conduction losses through all components of the building envelope. However, roof insulation is generally more critical than walls and should be given more attention.
4. The use of the thermal insulation of the roof, walls, floors, and double glazing system for windows effectively reduces the energy required for air conditioning can arrive where rationalization in energy consumption to about 32%.

7. RECOMMENDATIONS

1. Sectors of urban planning and environment in Iraq must be responsible to develop a national environmental strategy within the concept of sustainable development and issuance of new laws to construction by participation of the planning departments of cities and municipalities in the provinces and the implementation of these strategies during the next stage.
2. Proper treatment of building envelopes can significantly improve thermal performance especially for envelope-load dominated buildings, such as residences. Therefore, the proper selection and treatment of the building envelope components can significantly improve its thermal performance.

3. Designer is important joint in the development of the project in order to defend their own ideas, to clarify the reasons, high-performance projects.
4. Legislation of Determinants relating to the use of renewable energy systems in buildings and urban communities and modify construction systems to include special legislation to energy-saving systems.

REFERENCES

AL-Homoud, M, S., 2004, *Performance Characteristics and Practical Applications of Common Building Thermal Insulation Materials*, Journal: Building and Environment, Vol. 40, No. 3, p.p. 353-366.

American Society of Heating, Refrigerating, and Air Conditioning Engineers (ASHRAE), 2001, *Handbook of Fundamentals*, Chapter 23, USA.

Perkins and Stantec, 2003 ,*Sustainable Building Design Principles, Practices & Systems: A Study for BUILDSMART Program*, Metro Vancouver Body, Canada.

Garvin, S, L.; and Wilson, J, 1998, *Environmental Conditions in Window Frames with Double-Glazing Units,* Journal: Construction and Building Materials, Vol. 12, No. 5, p.p. 289-302.

Jain, S; Bhadouria, A., S; and Khare, A, 2013, *Sustainability in Building Design: Integrating Architecture with Technology to Achieve Energy Efficiency*, Special Issue of International Journal of Sustainable Development and Green Economics (IJSDGE), Vol. 2, No.1, p.p. 33-39. ISSN No.: 2315-4721

Kubba, S, 2009, *LEED® Practices, Certification, and Accreditation Handbook*, Elsevier Publishing, USA, ISBN: 978-1-85617-691-0.

Mohsen, M, S.; and Akash, B, A., 2001,*Some Prospects of Energy Savings in Buildings*, Journal: Energy Conversion and Management, Vol. 42, No.11, p.p. 1307-1315.

Song, S,Y; Jo, J, H; Yeo, M,S; Kim, Y,D; and Song. K,D, 2005,*Evaluation of Inside Surface Condensation in Double Glazing Window System with Insulation Spacer: A Case Study of Residential Complex*, Journal: Building and Environment, Vol. 42, No. 2, p.p. 940-950.

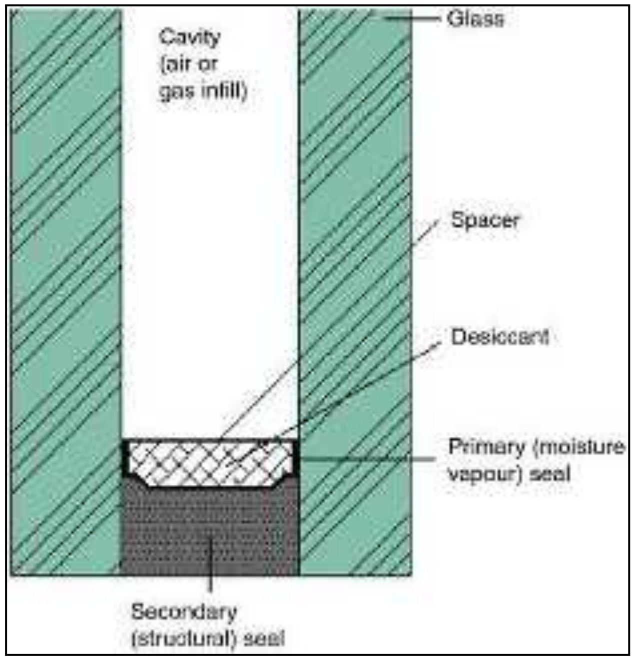

Figure 1. Cross section of a dual sealed double glazing unit,Song et al., 2005.

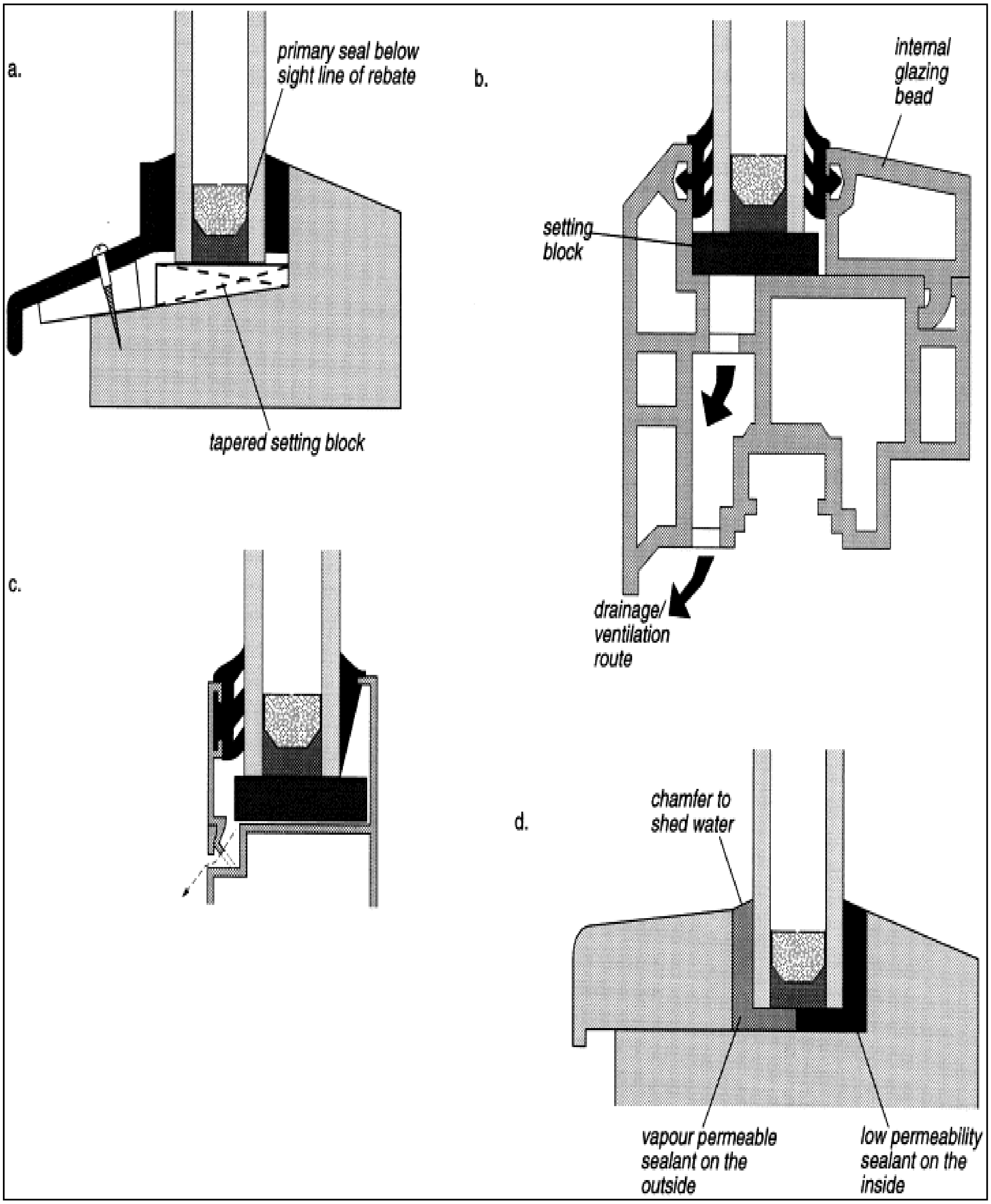

Figure 2. Drained and ventilated and fully bedded window frames. (a) Timber; (b) PVC; (c) aluminum; (d) timber fully bedded, Garvin and Wilson, 1998.

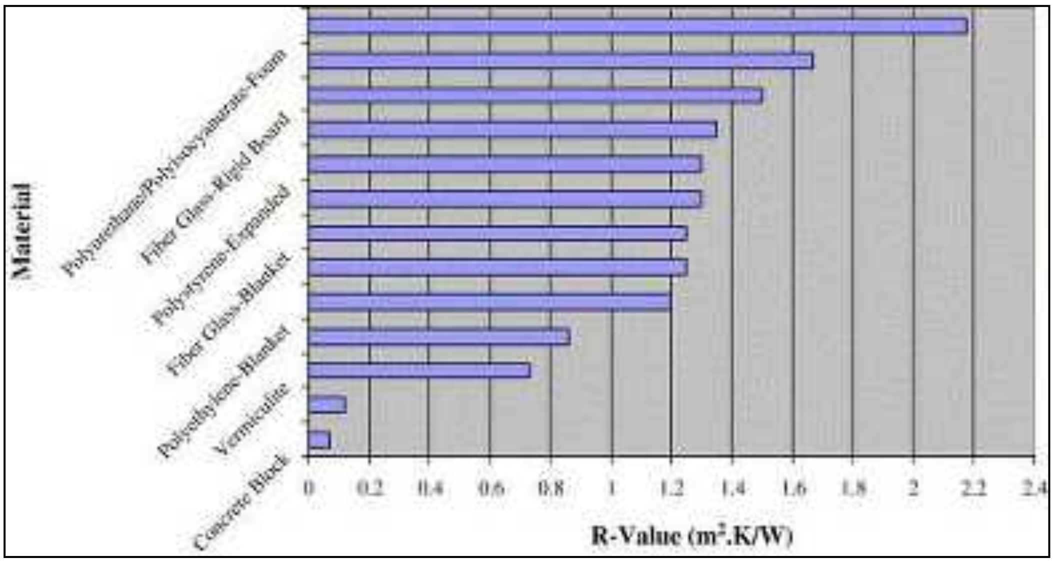

Figure 3. Thermal resistances (5cm thickness) of common building insulation materials (Concrete block is added for comparison purposes), Al-Homoud, 2004.

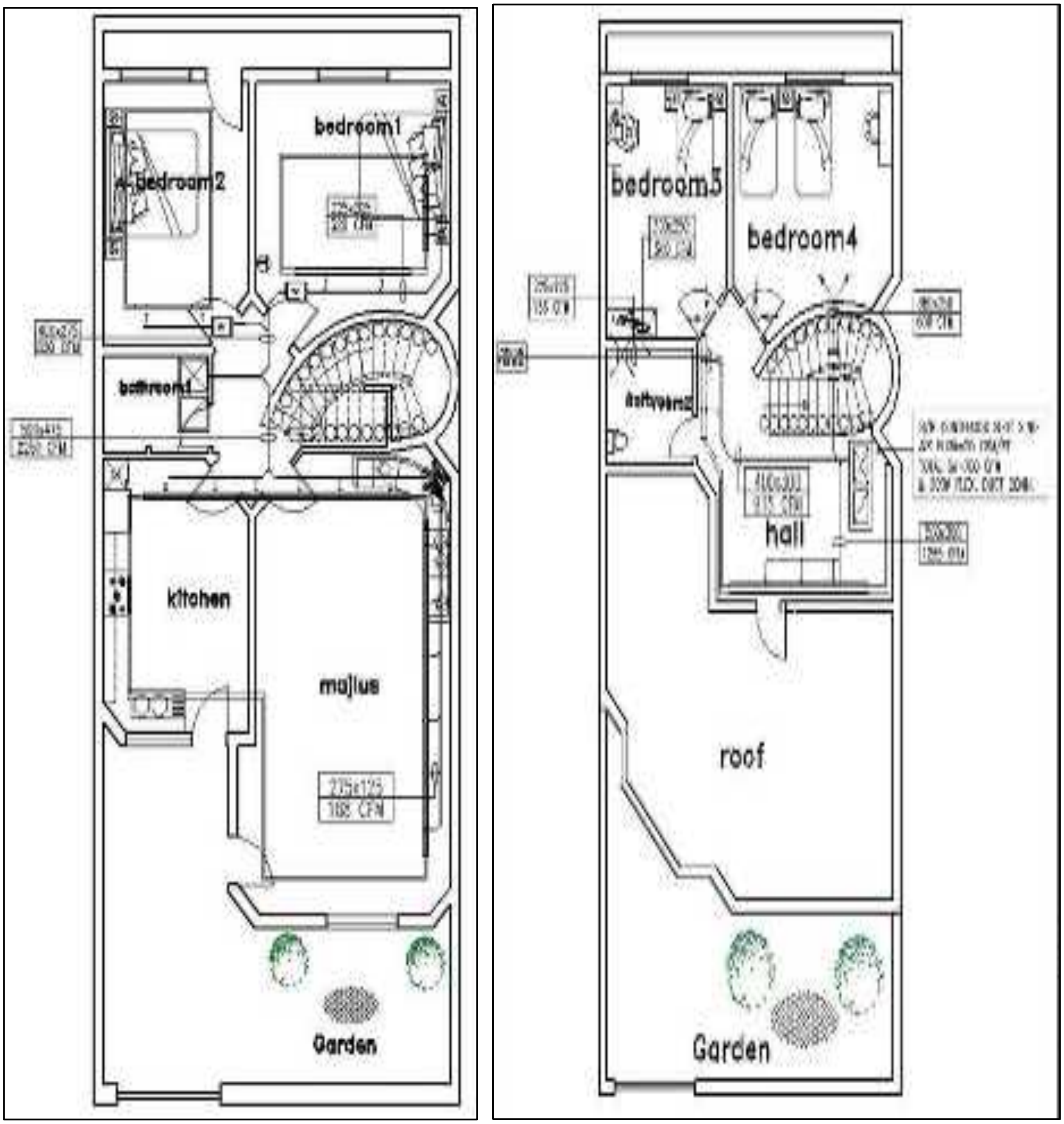

Figure 4. Air Conditioning plans layout.

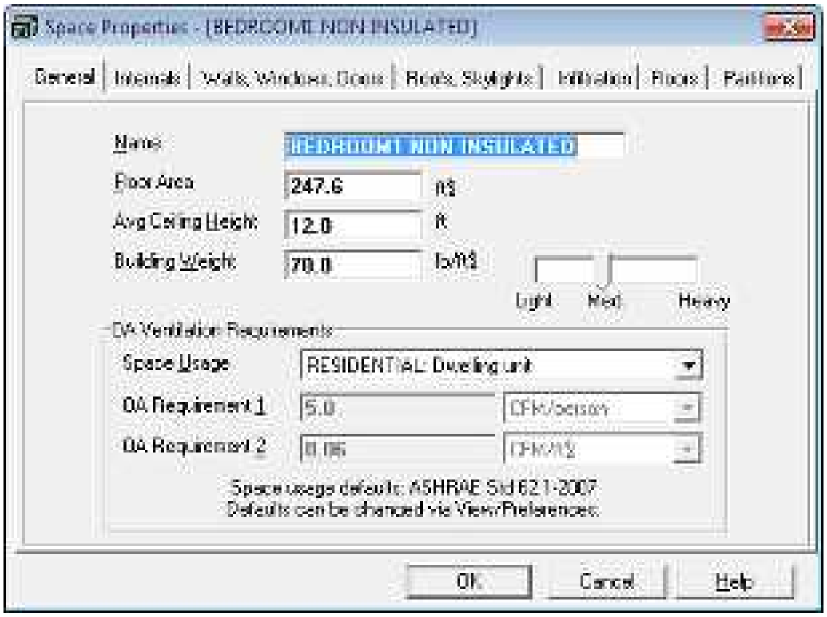

.**Figure 5.** HAP space properties.

Table 1. Monthly simulation results for non-insulated house package unit.

Month	Central Cooling Coil Load (kBTU)	Central Cooling Eqpt Load (kBTU)	Central Unit Clg Input (kWh)	Central Heating Coil Load (kBTU)	Central Heating Coil Input (kWh)	Zone Heating Coil Load (kBTU)	Zone Heating Coil Input (kWh)
January	0	0	0	0	0	0	0
February	0	0	0	0	0	0	0
March	0	0	0	0	0	0	0
April	22969	22969	1690	0	0	0	0
May	36201	36201	3058	0	0	0	0
June	44037	44037	4103	0	0	0	0
July	50368	50368	4940	0	0	0	0
August	50220	50220	4915	0	0	0	0
September	42022	42022	3815	0	0	0	0
October	30874	30874	2458	0	0	0	0
November	0	0	0	0	0	0	0
December	0	0	0	0	0	0	0
Total	276690	276690	24989	0	0	0	0

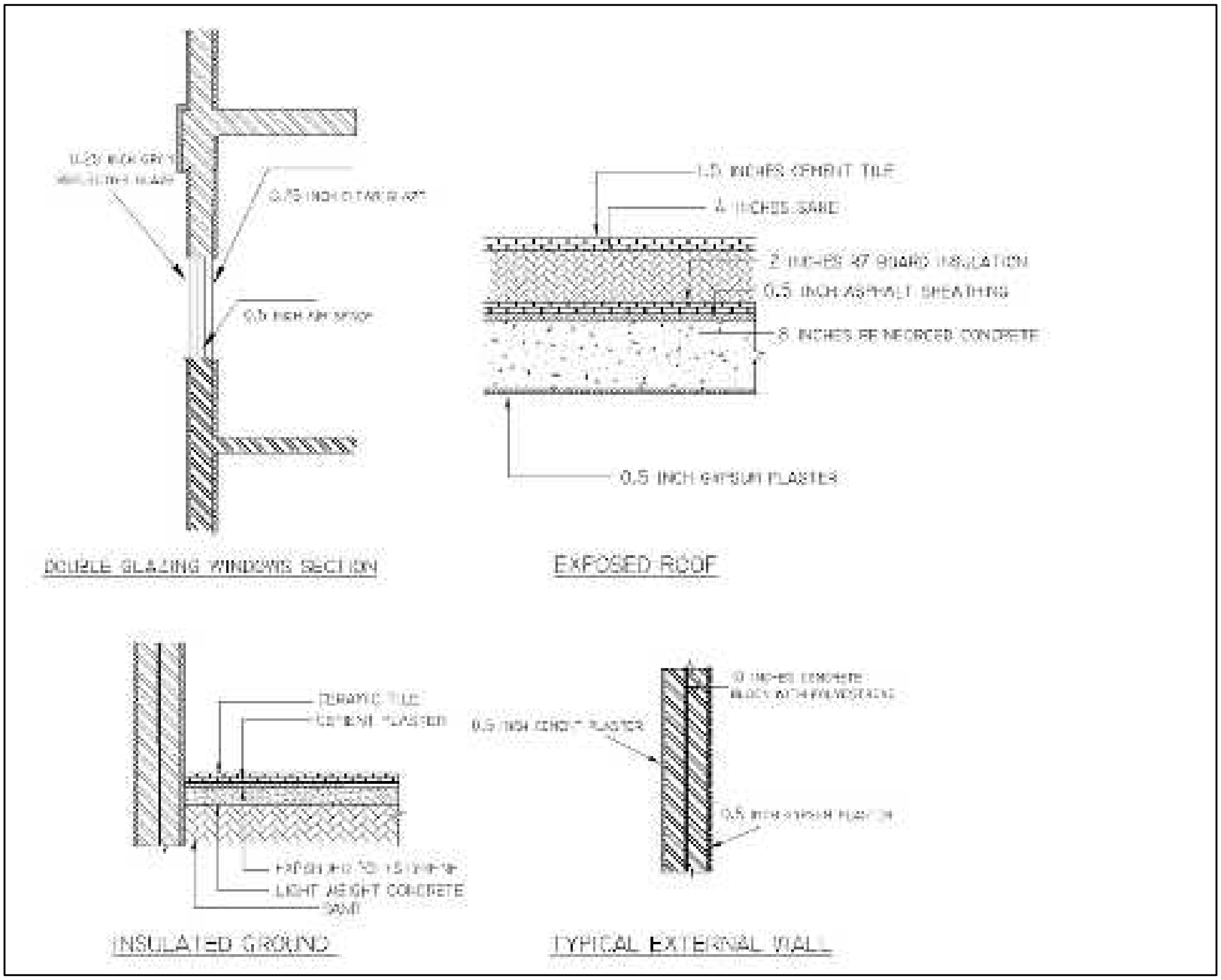

Figure 6. Insulated roofs, walls, floors, and double glazing windows (Researcher).

Table 2. U-Values.

Portion	**U-Value Non-insulated Btu/ F ft^2 h**	**U-Value insulated Btu/ F ft^2 h**
roofs	0.345	0.06
walls	0.301	0.085
windows	1.228	0.717

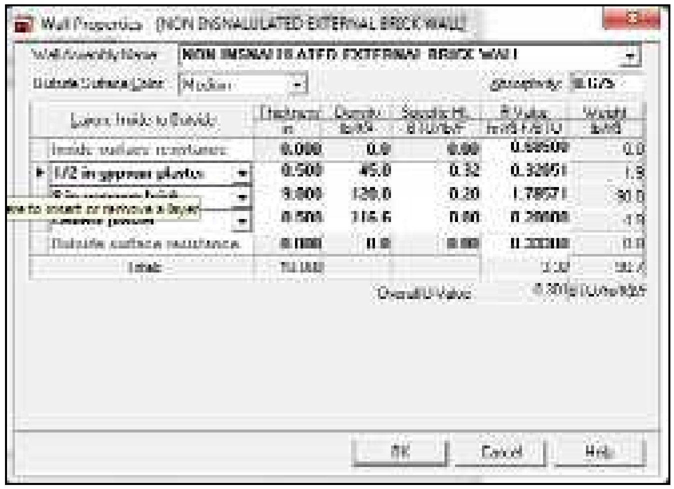

Figure 7. HAP U-Value and R-Values for Non-Insulated wall (Researcher).

Table 3. Monthly simulation results for insulated house package unit.

Month	Central Cooling Coil Load (kBTU)	Central Cooling Eqpt Load (kBTU)	Central Unit Clg Input (kWh)	Central Heating Coil Load (kBTU)	Central Heating Coil Input (kWh)	Zone Heating Coil Load (kBTU)	Zone Heating Coil Input (kWh)
January	0	0	0	0	0	0	0
February	0	0	0	0	0	0	0
March	0	0	0	0	0	0	0
April	18710	18710	1372	0	0	0	0
May	25253	25253	2136	0	0	0	0
June	28836	28836	2882	0	0	0	0
July	32050	32050	3184	0	0	0	0
August	32322	32322	3173	0	0	0	0
September	27873	27873	2533	0	0	0	0
October	22481	22481	1785	0	0	0	0
November	0	0	0	0	0	0	0
December	0	0	0	0	0	0	0
Total	187824	187824	18874	0	0	0	0

Studying the Effects of Contamination on Soil Properties Using Remote Sensing

Dr. Mahdi O. Karkush
Instructor
College of Engineering-University of Baghdad
mahdi_karkush@yahoo.com

Dr.Abdul Razak T .Ziboon
Professor
University of Technology
razzak56@yahoo.com

Hadeel M. Hussien
Researcher
College of Engineering-University of Baghdad
hadeel_mh_84@yahoo.com

ABSTRACT

The problem of soil contamination is increased recently due to increasing the industrial wastes such as petroleum hydrocarbon, organic solvents, and heavy metals as well as maximizing the use of agricultural fertilizers. During this period, wide development of data collection methods, using remote sensing techniques in the field of soil and environment applications appear and state the suitable technique for remediation. This study deals with the application of remote sensing techniques in geoenvironmental engineering through a field spectral reflectance measurements at nine spots of naturally hydrocarbons contaminated soil in Al-Daura Refinery Company site which is located to the south west of Baghdad using radiometer device to get standard curves of wavelengths and analyzing the satellite imagery of the site to get the spectral reflectance curves using GIS technique and EARDAS software package which help in producing thematic maps for the spatial distribution and concentration of contaminants. The comparison of results showed a good correlation between the spectral reflectance from field measurements and the spectral reflectance obtained from analyzing the satellite imagery. The study also improves a method to save cost, time, efforts and staff.

Key Words: contaminated soil, remote sensing, spectral reflectance and geoenvironmental engineering.

دراسة تأثير التلوث على خواص التربة بأستخدام طرق التحسس النائي والاستشعار عن بعد

د.مهدي عبيد كركوش
مدرس
كلية الهندسة/جامعة بغداد

د.عبدالرزاق طارش زبون
استاذ
الجامعة التكنولوجية

هديل ماجد حسين
باحثه
كلية الهندسة/جامعة بغداد

الخلاصة

ان مشكلة التلوث ازدادت بالوقت الحاضر نتيجة لزيادة المخلفات الصناعية بانواعها, النفطية, المذيبات العضوية, المعادن الثقيلة وكذلك الافراط في استخدام الاسمدة الزراعية. وبعد التطور الواسع, ظهر الاعتماد على طرق جمع البيانات الارضية والتطبيقات البيئية للاستشعار عن بعد في حقول هندسة مكيانيك التربة والبيئة لتحديد مقدار الضرر الناتج من وجود هذه الملوثات على التربة وتحديد طرق المعالجة المناسبة. هذه الدراسة تتعامل تستخدم تقنيات التحسس النائي والاستشعار عن بعد في هندسة التربة الملوثة وذلك من خلال قياس الانعكاسية الطيفية موقعيا لتسعة نقاط من التربة الملوثة طبيعيا بالهيدروكاربونات والرصاص في مصفى الدورة الواقع الى الجنوب الغربي من بغداد باستخدام جهاز الراديوميتر وتحليل الصورة الفضائية للموقع لغرض الحصول على منحيات الانعكاسية الطيفية باستخدام تقنيات نظم المعلومات الجغرافية واستخدام برنامج EARDAS. ربطت النتائج التي تم الحصول عليها من الراديوميتر مع النتائج التي تم الحصول عليها من الحقيبة البرامجية 10 EARDAS , وبينت النتائج وجود ربط جيد بين منحنيات قياس الانعكاسية الطيفية بالموقع والصورة الفضائية والذي بدوره يوفر في الجهد والكلفة والوقت اللازم لدراسة مشاكل تلوث التربة.

1. INTRODUCTION

The rapid growth of industrialization and urbanization has resulted in large quantities of waste gas, waste water, and waste solid being discharged into the environment, thus giving rise to serious environmental pollution problem. The occurrences of contaminants in soil above a certain level causing deterioration or loss some of geotechnical properties of soil , **Huang, 2000**. The most common soil contaminants are petroleum hydrocarbons, fertilizers and pesticides, and heavy metals. Iraq has several thousand contaminated sites resulting from a combination of general industrial activities, military activities and post-conflict damage and looting, **UNEP Report, 2005.**

The great demand for information about properties of surface and sub-surface soil which can be estimated by using spectral responses of surface soil for different bands of radiometer and short time available for the work arises to employ remote sensing techniques in geotechnical engineering which reduce the time, cost, efforts, and staff.

Yousif, 2004, used the remote sensing techniques to classify the soil of Al-Najaf city by comparing the results obtained from remote sensing techniques with those obtained from traditional classification method. **Al-Maliky, 2005.** constructed maps explained the zones of distributions and concentrations of pollutants in air, water and soil depending on an integrated measured and collected data base utilizing from GIS and Arcview software. **Carr et al. 2006,** used PXRF metal analyzer to obtain rabid in-situ elemental analysis for urban soil to produce a spatial maps for the distribution of contaminants in soil. **Nasir , 2008,** used the surface geoelectrical sounding data and remote sensing techniques in the evaluation of geotechnical properties of soil, the results of this study were five contour maps and digital geotechnical maps, as well as five geoelectrical sections to study the soil profile. **Wu et al., 2009,** studied the sensitivity of near-infrared diffuse reflectance sensing (NIRS) to trace metal concentration in (25) soil samples of silt loam soil. Detailed analysis indicates that the NIR spectrum is sensitive to sample handling, including the orientation of the samples in the NIRS instrument.

The purpose of the present work is to measure the reflectance ratio for nine naturally contaminated soil samples designated N1 to N9 by using three bands radiometer and compare with those data obtained from satellite image analysis using Arch GIS and ERDAS10 software.

2. EXPERIMENTAL WORK

2.1. Study Area

The study area is Al-Daura refinery company site which is located at Al-Daura district in the south-west of Baghdad governorate. Nine spots are selected in this site according to the advice of environmental staff in the Midland Refineries Company/Daura Refinery Company as well as the natural ground surface color. The soil profile of site is formed of top layer of very stiff to hard cohesive material about (8m) thick, overlying cohesion less layer of dense silty sand (6 to 8) m thick. The third layer at a depth of 16 m from ground surface consists of hard brown clayey silt. Groundwater table varied from (1.45 to 2.85) m below the ground surface (NCCL Report) as cited by , **Abdul Rasool , 1999**. Disturbed soil samples were obtained from ground surface to a depth of 15cm for chemical test and particle size analysis.

2.2. GPS Measurements

Soil samples location from the study area are determined by using global positioning system (GPS) receiver. The spatial position of target can be determined by the GPS receiver for soil samples location which are located on topographic map using the Universal Transverse Mercator (UTM) system which is a global spatial system based on the transverse Mercator projection , **Clarke, 1997**. The coordinates of position are referred to as Easting and Northing, being distances East and North of an origin. They usually expressed in meters. Under the UTM system, each East and North coordinate pair can refer to one of sixty points on Earth, one point in each of the sixty zones (World Geodetic System, WGS 84). The geo-referencing data of these locations are listed in **Table 1**. and the locations of these points are specified on the satellite imagery as shown in **Plate 1.**

2.3. Chemical Tests

The hydrocarbons and lead content of soil samples are determined in Ibn Sina State Company to measure the effects of hydrocarbons and lead on the reflectance ratio. The results of tests are given in **Table 2**.

2.4. Particle Size Analysis

The soil samples are collected from the surface layer of Al-Daura site to determine the particle-size distribution according to ASTM (D422). The results of particle size distributions are given in **Table 3.**

3. SPECTRAL REFLECTANCE MEASUREMENT

3.1 Radiometer

Radiometer is a device used for measuring the spectral reflectance of an object as a function of wavelength. It is used to measure the reflectance for different targets, which is reflected, scattered, transmitted, or emitted by an object , **Joseph and Simonett, 1976**. Any earth target receives solar radiation directly (irradiance E) by unit (Watt/m^2), otherwise, reflectance radiation from the same target (radiance L), with same unit radiometer records. This radiation as electrical signal must be transferred to radiation (Watt/m^2) by using the following equation:

$$L=C_1V_1 \tag{1}$$

where

C_1: constant transfer factor for each spectral band, each constant has two values: the first is used for radiance radiation and the second is used for the irradiance radiation.

V_1: electromagnetic radiation that is recorded by radiometer, similarly, the irradiance radiation (E) is given by:

$$E= C_2V_2 \tag{2}$$

In the present study, the radiometer (EXOTH, 1000BX) with three filters of spectral reflectance bands ranged from (0.45 to 0.7) micrometer as given in **Table 4** has been used to measure the intensity of the reflected waves that come from the soil in vertical direction. The measurements of radiometer are unit less and can be expressed as

percentage between the reflectance of falling waves from the sun and their reflected intensity from the soil , **Manual of Radiometer, 1983**.
The spectral reflectance of soils can be useful in their identification and characterization. The reflectance data from carefully selected wavelength bands radiometer can be used to extract information from bare soil areas that can be related to levels of organic matter, soil moisture, iron oxide content, particle size content, or used as an indicator of potential productivity such as: cation exchangeable capacity (CEC) for certain specified climatic areas. The soil contrast is often found in the wavelength interval from 0.6 to 0.7 µm , **Colwell, 1983**.

3.2 Conditions of Test

To use the radiometer device in measuring the reflectance ratio of surface soil, the following conditions must be satisfied:-

i. The target sample should be well represented to region in order to get more occurrences in measurement;

ii. Readings should be taken for several points closed from the target in the same soil specimen and calculate their average for more occurrences;

iii. The radiometer should be fixed on the target in order to get constant distance between the radiometer and soil sample surface. That is required to ensure no movement of the radiometer during reflectance testing;

iv. All readings are carried out in a sunny weather.

The spectral reflectance measurements of soil samples are carried out at the day time between 10 and 12 am in order to minimize the effect of the angle of in chiding from the sun.

3.3 Procedures of Test

The procedure of spectral reflectance test can be summarized as follows:-

i. The test is conducted on the surface of natural soil at the field;
ii. The radiometer is applied to the sunlight direction and recorded the reading;
iii. The radiometer is applied vertically above the target by a vertical distance of 15cm;
iv. The reflectance is read and recorded.

3.4 Spectral Reflectance Analysis

The properties of soils that govern their spectral reflectance are color, texture, structure and surface roughness, particle size, mineralogy, organic matter, free carbonates, salinity, moisture and the oxides/hydroxides of iron and manganese, emissivity, polarizing properties and soil normalization. Also, the chemical composition of the soil influences spectral signature of soils through the absorption processes , **Manchanda et al., 2002.**
Radiometer capacity to measure the visible adds a valuable dimension to the use of soil spectra to explain many soil characteristics and to predict soil response to different contaminations, management, and variations in climate , **Colwell, 1983**. Soils can often be distinguished by their photographic tone and/or color characteristics factors which depend on the properties of soil materials themselves.

Also, electromagnetic, radiation can be sensed by detectors that respond in spectral regions beyond those discernible by human eye , **Colwell, 1983**. In order to use remote sensing techniques to produce thematic map explain the zoning of soil contaminants distribution, it's necessary to understand the relationship between soil properties and soil color. The most important factors influencing soil color are mineralogy, chemical composition, moisture content and organic matter content.

4. SATELLITE IMAGE PROCESSING AND ANALYZING

The processing and analysis of satellite imagery can be summarized by the following procedure:

i. Geo-referencing Spatial Data

Geo-referencing is the conversion of spatial information from an existing format (collected data and tested samples) in to a digital format and data structure compatible with a GIS. Geo-referenced data to be encoded include hard copy paper maps and tables of attributes electron files of maps and associated attribute data, scanned aerial photographs and digital satellite remotely sensed data (form GPS device). The traditional digitizing of points is based on the use of Cartesian coordinates such as UTM coordinates , **Jensen, 1996**.

ii. Analyzing Spatial Data

The satellite image for AL-Daura site is analyzed by using software (EARDAS 10) to get the reflectance of geo-referenced data (soil samples locations) depending on the results of radiometer measurements for soil samples in the field. Data not in image form are difficult to reduce or associate with specific ground elements unless simultaneous bore-sighted photography is available.

iii. Classification Process

Multispectral classification is the process of sorting pixels into a finite number of individual classes, or categories of data, based on their data file values. If a pixel satisfies a certain set of criteria, the pixel will be assigned to the class that corresponds to that criterion. This process is also referred to as image segmentation. Depending on the type of information, extracted from the original data, classes can be associated with known features on the ground or can simply represent areas that look different to the computer.

The classification process breaks down into two parts: supervised and unsupervised. In supervised classification the analyst designates a set of ?training areas?in the image, each of which is a known surface material that represents a desired spectral class. The classification algorithm computes, the average spectral pattern for each training class, and then assigns the remaining image cells to the most similar class. In unsupervised classification the algorithm derives its own set of spectral classes from an arbitrary sample of the image cells before making the class assignments , **ERDAS Field Guide?2008.**

iv. Organization Spatial Data

The organization of spatial data component includes those functions needs to store and retrieve data from the data base. The methods used to implement these functions determine how efficiently the system performs all operations on the data; each variable is archived in a computer-compatible digital format as a geographically referenced plane (often called a GIS layer). Each layer contains features with similar attributes, like type of pollutant and concentration of pollutant that are located in the same geographic extent , **Jensen, 1996**.

5. RESULTS AND DISCUSSION

The results of field spectral ratio for nine locations (N1 to N9) are shown in **Fig. 1**. The suffix R in symbol of sample designations refers to the results obtained from radiometer measurement. From the results shown in Table 2 and **Fig. 1**, it can be noticed that the spectral reflectance ratios are decreased with increasing the hydrocarbons content in the soil samples which makes the color of soil samples darker. While in (N4R) the neutralities may be due to the soil texture or variation in the water content.

The satellite imagery of Al-Daura site with four bands was analyzed using EARDAS10 software for nine geo-referenced points and the summary of results is shown after redrawn in **Fig. 2**. The results obtained from radiometer tests as shown in **Fig. 1** are identical and have the same pattern of those obtained from the analysis of satellite imagery by EARDAS software which shown in **Fig. 2**, except (N6). Dealing with the behavior of (N6), the value appear with high different comparing with other values because of the randomly error through the image processing steps. The digital map of the study area can be divided into zones according to the type of contaminants and/or the concentration of contaminants in the surface layer of soil depending on the reflectance measurements, digital imagery and geotechnical properties of soil using GIS techniques. The integration between geotechnical properties of soil and GIS techniques help to generate missing spatial data.

The important application of remote sensing and GIS techniques in geotechnical engineering is production of digital maps with supervised classification operation with nine spectral classes for Al-Daura site; the first one explains the distribution zones and concentration of hydrocarbons as shown in **Plate 2**. While, the second is a digital map explains the distribution zones and concentration of lead as shown in Plate 3. Construction digital maps using GIS techniques are representative, easy to use, and saving time and cost. The predicted and measured (reference) contents and the spatial distributions of hydrocarbons and lead were interpolated by using EARDAS software to produce digital thematic maps of layers for the distribution and concentration of hydrocarbons and lead are shown in **Plate 4** and **Plate 5** respectively. This application of remote sensing and GIS techniques in geotechnical engineering is new and powerful in predicating the geotechnical properties of surface soil layer especially in the field of soil contamination.

6. CONCLUSIONS

The spectral reflectance depends on the soil sample color, so the reflectance ratio for natural contaminated soil with hydrocarbons decreases with increasing of hydrocarbons concentration except (N4R). The field simulation of the spectral reflectance in naturally contaminated soil with hydrocarbons using radiometer measurements corresponding to the bands used in the satellite image analysis using EARDAS software prove that this technique is very useful and powerful for the estimation of contaminants types in the surface layer of soil. Also, the use of satellite images with high resolution and different bands provides a very large amount of qualitative and quantitative information for study area to state the soil contamination states.

REFERENCES

Abdul Rasool H., 1999, *Some Geotechnical Properties of Oil Contaminated Soil*, M.Sc. Thesis, University of Baghdad.

Al-Maliky, M. A. S., 2005, *Evaluation of Air, Water and Soil Pollutants in Baghdad City Using Geographic Information System (GIS),* M.Sc. Thesis, College of Sciences, University of Baghdad. (in Arabic).

Annual Book of ASTM Standards, 2003, *Soil and Rock*; Building, Stone; Peats.

Carr R., Zhang C., Moles N., and Harder M., 2007, *Identification and Mapping of Heavy Metal Pollution in Soils of a Sports Ground in Galway City, Ireland, Using a Portable XRF Analyser and GIS*, Environ Geochem Health, Vol.30, PP. 45?52.

Clarke K.C., 1997, *Getting Started with Geographic Information Systems*, University of California, Santa Barbara. Prentice Hall, Upper Saddle River, New Jersey.

Colwell R.N., 1983, *Manual of Remote Sensing*, American Society of Photogrammetry, Volume II.

ERDAS Field Guide? 2008, Volume I, II.

Huang P. M., 2000, *Soils and Ground Water Pollution and Remediation. Asia, Africa, and Oceania*, Lewis Publishers.

Jensen J. R., 1996, *Introductory Digital Image Processing a Remote Sensing Perspective*, Second Edition. Prentice Hall. Upper Saddle River, New Jersey.

Joseph L. J. and Simonett D. S., 1976, *Remote Sensing of Environmen*t, Addison-Wesley Publishing Company.

Manchanda, M. L., Kudrat, K. & Tiwari, A. K., 2002, *Soil Survey and Mapping Using Remote Sensing*, Regional Remote Sensing Service Centre, Dehradun 248001, India.

Manual of Radiometer, 1983, Exoth Company, U. S. A.

Nasir, A. N. I., 2008, *Geotechnical Engineering Study for Salah Al-Din Governorate Using Geophysical and Remote Sensing Techniques*, Ph.D. Thesis, Building and Construction Engineering Department, University of Technology;

UNEP Report, 2005, *Assessment of Environmental ?Hot Spots? in Iraq*, Report ISBN 92-807-2650-1, France.

Wu C. Y., Jacobson A. R., Laba M., Kim B., and Baveye P. C., 2009, *Surrogate Correlations and Near-Infrared Diffuse Reflectance Sensing of Trace Metal Content in Soils*, Water Air Soil PoVol.209, PP. 377-390.

Yousif, B. F., 2004, *The Use of Remote Sensing Techniques in the Classification of Al-Najaf Soil*, M.Sc. Thesis, Building and Construction Engineering Department, University of Technology.

NOMENCLATURE

C_1 and C_2: constant transfer factors for each spectral band.
E: the irradiance radiation (Watt/m^2).

L: reflectance radiation from the target (Watt/m^2).
V_1 and V_2: electromagnetic radiation that is recorded by radiometer.

Table 1. GPS coordinates of soil samples locations.

Sample No.	GPS Coordinates	
	Northing	Easting
N1	0447612	3681802
N2	0447607	3681742
N3	0447247	3681867
N4	0447277	3681886
N5	0446932	3682403
N6	0446836	3682350
N7	0446832	3682340
N8	0446761	3681643
N9	0446757	3681650

Table 2. Hydrocarbons and lead contents and particle-size distribution of soil.samples.

Soil Sample	Hydrocarbons Content %	Lead Content %	Silt %	Clay %
N1	0	0.0025	100	-
N2	0.185	0.0022	40	60
N3	0.285	0.0048	50	50
N4	0.644	0.0034	60	40
N5	22.44	0.0233	100	-
N6	3.629	0.0035	15	85
N7	3.225	0.0027	40	60
N8	0	0.0043	50	50
N9	0	0.0035	30	70

Table 3. Particle-size distribution of soil samples.

Soil Sample	Silt %	Clay %
N1	100	-
N2	40	60
N3	50	50
N4	60	40
N5	100	-
N6	15	85
N7	40	60
N8	50	50
N9	30	70

Table 4. Wavelength of radiometer bands.

Band	Range of Band (μm)	Peak (μm)
Blue	0.45-0.49	0.48
Yellow	0.56-0.59	0.56
Red	0.63-0.70	0.66

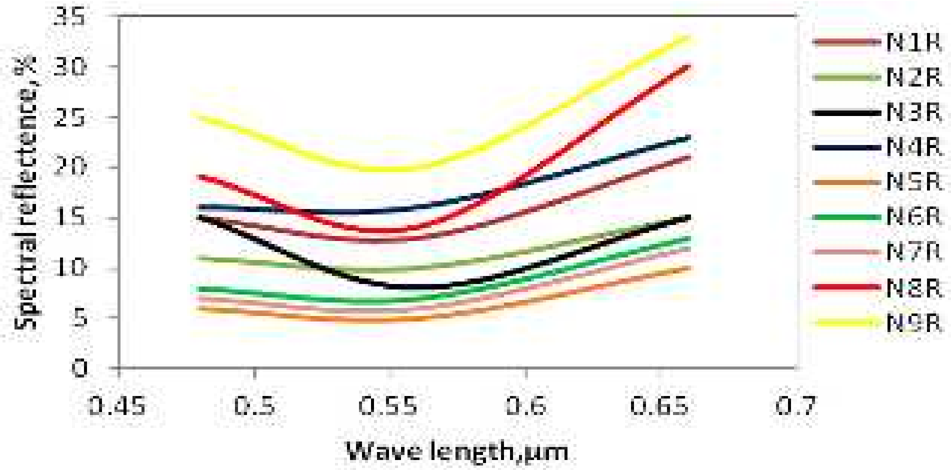

Figure 1. Spectral reflectance curves from radiometer tests.

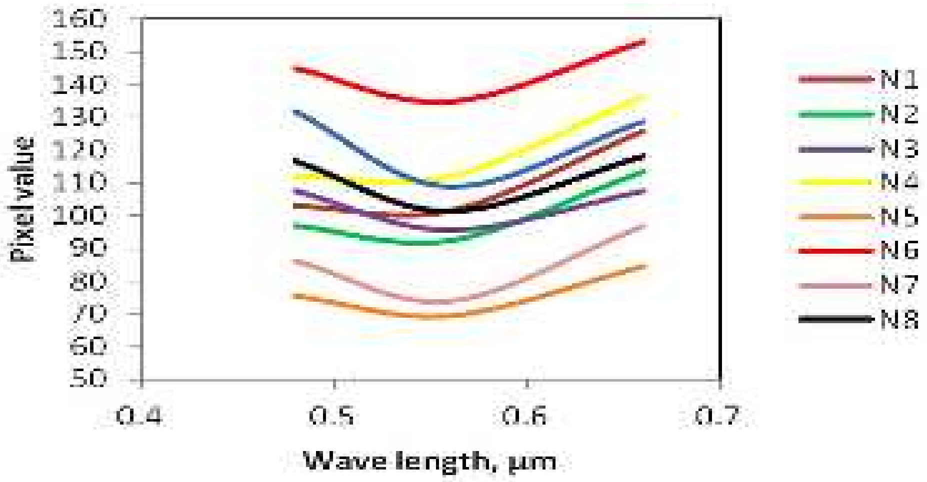

Figure 2. Spectral reflectance curves from satellite image.

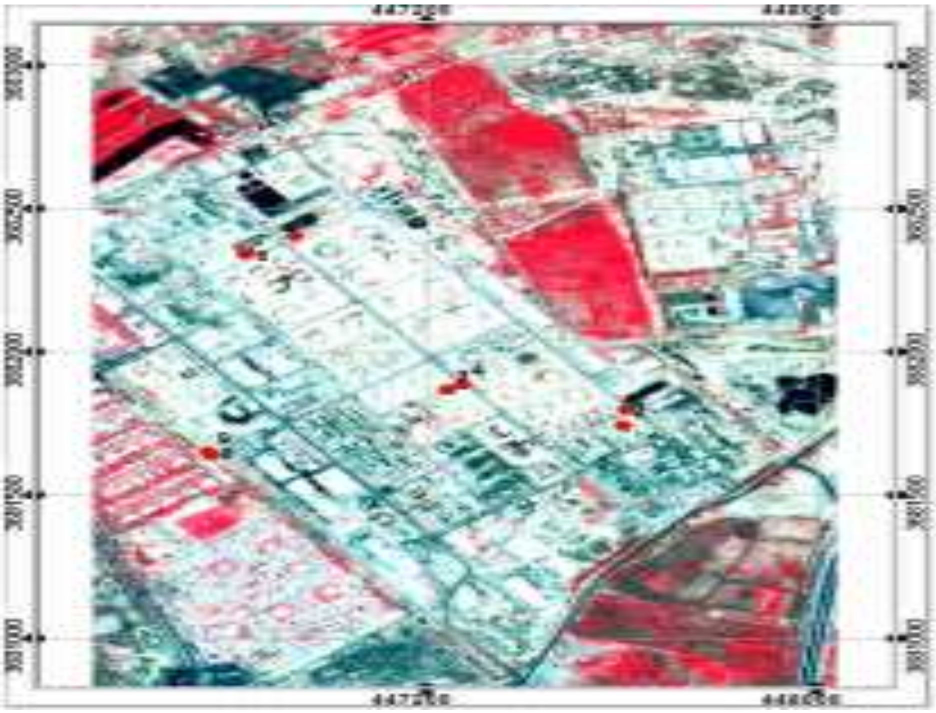

Plate 1. Locations of nine spots on satellite image.

Plate 2. Distribution and concentration of hydrocarbons.

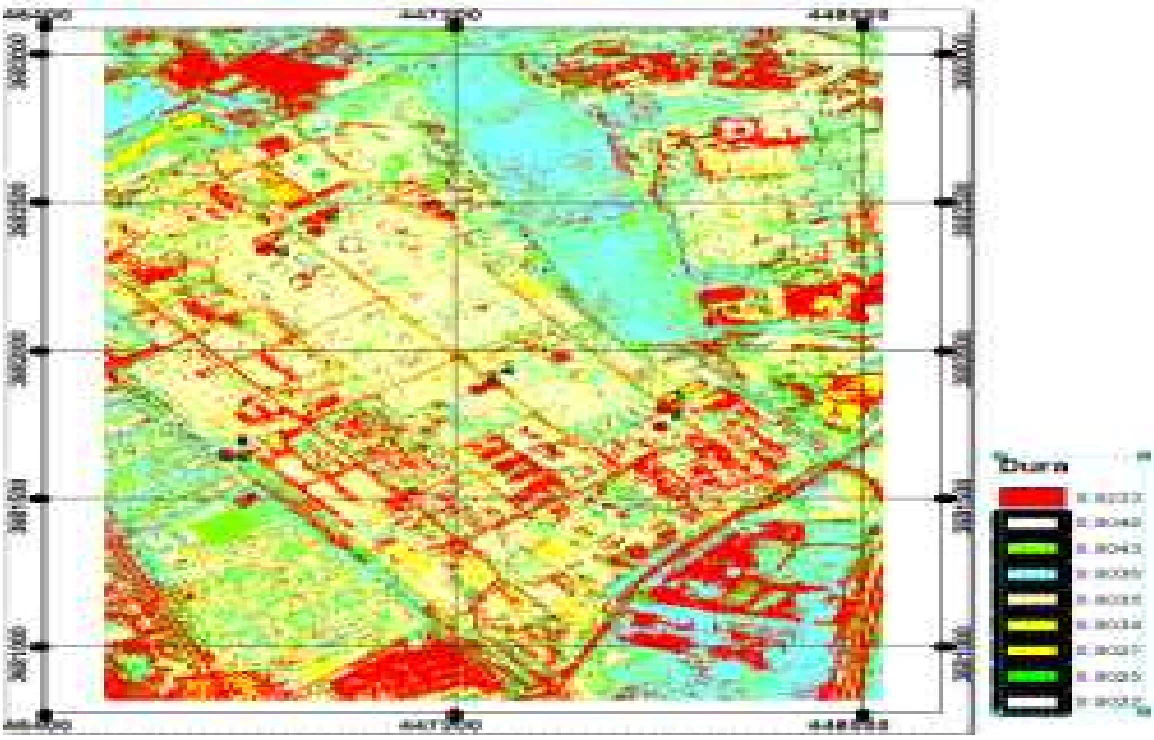

Plate 3. Distribution and concentration of lead.

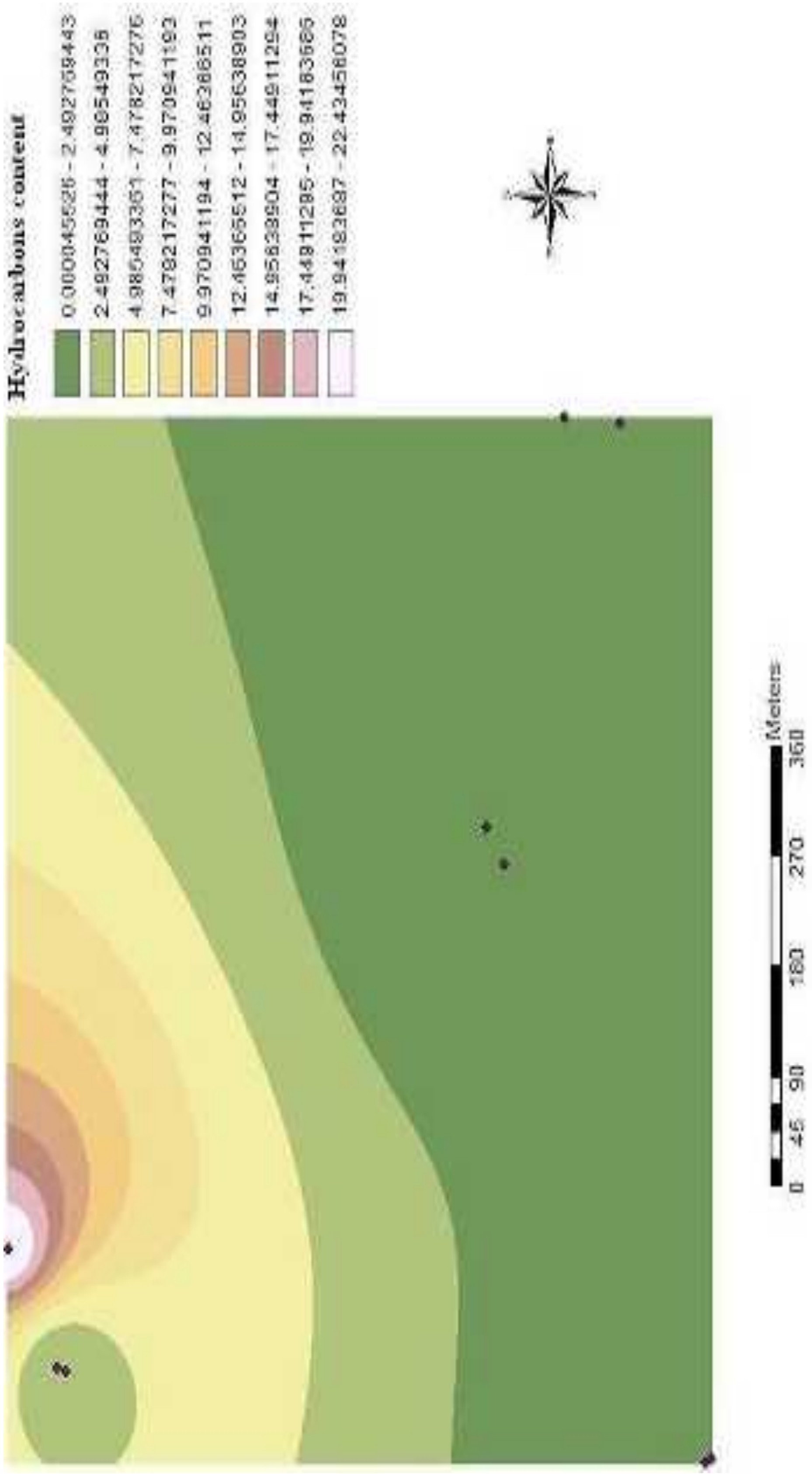

Plate 4. Distribution and concentration of hydrocarbons content in the soil.

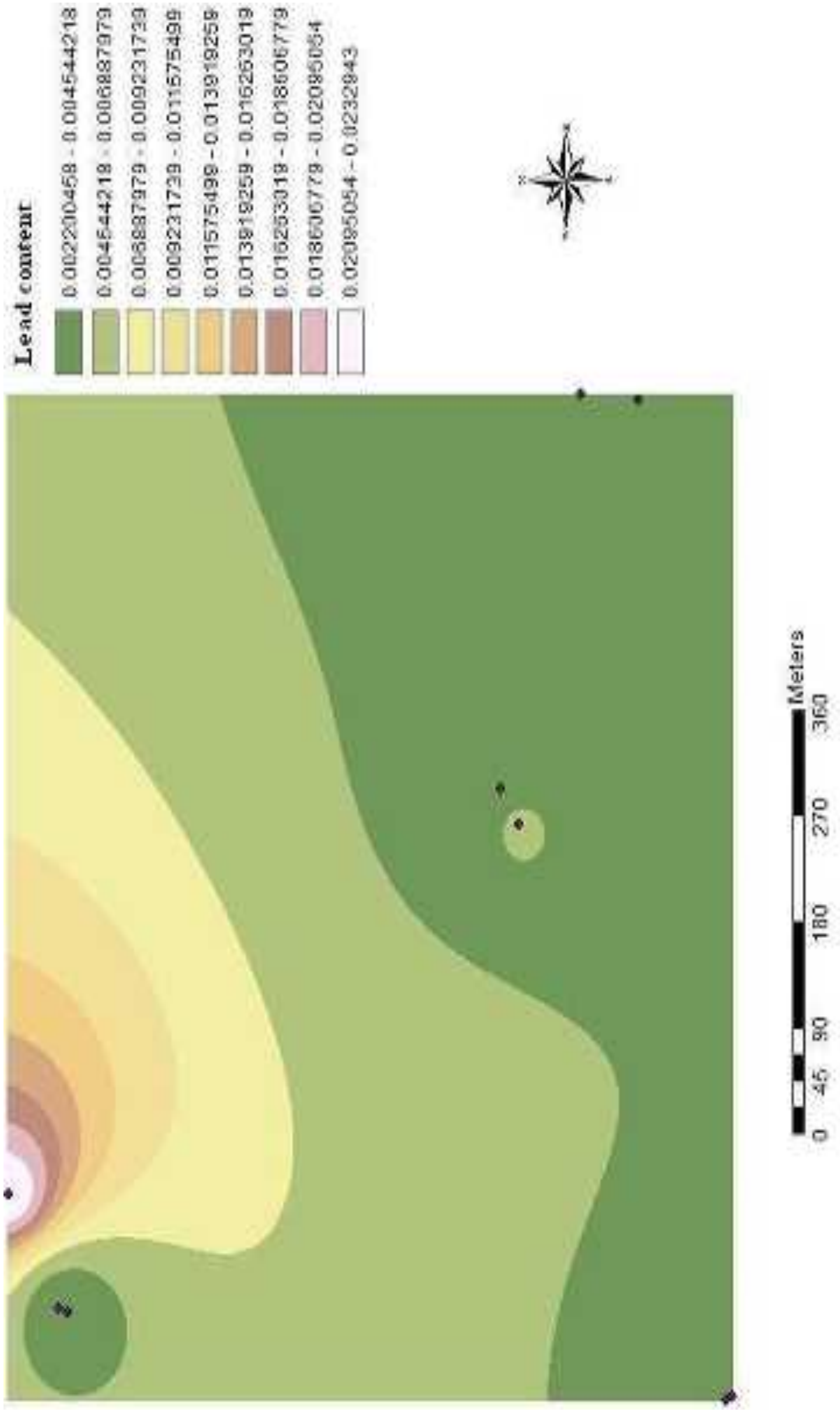

Plate 5. Distribution and concentration of lead content in the soil.

The Effect of Ceramic Coating on Performance and Emission of Diesel Engine Operated on Diesel Fuel and Biodiesel Blends

Dr. Ibtihal Al-Namie
Assistant Professor
Mechanical Engineering Department-University of Technology
Email: IbtihalNamie@yahoo.com

Dr. Mahmoud A. Mashkour
Assistant Professor
Mechanical Engineering Department-University of Technology
Email: mahmoud_ Mashkour@hotmail.com

Ali Abu Al-heel Qasim
Email: alialgabry915@yahoo.com

ABSTRACT

In this work, the effect of ceramic coating on performance, exhaust gas temperature and gases emissions of diesel engine operated on diesel fuel and biodiesel blends was investigated. A conventional four stroke, direct injected, single cylinder, diesel engine was tested at constant speed and at different load conditions using diesel fuel and biodiesel blends. The inlet and exhaust valves, the head of piston and cylinder head of the engine were coated by ceramic materials. Ceramic layers were made of (210-240) µm of Al2O3 and (30-60) µm of 4NiCr5Al as a bond coat for inlet and exhaust valves and (350-400) µm of YSZ and (50-100) µm of 4NiCr5Al as a bond coat for head of piston and (280-320) µm of Sic and (40-80) µm of 4NiCr5Al as a bond coat for cylinder head. The coating technique adapted in this work is the flame spray method. The engine with valves, piston and cylinder head ceramic coated research was tested for the same operation conditions of the engine (without coating). The results showed that a reduction in brake specific fuel consumption of 19.29%, 15.91%, 14.65% and 7.06%, an increase in brake thermal efficiency of 23.68%, 19.77%, 16.51% and 6.32%, the increase in exhaust gas temperature of 9.01%, 7.22%, 15.7% and 11.42%, the reduction of CO emission of 18.57%, 20%, 20.5% and 27.77%, the reduction of HC emission of 28.97%, 43.9%, 38.88% and 36.41% for diesel, B5,B10 and B100 respectively.

Key words: ceramic coating, diesel engine, engine performance, emission, biodiesel.

تأثير الطلاء الخزفي على أداء وأنبعاث محرك ديزل يعمل بوقود الديزل وخليط ووقود الديزل الحيوي

د.أبتهال عبد الرزاق محمود
أستاذ مساعد
قسم هندسة المكائن والمعدات-الجامعة التكنولوجية

د.محمود عطا الله مشكور
أستاذ مساعد
قسم هندسة المكائن والمعدات-الجامعة التكنولوجية

الباحث علي ابو الهيل قاسم

الخلاصة

في هذا البحث، تم دارسة تأثير الطلاء الخزفي على أداء ودرجة حرارة غاز العادم وأنبعاث الغازات لمحرك ديزل رباعي الاشواط وحقن مباشر وأحادي الاسطوانة. تم دراسة الاداء لهذا المحرك بسرعة ثابتة وحمل متغير باستخدام وقود الديزل الحيوي. تم طلاء وجه صمامي الدخول والعادم ووجه البستن ووجه الاسطوانة بمواد خزفية. حيث تم استخدام طبقة مكونة من (210-240) ميكرون من الألومينا كمادة طلاء و (30-60) ميكرون من نيكل-كروم-الالومينيوم كمسحوق طلاء رابط لطلاء صمامي الدخول والعادم وتم استخدام طبقة مكونة من (350-400) ميكرون من الزركونيا المثبتة بالياتيريا كمادة طلاء و (50-100) ميكرون من نيكل –كروم-الالومنيوم كمسحوق طلاء رابط لطلاء وجه لبستن وتم استخدام طبقة مكونة (280-320) ميكرون من سليكون

الكاربيد كمادة طلاء و (40-80) ميكرون من نيكل-كروم-الالومنيوم كمسحوق طلاء رابط لطلاء وجه الاسطوانة. في هذا العمل، اعتمدت تكنلوجيا الطلاء الحرارية بتقنية الرش باللهب. اختبر المحرك تحت نفس ظروف التشغيل قبل الطلاء وقد اعطت النتائج العملية انخفاض في معدل استهلاك الوقود المكبحي بمقدار (19.29%، 15.91%، 14.65%، 7.06%) وزيادة في كفاءة الكبح الحرارية بمقدار (23.68%، 19.77%، 16.51%، 6.32%) وزيادة في درجة حرارة غاز العادم بمقدار (9.01%، 7.22%، 15.7%، 11.42%) وانخفاض في غاز اول اوكسيد الكاربون بمقدار (18.75%، 20%، 20.5%، 27.77%) وانخفاض في انبعاث الهيدروكاربونات غير المحترقة بمقدار (28.97%، 43.9%، 38.88%، 36.41%) لوقود الديزل ووقود الديزل الحيوي بنسبة خلط (5:95) و (10:90) ووقود الديزل الحيوي (100%) على التوالي.

مفاتيح الكلمات: طلاء السيراميك، ماكنة الديزل، اداء الماكنة، الانبعاث، الديزل الحيوي.

1. INTRODUCTION

The effect of ceramic coating on performance, exhaust gas temperature and gases emissions of diesel engine operated on diesel fuel and biodiesel blends was investigated using a conventional four stroke, direct injected, single cylinder, diesel engine. The standard engine (without coating) was fully instrumented and connected to the dynamometer. The tests were performed at different engine loads and constant speed. The experiments were conducted at six load levels, viz. 1, 2, 3, 4 and 5 (N.m) and constant speed (3000 rpm). The required engine load percentage was adjusted by using the hydraulic dynamometer. These procedures were repeated to cover the engine load range at the specified speed. This work is adopted with an investigation of ceramic coating when the inlet and exhaust valves, head of piston and cylinder head insulation were applied. The valves were coated with (30-60) µm bond coating ( ) then coated with a (210-240) µm coating of the head of piston was coated with (50-100) µm bond coating ( ) then coated with a (350-400) µm coating of 8% - and the cylinder head was coated with (40-80) µm bond coating ( ) then coated with a (280-320) µm coating of Sic by the flame spray technique. To ensure the repeatability of experimental results, every test was repeated another one time. The average value of the repeated testes was adopted in the analysis. Points of large discrepancy were neglected. There were some differences between the tests of the same conditions. The reasons behind that are the instruments error, the change in the ambient conditions, and the human error.

2. BACKGROUND

Until the middle of the 20th century the number of IC engines in the world was small enough that the pollution they emitted was tolerable, and the environment, with the help of sunlight, stayed relatively clean. As world population grew, power plants, factories, and an ever-increasing number of automobiles began to pollute the air to the extent that it was no longer acceptable, **Willard W. P, 1997**.

Engine efficiency improvement efforts via constructional modifications are increased today; for instance, parallel to development of advanced technology ceramics, ceramic coating applications in internal combustion engines grow rapidly, **Murat et al, 2012**.

A TBC system, usually, consists of two layers - a metallic bond coat and top ceramic coat. The function of the bond coat is to protect the substrate from oxidation and provide sufficient bonding of the top ceramic coat to the substrate. The insulating ceramic layer provides a reduction of the temperature of the metallic substrate, which leads to improved component durability, **Satrughna Das, 2007**.

Thermal barrier coatings (TBC) provide the potential for higher thermal efficiencies of the engine, improved combustion and reduced emissions. In addition, ceramics show better wear characteristics than conventional materials. Lower heat rejection from the combustion chamber through thermally insulated components causes an increase in available energy that would increase the cylinder work and the amount of energy carried by the exhaust gases, which could be also utilized. Thermal barrier coatings are becoming increasingly important in providing thermal insulation for LHR engine components, **Sivakumar et al, 2012**.

Dennis Assanis and **Kevin Wiese, 1991** studied the effects of ceramic coatings on diesel engine performance and exhaust emissions. Tests were carried out over a range of engine speeds at full load for a standard metal piston and two pistons insulated with 0.5 mm and 1.0 mm thick ceramic coatings. The 0.5mm ceramic coated piston produced 10% higher thermal efficiency than the metal piston and exhaust CO levels were between 30% and 60% lower than baseline levels. Similarly, unburned HC levels were 35% to 40% lower for the insulated pistons.

Holloman L. and **Levy A.V., 1992,** discussed the use of ceramic coatings on the combustion zone surfaces of large, natural gas-fueled, internal combustion engines was. The performance was measured in the field before and after coating. It was determined that the durability, power output, fuel consumption, exhaust emissions, and other operating characteristics all improved due to ceramic coating of the flame side surfaces of cylinder heads, power pistons, and valves.

Hejwowski T. and **Weronski A., 2002,** evaluated the effects of thin thermal barrier coatings on the performance of a diesel engine. Results obtained from the engine with thermally insulated pistons were compared with the baseline engine data. The performance of the modified engine-driven car was found satisfactory. The ceramic coating did not produce observable knock in the engine, no significant wear of piston skirts or cylinder liners was found.

Shrirao P. N. and **Pawar A. N., 2011,** studied the effect of mullitecoating (Al_2O_3= 60%, SiO_2= 40%) on a single cylinder, four stroke, direct injection, diesel engine. Tests were carried out on standard engine (uncoated) and low heat rejection (LHR) engine with and without turbocharger. The results showed that there was 2.18% decreasing in specific fuel consumption, 12% increasing in exhaust gas temperature, 22.05% decreasing in CO emission and 28.20% decreasing in HC emission of LHR engine with turbocharger compared to standard engine at full load.

The aim of this paper is to study the effect of ceramic coating inlet and exhaust valve, head of piston and cylinder head of diesel engine on the performance of diesel engine operated on diesel fuel and biodiesel blends and emissions like (CO, CO_2, and HC). The results of the two cases are compared.

3.EXPERIMENTAL WORK

3.1 Coatings Technique

The coating technique adopted in this work is the flame spray method type (rototec 800) as shown in **Fig.1**. This apparatus consists of a chamber containing a flange to hold the specimen and an Oxy- Acetylene flame. The powder particles flow with the flame and is deposited on the specimen. The powder was supplied through a special tube in the flame gun.

3.2 Coating Procedure

The following procedure was adopted during coating process:

1. The substrates were cleaned and roughened using emery paper (p220) and grit-blasted using sand blast system with pressure (4-6) bar by sand blast device.
2. The grit-blasted substrates were cleaned using anhydrous ethanol alcohol and dried at 200 °C by a furnace for 30 min.

3. The ceramic powder type Al2O3 (400 mesh) and 4NiCr5Al metal powder (bond coat) with particle sizes ranging from 50 to 90 µm for inlet and exhaust valves coating – **Fig. 2**, 8%Y2O3-ZrO2 (325 mesh) and (4NiCr5Al) metal powder (bond coat) with particle sizes ranging from 50 to 90 µm for piston coating – **Fig. 3** and Sic (200 mesh) and (4NiCr5Al) metal powder (bond coat) with particle sizes ranging from 50 to 90 µm for cylinder head coating – **Fig. 4**, were used.
4. The substrate is fixed on the flange normal to the flame and powder flow.
5. The cooling system (air compressor) is switched on to cool the substrates and protect it from melting during spraying process.
6. The system is switched on and the flame is ignited. The flame holder is controlled manually.
7. The bond powder required for the first layer is loaded into the holder.
8. The substrate is heated to a suitable temperature around (300 °C) by the flame.
9. The coating process is started by moving a lever on the hopper to allow all the powder to flow through the holder with the flame. A distance of about (20 cm) between the flame and the specimen is maintained.
10. Step 8 is repeated until 30-60 µm as a thickness of bond layer is obtained for valves, 50-100 µm for piston and 40-80 µm for cylinder head.
11. The ceramic powder (required for the top coat) is then loaded and step 7 is repeated until 210-240 µm thickness for valves is obtained, 350-400 µm for piston and 280-320 µm for cylinder head.
12. The temperature for bond coat and top coat is controlled by adjusting the distance between the flame and the specimen and the pressure of Oxy-Acetylene.
13. For adhesion process, the topcoat is preheated to about 1500°C directly after completing the spray process.
14. The flame is then withdrawn gradually away from the valve to minimize thermal shock.
15. After the thermal coating process is completed, the excess parts of coating material are removed by grinding process to avoid crankshaft breakdown.

3.3 Evaluation of Coating (Bond Strength and Hardness)

The bond strength of coatings is the most important property which determines the field of use of coatings especially for thermal barrier coatings. The Adhesion strength value between the substrate and the coating layers was measured using the apparatus type (Microcomputer Controlled Electronic Universal Testing Machine (WDW-50E). The strength found equals to (26.8) MPa for 8%YSZ, (31.6) MPa for alumina coating and (39.64) MPa for silicon carbide coating. The Adhesion strength depends on the type of bonding layer and, spraying distance. The hardness value of (8%YSZ) coating was measured using a Vickers-hardness and found equal to (710) Hv and (788) Hv for alumina coating and (855) Hv for silicon carbide coating.

3.4 Test Engine Setup and Procedure

The engine tests were conducted in a single cylinder, direct injection (F 170) type diesel engine. Table 1 presents the main technical specifications of the engine used and **Fig. 5** shows it. This engine was coupled to a calibrated hydraulic dynamometer for speed and torque measurements. They were fixed on the stainless steel base type (TD 114) which was designed for this purpose. The water is used as a friction fluid for dynamometer. The system of fuel measurement consumption consists of a tank with capacity (4.5 l) and a glass tube of known volume was used. The measurement of air consumption consists of an air box which is used to reduce the vibration presented when the engine is working with a water manometer. The schematic diagram of the experimental set up is shown in **Fig. 5**. The temperature of exhaust gases was measured by temperature digital indicator (code 952416) that is fixed at the entrance of exhaust gas pipe (the beginning of the exhaust gas exit). The exhaust gases analyzer type (FLUX 2000-4) was used to analyze exhaust gases. The gases are picked up from the engine exhaust pipe by means of the probe. They are separated from the water they contain through the condensate filter and then they are conveyed to the measuring cell. A ray of infrared light is sent through the optical filters on to the measured elements. The gases which contain the measuring cell absorb the ray of light at different wavelength, according to their concentration. The engine was allowed to run with neat diesel fuel and biodiesel blends at a constant speed for nearly 10 min to attain the steady-state condition at the lowest possible load. The performance of engine was observed at a constant speed of 3000 rpm and varying load. To avoid interface between valves and the piston head due to valves coating, a gasket with 0.3 mm thickness (thickness of valve coating) was inserted between valves and piston head which works to withdraw valves from the piston head and thus maintain the overlap time and the standard piston was machined to remove material equal to the desired coating thickness and to keep the compression ratio unchanged.

3.5 Fuels Used

In this study the commercial diesel fuel employed in the tests was obtained locally and alternative used fuel substitute for diesel fuel was biodiesel with the mixing ratio of 5:95, 10:90 of biodiesel to diesel fuel and 100% biodiesel. The marketing specifications of fuel used as provided from chemical engineering department in technology of university are shown in table 2. To avoid isolation when biodiesel mixed with diesel fuel, solenoid driven dosing pump type (AQUA) was used as a fuels mixer. Where each type of fuel enters the pump through two different tubes and go out of one tube, thus both types of fuel are mixed well. Laboratory samples of Biodiesel was prepared by mixing alcohol (methanol) with KOH as a catalyst in a tank and then added sunflower oil heated to 55°C to the tank and then the resulting solution was mixed well for about 30 minutes and stored for 24 hour. Then be observed biodiesel layer to the top and glycerol layer to the bottom. Then biodiesel layer was separated from the lower layer and mixed well with water for 10 minutes as well as the resulting solution was left for 24 hour. Then the upper biodiesel layer was separated from water layer and heated to 100°C to eliminate water moisture. The biodiesel production is shown in **Fig. 6**.

Mathematical relationships used to calculate engine performance is, Ganesan, 2008, Mohanty, 2007.

1. Fuel consumption:(Kg/s)

$$\dot{} \quad \frac{}{} \tag{1}$$

where:

- volume of fuel consumption ( )

2. Brake power :(kW)

$$\dot{} \quad \frac{}{} \tag{2}$$

Where:

Tb - torque of engine (*N.m*)
N- rotational speed (*rpm*)

3. Brake Specific Fuel Consumption:

(3)

4. Brake thermal efficiency:

(4)

(5)

Where:
L.C.V- lower calorific value of kilogram fuel (*kJ/kg*)
-combustion efficiency (assuming=97%)

The coating technique in this work is the flame spray method type (rototec 800).this apparatus consists of a chamber containing a flange to hold the specimen and an Oxy-Acetylene flame. The powder particles flow with the flame and is deposited on the specimen. The powder was supplied through a special tube in the flame gun.

4. RESULTS AND DISCUSSION:

4.1 Brake Specific Fuel Consumption:

Figs. 7, 8, 9 and 10 indicate the variations of the BSFC for diesel fuel and biodiesel blends before and after ceramic coating under various engine torques. The BSFC of LHR engine at all torques is lower than the standard engine with diesel fuel and biodiesel blends. The main reason is that the ceramic materials will act as barrier for the heat transfer to the surroundings from the components engine's combustion chamber and reduces the heat loss from the engine. Also as per first law of thermodynamics, the heat reduction in heat loss will ultimately increase the power output and thermal efficiency of the engine and this lead to reduce the BSFC.

4.2 Brake Thermal Efficiency:

The variation of BTE with engine torque is shown in **Figs.11, 12, 13 and 14** for base engine and TBC engine for different fuels under various engine torques. The TBC engine reports better performance than the base engine. Improved brake thermal efficiency was observed in TBC engine at all torques. The thermal barrier coating in combustion chamber improves the BTE when compared with base engine. Since the thermal barrier coating prevents the heat loss from the walls to the surroundings. The BTE was increased due to the reduction in heat transfer from the gases to the walls during the combustion or expansion because of the higher wall temperatures. Thin thermal barrier coating shifts the combustion from premixed to diffusion stage.

4.3 Exhaust Gas Temperature:

Figs. 15, 16, 17 and 18 show the variations of EGT for base engine and TBC engine for different fuels. It is concluded that the EGT is higher for the engine with ceramic coated components than the engine under normal conditions and with different fuels. This is due to the raise in the temperature of the mixture inside the combustion chamber and decrease in heat losses going into the cooling system and outside due to the coating and due to increase in amount of fuel burnt per unit time.

4.4 Emissions:

Figs. 19, 20, 21 and 22 show CO variations for base engine and TBC engine for different fuels under various engine torques. It is clear that CO is decreased after the coating due to the complete combustion. CO emission from diesel engine is related to the fuel properties as well as combustion characteristics. It is well known that better fuel combustion usually resulted in lower CO emission. The carbon monoxide, which arises mainly due to incomplete combustion, is a measure of combustion efficiency. Generally, oxygen availability in diesel fuel and biodiesel blends is high so at high temperatures carbon easily combines with oxygen and reduces the CO emission.

Figs. 23, 24 and 25 show variations of HC emissions with torque of the engine before and after ceramic coating. In general, it is clear that the unburned hydrocarbon emissions are reduced when the engine works with coating. HC emission is low in the LHR engine with compared with the standard engine. The emission of unburned hydrocarbon from the LHR engines is more likely to be reduced because of the decreased quenching distance and the increased lean flammability limit. The higher temperatures both in the gases and at the combustion chamber walls of the LHR engine assist in permitting the oxidation reactions to proceed close to completion.

5. CONCLUSION

In this study, the effect of ceramic coating on the performance, exhaust gas temperature and gases emissions characteristics of a diesel engine operated on diesel fuel and biodiesel blends were experimentally investigated. Based on the experimental results of this study, the following conclusions were drawn.

- The BSFC of LHR engine were found to be lowered than BSFC of SE due to the effect of ceramic insulation which act as a barrier for the heat transfer to the surrounding and reduces the heat loss from the engine. These reductions were up to 19.29%, 15.91%, 14.65% and 7.06% for diesel fuel, B5, B10 and B100 respectively.
- The BTE of LHR engine were found to be higher than BTE of SE due to the reduction in heat transfer from the gas to the walls during the combustion or expansion because of the higher wall temperatures. These increasing were up to 23.68%, 19.77%, 16.51% and 6.32% for diesel fuel, B5, B10 and B100 respectively.
- The EGT of LHR engine were found to be higher than EGT of SE due to the raise in temperature of mixture inside the combustion chamber and decrease in heat losses going into the cooling system. These increasing were up to 9.01%, 7.22%, 15.7% and 11.42% for diesel fuel, B5, B10 and B100 respectively.
- Particulate emissions decreased clearly in LHR engine compared with SE engine due to the more complete combustion in the insulated configurations. These reductions were up to 18.57%, 20%, 20.5% and 27.77% for CO of diesel, B5, B10 and B100 respectively and 28.97%, 43.9%, 38.88% and 36.41% for HC of diesel, B5, B10 and B100 respectively.

NOMENCLATURE

CO-carbon monoxide
HC- hydrocarbons (ppm)
CO2-carbon dioxide
B5-5:95 of biodiesel to diesel fuel mixing ratio
B10-10:90 of biodiesel to diesel fuel mixing ratio
B100-100% biodiesel
BSFC-brake specific fuel consumption
YSZ- yttria-stabilized zirconia
LHR- low heat rejection
SE-standard engine
KOH- potassium hydroxide
EGT-exhaust gas temperature
BTE-brake thermal efficiency

Figure 1. The flame spray gun type (rototec 800).

Figure 2. Photographic view of valves (before and after ceramic coating).

Figure 3. Photographic view of piston (before and after ceramic coating).

Figure 4. Photographic view of cylinder head (before and after ceramic coating).

Table1. Main technical specifications of engine.

Item	Technical specification
Model	170F China
Type	Single-cylinder, vertical, 4-stroke, air-cooled, direct-injection
Bore×Stroke (mm)	70x50
Displacement (l)	0.211
Compression ratio	20:1
Fuel tank capacity (l)	4.5
Max. speed (rpm)	3600
Max. power (kW)	3.4

Figure 5. Diesel engine (the board and engine).

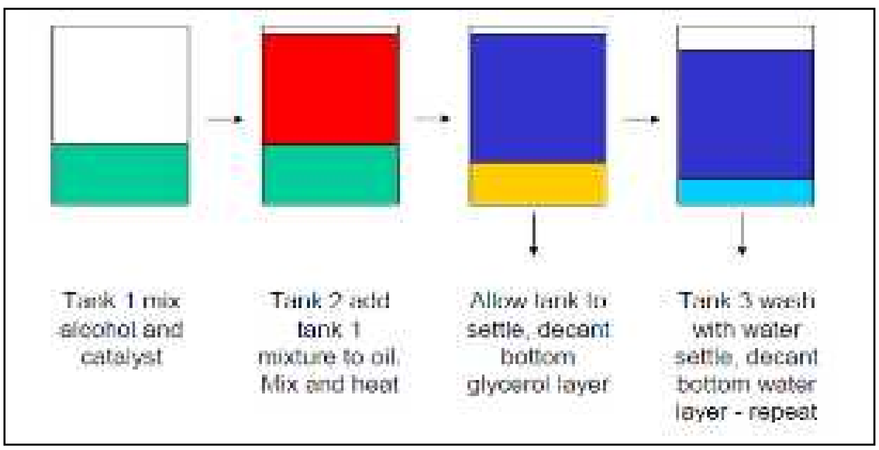

Figure 6. Biodiesel production (Daniel Geller).

Table 2. The marketing specifications of fuel used as provided from chemical engineering department in technology of university.

Property of fuel	Cetane number at 23°C	Pour point(°C)	Specific Gravity at 15 °C	Kinematic Viscosity at 40 °C	Flash Point(°C)	Carbon Residue (Wt. %)	Lower calorific value (kJ/kg)
Diesel	46.8	-25	0.826	3.5	77	2	45208.8
5% Biodiesel + Diesel	49.6	Less than -10	0.828	3.420	89	2.63	41678
10% Biodiesel + Diesel	51.5	Less than -10	0.831	3.7	92	3.1	41422
100% Biodiesel	69.5	Less than -10	0.884	5.486	178	6.25	40834

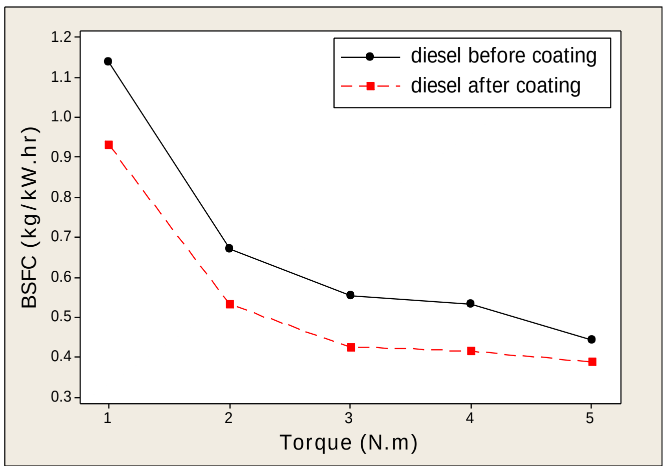

Figure 7. BSFC versus torque before and after ceramic coating for diesel fuel.

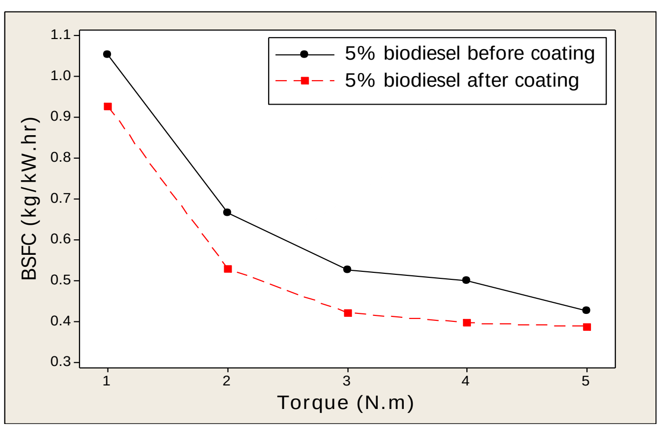

Figure 8. BSFC versus torque before and after ceramic coating for 5% biodiesel.

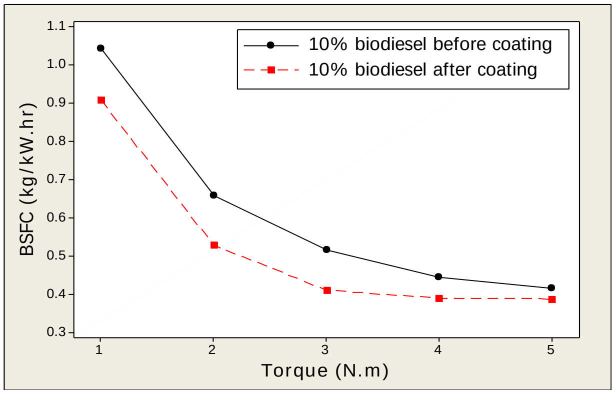

Figure 9. BSFC versus torque before and after ceramic coating for 10% biodiesel.

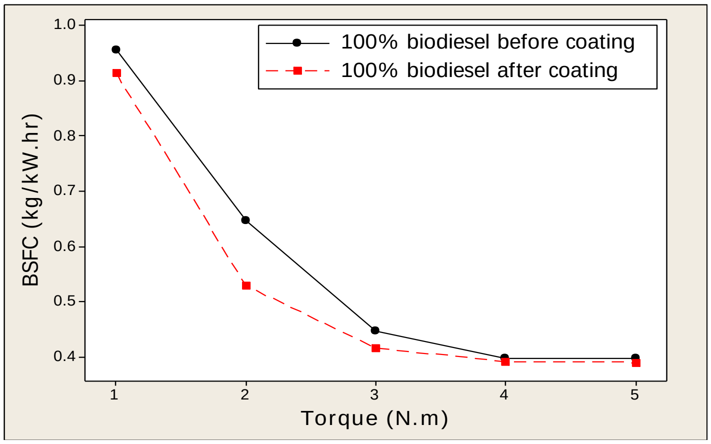

Figure 10. BSFC versus torque before and after ceramic coating for 100% biodiesel.

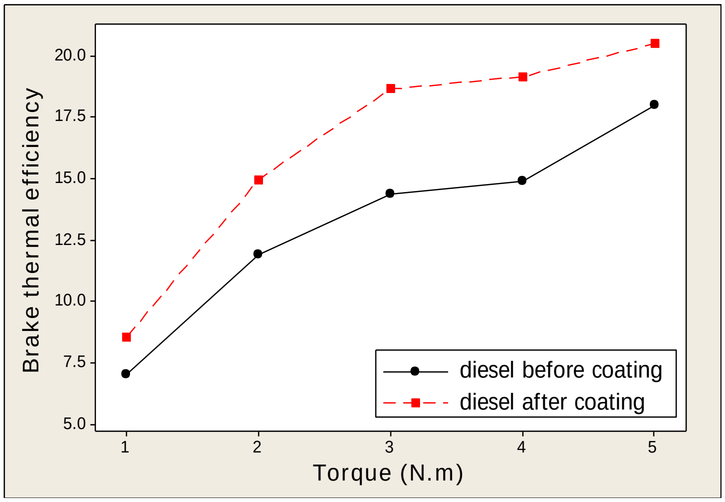

Figure 11. BTE versus torque before and after ceramic coating for diesel fuel.

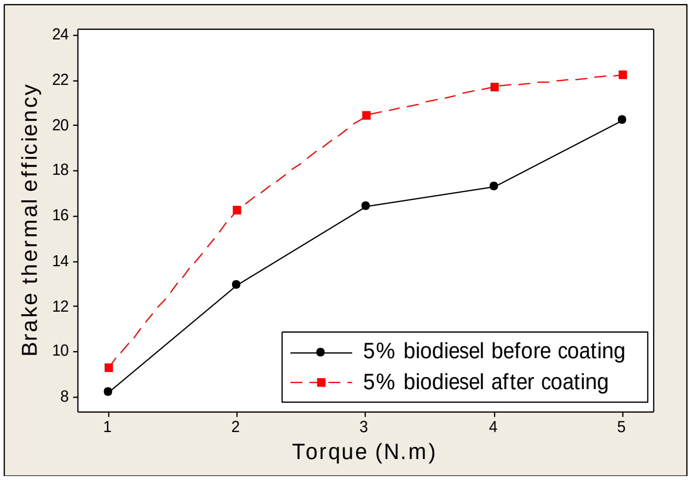

Figure 12. BTE versus torque before and after ceramic coating for 5% biodiesel.

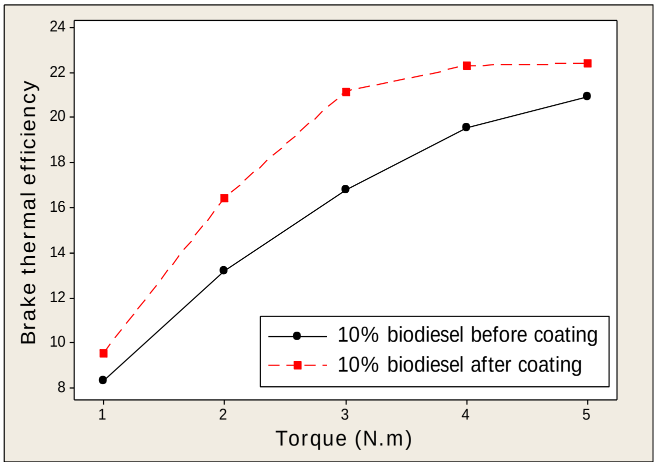

Figure 13. BTE versus torque before and after ceramic coating for 10 % biodiesel.

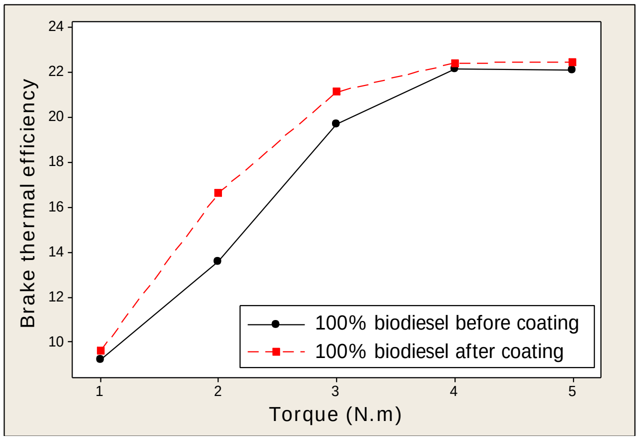

Figure 14. BTE versus torque before and after ceramic coating for 100 % biodiesel.

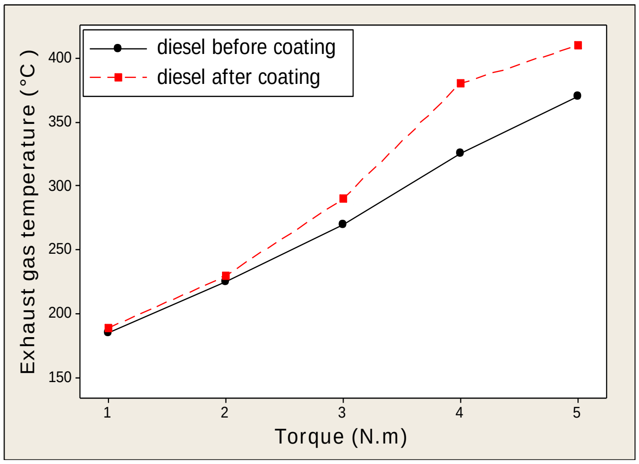

Figure 15. EGT versus torque before and after ceramic coating for diesel fuel.

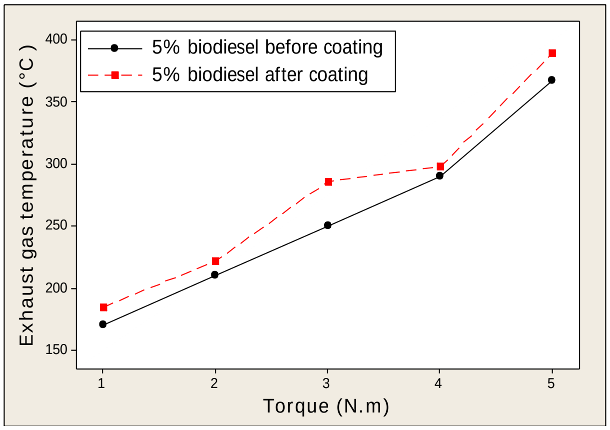

Figure 16. EGT versus torque before and after ceramic coating for 5% biodiesel.

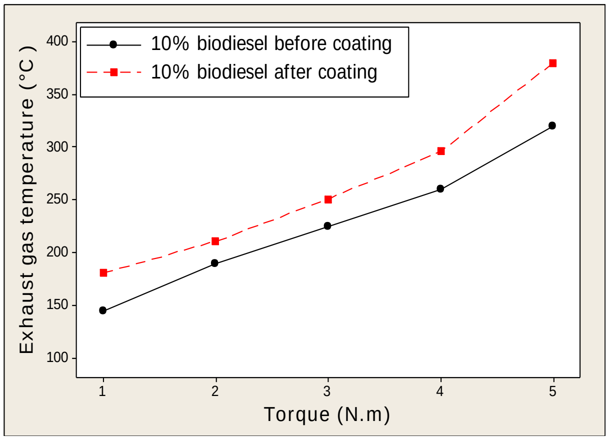

Figure 17. EGT versus torque before and after ceramic coating for 10% biodiesel.

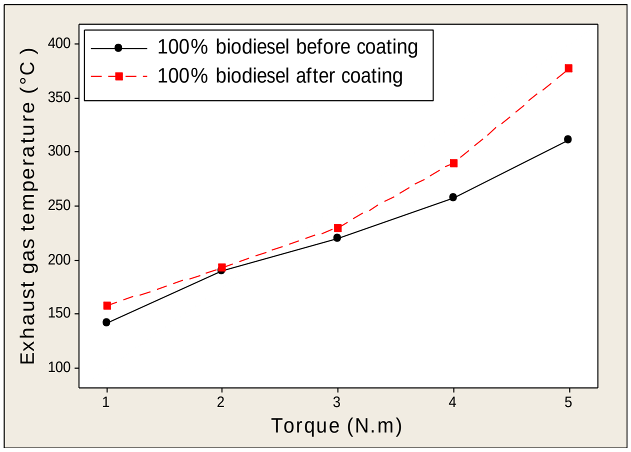

Figure 18. EGT versus torque before and after ceramic coating for 100% biodiesel.

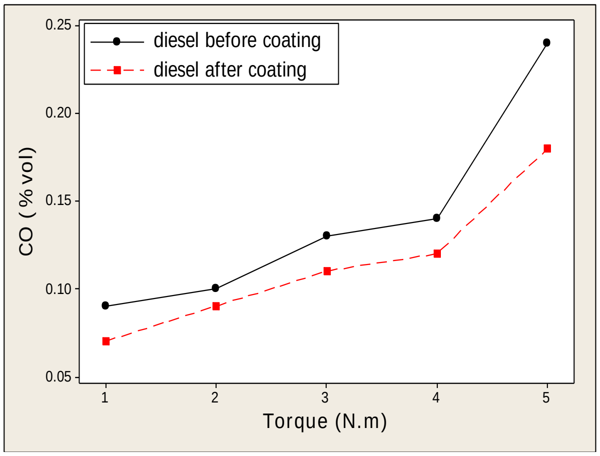

Figure 19. CO emission versus torque before and after ceramic coating for diesel fuel.

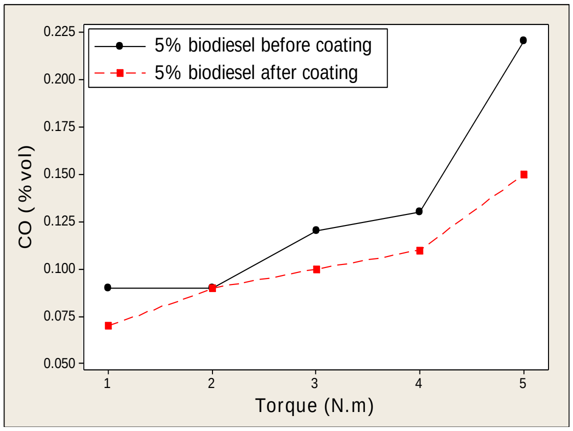

Figure 20. CO emission versus torque before and after ceramic coating for 5% biodiesel.

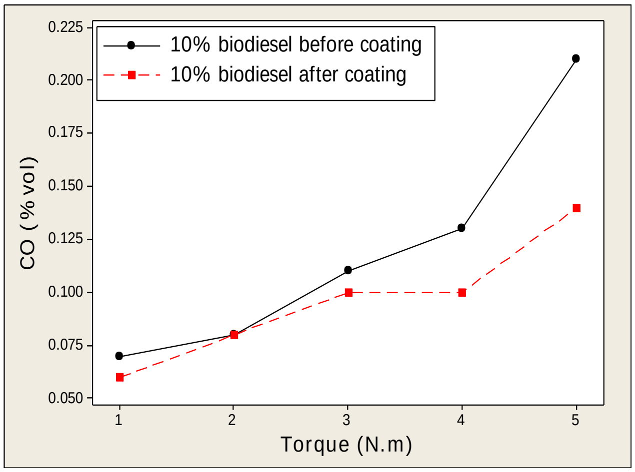

Figure 21. CO emission versus torque before and after ceramic coating for 10% biodiesel.

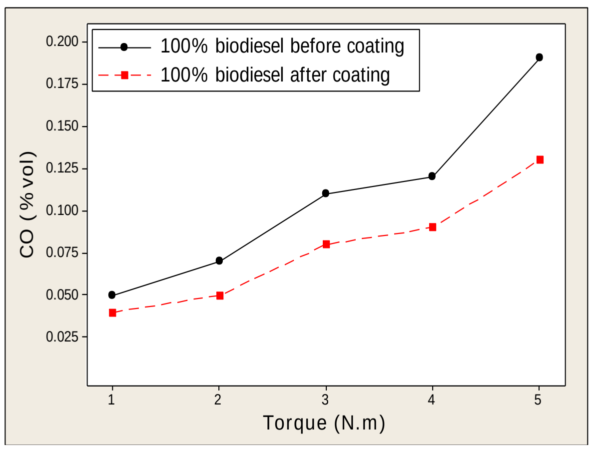

Figure 22. CO emission versus torque before and after ceramic coating for 100% biodiesel.

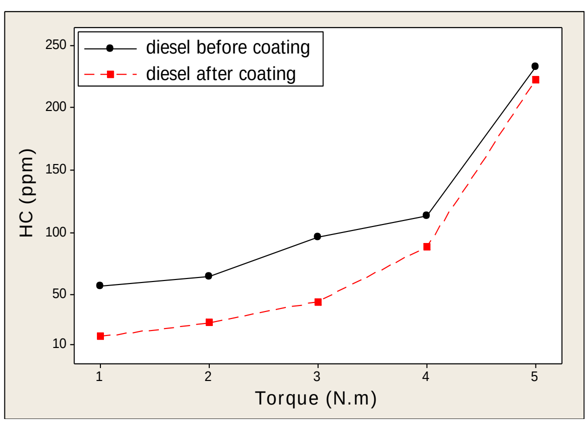

Figure 23. HC emission versus torque before and after ceramic coating for diesel fuel.

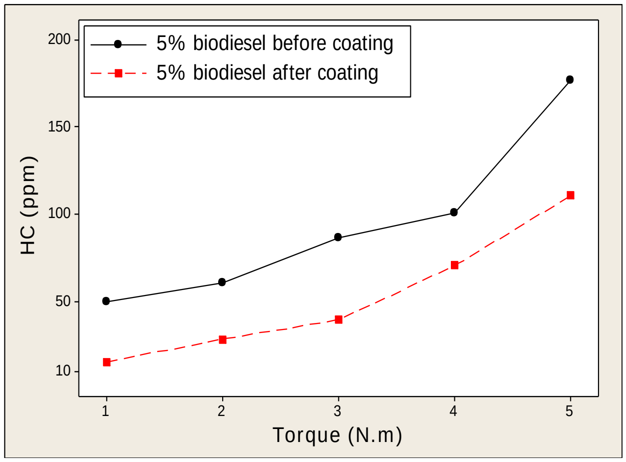

Figure 24. HC emission versus torque before and after ceramic coating for 5% biodiesel.

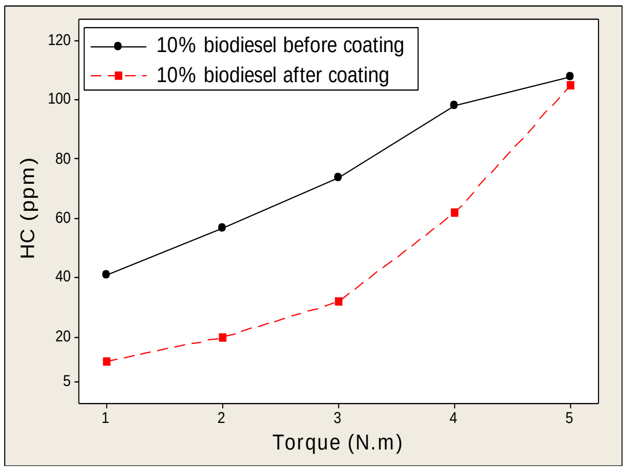

Figure 25. HC emission versus torque before and after ceramic coating for 10% biodiesel.

6. REFERENCES

Dennis, A. and Kevin, W., 1991, *The Effects of Ceramic Coatings on Diesel Engine Performance and Exhaust Emissions*, International Congress and Exposition, Detroit, Michigan, Vol.1.

Daniel, G., *UGA Engineering Outreach*, http://outreach.engineering.uga.edu/.

Sivakumar, G., et al., 2012, *Is Thermal Barrier Coating for Low Heat Rejection in SI Engine or Diesel Engine*, International Journal of Emerging Technology and Advanced Engineering,Vol.2, Issue12, pp.460-466.

Holloman, L. and Levy, A.V., 1992, *Ceramic-Coated Components for the Combustion Zone of Natural Gas Engines*, Journal of Thermal Spray Technology, Vol. 1.

Murat, C., et al., 2012, *Ceramic Coating Applications and Research Fields for Internal Combustion Engines*, Ceramic Coatings - Applications in Engineering, Vol.6, pp.978-953.

Shrirao, P. N. and Pawar, A. N., 2011, *Evaluation of Performance and Emission Characteristics of Turbocharged Diesel Engine with Mullite as Thermal Barrier Coating*, International Journal of Engineering and Technology Vol.3, pp.256-262.

Mohanty, R. K., 2007, *Internal Combustion Engine*, McGraw-Hill book.

Satrughna D., 2007, *Study of Plasma Spray Alumina - aluminide Composite Coating on Metals*, National Institute of Technology, Rourkela, India.

Hejwowski T. and Weronski, A., 2012, *The Effect of Thermal Barrier Coatings on Diesel Engine Performance*,3rd International Symposium on Applied Plasma Science (ISAPS 01), Vol. 65, pp.427-432.

Ganesan, V., 2008, *Internal Combustion Engine*", 3rd Edition, Tata McGraw Hill Book.

Willard, W.P., 2010, *Engineering Fundamentals of the Internal Combustion Engin*", prentice Hall, Platteville, 1997. Published by IEEE.

Compression of an ECG Signal Using Mixed Transforms

Sadiq Jassim Abou-Loukh
Assistant Professor
College of Engineering-University of Baghdad
Email: doctor_sadiq@yahoo.com

Jaleel Sadoon Jameel
Instructor
College of Engineering-University of Baghdad
Email: jaleel28@yahoo.com

ABSTRACT

Electrocardiogram (ECG) is an important physiological signal for cardiac disease diagnosis. With the increasing use of modern electrocardiogram monitoring devices that generate vast amount of data requiring huge storage capacity. In order to decrease storage costs or make ECG signals suitable and ready for transmission through common communication channels, the ECG data volume must be reduced. So an effective data compression method is required. This paper presents an efficient technique for the compression of ECG signals. In this technique, different transforms have been used to compress the ECG signals. At first, a 1-D ECG data was segmented and aligned to a 2-D data array, then 2-D mixed transform was implemented to compress the ECG data in the 2-D form. The compression algorithms were implemented and tested using multiwavelet, wavelet and slantlet transforms to form the proposed method based on mixed transforms. Then vector quantization technique was employed to extract the mixed transform coefficients. Some selected records from MIT/BIH arrhythmia database were tested contrastively and the performance of the proposed methods was analyzed and evaluated using MATLAB package. Simulation results showed that the proposed methods gave a high compression ratio (CR) for the ECG signals comparing with other available methods. For example, the compression of one record (record 100) yielded CR of 24.4 associated with percent root mean square difference (PRD) of 2.56% was achieved.

Key words: ECG Compression, Wavelet, Multiwavelet and Slantlet Transforms, Vector Quantization

ضغط اشارة تخطيط القلب باستخدام التحويلات الخليطة

ا.م.د. صادق جاسم ابو اللوخ
قسم الهندسة الكهربائية
كلية الهندسة / جامعة بغداد

م.م. جليل سعدون جميل
قسم الهندسة الكهربائية
كلية الهندسة / جامعة بغداد

الخلاصة

اشاره تخطيط القلب (ECG) تستخدم على نطاق واسع في تشخيص وعلاج امراض القلب. هذه الاشارة عادة تراقب بشكل مستمر , وهذا سيؤدي الى كميات كبيره من البيانات يحتاج تخزينها او نقلها .لذلك يتطلب وسيله فعاله لضغط هذه البيانات .

في هذا البحث تحويلات مختلفة لضغط اشارات تخطيط القلب تم أستخدامها . في البداية يتم تحويل اشارات تخطيط القلب اشارات ذات بعد واحد الى اشارات ذات بعدين , ثم بعد ذلك يتم ضغط عذه الاشارات بأستخدام خليط من التحويلات .طريقة الضغط تم تنفيذها باستخدام التحويات multiwavelet وWavelet و slantet حيث تم تشكيل طرق مختلفة اعتمادها على خلط مختلف لهذه التحويات .ثم بعد ذلك تم استخدام VQ لتشفير المعاملات الناتجة من التحويلات المختلطة .

تم أختيار اشارات تخطيط القلب من قاعدة البيانات (Mit-BHI arrhythmia database) وتم تحليل اداء الطرق المقترحة وتقيمها من خلال استخدام برنامج MATLAB.بينت نتائج المحاكاة ان الطرق المقترحة تعطي نسب ضغط عالية لاشارات تخطيط

القلب بالمقارنه مع الطرق الاخرى المتوفرة .على سبيل المثال، ضغط اشاره تخطيط قلب واحده (record 100) باستخدام الطريقه المقترحه اعطت نسبه ضغط تساوي 24,4 مه نسبه خطا تساوي 2,56 % .

1. INTRODUCTION

ECG is widely used in the diagnosis and treatment of cardiac disease. ECG signals usually continuously monitored and this will lead large amount of data needs to be stored or transmitted. ECG compression becomes mandatory to efficiently store and retrieve this data from medical database, **Polania, et al., 2011**. Compression of ECG is necessary for efficient storage and transmission of the digitized ECG signals. A typical ECG monitoring device generates a large amount of data in the continuous long-term (12-24 hours) ambulatory monitoring tasks. For good diagnostic quality, up to 12 different streams of data may be obtained from various sensors placed on the patient's body, **Hossain, et al., 2008**. Thus, efficient ECG data compression to dramatically reduce the data storage capacity is a necessary solution. On the other hand, it makes possible to transmit ECG data over a telephone line from one cardiac doctor to another to get opinions, **Wang, et al., 2008**.

Compression methods have gained an importance in recent year in many medical areas like telemedicine and health monitoring. Many ECG data compression methods have been proposed to achieve a high compression ratio (CR) result and preserve clinical information. These methods can be categorized into time-domain, and transform-domain groups. Recently, a wavelet-based approach attracted much attention of researchers due to both its simplicity and high-compression performance, **Ku, et al., 2010**.

There are different ways of merging two or more transforms to form a mixed transforms. The proposed mixed transforms consists of two transforms in cascading form to be used to enhance compressing performance. Different schemes of applying wavelet, multiwavelet, and slantlet transforms are implemented. The results are obtained through simulation by MATLAB package in this work.

This paper is organized as follows: ECG compression techniques are explained in section II. The standard quantitative measurements that used for ECG are presented in section III. Section IV describes the proposed compression algorithms. Simulation results and comparisons with other compression algorithm in the literature are presented in section V. Finally the conclusion is given in section VI.

2. ECG COMPRESSION TECHNIQUES

The main goal of any compression technique is to achieve maximum data volume reduction while preserving the significant features, **Khalaj, and Naimi, 2009**. A compression algorithm takes an input X and generates a representation XC that hopefully requires fewer bits. There is a reconstruction algorithm that operates on the compressed representation XC to generate the reconstructed presentation Y.

2.1 Discrete Wavelet Transform

Wavelets are mathematical functions that provide the time-frequency representation. It cuts up data into different frequency components, and then study each component with a resolution matched to its scale. Most interesting dissimilarities between wavelet and Fourier transforms is that individual wavelet functions are localized in space, Fourier sine and cosine functions are not,

Graps, 1995. In discrete wavelet transform (DWT) the scale and translate parameters are chosen such that the resulting wavelet set forms an orthogonal set, i.e. the inner product of the individual wavelets ψ (j,k) is equal to zero. To this end, dilation factors are chosen to be powers of 2. For DWT, the set of dilation and translation of the mother wavelet is defined as, **Cohen, and Jelena, 1996.**

$$\psi_{j,k}(t) = 2^{j/2}\psi\left(2^{j}t - k\right) \tag{1}$$

Where j is the scaling factor and k is the translation factor. It is obvious that the dilation factor is a power of 2. Forward and inverse transforms are then calculated using the following equations, **Cohen, and Jelena, 1996**.

$$C_{\tau,s} = \int_{-\infty}^{+\infty} f(t)\, \psi\, j,k\, (t)\, d(t) \tag{2}$$

$$f(t) = \sum_{j,k} C_{j,k}\, \psi_{j,k}(t) \tag{3}$$

For efficient decorrelation of the data, an analysis wavelet set ψ (j,k) should be chosen which matches the features of the data well. This together with orthogonally of the wavelet set will result in a series of sparse coefficients in the transform domain, which obviously will reduce the amount of bits needed to encode it, **Zafarifar, 2002**. A typical 2-D DWT, used in image compression, it generates the hierarchical pyramid structure shown in **Fig.1**.

2.2 Multiwavelet Transform

Multiwavelet has been introduced as a more powerful multi-scale analysis tool. A scalar wavelet system is based on a single scaling function and mother wavelet. On the other hand, a multiwavelet uses several scaling functions and mother wavelets, **Strela, and Heller, 1999**. Multiwavelets, namely, vector-valued wavelet functions, are a new addition to the classical wavelet theory that has revealed to be successful in practical applications, such as signal and image compression. In fact, multiwavelets possess several advantages in comparison to scalar wavelets, since a multiwavelet system can simultaneously provide perfect reconstruction while preserving orthogonality, symmetry, a high order of approximation (vanishing moments), etc. Nevertheless, multiwavelets differ from scalar wavelet systems in requiring two or more input streams to the multiwavelet filter bank, **Liang, et al., 1996.**

The multiwavelet idea originates from the generalization of scalar wavelets; instead of one scaling function and one wavelet, multiple scaling functions and wavelets are used (see **Fig. 2**). This leads to more degree of freedom in constructing wavelets. Therefore, opposed to scalar wavelets, properties such as compact support, orthogonality, symmetry, vanishing moments, short support can be gathered simultaneously in multiwavelets, which are fundamental in signal process. The increase in the degree of freedom in multiwavelets is obtained at the expense of replacing scalars with matrices, scalar functions with vector functions and single mattresses with a block of matrices. Also, prefiltering is an essential task which should be performed for any use of multiwavelet in the signal processing, **Al-Sammaraie, 2011**. Many types of multiwavelet such as Geronimo-Hardin-Massopust (GHM) and Chui-Lian (CL) multiwavelets have been developed, **Xia, et al., 1996**.

To implement the multiwavelet transform, a new filter bank structure is required where the lowpass and highpass filter banks are matrices rather than scalars. That is, the GHM two scaling and wavelet functions satisfy the following two-scale dilation equations, **Liang, et al., 1996**.

$$\begin{bmatrix}\phi_1(t)\\ \phi_2(t)\end{bmatrix}=\sqrt{2}\sum_k H_k\begin{bmatrix}\phi_1(2t-k)\\ \phi_2(2t-k)\end{bmatrix} \qquad (4)$$

$$\begin{bmatrix}\psi_1(t)\\ \psi_2(t)\end{bmatrix}=\sqrt{2}\sum_k G_k\begin{bmatrix}\psi_1(2t-k)\\ \psi_2(2t-k)\end{bmatrix} \qquad (5)$$

The (2×2) matrix filters in the multiwavelet filter bank require vector inputs. Thus, a 1-D input signal must be transformed into two 1-D signals.

This transformation is called pre-processing. For some multiwavelet, the pre-processing must be accompanied by an appropriate pre-filtering operation that depends on the spectral characteristics of the multiwavelet filters, **Xia, 1998**.

2.3 Slantlet Transform

Slantlet transform (SLT) has been recently proposed as an improvement over the usual DWT. The SLT is an equivalent form of the DWT implementation but provides better time-localization due to the shorter supports of component filters. The SLT filters are essentially piecewise linear filters, have desirable properties of orthogonality and two vanishing moments, have an octave-band characteristic, can exactly provide a scale dilation factor of 2, provides a multiresolution decomposition. The SLT filter-bank is implemented in the form of a parallel structure, employing different filters for each scale whereas DWT is usually implemented in the form of an iterated filter-bank, utilizing a tree structure. SLT can exactly provide a scale dilation factor of 2 and is less frequent selective due to shorter supports of the component filters whereas DWT filters can approximately provide a scale dilation factor of 2 and provide short windows at high frequencies and long windows at low frequencies, **Kummar, and Muttoo, 2010**.

The usual iterated DWT filter-bank and its equivalent form are shown in **Fig.3**. The slantlet filter-bank is based on the equivalent structure that is occupied by different filters that are not products. With this extra degree of freedom obtained by giving up the product form, filters of shorter length are designed to satisfy orthogonality and zero moment conditions, **Selenick, 1999**.

For the two-channel case, the shortest filters for filter-bank is orthogonal and has K zero moments are well known filters described by Daubechies. For K = 2 zeros moments, filters H(z) and F(z) are of length 4. For this system, the iterated filters in Fig.4 are of length 10 and 4. Without the constraint that the filters are products, an orthogonal filter-bank with K = 2 zeros moments can be obtained where the filter lengths are 8 and 4, as shown in **Fig.4**. That is a reduction by two samples, which is a difference that grows with the number of stages. This reduction in length, while maintaining desirable orthogonality and moment properties, is possible because these filters are not constrained by the product form arising in the case of iterated filter-banks, **Selenick, 1999.**

2.4 Vector Quantization

Vector quantization (VQ) is used for both image and sound compression. In practice, VQ is commonly used to compress data that have been digitized from an analog source, such as sampled sound and scanned images. Vector quantization is based on two facts, **Cosman, et al., 1996**.

- The compression methods that compress strings, rather than individual symbols can, in principle, produce better results.
- Adjacent data items in an image (i.e., pixels) and digitized sound (i.e., samples) are correlated. There is a good chance that the nearest neighbors of a pixel P will have the same values as P or very similar values. Also consecutive sound samples rarely differ much.

For signal compression, VQ divides the signal into small blocks of pixels, typically 2×2 or 4×4. Each block is considered a vector. The encoder maintains a list (called a codebook) of vectors and compresses each block by writing to the compressed stream a pointer to the block in the codebook. The decoder has the easy task of reading pointers, following each pointer to a block in the codebook, and joining the block to the image so far (see **Fig.5**). Vector quantization is thus an asymmetric compression method.

An improved algorithm of VQ, codebook generation approaches such as the LBG algorithm has been developed. LBG algorithm designing a codebook that best represents the set of input vectors is very-hard. That means that it requires an exhaustive search for the best possible codewords in space, and the search increases exponentially as the number of codewords increases, therefore, we resort to suboptimal codebook design schemes, and the first one that comes to mind is the simplest. It is named LBG algorithm for Linde-Buzo-Gray and also it is known as K-means clustering.

The LGB algorithm is in fact designed to iteratively improve a given initial codebook. The design of a codebook with N-codewords can be stated as follows, **Bardekar, and Tijare, 2011**:-

1. Determine the number of codewords, N, or the size of the codebook .
2. Select N codewords at random, and let that be the initial codebook. The initial codewords can be randomly chosen from the set of input vectors .
3. Use the Euclidean distance to measure cluster size the vectors around each codeword. This is done by taking each input vector and finding the Euclidean distance between it and each codeword. The input vector belongs to the cluster of the codeword that yields the minimum distance .

Compute the new set of codewords. This is done by obtaining the average of each cluster. Add the component of each vector and divide by the number of vectors in the cluster, **Bardekar, and Tijare, 2011**.

$$y_i = \frac{1}{m} \sum_{j=1}^{m} x_{ij} \tag{6}$$

Where i is the component of each vector (x, y, z, directions) and m is the number of vectors in the cluster.

Repeat steps 1, 2 and 3 until either the codewords do not change or the change in the codewords is small.

This algorithm is by far the most popular, and that is due to its simplicity. Although it is locally optimal, yet it is very slow. The reason it is slow is because for each iteration, determining each cluster requires that each input vector be compared with all the codewords in the codebook.

3. PROPOSED METHOD

3.1 2-D ECG Construction

In the ECG signal, there are two kinds of dependencies, which are the dependencies in a single ECG cycle (interbeat dependencies) and the dependencies across ECG cycles (intrabeat dependencies), **Rezazadeh, et al., 2005**. Because of the intrabeat and interbeat correlations of ECG signals, 2-D ECG signal compression algorithms have better performance. An efficient compression scheme needs to exploit both dependencies to achieve maximum compression and minimum errors. The 1-D ECG sequence is treated to produce a two dimensional matrix. To map 1-D ECG signal to 2-D arrays, at first, the peak of QRS complex should be detected to identify each heartbeat period (which is named the R-R interval). In this array, each row contains one or more periods of ECG beat, so the interbeat dependencies can be seen in each row and intrabeat dependencies can be seen in each column of the matrix. Then, the original 1-D ECG signal is cut at nth samples. In order to period irregularity of ECG signals that presents a challenge to the 2-D matrix construction, resampling and normalizing are applied to the time duration of each cycle and set it to a constant number, i.e. 256 samples are in each cycle . After the 2-D array is produced, the amplitude should be normalized by scaling the value of the array from 0 to 255. Now, there is a grayscale image and a 2-D ECG signal. These processes are named cut and align (C&A), **Mohammadpour, and Mollaei, 2009**. **Fig.6** and **Fig.7** show the 1-D and 2-D ECG signals, respectively.

3.2 The Proposed Mixed Transform

Mainly it consists of applying the multiwavelet, wavelet and slantlet transforms in a cascaded manner to the ECG signal. This mixed transform is implemented by applying MWT first, this in turn introduced the four approximation subbands (L1L1, L1L2, L2L1 and L2L2), then wavelet and slantlet transforms and VQ algorithm are applied in different procedure.

The description of the procedure used in the compression process for this mixed transforms schemes, are as follows:

Step.1 Apply the MWT to the ECG signal which results four square bands as shown in **Fig.2**. The four square bands results are splits and each is processed individually.

Step.2 Apply the WT to the first approximation square which consists of four approximation subbands (L1L1, L1L2, L2L1, and L2L2) which in tern introduce four subbands (LL, LH, HL, and HH), then apply SLT to the three bands (LH, HL, and HH) and the results of SLT are treated by VQ.

Step.3 Apply SLT to the three details square remains from applying MWT in step 1, then the results of SLT are treated by VQ.

Fig.8 shows the proposed scheme of using the proposed mixed transforms on ECG signals.

4. PERFORMANCE MEASUREMENTS

Evaluation of lossy ECG encoders uses measurements related to the amplitude difference between the original and the reconstructed signal. The standard quantitative measurement is the percent root mean square difference (PRD), which is given by the following, **Lee, et al., 2012**:

$$PRD = \sqrt{\frac{\sum_{n=1}^{N}(x(n)-\tilde{x}(n))^2}{\sum_{n=1}^{N}(x(n))^2}} \times 100 \tag{7}$$

Where $x(n)$ is the original signal, $\tilde{x}(n)$ is the reconstructed signal and n is the number of samples.

Since a lower PRD value indicates that the reconstruction approximates more closely to the original. However, qualitative evaluations are almost invariably used due to human beings better judgment of which details of the signal are important

The compression ratio (CR) is a measure of the amount of data size reduction achieved and it is calculated by, **Polania, et al., 201**1:

$$CR = \frac{uncompressed\ \text{size}}{compressed\ \text{size}} :1 \tag{8}$$

5. RESULTS AND DISCUSSION

The proposed algorithm was tested and evaluated by using an actual data from the MIT-BIH arrhythmia database, **MIT-BIH**. This database includes different shapes of ECG signals arranged in different records. The records used are 100, 107, 109, and 117, which are different in shape of the ECG signals. Records 100 and 109 have a regular period of QRS compared with the other signals while records 107 and 117 have an almost regular QRS period.

The results of performing the compression algorithm for the proposed mixed transform using different types of records are given in the table 1.

This results show that each signal has a different CR than the other signals after applying the same algorithm. The variation in performance parameters depends on the shape and size of each ECG signal. For nearly the same values of CR, it is shown that records 100 and 109 have a lower PRD than records 107 and 117 at the all codebook sizes (256), (64), and (16). This difference in PRD is due to the regularity of QRS periods in records 100 and 109 compared with records 107 and 117 which have an almost regular QRS period.

The proposed algorithms are also compared to other ECG coders through their reports performance in the literature. In table 2, PRD and CR comparisons of different coding algorithms were shown. As the results show, the proposed schemes exhibits better performance than well-known methods such as those based on matrix completion, **Polania, et al., 2011**, wavelet transform, **Hossain et al., 2008**, and new efficient fractal, **Khalaj, and Naimi, 2009**.

Figures 9, 10, and 11 show samples of original, reconstructed and error signals for different types of ECG signals.

6. CONCLUSION

Difference transforms have been used in this paper, using MWT, WT, and SLT which are employed with the VQ algorithm in different distribution. This distribution was exploited by cascading manner. The work includes an ECG signal compression method using 2-D mixed transform. The following points are the summary of the important conclusions:

1. The proposed method offers a compression performance of ECG signal up to 27 with little effects will be noticed on the ECG quality.
2. The codebook size refers to the total numbers of code vectors in the codebook. As the size of codebook increase the quality of the reconstructed signal improves, but the compression ratio reduces. Therefore, there is a tradeoff between the quality of the reconstructed signal and the amount of compression achieved.
3. The compression performances of the proposed mixed transforms are different from one ECG signal to another depending on the regularity of the ECG signals. For records that have regular QRS-complex the PRD will be less than records that has irregular QRS-complex.

7. REFERENCES

- Al-Sammaraie, M. F., 2011, *Medical Images Compression Using Modified SPIHT Algorithm and Multiwavelet Transformation*, Computer and Information Science, Vol. 4, No. 6, PP. 2-17.

- Bardekar, A. A., and Tijare, P. A., 2011, *Implementation of LBG Algorithm for Image Compression*, International J. of Computer Trends and Technology, Vol. 2, Issue 2, PP. 86-91.

- Cohen, A., and Jelena K., 1996, *Wavelets: The Mathematical Background*, Proceeding of the IEEE, Vol. 84, No. 4, PP. 514-522.

- Cosman, P. C., Gray, R. M., and Vetterli, M., 1996, *Vector Quantization of Image Sub-bands: A Survey*, IEEE Trans. on Image Processing, Vol. 5, No. 2, PP. 202-225.

- Graps, A., 1995, *An Introduction to Wavelets*, IEEE Computational Science and Engineering, Vol. 2, No. 2, PP. 1-18.

- Hossain, M.S., Aziz, T., and Haque, M., 2008, *ECG Compression Using Multilevel Thresholding of Wavelet Coefficients*, International Conference on Digital Object Identifier, PP. 321-326.

- Khalaj, A., and Naimi, H. M., 2009, *New Efficient Fractal Based Compression Method for Electrocardiogram Signals*, Canadian Conference on Electrical and Computer Engineering CCECE'09, PP. 983-986.

- Ku, C. T., Hung, K. C., Wu, T. C., and Wang, H., 2010, *Wavelet-Based ECG Data Compression System with Linear Quality Control Scheme*, IEEE Trans. on Biomedical Engineering, Vol.57, No.6, PP. 1399-1409.

- Kumar, S., and Muttoo, S. K., 2010, *An Overview of Wavelet-Like Transform and Image Data Hiding*, Proceeding of the 4th National Conference, INDIA.

- Lee, H. W., Hung, K. C., Wu, T. C., and Ku, C. T., 2012, *A Modified Run-Length Coding for the Realization of Wavelet-Based ECG Data Compression System*, Journal of Next Generation Information Technology, Vol. 1, No. 1, PP. 202-210.

- Liang, K.C., Li, J., and Kuo, C. J., 1996, *Image Compression with Embedded Multiwavelet Coding*, SPIE Proceeding on Wavelet Applications, Vol. 2762, PP. 165-176.

- Mohammadpour, T. I., and Mollaei, M. R., 2009, *ECG Compression With Thresholding of 2-D Wavelet Transform Coefficients and Run Length Coding*, European Journal of Scientific Research, Vol. 27, No. 2, PP. 248- 257.

- Polania, L. F., Corrillo, R. E., Velasco, M. B., and Barner, K. E., 2011, *Matrix Completion Based ECG Compression*, 33rd Annual International Conference of the IEEE EMBS, Boston, Massachusetts, PP. 1757-1760.

- Rezazadeh, I. M., Moradi, M. H., and Nasrabadi, A. M.,2005, *Implementing of SPIHT and Sub-band Energy Compression Method on 2-D ECG Compression: A Novel Approach*, Proceeding of the IEEE, PP. 1-4.

- Selenick, I. W., 1999, *The Slantlet Transform*, IEEE Trans. on Signal Processing,Vol.47, No.5, PP. 1304-1313.

- Strela, V., Heller, P., Strang, G., Topiwala, P., and Heil, C., 1999, *The Application of Multiwavelet Filterbanks to Image Processing*, IEEE Trans. on Image processing, Vol. 8, No. 4, PP. 548-563.

- Wang, Z., Zhu, P., and Chen, Y., 2008, *A 2-D ECG Compression Algorithm Based on Modified SPIHT*, Proceedings of the 5th International Workshop on Wearable and Implantable Body Sensor Networks, PP. 305-309.

- Xia, X. G., 1998, *A New Prefilter Design for Discrete Multiwavelet Transforms*, IEEE Trans. on Signal Processing, Vol. 46, No. 6, PP. 1558-1570.

- Xia, X. G., Geronimo, J. S., Hardian, D.P., and Suter, B. W., 1996, *Design of Prefilter for Discrete Multiwavelet Transform*, IEEE Trans. on Signal Processing , Vol. 44, No. 1, PP. 25-35.

- Zafarifar, B., 2002, *Micro-codable Discrete Wavelet Transform*, M. Sc. Thesis, Faculty of Information Technology and Systems, Delft University of Technology, Netherlands.

- MIT-BIH Arrhythmia Database http://www.physionet.org/physiobank/database/mitdb/

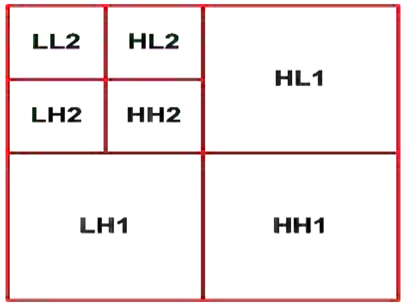

Figure1. Pyramid structure of wavelet decomposition**.**

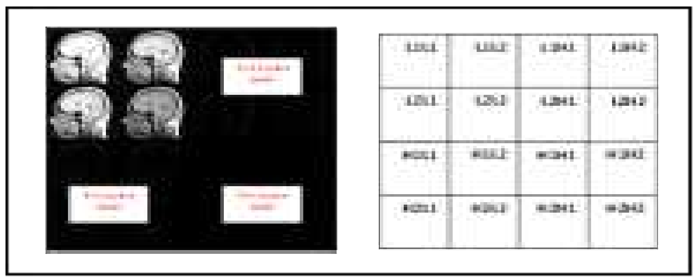

Figure 2. Resultant multiwavelet transform bands.

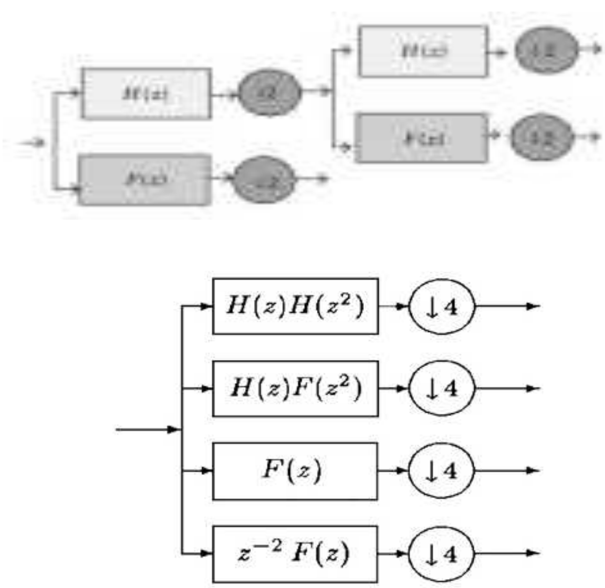

Figure 3. Two-scale filter bank and an equivalent structure.

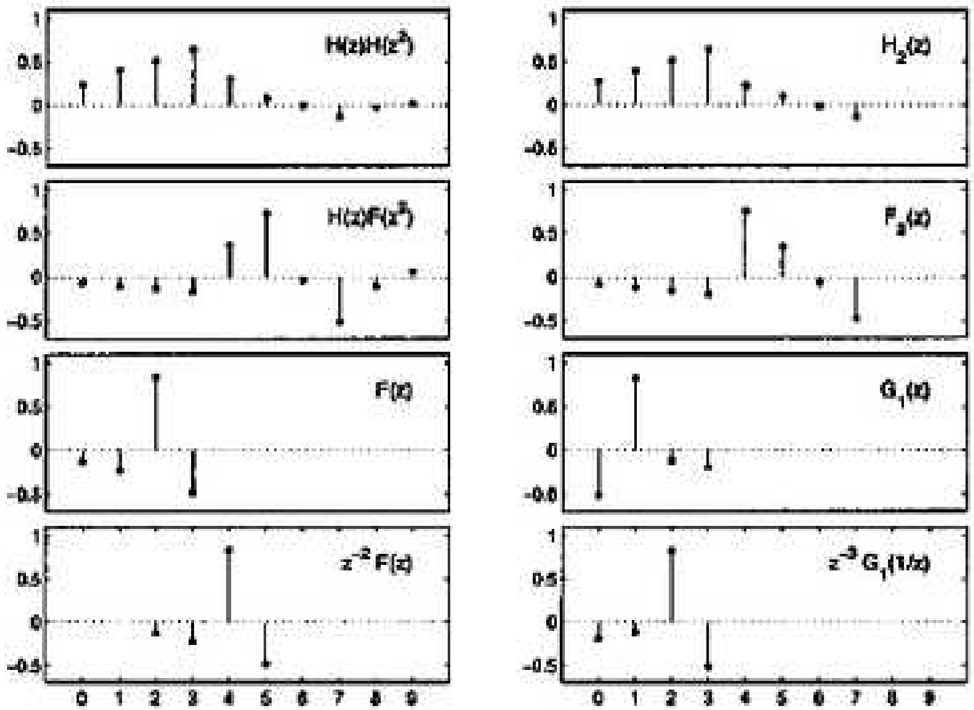

Figure 4. Comparison of two-scale iterated D2 filter bank (left-hand side) and two-scale slantlet filter bank (right-hand side).

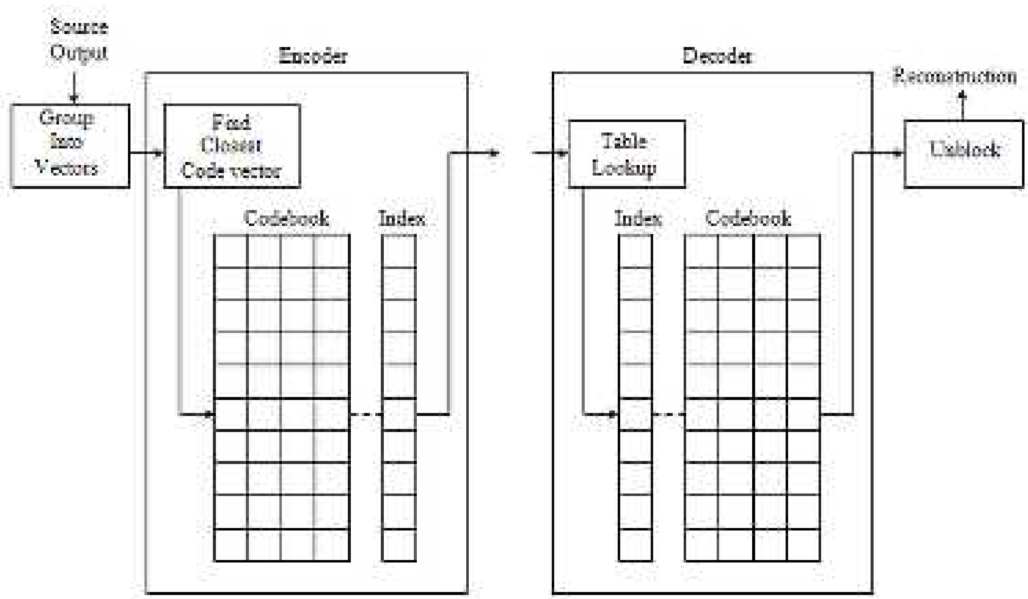

Figure 5. The encoder and decoder in a vector quantization.

Amplitude

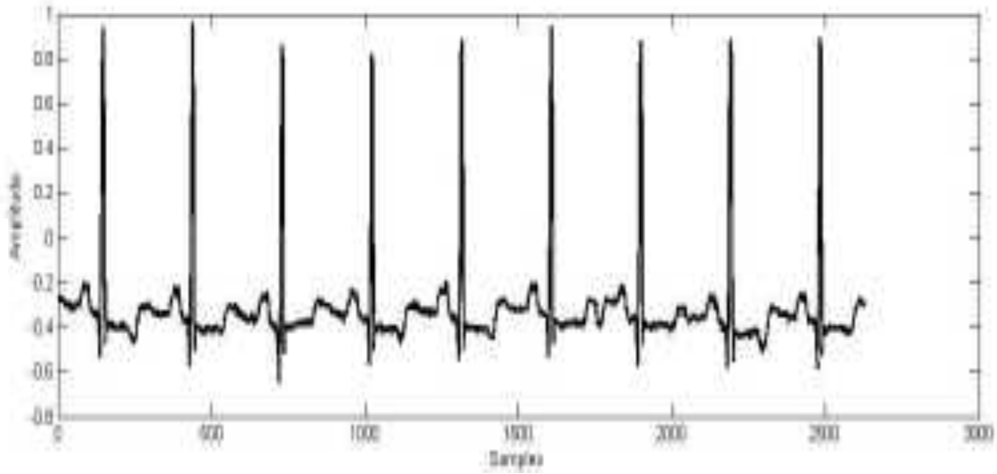

Samples

Figure 6. Waveform of 1-D ECG signal.

Amplitude

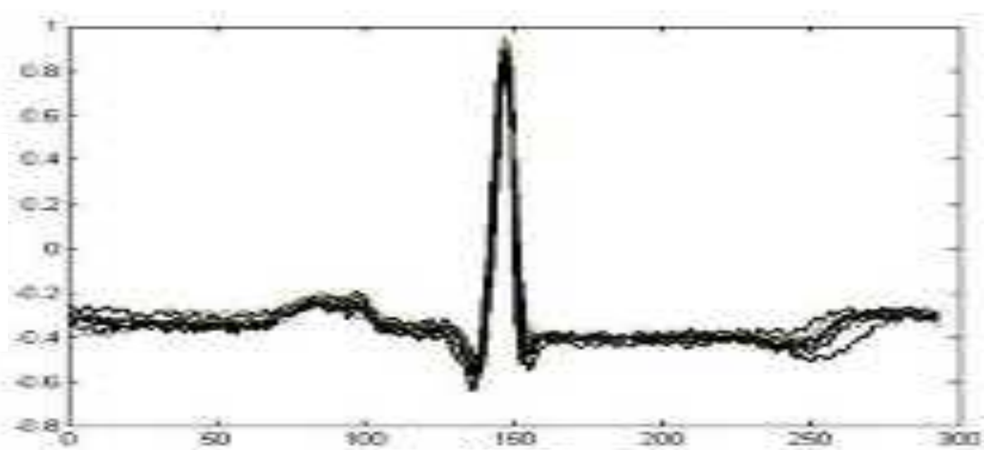

Samples

Figure 7. Waveform of 2-D ECG signal.

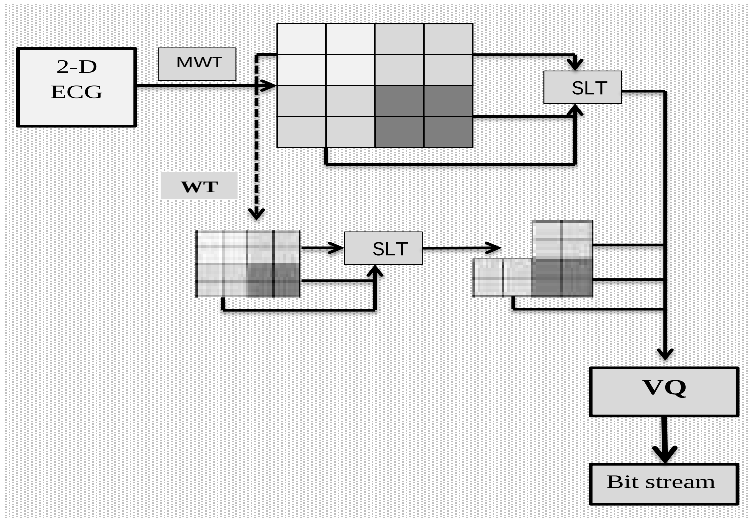

Figure 8. Proposed scheme of mixed transform and their compression processing.

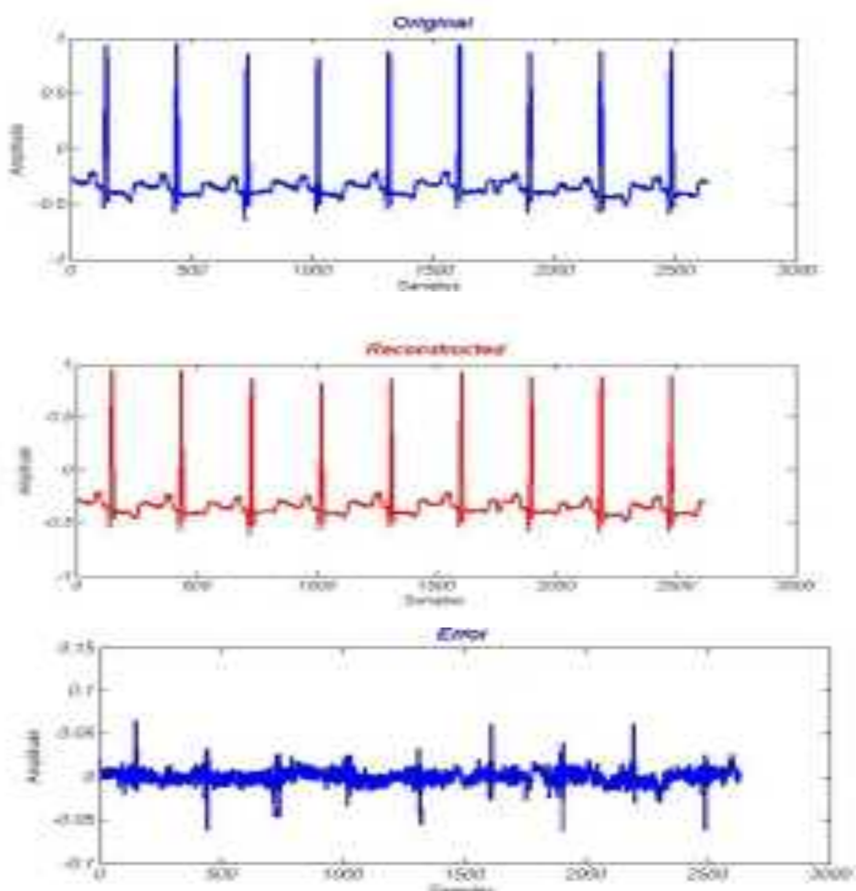

Figure 9. Original, reconstructed and error for ECG signal of record 100 for CR=24.4 and PRD=2.5%.

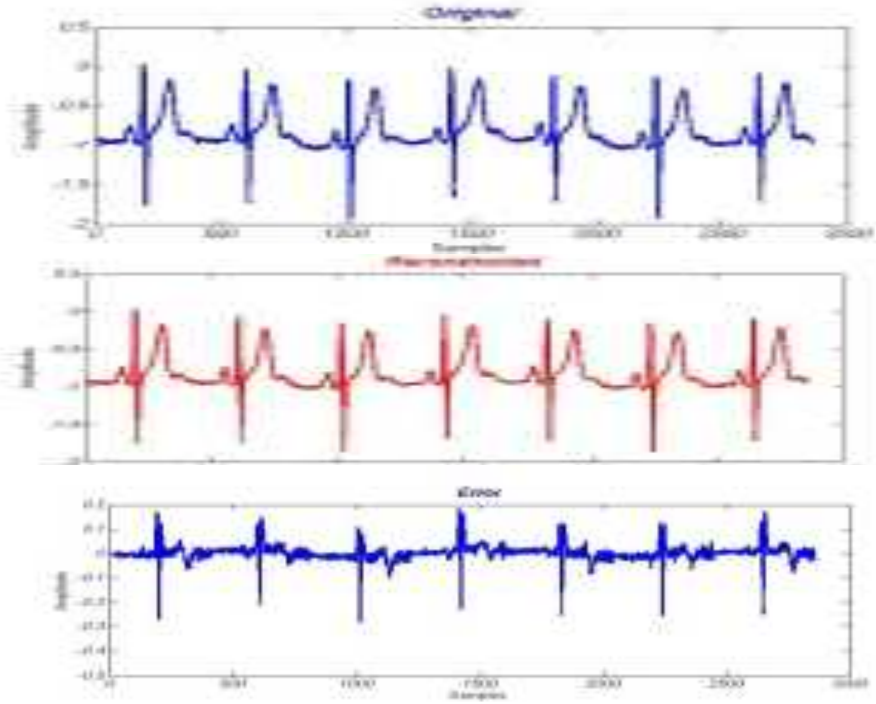

Figure 10. Original, reconstructed and error for ECG signal of record 109 for CR=24.3 and PRD=3.1%.

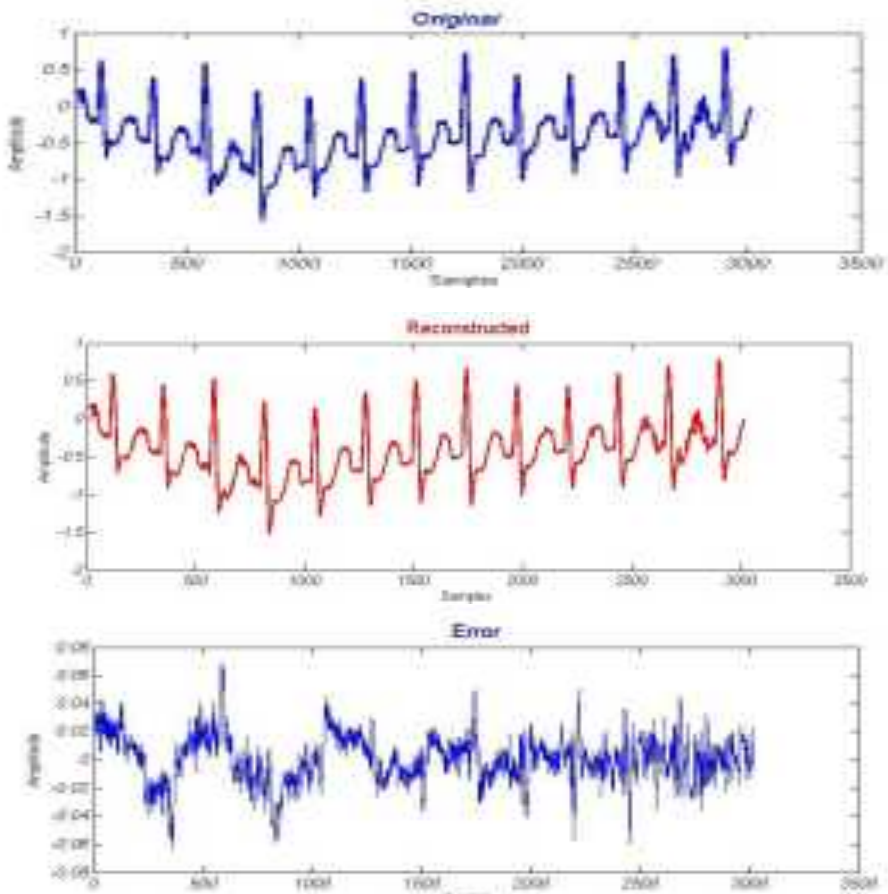

Figure 11. Original, reconstructed and error for ECG signal of record 117 for CR=24.2 and PRD=4.7%.

Table 1. CR and PRD for the proposed mixed transform.

Codebook size		256	64	16
Record 100	**CR**	10.5	21.5	26.9
	PRD%	3.27	4.1	4.77
Record 107	**CR**	11.19	21.77	26.6
	PRD%	4.7	5	5.2
Record 109	**CR**	10.5	20.4	24.9
	PRD%	3.22	3.4	3.53
Record 117	**CR**	10.47	20.38	24.9
	PRD%	5.34	5.69	5.89

Table 2. Comparison of different ECG compression algorithms.

Algorithm	Record	CR	PRD%
Polania, et al., 2011	100	23.61	8.4
	117	10	2.5
Hossain, et al., 2008	100	13.89	5.16
	107	14.18	5.39
	109	12.01	3.92
	117	15.12	2.33
Khalaj, Naimi 2009	100	13.79	11.06
	109	17.39	11
	117	14.64	4.5
Proposed	100	24.4	2.56
	107	23.6	4.3
	109	24.33	3.1
	117	24.2	4.74

Study the Effect of Face Sheets Material on Strength of Sandwich Plates with Circular Hole

Dr. Hatem Rahem Wasmi
Assistant Professor
College of Engineering-University of Baghdad
hatenrwa@yahoo.com

Nawal Falkhous Eshaut
Instructtor
College of Engineering -University of Baghdad
an.rn.fn.ali@gmail.com

ABSTRACT

This study aims to investigate the effect of changing skins material on the strength of sandwich plates with circular hole when subjected to mechanical loads. Theoretical, numerical and experimental analyses are done for sandwich plates with hole and with two face sheet materials. Theoretical analysis is performed by using sandwich plate theory which depends on the first order shear deformation theory for plates subjected to tension and bending separately. Finite element method was used to analyse numerically all cases by ANSYS program.

The sandwich plates were investigated experimentally under bending and buckling load separately. The relationship between stresses and the ratio of hole diameter to plate width (d/b) are built, by studying the effect of hole size on strength of sandwich plates. The maximum stress were developed at the hole region in sandwich plates clarified the dropped in their strength. So, the experimental maximum stress was found by means of multiplying the experimental nominal stress obtained from Stress-strain curve by the stress concentration factor.

All results which obtained, theoretically, numerically and experimentally are compared to find that the hole weaken the strength of sandwich plates because of the stress concentration and that weakness is depending on the hole size and the face sheets materials.

Keywords: sandwich plate, hole size, sandwich plate theory, stress concentration.
الكلمات الرئيسية: الصفائح الشطيرية, حجم الثقب, نظرية الصفائح الشطيرية, تمركز الإجهادات

دراسة تأثير مادة القشرة على مقاومة الصفائح الشطيرية المثقوبة

الخلاصة

تهدف هذه الدراسة إلى بحث تأثير مادة القشرة على مقاومة الصفائح الشطيرية المثقوبة عند تعرضها الى الأحمال الميكانيكية. تم تحليل الصفائح الشطيرية المثقوبة وباستعمال نوعين من المعادن كقشرة تحليلا نظريا وعمليا. تم التحليل النظري بطريقتين: الاولى استعمال نظرية الصفائح الشطيرية التي تعتمد على نظرية تشوه القص من الدرجة الأولى للصفائح المعرضة الى حملي الشد و الانحناء بشكل منفصل. اما الثانية فهي التحليل العددي حيث تم باستخدام طريقة العناصر المحدودة لتحليلها عدديا ولجميع الحالات عن طريق استعمال برنامج ANSYS .
وقد تم بحث الصفائح الشطيرية تجريبيا تحت تاثير احمال الانحناء و الانبعاج بشكل منفصل. تم ربط العلاقة ما بين الاجهادات و نسبة قطر الفجوة على عرض الصفيحة a/b. من خلال دراسة تأثير حجم ثقب على قوة الصفائح الشطيرية . ان االاجهاد الأقصى للاجهاد الذي تم الحصول عليه من التجارب العملية في منطقة الثقب في الصفائح الشطيرية أوضح الانخفاض في قوتها. لذلك ، تم العثور على أقصى إجهاد التجريبية عن طريق ضرب الإجهاد الاسمي التجريبية التي تم الحصول عليها من منحنى الإجهاد والانفعال في عامل تركيز الإجهاد.

وتمت مقارنة جميع النتائج التي حصلنا عليها، نظريا ، عدديا و تجريبيا وتبين أن الثقوب تضعف من مقاومة المواد الشطيرية بسبب تركيز الاجهادات و هذا الضعف يعتمد على حجم الثقب وكذلك المادة التي تم استعمالها كقشرة للسطوح .

1. INTRODUCTION

A sandwich structure results from the assembly by bonding -or welding- of two thin facings or skins on a lighter core that is used to keep the two skins separated. Sandwich is built up of three elements as shown in **Fig.1**: two faces, core and joints**.**

Every part has its specific function to make as a unit. The aim is to use the material with a maximum of efficiency. The two faces are placed at a distance from each other to increase the moment of inertia, and thereby the flexural rigidity, about the neutral axis of the structure.

The faces carry the tensile and the compressive stresses in the sandwich. The core has several important functions. It has to be stiff enough to keep the distance between the faces constant. It most also be so rigid in shear that the faces do not slide over each other.

To keep the face and the core co-operating with each other the adhesive between the faces and the core, must be able to transfer the shear forces between the faces and the core. The adhesive must be able to carry shear and tensile stresses. It is hard to specify the demands on the joints. A simple rule is that the adhesive should be able to take up the same shear stress as the core.

The quality of the bond is fundamental for the performance and life duration of the piece. In practice we have**, Daniel, et al., 2003.**

$$0.025 \text{ mm} \leq \text{adhesive thickness} \leq 0.2 \text{ mm}$$

Many applications for sandwich plates in many engineering fields namely: aerospace, biomedical, civil, marine, and mechanical engineering because of their ease of handling, good mechanical properties and low fabrication cost.

Sandwich plates and sandwich beams are widely used in engineering applications and industrial fields as previously described. Holes and other openings are extensively used as structural members, mainly for practical considerations. Holes are commonly found as access ports for mechanical and electrical systems or simply to reduce weight. Cutouts are also needed to provide access for hydraulic lines, for damage inspection, to lighten the loads, provide ventilation and for altering the resonant frequency of the structures. Also cutouts have wide use with composite material such as in aircraft fuselage, ships, and other high performance structures. In addition, the designers often need to incorporate cutouts or openings in a structure to serve as doors and windows. In some cases holes are used to reduce the weight of the structure.

The study here is compared between two groups of sandwich plate: one consists of Low carbon steel as face sheets and polyvinylchloride as a core. The other group consists of aluminum alloy 7075-T6 sheets (AA7075-T6) and polyvinylchloride as a core. The sandwich plate was either solid or had a central circular hole with diameter (10, 15 or 20mm) and subjected to tension, bending and buckling loads to study the effect of hole size on its strength. **Qing-Sheng,** and **Wilfried, 2004,** modeled laminated plates with holes by an inclusion problem with anisotropic matrix. The effective stiffness's are calculated by different homogenization methods and the microscopic deformation of a RVE is modeled by the finite element method for the plate with arbitrarily shaped holes. All of the effective stiffness coefficients, especially stretching−shear coupling coefficients are evaluated. **Podruzhin,** and **Ryabchikov, 2004,** studied distribution of bending stresses in anisotropic plates with stress concentrators. Stresses in the vicinity of the tips of defects of the type of a crack or rigid inclusion are determined. The effect of holes and interaction between the defects on the stress intensity factors is analyzed, **Ali,** and **Masood, 2010**. The aim of the work presented in this research is to deal with some of the aspects in the FEM with some of the aspects in the FEM analysis of sandwich panels containing holes which comprised with foam core. In this research, the FEM modeling was produced, analyzed and computed considering laboratory conditions. An extensive parametric study was investigated under different load conditions; different geometrical parameters, such as; dimensions, face thickness, core thickness, size and location of the opening.

2. STATIC ANALYSIS OF SANDWICH PLATE STRUCTURES

2.1 Sandwich Plate Theory

The theory of sandwich plates is based on the following basic hypotheses**, Berthelot, 2010.**:

1. The thickness of the core is much greater than that of the skins: $h \gg h_1, h_2$.
2. The in-plane displacement in the core u_c and v_c in the x and y directions are linear functions of the z coordinate.
3. The in-plane displacements and in the x and y directions are uniform through the thickness of the skins.
4. The transverse displacement w is independent of the coordinate: the strain $_{zz}$ is neglected.
5. The core transmits only the transverse shear stresses σ_{xz}, σ_{yz}: the stresses σ_{xx}, σ_{yy}, σ_{xy} and σ_{zz} are neglected in the core.
6. The transverse shear stresses σ_{xz} and σ_{yz} are neglected in the skins. Lastly, the theory considers the elasticity problems of small deformations.

By using these assumptions the governing equations are derived for isotropic symmetric sandwich plates for the in-plane and flexural field Eq.(1) and for transverse shear field Eq.(2):

(1)

[ ] [ ] [ ]

[ ] [ ]* + (2)

In the case of isotropic symmetric sandwich plates (a sandwich plate is isotropic when the core of the sandwich plate is made of an isotropic (such as foam) or transversely isotropic material (such as honeycomb) and the face-sheets are made of identical isotropic materials or quasi-isotropic laminates**, Springer,** and **Kollar, 2003**, hence:

$$0 \qquad (3)$$

$$(\quad)$$

$$-(\quad)\quad(\quad)\qquad(\quad)$$

and

$$[\quad]\ \frac{}{(\quad)}[\quad \frac{}{}\ ]\qquad(\quad)$$

In the case of statics problems, the fundamental equations of sandwich plates are:

$$\frac{}{}\quad \frac{}{}\quad (\quad)\frac{}{}$$
$$(\quad)\frac{}{}\quad\frac{}{}\quad\frac{}{}$$
$$\frac{}{}\quad\frac{}{}\quad\frac{}{}\quad(\frac{}{}\quad)\qquad(6)$$
$$(\quad)\frac{}{}\quad\frac{}{}\quad\frac{}{}\quad(\frac{}{}\quad)$$
$$(\frac{}{}\quad\frac{}{})\quad(\frac{}{}\quad\frac{}{})$$

2.2 Tension

A sandwich plate consists of two identical skins made of an isotropic material with thickness h_1 and of an isotropic core with thickness h. The plate is clamped along the edges $x = 0$ and free at x = . This plate is subjected to axial load in x-direction at the free end and there is no coupling between in-plane and flexural behaviors so the stress equation is**, Berthelot, 2010.**

$$[\quad]\quad[\qquad]\,[\quad]\qquad(7)$$

By substituting Eq.(1) in Eq.(7):

[ ] [ ][ ][ ] (8)

where the coefficients are the components of the inverse matrix of [A_{ij}]. In the case of tension along the x direction, the tension and twisting results N_y and N_{xy} are zero:

(9)

where is defined in Eq.(5) and:

$$\frac{\quad}{(\quad)} \qquad (10)$$

(11)

By substituting Eqs.(5, 10 and 11) in Eq.(9):

$$\frac{\quad}{(\quad)} \qquad (\quad)$$

2.3 Bending

The square sandwich plate, see **Fig.2**, having two identical skins constituted of an isotropic material with thickness h_1 and of an isotropic core with thickness h. The plate is simply supported along the edges $x = 0$ and x = a while the other two edges y = a/2 and y = - a/2 may be simply supported. By Levy Solutions, this plate is subjected to the transverse load:

$$(\;) \quad \Sigma \quad \frac{\quad}{\quad} \qquad (\quad)$$

where:

$$-\int (\;) \quad \frac{\quad}{\quad} \qquad (\quad)$$

When the plate is subjected to a line load ( ) along −, see **Fig.2**, Eq.(14) will be**, Ansel, 1999.**:

$$\frac{\quad}{\quad} \quad \frac{\quad}{\quad} \qquad (\quad)$$

The fundamental bending relations are given by Eq.(6), the coefficients being defined by Eq.(4) imply for a symmetric sandwich plate:

( )

These conditions are satisfied by functions of the form [3]:

( )

By substituting Eq.(16) and Eq.(17) in Eq.(6):

( )

From Eqs.(15, 17 and 18), we derive that the case of bending is cylindrical bending and the deformation state of the sandwich plate is described as**, Berthelot, 2010.**

( )
( ) ( )

By substituting Eq.(19) into Eq.(6):

( ) ( )

( ) ( )

By considering the case of a plate simply supported along the edges $x = 0$ and $x = a$:

( )

Integration of Eq.(20a) with respect to x and substituting the result in Eq.(20b), then integration of the final result with respect to x again leads to:

( )

Associated with condition Eq.(21) for the supports, leads to:

For the symmetric isotropic sandwich the coefficients and there is no coupling between in-plane and flexural behaviors, then:

The substitution of Eq.(23) into Eq.(24) leads to:

For and defined in Eq.(5) and Eq.(4) respectively and:

Then Eq.(25) for the maximum bending stress at – will be:

2.4 Stress Concentration Factors

The stress concentration factor, listed in **Table 1** *K* can be defined as the ratio of the peak stress in the body (or stress in the perturbed region) to some other stress (or stress like quantity) taken as reference stress:

where the stresses represent the maximum stresses to be expected in the member under the actual loads and the nominal stresses is reference normal stress. In the case of the theory of elasticity, a two-dimensional stress distribution of an elastic body under known loads is a function only of the body geometry and is not dependent on the material properties as shown in Eq.(27).
Suppose that the thickness of the plate is *t*, the width of the plate is *b*, and the diameter of the hole is *d*. The reference stress could be defined in two ways**, Walter, 1997.**

1. Use the stress in a cross section far from the circular hole as the reference stress. The area at this section is called the gross cross-sectional area. Thus define:

( )

so that the stress concentration factor becomes

( )

Use the stress based on the cross section at the hole, which is formed by removing the circular hole from the gross cross section. The corresponding area is referred to as the net cross-sectional area. If the stresses at this cross section are uniformly distributed and equal to :

( )

( )

2.2 F.E Static Modeling of Sandwich Plate

Four nodes element (SHELL181) is used to analyze rectangular sandwich plates under tension and buckling loads respectively and square sandwich plates under bending load.

SHELL181 used for layered applications for modeling laminated composite shells or sandwich construction. The accuracy in modeling composite shells is governed by the first order shear deformation theory. To define the thicknesses and materials properties of the three layers of the sandwich plates, section definition can use.

2.2.1 **In plane loads (tension and buckling loads)**

. The sandwich plates are built-in at edge (x=0) and free at edge (x=a, y=0 and y=b) and the in plane loads load is applied at the free end (x=a). the modeling and meshing of sandwich plates under tension and buckling is same, while the solution of each case is different.

The best meshed method for solid plate is that 20 elements along the vertical edges of plate (x=0 and x=a) by interring the element edge length is 5, while 30 elements along horizontal edges of plate (y=0 and y=b) by interring the element edge length is 5, as shown in **Fig.3.**

The best meshed method for plate with central circular hole is that**, Erdogan,** and **Ibrahim, 2006**, as shown in **Fig.4**:

- Draw square area has edge length equal to double of hole diameter **(A_1)**.
- Draw rectangular area represented the plate **(A_2)**, then glue the two areas.
- Draw circular area in the middle **(A_3)**, then subtracting it from the other areas to obtain the finally shape (plate with central hole).
- The outer edge are meshed as in solid plate (lines 1 & 2 have 20 elements while lines 3 & 4 have 30), but the edges of square area (lines 5, 6, 7 and 8) and the curves of circle are meshed by interring the element edge length is 0.1 as shown in**.**

2.2.2 **Bending**

The sandwich plates are simply supported at edges (x=0 and x=a) while free at edge (y=0 and y=a) and loaded by transverse line load at x=a/2.

The solid plate meshed as in tension **Fig.3,** while the plates with central circular hole as shown in **Fig. 5**:

- Draw square area represented the plate **(A_1)**.
- Draw circular area in the middle the square area **(A_2)**, then subtracted it from the square area.
- The vertical edges of plate(x=0 and x=a) have the element edge length is 1 while the horizontal edges of plate(y=0 and y=a) have the element edge length is 5.
- The curves of the circle have the element edge length is 0.1**.**

2.3 Experimental Method for Size Effect-Related Static Analysis

The experimental analysis will be done by several steps:

2.3.1: **Selection basic materials and manufacturing the sandwich plates**

Tensile test used to find the mechanical properties of the basic materials which represented by Low Carbon Steel and AA7075-T6 for face sheets and PVC for core of sandwich plates. The stress-strain curves of the tensile for these materials are shown in **Fig.6** and mechanical properties obtained from them are listed in **Table 2**.

After selecting the basic materials, these materials are cutting to the suitable dimensions depended on the thin plate theory.

Tensile test is done again for three sandwich specimens each one is bonded by different adhesive (Polyester, Epoxy and Titan). The load-deformation curves show that the sandwich specimen bonded by Epoxy adhesive has the highest load as shown in **Fig.7.**

Depending on the results the Epoxy adhesive will be used to bond the sandwich plates.

2.3.2 **Tensile test of the sandwich plates**

Tensile tests are passes in room temperature at maximum load 200KN and 2mm/min for all specimens. The results of the tensile test are the maximum elastic loads from load-deformation curves which using to obtain the theoretical stress by Eq.(12) and in ANSYs program input data and the maximum elastic stresses from stress-strain curves.

2.3.3 **Bending test of the sandwich plates**

The bending tests are passed through the room temperature under maximum load 10KN and speed 3mm/min for all sandwich plate specimens.

The results of the bending test are the maximum elastic loads from load-deformation curves which using to obtain the theoretical stress by Eq.(27) and in ANSYs program input data and the maximum elastic stresses from stress-strain curves.

2.3.4 **Buckling test of the sandwich plates**

The buckling tests are passed through the room temperature under maximum load 10KN and speed 2mm/min for all sandwich plate specimens. The results of the buckling test are the maximum elastic loads from load-deformation curves.

3. RESULRS AND CONCLUSION

The main conclusion from the results of this study is that the hole in the plate is weaking its strength under mechanical loads. The weakness in strength of plate appears as decreasing in nominal stress of sandwich plate because of concentration stresses around it as shown in **Fig.8** for analytical nominal stress of sandwich plates with hole under tension as well as **Fig.9** and **Fig.10** for analytical and experimental nominal stress of sandwich plates with hole under bending

Fig.8 shows that the AA7075-T6/PVC/AA7075-T6 can be had strength more than ST/PVC/ST sandwich plates. The effect of the hole in the plate under tensile makes strength be dropped at (d/b = 0.1), then the curves can be risen at (d/b = 0.15). The behavior can be explained by the increase in diameter of hole may be reduced the stress concentration but did not eliminate the influence. The second drop of the curves can be clarified by that the hole diameter at this point (20 mm) was approximately equal to the half of plate width (100 mm) and that will reduce the stress concentration effect as compared with other hole dimensions.

This discussion can be applied to both of **Fig.9** and **Fig.10,** but it can be noted that the ST/PVC/ST sandwich plate were had strength more than the AA7075-T6/PVCAA7075-T6 plate sandwich. After (d/b = 0.15), this difference in strength between the two sandwich materials was decreased as well as the effect of increasing in a hole size and can be stabled for each materials.

Fig.11 and **Fig.12** were represented the relationship between the analytical and numerical maximum stress of sandwich plates under tensile load respectively. The two figures can be shown two important things. The first thing, the use of (K_{tg}) stress concentration factor with gross nominal stress or (K_{tn}) stress concentration factor can be obtained same results of the maximum stress with maximum difference (5.88%). The second thing, the maximum strength in the hole can be caused the weakness of sandwich plates and beams.

Fig.13, **Fig.14** and **Fig.15** can be showed the relationship between the analytical, numerical and experimental maximum stress of sandwich plate under bending load. In these figures, it can be noted the obvious difference between the two maximum stresses obtained from (σ_{nom}*K_{tg}) and (σ_n*K_{tn}) for each sandwich materials, because of the studied sandwich plates were square and the effect of the width in Eq.(27) can be canceled.

The numerical values of stress concentration factors can be shown in **Fig.16** and **Fig.17.** From these figures, it can be noted that the curves of K_{tn} have same behavior while the curves of K_{tg} appears different behavior. Where K_{tn} is proved the fact of reducing the stress concentration with increasing of hole size, K_{tg} can be behaved randomly with increasing of hole size.

The buckling load decreased when the hole size is increase because of the hole became region to concentrate the stresses and weaken the plates. ST/PVC/ST sandwich plate is undergoing buckling load more than AA7075-T6/PVC/AA7075-T6 sandwich plate as shown in **Fig.18** and **Fig.19** for numerical and experimental buckling load of sandwich plate respectively.

When the deformation shape modes are discussed, the solid plates have different forth deformation shape mode for the two sandwich materials shown in **Fig.15 a and b**.

While the deformation shape modes are differed and changed for sandwich plates with hole but they remain the same in each sandwich materials as shown in **Fig.16 a and b**. The hole not only causes a decrease in resistance but is changing the deformation shape modes of the sandwich plate since each sandwich materials varies in response the deformation shape modes are differed for each one because of the different in faces materials.

The comparisons between the theoretical, numerical and experimental results are shown in **Fig.17** and **Fig.18.**

REFFRENCES

Ali, V. S. and Masood, M.,2010, *Parametric Studies on the FEM Analysis of Foam Core Sandwich Panels with Holes*, 5th National Congress on Civil Engineering, Ferdowsi University of Mashhad, Mashhad, Iran, May 4-6, 2010.

Ansel, C. U., 1999, *Stresses in Plates and Shells*, 2nd edition, New York: McGraw-Hill,

Berthelot, J.-M, 2010, *Mechanics of Composite Materials and Structures*, by Springer.

Daniel, G., Suong, V. H. and Stephen W.T., 2003, *Composite Materials Design and Application*, 2nd Edition, by CRC Press LLC.

Erdogan, M. and Ibrahim, G., 2006,*The Finite Element Method and Applications in Engineering Using ANSYS*, by Springer.

Podruzhin, E.G., and Ryabchikov, P.E., 2004, *Bending of Anisotropic plates with Stress Concentrations*, by IEEEXplore

Qing-Sheng, Y. and Wilfried, B., 2004, *Effective Stiffness and Microscopic Deformation of an Orthotropic Plate Containing Arbitrary Holes*, Computers and Structures, Vol.82, p.p:2301−2307.

Saeed, M., 1999, *Finite Element Analysis Theory and Application with ANSYS*, by Shashi Bhushan Patel

Springer, G.S. and Kolla'r, L.P., 2003, *Mechanics of Composite Structures*, by Cambridge University Press.

Walter, D. P., 1997, *Peterson's Stress Concentration Factor*, 2nd edition, by John Wiley & Sons.

Wang, C.M., Reddy, J.N. and Lee, K.H., 2000, *Shear Deformable Beams and Plates Relationships with Classical Solution*, 1st Edition, by Elsevier.

NOMENCLAUTURE

shear strain components of middle-plane in (z) directions respectively.

, strain components of middle-plane in (x, y) directions respectively.

.

curvatures components of the middle-plane.

, MPa.

, MPa.

, rotation of the cross section in the x-y and x-z planes respectively.

, : extensional stiffness, the coupling stiffness, and the bending stiffness.

.

, mm.

b: beam and plate width, mm.

.

E_f, E_c: Young modulus of skin and core respectively, Pa.

.

G_f, G_c: shear modulus of skin and core respectively, Pa.

thickness of lower and upper skins respectively, .

, .

.

.

, , N.

.

,

q: external load.

: middle-plane displacement components along (x, y and z) directions respectively

, mm.

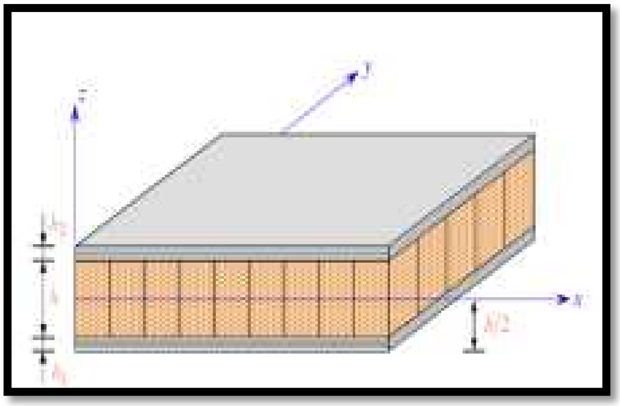

Figure 1. Sandwich materials.

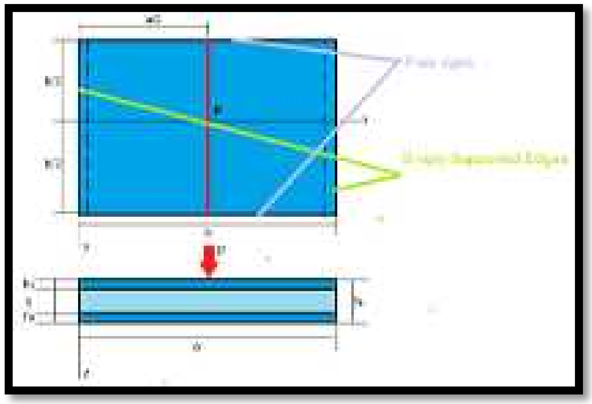

Figure 2. Sandwich plate under bending load.

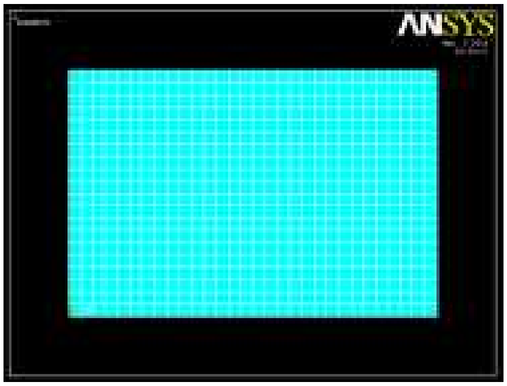

Figure 3. Mesh of solid sandwich plate.

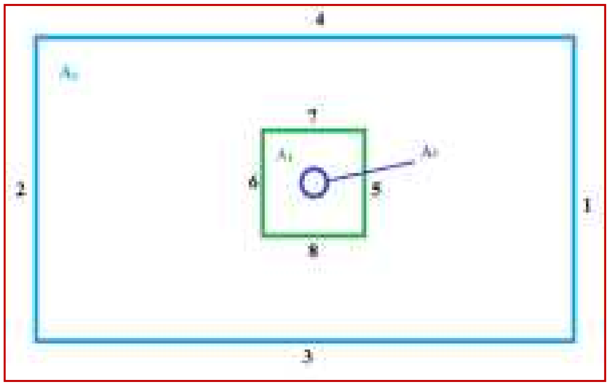

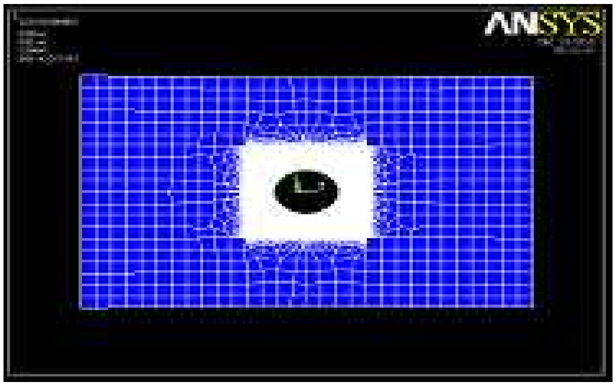

Figure 4. Mesh of sandwich plate with hole under tension and buckling.

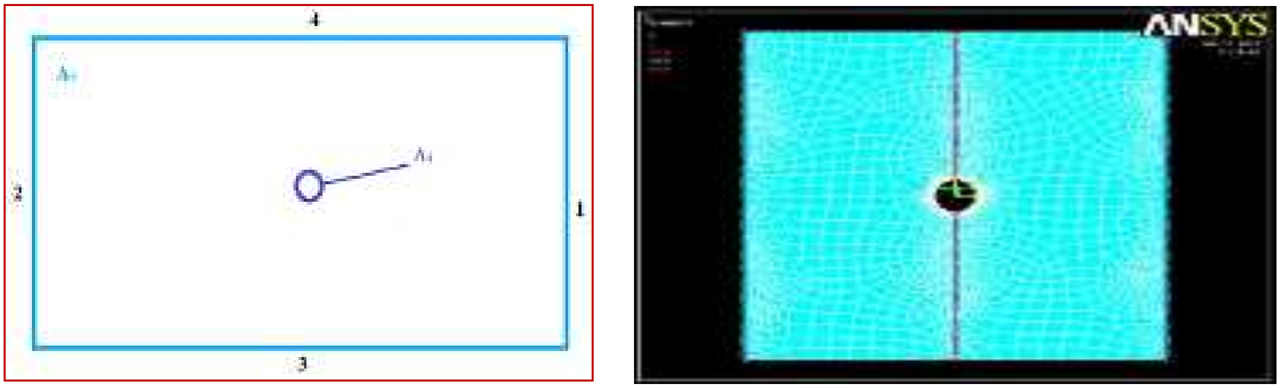

Figure 5. Mesh of sandwich plate with hole under bending.

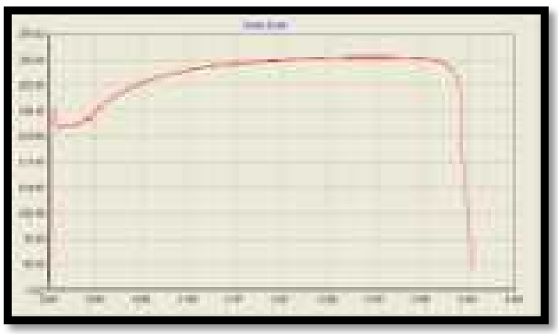

(a)

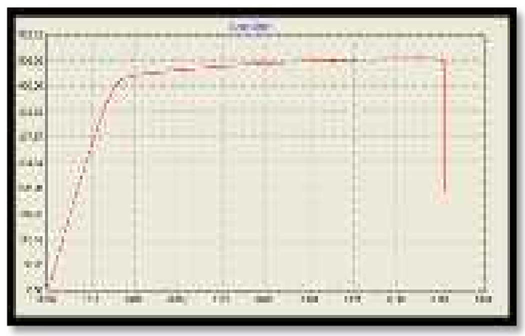

(b)

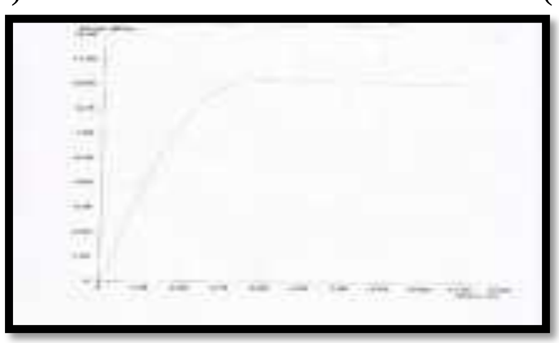

(c)

Figure 6. Tensile test curves: (a) Steel, (b) AA7075-T6, (c) PVC.

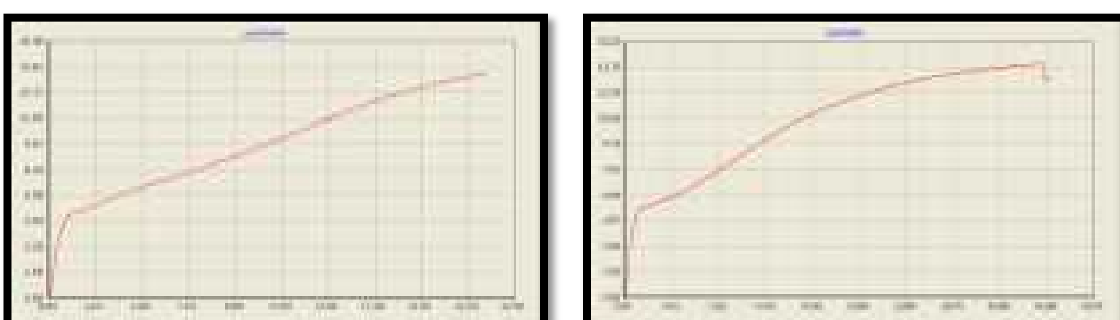

(a) Epoxy (b) Polyester

(c) Titan

Figure 7a. Tensile test curve of specimens to adhesive selection.

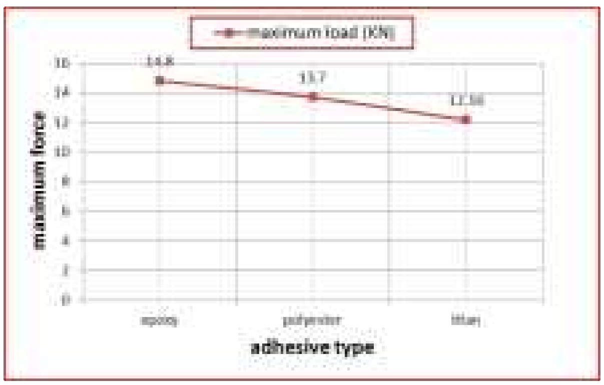

Figure 7b. Maximum load (KN) of adhesive selected Specimens tensile test.

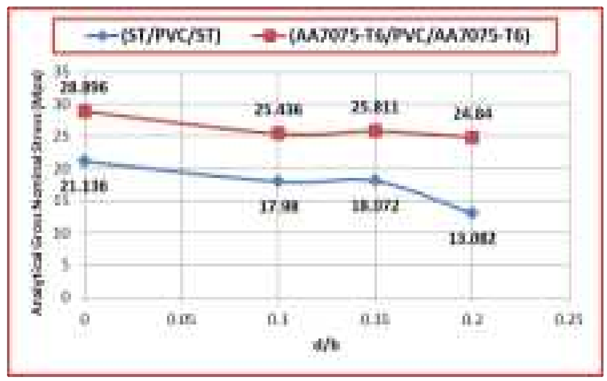

Figure 8. Analytical elastic nominal maximum stress of sandwich plates subjected to tensile load.

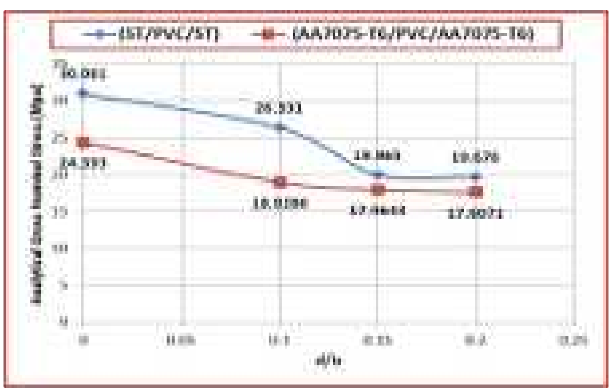

Figure 9. Analytical elastic nominal maximum stress of sandwich plates subjected to bending load.

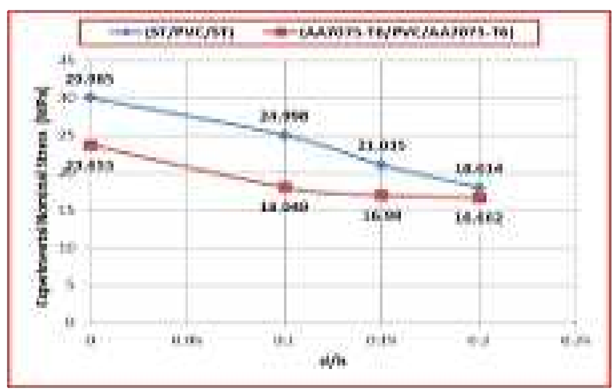

Figure 10. Experimental nominal stress of sandwich plates under bending load.

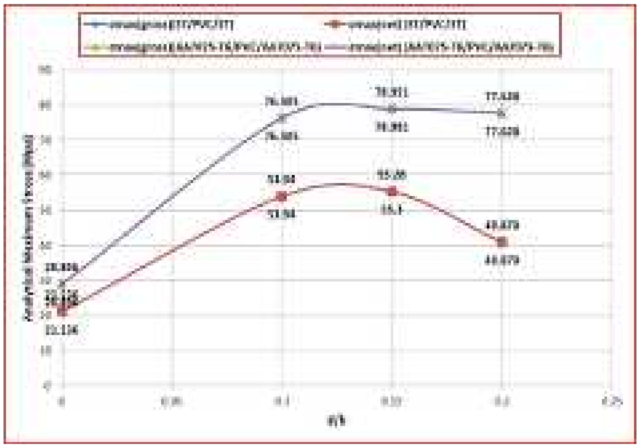

Figure 11. Analytical maximum stresses of sandwich plates under tensile load.

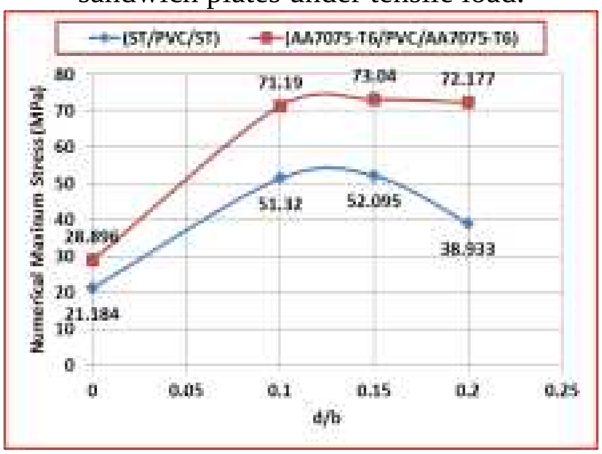

Figure 12. Numerical maximum stress of sandwich plates under tensile load.

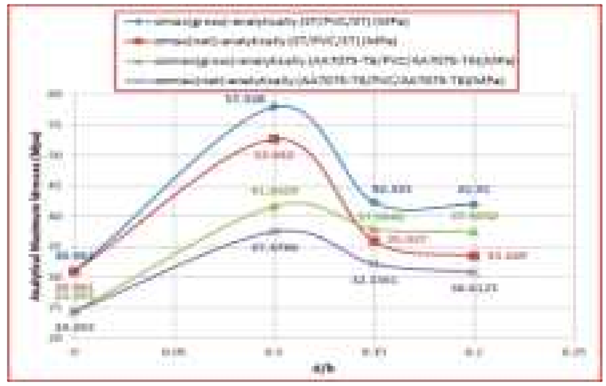

Figure 13. Analytical maximum stresses of sandwich plates under bending load.

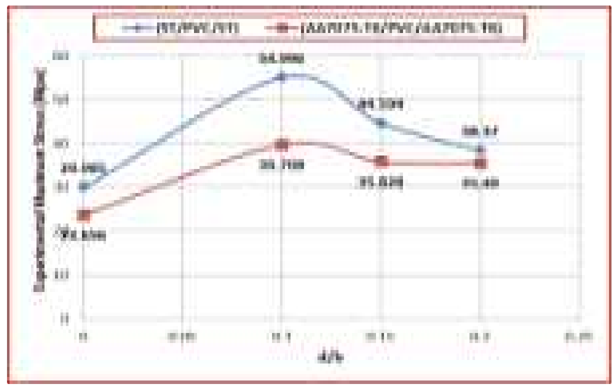

Figure 14. Experimental maximum stresses of sandwich plates under bending load.

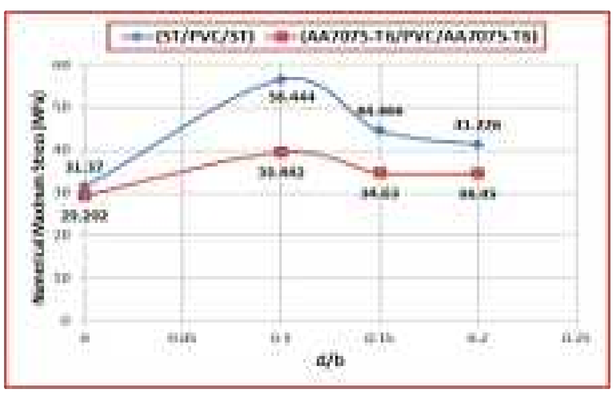

Figure 15. Numerical maximum stress of sandwich plates under bending load.

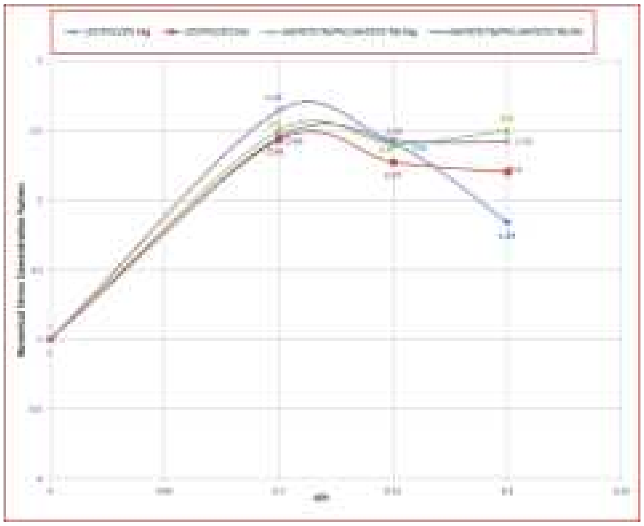

Figure 16. Numerical stress concentration factors of sandwich plates under tensile load.

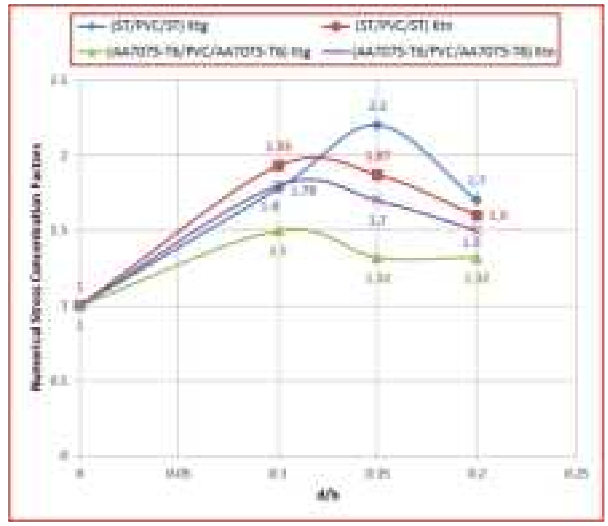

Figure 17. Numerical stress concentration factors of sandwich plates under bending load.

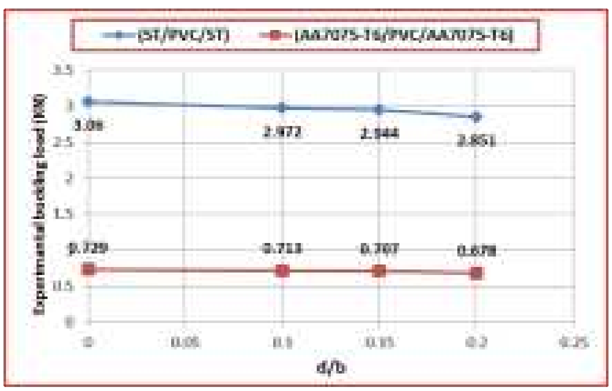

Figure 18. Experimental buckling load of sandwich plates under compression load.

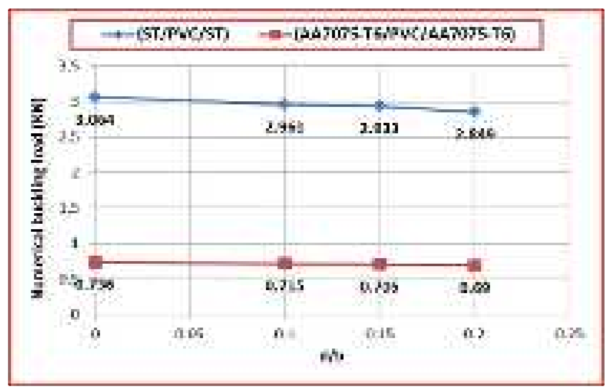

Figure 19. Numerical buckling load of sandwich plates subjected to compression.

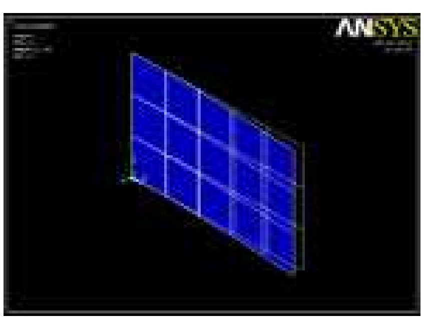

First mode

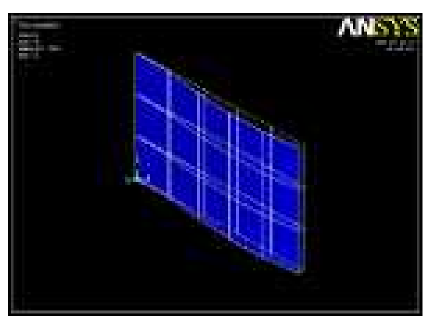

Second mode

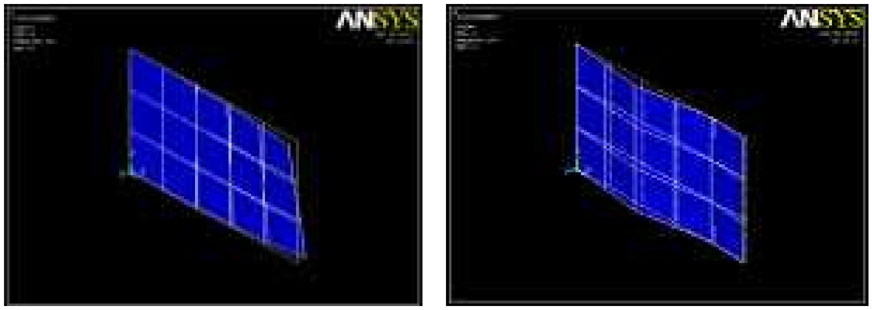

Third mode Fourth mode

Figure 20a. Deformation shape modes of ST/PVC/ST solid sandwich plates under buckling.

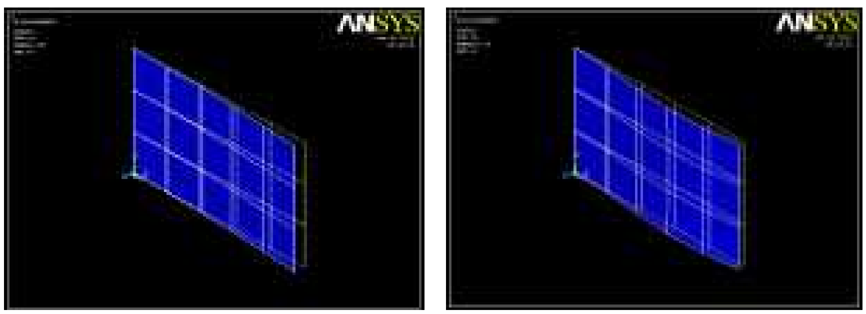

First mode Second mode

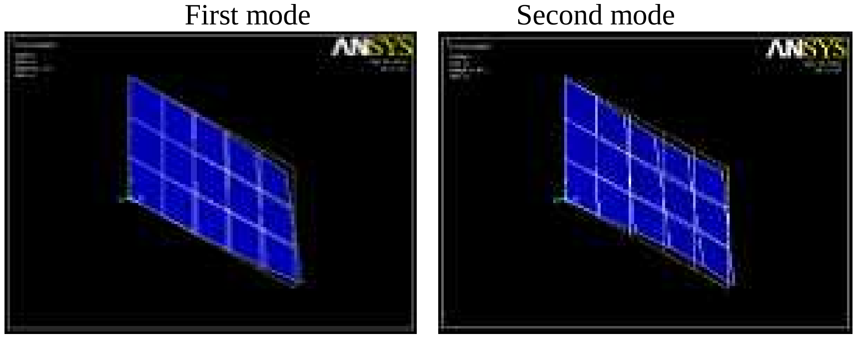

Third mode Fourth mode

Figure 20b. Deformation shape modes of AA7075-T6/PVC/AA7075-T6 solid sandwich plate under buckling.

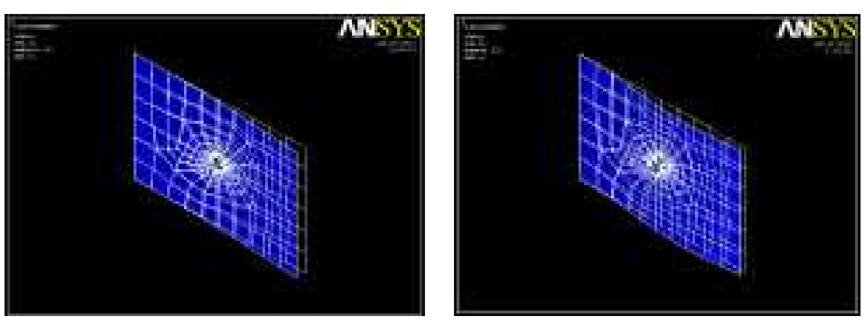

First mode Second mode

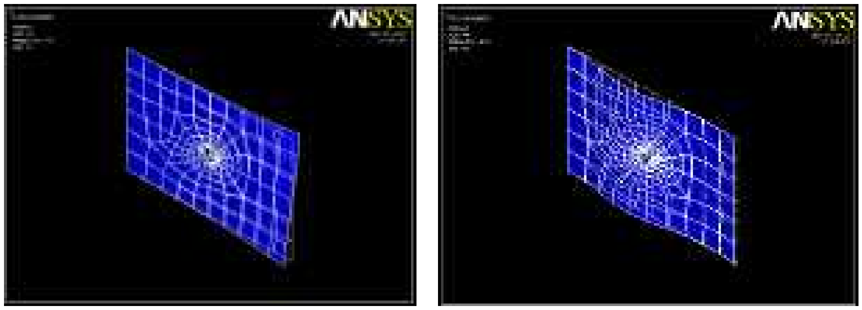

Third mode Fourth mode

Figure 21a. Deformation shape modes of ST/PVC/ST sandwich plate with hole under buckling.

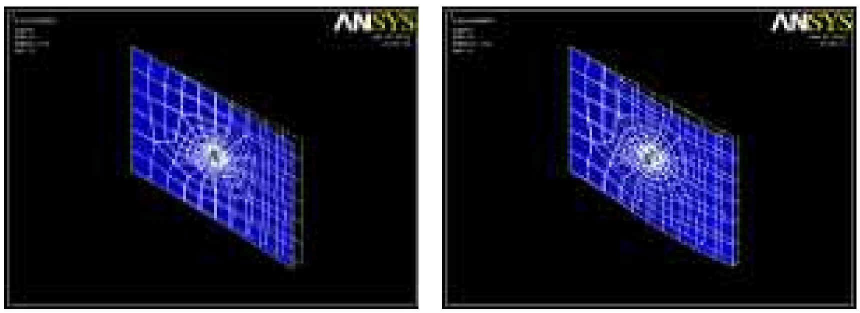

First mode Second mode

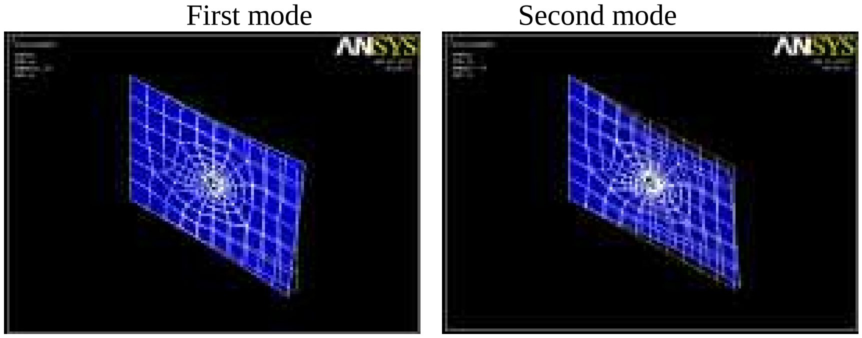

Third mode Fourth mode

Figure 21b. Deformation shape modes of AA7075-T6/PVC/AA7075-T6 sandwich plate with hole under buckling.

Table 1. Stress concentration factors for beams and plates under tension and bending loads.

Tension				
ST/PVC/ST PLATES and AA7075-T6/PVC/AA7075-T6 PLATES	D	10	15	20
		3	3.06	3.125
		2.7	2.6	2.5
Bending				
ST/PVC/ST PLATES	D	10	15	20
		2.2	2.12	2.13
		2	1.8	1.7
AA7075-T6/PVC/AA7075-T6 PLATES	d	10	15	20
		2.2	2.11	2.13
		1.98	1.79	1.79

Table 2. Mechanical properties of constitutions materials.

Mechanical Properties	Steel	AA7075-T6	PCV
Young Modulus(GPa)	212	72	4
Yield Stress(MPa)	**255.128**	**447.84**	**7.746**
Maximum Stress(MPa)	**325.118**	**515.352**	**11.93**
Possin's Ratio	**0.3**	**0.33**	-

Kinetics of the Saponification of Mixed Fats Consisting of Olein and Stearin

Dr. Raghad Fareed Kassim Almilly
Lecturer
Department of Chemical Engineering
College of Engineering - Baghdad University
Email: rfkalm@yahoo.com

ABSTRACT

This research presents the kinetics of the saponification reaction using mixed fats of olein and stearin [in the ratio (3:1)] with NaOH solution . In this reaction , excess solution of NaOH was used to ensure the reaction being irreversible . Three parameters were varied to show their effects on the reaction rate .They are : percentage excess of NaOH solution (10 % - 100 %) , temperature (100-150)^{o}C , and stirring speed (400-1100) rpm. It was noticed that increasing the percentage excess of NaOH solution enhances the rate of reaction while increasing temperature decreases the reaction rate since it is exothermic reaction. Increasing stirring speed also improves the reaction rate because it is mass transfer controlled .Calculations of the activation energy and the frequency factor were also performed.

A new mathematical model for calculation of the reaction – rate constant was derived . It is shown that a good approximation was obtained between the experimental and calculated values of the reaction – rate constant k .

Key words: kinetics, saponification reaction , mixed fats , olein and stearin , mathematical model**.**

حركية تفاعل الصوبنة لمزيج من زيتي الاولين والستيارين

د. رغد فريد قاسم الملي
مدرس
قسم الهندسة الكيمياوية
كلية الهندسة - جامعة بغداد

الخلاصة

يقدم هذا البحث حركية تفاعل الصوبنة باستخدام خليط من زيتي الاولين والستيارين [بنسبة (1:3)] مع محلول هيدروكسيد الصوديوم .يستخدم في هذا التفاعل نسبة زائدة من محلول هيدروكسيد الصوديوم لضمان كون التفاعل غير عكسي . تم تغيير ثلاثة عوامل لبيان تأثيرهم على سرعة التفاعل وهم نسبة الزيادة المئوية لمحلول هيدروكسيد الصوديوم (10% - 100%) , درجة الحرارة (100-150)°م , و سرعة الخلط (400-1100) دورة/ دقيقة. وقد لوحظ ان زيادة نسبة الزيادة المئوية لمحلول هيدروكسيد الصوديوم تؤدي الى زيادة سرعة التفاعل بينما زيادة درجة الحرارة تقلل سرعة التفاعل لأنه تفاعل باعث للحرارة. أيضا زيادة سرعة الخلط تؤدي الى زيادة سرعة التفاعل لأنه من التفاعلات التي يسيطر عليها انتقال المادة. كذلك تم احتساب طاقة التنشيط وعامل الذبذبة. تم اشتقاق نموذج رياضي جديد لحساب ثابت سرعة التفاعل . لقد تبين وجود تقارب جيد بين القيم العملية والقيم المحسوبة لثابت سرعة التفاعل.

الكلمات الرئيسية: الحركية , تفاعل الصوبنة , مزيج من الزيوت , الاولين والستيارين , نموذج رياضي .

1. INTRODUCTION

It has been said that the use of soap is a gauge of the civilization of a nation . Many literature were published in the field of saponification of various fats and fatty acids.**Frost and Schwemer**,**1952**. had studied the differential rate equations for the kinetics of competitive consecutive second – order reactions . Measurements of the rate of saponification of ethyl adipate and ethyl succinate were used to verify the theoretical approach . **Newberger and Kadlec** , **1973** had studied the kinetics of the saponification of diethyl adipate between 302K and 358K , for both stirred and tubular reactors . They had suggested numerical search method to verify the proposed model. **Vicente**, **et al.**, **2006**. Studied the kinetics of Brassica Carinata oil methanolysis . They found that the methanolysis reaction can be described as a pseudo – homogeneous catalyzed reaction , following a second – order mechanism for the forward and reverse reactions . They also found that higher temperature and catalyst concentrations increased the reaction rates . Appleton **Appleton**, **2007**, had published a handbook of soap manufacture . He had made a review of oils and fats and their saponification . He had presented the steps of soap – making even soap perfuming and molding . **Lab. Report** , **2012**, was presented to determine the order, rate constant , activation energy , and pre – exponential factor for the reaction of ethyl acetate with base using conductance measurements. An experimental study of the reaction kinetics of a simple homogenous liquid – phase system was published , **Chem. Eng. Lab.** , **2013**. The reaction kinetics of the saponification of isopropyl acetate with sodium hydroxide was presented.

There are some aspects of interest still need to be studied . Determination the order , rate constant and many other parameters in the saponification kinetics are of great importance . The objective of this research is to study the parameters that affect saponification reaction. These parameters can be used to model the reaction to a large – scale applications , enhance an existed production and adopt an optimum set of parameters for a new production .

2. THEORITICAL ASPECTS

2.1 Saponification Reaction

The saponification reaction is of the form

Fat + sodium hydroxide = soap + glycerol

The fat used is a mixture of olein and stearin with a ratio (3:1) . These fats are the most important ones from a soap –maker's point of view , **Appleton** , **2007** . Using (3:1) ratio ensures the product (soap) to be soft enough (by using olein) and solid enough (by using stearin) for toilet use. Appleton had published various types of fats and fatty acids . Olein (derived from olive and cotton – seed oil) is saponified according to the following reaction :

$$\underset{\text{olein}}{C_3H_5(C_{18}H_{33}O_2)_3} + \underset{\text{sodium hydroxide}}{3NaOH} = \underset{\text{sodium oleate (soap)}}{3NaO_2C_{18}H_{33}} + \underset{\text{glycerol}}{C_3H_5(OH)_3}$$

Stearin (derived from tallow) is saponified according to the following reaction :

$$C_3H_5(C_{18}H_{35}O_2)_3 + 3NaOH = 3NaO_2C_{18}H_{35} + C_3H_5(OH)_3$$

stearin sodium sodium stearate glycerol
hydroxide (soap)

Therefore; the chemical equation for saponification reaction can be represented by :

$$A + B = R + S$$

Where A , B refer to the reactants (fat and caustic soda) and R , S refer to the products (soap and glycerol). The reaction rate is , **Smith** ,**1981**.

$$r_A = k\ C_A\ C_B - k'\ C_R\ C_S$$

where : k is the forward reaction – rate constant
k' is the backward reaction – rate constant
C represents the molar concentration of the specified substance in (mol / l)

If an excess of NaOH solution is added , the reaction will be considered as irreversible , such as **Smith** , **1981**.

$$A + B \rightarrow R + S$$

and the rate equation will be :

$$r_A = k\ C_A\ C_B$$

Since the reaction is in liquid phase (constant volume),**Smith** , **1981**.

$$r_A = - dC_A / dt = k\ C_A\ C_B \tag{1}$$

2.2 Kinetics of Saponification Reaction

The kinetics study of this work consists of the following:

(i) Determination of the order of the reaction
(ii) Determination of the rate constant
(iii) Determination of the activation energy
(iv) Determination of the frequency factor or (pre - exponential) factor

under the variation of three parameters : the percentage excess of NaOH , the temperature and the stirring speed.

The basic relation in kinetics study is the concentration –time relation of the reactants. The concentration – time data can be detected using titration of samples and refractive indices determination.

2.3 Modeling the Rate Equation

Previous works that studied the kinetics of saponification reaction had either simplified the solution of the differential equation by approximation, **Lab. Report**, **2012** or solved it by iteration , **Newberger**, and **Kadlec** , **1973**.

In this work, the differential equation will be dealt as it is and solved with somewhat tedious integration method , as follows:

$r_A = - dC_A / dt = k\, C_A\, C_B$ (1)

The fractional conversion , x_A , is defined as :

$x_A = (C_{Ao} – C_A) / C_{Ao}$

Differentiation:

$- dC_A / dt = C_{Ao}\, dx_A / dt$ (2)

C_A and C_B are defined through x_A as:

$C_A = C_{Ao} (1 – x_A)$ (3)

$C_B = C_{Bo} – 3 (C_{Ao} - C_A)$ (4)

Where Eq. (3) is the stoichiometric factor and C_{Ao} , C_{Bo} are the initial concentrations of reactants A and B , respectively. Dividing Eq. (4) by C_{Ao} yields:

$C_B / C_{Ao} = C_{Bo} / C_{Ao} – 3(C_{Ao} - C_A) / C_{Ao}$

$C_B / C_{Ao} = C_{Bo} / C_{Ao} – 3\, x_A$

or $C_B = C_{Bo} – 3\, x_A\, C_{Ao}$ (5)

Substituting Eqs. (2) , (3) , and (5) into Eq. (1) , yields :

$C_{Ao}\, dx_A / dt = k\, C_{Ao} (1 – x_A) (C_{Bo} –3x_AC_{Ao})$

Dividing by C_{Ao} leads to:

$dx_A/dt= k\, (1–x_A)\, (C_{Bo}–3x_AC_{Ao})$ (6)

Separating the variables , yields :

$dx_A/(1–x_A)(C_{Bo}–3x_AC_{Ao})=kdt$ (7)

Integrating from $t = 0$, $x_A = 0$ to $t = t$ and $x_A = x_A$ yields :

$$\int \frac{\quad}{(\quad)(\quad)} \quad \int \tag{8}$$

Using fractional integration :

$$\frac{\quad}{(\quad)(\quad)} \quad \frac{\quad}{\quad} \quad \frac{\quad}{\quad} \tag{9}$$

Multiplying by ($1- x_A$) ($C_{Bo} – 3\, x_A\, C_{Ao}$), yields :

$1 = E\, (C_{Bo}–3\, x_A\, C_{Ao}) + F\, (1–x_A)$ (10)

$1 = E\, C_{Bo} - 3\, E\, x_A\, C_{Ao} + F – F\, x_A$

Equating the coefficients of x_A^o :

$1 = E\, C_{Bo} + F$ (11)

Equating the coefficients of x_A^1 :

$0 = -3\,E\,C_{Ao} - F$ (12)

Therefore; $F = -3\,E\,C_{Ao}$

Substituting into Eq. (11) , yields:

$1 = E\,C_{Bo} - 3\,E\,C_{Ao}$ (13)

or $E = 1 / (C_{Bo} - 3C_{Ao})$ (14)

and $F = -3\,C_{Ao} / (C_{Bo} - 3C_{Ao})$ (15)

Substituting Eqs. (14) and (15) into Eq. (9) , yields :

( ) ( ) ( ) ( ) ( ) ( )

and

∫ ( )( ) ( ) ∫ ( ) ( ) ∫ ( )

Substituting into Eq. (8) , yields :

( ) [∫ ( ) ∫ ( )] ∫

Integrating , yields :

( ) [( ) ( )]

or ( ) * +

so * +( )

is the proposed model . This model can be verified through the experimental work .

3. EXPERIMENTAL WORK

3.1 Apparatus

The apparatus used in this work consists of 1000 ml- beaker (modified with lower tapped glass tube to ensure the separation of the lower glycerol layer from the upper soap layer) , hot plate stirrer (RLABINCO , Model L-81,The Netherlands) . It's provided with two nobs ; one for controlling the temperature (100 - 150) ^{o}C and the other for controlling the stirring speed (400 – 1100) rpm . The apparatus also consists of thermometer (for measuring the actual temperature of the reacting mixture) , various glassware for preparation of solutions and titration of samples , Refractometer (Model Optika , no. 2WAJ SN 281006 , Italy) . The refractometer is used to measure the refractive index of the samples .

3.2 Materials

Materials used are : olein and stearin fats (source: Republic Company of Vegetable Oils) , sodium hydroxide (NaOH) solution (Aldrich mark) standardized against standard hydrochloric acid (HCl) solution (commercial grade) , **Vogel** , **1961**. , saturated solution of brine , distilled water .

3.3 Procedure

The procedure consists of the following steps:

1-Weighing the required amounts of fats then transferring them to the beaker.

2- Switch on the heater and stirrer and fixing them on certain values.

3-Adding an excess amount of sodium hydroxide solution with changeable percentage excess (10% - 100%).

4-Beginning the reaction for specified C_{Ao} and C_{Bo} .

5-Taking a sample every 5-10 minutes till the end of the reaction (soap formation). Samples were titrated against standard HCl solution using methyl orange as an indicator ,**Vogel** , **1961**. also the refractive indices were measured for these samples.

6-Adding distilled water to cool the reaction mixture and to suppress the froth of the soap when necessary .

7-Adding saturated brine solution to facilitate the separation of layers.

8-The soap was then molded, dried, and used.

4. RESULTS AND DISCUSSION

Experiments were performed at different levels of the three parameters (percentage excess of NaOH solution (10%-100%) , temperature (100-150) ^oC , and stirring speed (400-1100) rpm . Each experiment depicted a concentration – time curve . To calculate the order of the reaction and the rate constant , the differential method was adopted . This was achieved by calculating different slopes at different concentrations of tangent points of the concentration – time curve . These slopes represented dC_A/dt (reaction rate with respect to the limiting reactant A) . Taking the natural logarithms for each dC_A/dt and C_A , then drawing data gives a straight line of slope equal n_A (the order of the reaction with respect to A) and of intercept equals ln k. The inverse of ln k gives the experimental value of k (reaction – rate constant).**Table 1** shows a sample of concentration –time data for both reactant A and reactant B , with the refractive indices and conversions for run no.(4).**Fig.1** shows the concentration - time curve of reactant A. The curve shows decreasing of C_A with time until complete consumption. This is because reactant A is the limiting reactant . **Table 2** shows data for the slopes determined at the tangent points of **Fig. 1**. The data illustrate decreasing of slopes' magnitudes for the points . This means decreasing the rate of reaction with the concentration decrease, which indicates the progress of reaction. **Table 3** shows the logarithm of the rate of reaction ln ($-dC_A/dt$) with the logarithm of the concentration $\ln C_A$. **Fig. 2** depicted these data. It was shown that the order of reaction with respect to A is approximately 1. The value of the rate constant was also determined. These calculations were also done for the excess reactant B (NaOH solution) to find the order of the reaction with respect to it (n_B). **Fig. 3** traces the concentration - time profile of reactant B. It is clear that reactant B dose not tend to complete consumption , since it is the excess reactant. **Table 4** shows ($- dC_B / dt$) versus C_B data . Similarly , the rate of reaction decreased with decrease in concentration .**Table 5** shows the variation of ln ($-dC_B/dt$) with ln C_B .**Fig. 4** traces ln($-dC_B/dt$) against lnC_B. The relation is linear with slope equals n_B. Again the value of n_B is about 1 . Experimental results showed that the order of reaction for each reactant n_A , $n_B \approx 1$, so the overall order of reaction was second order . This result agreed with the fact that most of esterification reactions are second order .Saponification reaction is an example of these reactions. It was also noticed that the values of the refractive index RI decreases as the conversion increases. After approximately 50% conversion, the values of RI increases again. To explain this behavior, the relationship between RI and the density must be noticed. RI is a physical property that inversely proportional to density. As NaOH solution was added to the fat , the density of the fat is increased (RI is decreased).When the soap was produced the density again decreased (RI is increased). The concentration - time data were substituted in the mathematical model using conversions instead of concentrations.

Fig. 5 shows the relation between the expression ln D ($\frac{*}{\;} + \overline{\;\;\;}$) and time. The relation is linear with slope equal k_{calc} . The calculated values of the reaction-rate constant were somewhat deviate from the experimental ones. It was noticed that k values obtained from the mathematical model were overestimated when the percentage excess of NaOH solution were too low or too high. At medium levels of % excess of NaOH solution the calculated values of k were underestimated. This can be discussed as follows: at low values of % excess of NaOH solution , the reaction rate decreases because of the decreased concentration of NaOH giving reduced values of reaction –rate constant k_{exp} .This makes the calculated values be higher . High values of % excess of NaOH solution reduce the number of reacting molecules , as a result of hindering their movement , causing reduced values of k_{exp} again. This also makes k_{calc} be higher. The average error between experimental and calculated values of k was calculated by the following equation:

$$\text{Av. Error} = \frac{\Sigma \left(\frac{\;}{\;} \right)}{\;}$$

Where N is the number of runs . The average error was approximately 20%. This figure may be accepted because the experimental errors were thought to be lumped within it . Fortunately; the underestimated values of k_{calc} resulted from the mathematical model allow safe design and simulation calculations.

Fig. 6 shows the effect of increasing the percentage excess of NaOH solution on reaction – rate constants (k_{exp} and k_{calc}) . The calculated values trace lower curve than experimental ones except at approximately 100% excess . Evidently, increasing NaOH solution enhances the rate of reaction because it suppresses the backward reaction according to Le Chatelier rule .

The effect of temperature is presented in **Fig. 7** . The natural logarithms of k is plotted against the reciprocal of the absolute temperature . This figure shows a linear relation between ln k and 1/T as it was predicted by Arrhenius.

— (–)

where the slope (—) represents the negative value of the activation energy divided by the universal perfect-gas law constant . The intercept of the plot (ln A^o) determines the frequency factor . The values of the activation energy and the frequency factor were found to be as follows:

$E_{a\ exp}$ = -20.44 J.mol^{-1} and

A^o_{exp} =9.8358×10^{-5} l.mol^{-1}.min^{-1}

While $E_{a\ calc}$ = -4.67 J.mol^{-1} and

A^o_{calc} = 6.2×10^{-3} l.mol^{-1}.min^{-1}

The experimental and calculated values are different by an order of magnitude which is attributed to the experimental error .The value of the activation energy is rather low. This indicates that the reaction is fast since the activation energy represents the energy barrier that molecules must gain to reach the final product .

Fig. 8 shows the effect of stirring speed upon the rate constants. It is clear that the effect of stirring is considerable on the reaction rate. This leads to the conclusion that the reaction is mass - transfer controlled. This viewpoint agrees well with the notation of underestimated values of k_{exp} at high values of percentage excess of NaOH solution. Therefore; increasing stirring speed enhances the reaction rate. However, there is a constraint limited by the soap - froth rising .If the values of k_{exp} were normalized (i.e. making the total increase in k_{exp} corresponds 100%) as shown in **Table 6**. This was done for the runs that have only the excess ratio varied , i.e. the temperature and stirring speed were fixed . The normalization shows that percentage excess over 50% has less effect on the value of k_{exp} than the percentage excess below 50%. This may be attributed to the hindrance of reacting molecules by the NaOH molecules which confirms the mass- transfer control on the reaction.

5. CONCLUSIONS

- The % excess of NaOH solution plays an important role in the saponification reaction. 88% of increased value of the rate constant k can be achieved at 50% excess . Adding more solution of NaOH seems to be unnecessary and costing .

- The saponification reaction is mass – transfer controlled and stirring speed appears as an effective parameter , although excessive stirring may raise the froth of the soap .

- The derived mathematical model is adequately described the system especially at moderate values of % excess of NaOH solution .

- The mathematical model can be applied to scale – up the laboratory batch reactor to a large – scale continuously stirred tank reactor (CSTR).

REFERENCES

- Appleton, H.A.,2007, *The Handbook of Soap Manufacture* , Scott , Greenwood & Son , London.

- Chemical Engineering Laboratory,2013, *Saponification of Isopropyl Acetate with Sodium Hydroxide*, (Internet Document).

- Frost, A. A., and Schwemer, W. C.,1952, *The Kinetics of Competitive Consecutive Second Order Reactions:The saponification of Ethyl Adipate and of EthylSuccinate*, Journal of American Chemical Society, Vol.74, No.5, PP. 1268-1273.

-Laboratory Report, 2012 , *The Kinetics of the Saponification of Ethylacetate* , (Internet Document).

- Newberger , M. R., and Kadlec , R. H.,1973, *Kinetics of the Saponification of Diethyl Adipate*, American Institute of Chemical Engineers Journal ,Vol.19, No.5 , PP. 1272 - 1275 .

- Smith, J. M., 1981, *Chemical Engineering Kinetics* , 3rd ed. , Mc-Graw Hill.

- Vicente,G. , Martinez, M. , and Aracil, J., 2006, *Kinetics of Brassica Carinata Oil Methanolysis* , Energy Fuels ,Vol. 20,No.4 , PP. 1722 – 1726.

- Vogel, A.I.,1961, *Quantitative Inorganic Analysis* , 3rd ed. , Longmans.

NOMENCLATURE

A   limiting reactant (fat)

A^o frequency factor ($l \cdot mol^{-1} \cdot min^{-1}$)

B   excess reactant (NaOH solution)

C   concentration ($mol \cdot l^{-1}$)

D   expression (* +)

E   arbitrary constant

E_a activation energy ($J \cdot mol^{-1}$)

F   arbitrary constant

k forward reaction-rate constant   ($l \cdot mol^{-1} \cdot min^{-1}$)

k' backward reaction-rate constant($l \cdot mol^{-1} \cdot min^{-1}$)

N number of runs

n order of reaction

R product 1 (soap)

R_g universal gas-law constant (8.314 $J \cdot mol^{-1} \cdot K^{-1}$)

RI refractive index

r   reaction rate ($mol \cdot l^{-1} \cdot min^{-1}$)

rpm revolution per minute

S product 2 (glycerol)

T absolute temperature (K)

t time (min)

x fractional conversion (-)

Subscripts

$_o$ initial (C_{Ao} initial conc. of reactant A)

Table 1. Concentration – time data of reactant A (fat) with refractive indices and conversions for run no.(4) [%excess=50 , Temp.=100^{o}C , rpm=400].

t (min)	C_A (mol . l^{-1})	RI (-)	x_A (-)	C_B (mol . l^{-1})
0	0.3119	1.468	0	2.844
10	0.0815	1.42	0.7387	2.1528
20	0.0789	1.412	0.7471	2.1449
30	0.0577	1.428	0.8151	2.0813
35	0.0471	1.472	0.8490	2.0496
40	0.0259	1.52	0.917	1.986

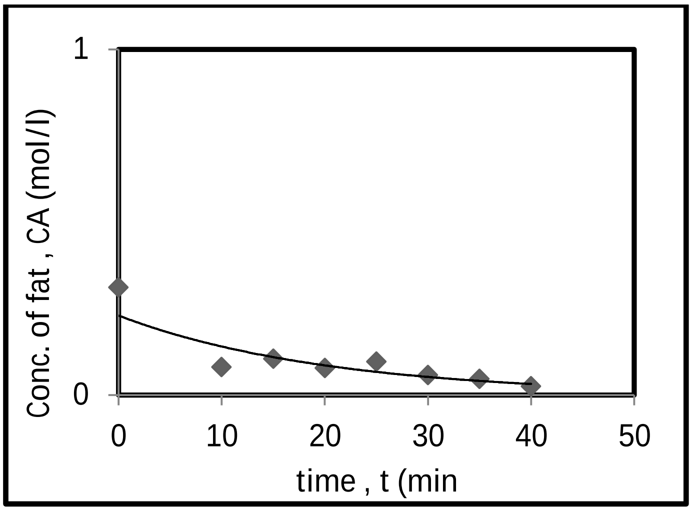

Figure 1. Concentration-time profile with respect to reactant A (fat) of run no.(4) [% excess=50 , Temp.=100^{o}C , rpm=400].

Table 2. Rate of reaction with respect to reactant A(slope) versus the concentration of A of run no.(4) [% excess=50 , Temp.=100^{o}C , rpm=400].

Slope (dC_A/dt)	C_A
-0.0115	0.22
- 0.0086	0.20
-0.0063	0.16
-0.0043	0.11

Table 3. Logarithm of reaction rate versus logarithm of concentration of reactant A (fat) of run no.(4) [% excess=50 , Temp.=100^{o}C , rpm=400].

$\ln(-dC_A/dt)$	$\ln C_A$
-4.4654	-1.5141
-4.7560	-1.6094
-5.0672	-1.8326
-5.4491	-2.2073

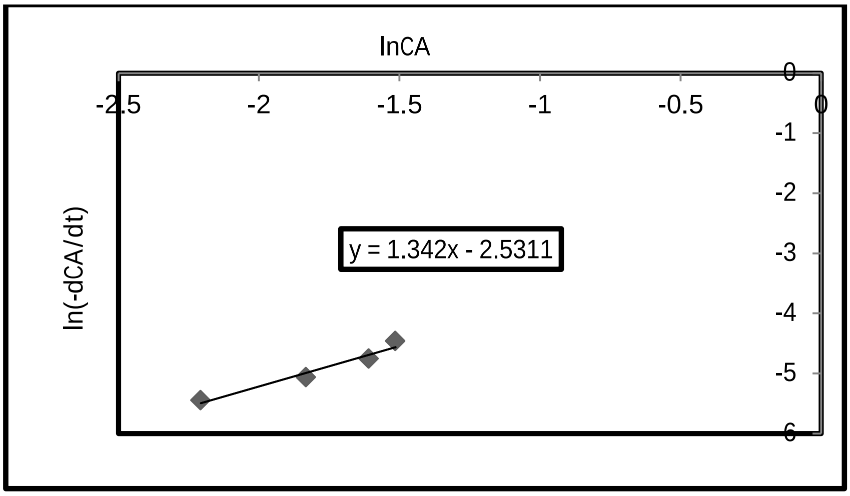

Figure 2. The linear relation between $\ln(-dC_A/dt)$ and $\ln C_A$ gives the order of reaction with respect to reactant A. n_A(slope) and $\ln k_{exp}$ (intercept) of run no. (4) [% excess=50 , Temp.=100^{o}C, rpm=400].

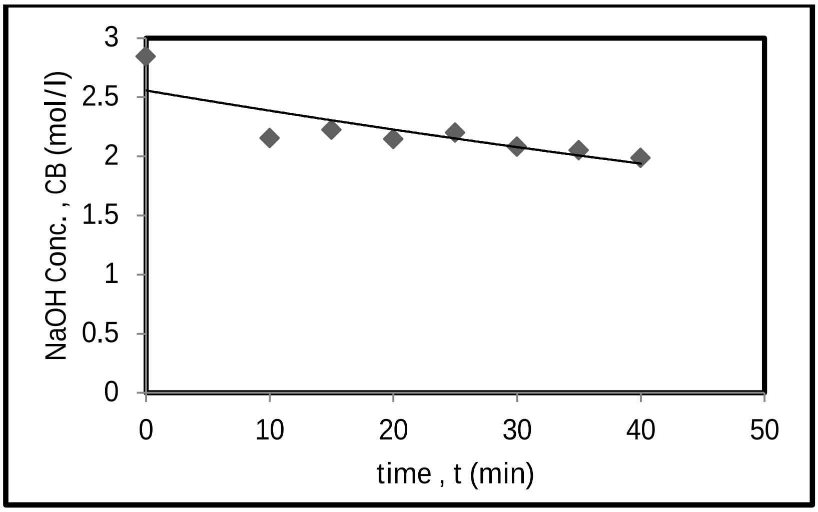

Figure 3. Concentration-time profile with respect to reactant B (NaOH solution) of run no. (4) [% excess=50 , Temp.=100^{o}C , rpm=400].

Table 4. Rate of reaction with respect to reactant B(slope) versus the concentration of B of run no.(4) [% excess=50 , Temp.=100^{o}C , rpm=400].

Slope (dC_B / dt)	C_B
-0.1556	2.5
-0.1183	2.0
-0.0942	1.7
-0.0740	1.2
-0.0663	1.1

Table 5. Logarithm of reaction rate versus logarithm of concentration of reactant B(NaOH solution) of run no. (4) [% excess=50, Temp.=100^{o}C , rpm=400]

$\ln(-dC_B/dt)$	$\ln C_B$
-1.86	0.92
-2.13	0.69
-2.36	0.53
-2.60	0.18
-2.71	0.10

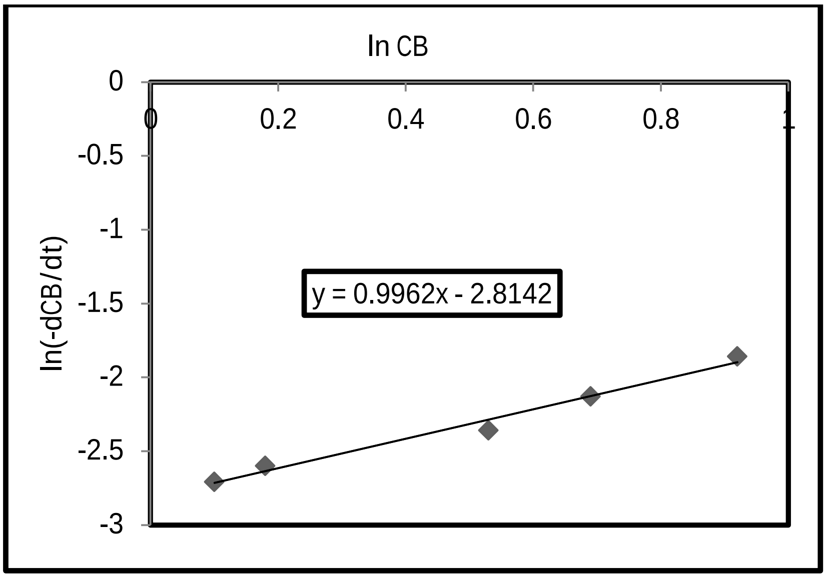

Figure 4 . The linear relation between ln ($-dC_B/dt$) and ln C_B gives the order of reaction with respect to reactant B n_B (slope).

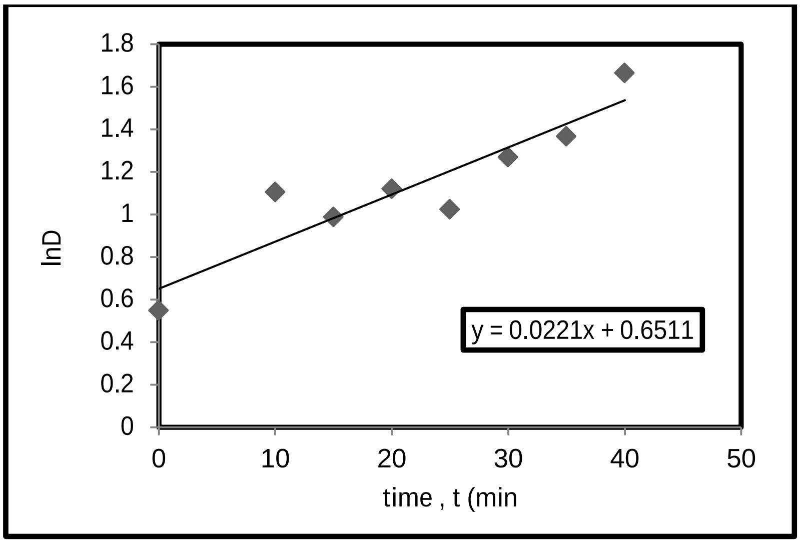

Figure 5. The proposed model shows linearity between ln D (*————+) and time with C_{Ao} and C_{Bo} of run no. (4) the slope determines $k_{calc.}$

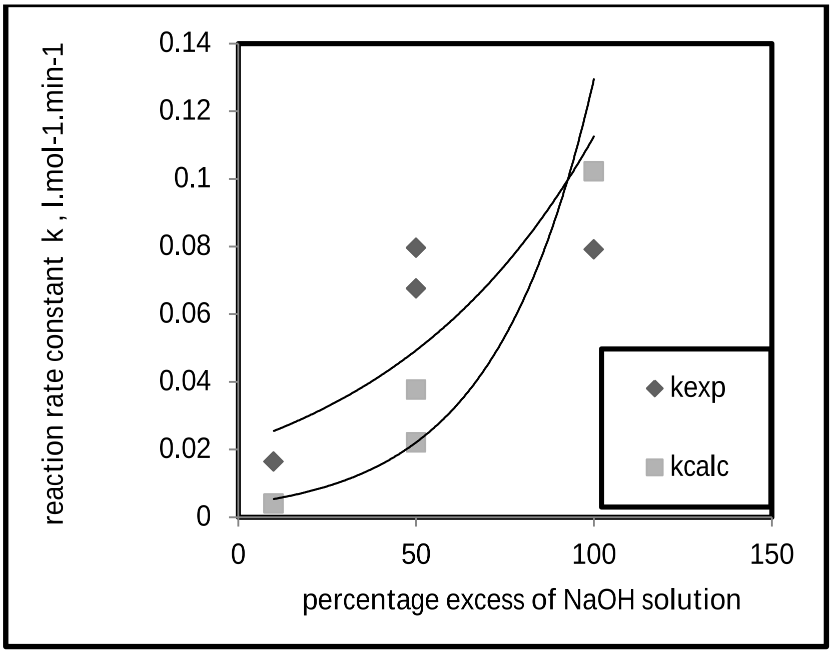

Figure 6. The effect of % excess of NaOH solution on the experimental and calculated reaction - rate constants k_{exp} and $k_{calc.}$

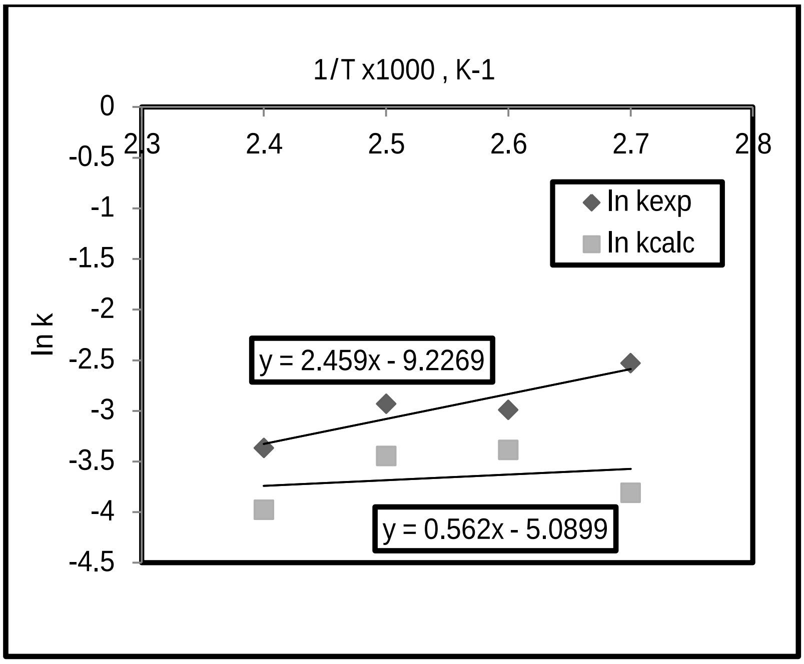

Figure 7. Plot of Arrhenius equation for saponification of mixed olein and stearin with NaOH solution .The slope gives($-E_a/R_g$) and the intercept gives ln $A^{o.}$

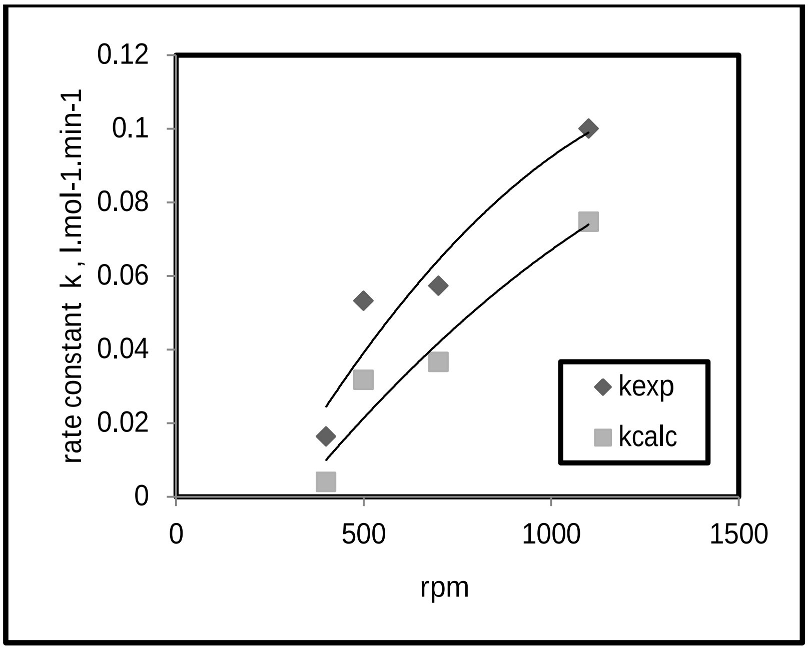

Figure 8. The effect of stirring speed on the experimental and calculated reaction- rate constants.

Table 6. The effect of % excess of NaOH solution on the value of k_{exp}

%excess	Temp. (^oC)	rpm	k_{exp} ($l.mol^{-1}.\ min^{-1}$)	% increase in k_{exp}
10	100	400	0.0164	0
50	100	400	0.0716	88
100	100	400	0.0791	100

Analysis and Control of PWM Buck-Boost AC Chopper Fed Single-Phase Capacitor Run Induction Motor

Prof. Dr. Jafar H. Alwash
Engineering College
Baghdad University

Asst. Prof. Dr. Turki K. Hassan
Engineering College
Al-Mustansiriya University
E-mail: thassan2013@yahoo.com

Shams W. Kamel
Engineering College
Baghdad University
E-mail: shams.201057@yahoo.com

ABSTRACT

Single phase capacitor-run induction motors (IMs) are used in various applications such as home appliances and machine tools; they are affected by the sags or swells and any fault that can lead to disturb the supply and make it produce rms voltage below or above the rated motor voltage, which is 220V. A control system is designed to regulate the output voltage of the converter irrespective to the variation of the load and within a specific range of supply voltage variation. The steady-state equivalent circuit of the Buck-Boost chopper type AC voltage regulator, as well as the analysis of this circuit are presented in this paper. Switching device for the regulator is an IGBT Module. The proposed chopper uses pulse width modulation (PWM) control technique to chop the input voltage into segments in order to guarantee rated rms voltage supplied to the load, which is capacitor-run induction motor. Proportional integral (PI) controller is used to obtain very small steady state error, stable and fast dynamic response, and robustness against variations in the line voltage. The complete system is simulated using software package, and the results are obtained to verify the proposed control method.

Keywords:- AC chopper, voltage controller, pulse width modulation, duty cycle, damped input filter.

تحليل وسيطرة لمنظم الفولتية المتناوبة الخافض- الرافع لسواقة محرك حثي احادي الطور ذو متسعة دائمة العمل

أ. د. جعفر حميد علوش
كلية الهندسة
جامعة بغداد

أ. م. د. تركي كحيوش حسن
كلية الهندسة
جامعة المستنصريه

شمس وائل كامل
كلية الهندسة
جامعة بغداد

الخلاصة

ان المحركات الحثية الاحاديه الطور ذات المتسعة الدائمة العمل، شائعة الاستخدام في التطبيقات المختلفه مثل بعض الاجهزة الكهربائية المستخدمه داخل البيت والمكائن، والتي تتاثر بالانخفاض اوالارتفاع بالفولتية او اي خطأ يحصل بالنظام والذي ممكن ان يؤدي الى ارباك مصدر الفولتيه ويجعله يولد متوسط قيمة فعالة مقدارها ادنى او اعلى من القيمة المطلوبة لتشغيل المحرك بصورة طبيعية، والتي مقدارها (220فولت). نظام السيطرة المقدم في هذا البحث تم تصميمة لتعديل الفولتية المسلطة على الحمل ضمن مدى معين من التغير في فولتية المصدر برغم التغير بالحمل.الدائرة المكافئة للمنظم الرافع-الخافض في الحالة المستقرة وكذلك طريقة التحليل لدائرة الخافض-الرافع للفولتية المتناوبه تم عرضها في هذا البحث. المفتاح المستخدم بجهاز السيطرة يمثل بالحقيقة مفتاح قدرة الكتروني شبة موصل نوع (IGBT Module). منظم الفولتيه المقترح يستخدم طريقة التحكم بعرض الموجة (PWM) للسيطرة على الفولتية الداخلة واعادة توليدها وفق مديات محددة لضمان القيمة المطلوبة للفولتية المسلطة على الحمل المتمثل بالمحرك الاحادي الطور ذو المتسعة دائمة العمل. في هذا البحث تم استخدام المسيطر نوع تناسبي تكاملي (PI) حيث ان هذا المسيطر يوفر الحصول على نسبة خطأ قليلة للتخلص من الفرق بين فولتية المصدرالمعرضة للخطأ والفولتية المطلوب الثبات عند قيمتها بسرعة استجابة عالية ويجعل سير العمل مستقر ومتين ضد اي اختلال يحصل بفولتية المصدر. تمت محاكاة النظام المصمم ككل نظريا باستخدام (Matlab/Simulink)، وتم الحصول على النتائج لتاييد صلاحية النظام المقدم.

كلمات رئيسية:- مقطع الجهد المتناوب، منظم فولتية، التحكم بعرض الموجة، الزمن الدوري للمقطع، مرشح الدخول المثبَط.

1. INTRODUCTION

Single-phase capacitor-run (IMs) are widely used because they have good power factor and efficiency under load. It is required to develop the methods of controlling its operation to reach the best performance. Several methods exist for variable speed operation of a single-phase(IMs). Considering simplicity and low cost, most common type is the line-frequency AC choppers, which can be found as a conventional phase-controlled AC controllers using thyristors, which have the advantages of simplicity of the control circuit and large power capability. However, these have the inherent drawbacks that power factor decreases when the firing angle increases and that, since the content of the line current harmonics is relatively large, the size of the passive filter circuit becomes bulky. There are also other methods which use a tapped winding transformer to regulate the input voltage to a lower or higher output voltage. However, because the winding ratio is changed by servo motor or by manual regulation, it has low regulation speed, **Kwon, et al., 1996** and **Nan, et al., 2009**.

The PWM Buck-Boost AC chopper can overcome all these drawbacks and guarantee the best control for this kind of motors since it offers several advantages such as sinusoidal input current, fast dynamics, and significant reduction in filter size. In addition the problems caused by the sags or swells of the input voltage can be solved by proposing voltage controller which uses output peak voltage as feedback signal and adopts proportional integral (PI) control strategy to regulate the output voltage, **Kown, et al., 1999**.

The object of this paper is to present the analyses and design of PWM AC chopper circuit suitable to drive a single phase capacitor run induction motor.

2. CIRCUIT CONFIGURATION AND PRINCIPLE OF OPERATION

The basic circuit configuration of the Buck-Boost AC converter is shown in **Fig.1**. It can operate directly from the single-phase line (source) voltage *vs* and regulate the output voltage higher or lower steplessly, by using two bidirectional standard switches modules capable of bidirectional current control and regenerative DC snubbers consisting of capacitor only C_b, to absorb bidirectional turn-off spike energy due to line stray inductance. The input filter consisting of inductor L_i and capacitor C_i , absorbs the harmonic currents. The used bi-directional switch module is composed of two insulated gate bipolar transistors (IGBT). The switches S_1, S_2, S_3 and S_4 are unidirectional. The inductor L is used to store the input energy and transfer it to the output side, the filter capacitor C_o at the output side reduces the output voltage ripple, **Kown, et al., 1999**.

A switching policy solving the commutation problem is based on the polarity of the switch-to-switch voltage v_t across two bidirectional switches: two unidirectional switches S_3 and S_4 are additionally turned on during the positive period of v_t and the switches S_1 and S_2 during the negative period of v_t, to avoid voltage spikes, without affecting the value of the duty ratio (D). Then the inductor current is bypassed through the input side or output side, depending on its direction during the dead-time. The control of the switches is based on the symmetrical PWM techniques. This ensures that the output voltage is sinusoidal for a sinusoidal AC input voltage. The output voltage is controlled by changing the duty cycle of the control pulses. Three modes of operation are possible during one switching cycle for $v_t>0$:

1. Charging mode; the inductor current flows through the input side via S_1 and the diode across S_3 for $i_L>0$, or S_3 and diode across S_1 for $i_L<0$.
2. Discharging mode; the inductor current flows through the output side via S_4 and the diode across S_2 for $i_L>0$, or S_2 and the diode across S_4 for $i_L<0$.
3. Dead-time mode; the inductor current is bypassed through the input or output side depending on its direction.

Fig. 2a-c show the inductor current and voltage waveforms for $v_t > 0$ during one switching cycle. The inductor voltage v_L is v_i during the charging mode and v_o during the discharging mode as shown in **Fig. 2b** and **c.** Because the switches S_3 and S_4 are turned on for $v_t > 0$, the inductor voltage v_L is v_o or v_i, according to the direction of i_L during the dead-time mode, **Kim, et al., 2011**.

3. ANALYSIS

To facilitate the analytical procedure in order to obtain an equivalent circuit for the buck-boost AC chopper, all components are assumed ideal and the switching frequency f_s is much greater than the line frequency f, so that during a switching period, the input and output voltage can be cosidered constant. The average inductor voltage during one switching period $T_s = 1/f_s$ is given by, **Kown, et al., 1999**:

$$v_L(t) = Dv_i(t) - (1-D)v_o(t) \tag{1}$$

Where $v_i(t)$ and $v_o(t)$ are the average AC input voltage and output voltage, respectively, during the switching period, and D is the duty ratio. The inductor voltage is given by:

$$v_L(t) = L\frac{di_L(t)}{dt} \tag{2}$$

Where $i_L(t)$ is the average inductor current during the switching period. If charging the inductor by the input current will take a time equals to (T_{on}), then discharging the inductor current to the load can be represented by the following equation:

$$i_o(t) = (1-D)i_L(t) \tag{3}$$

Where:

$$i_i(t) = Di_L(t) \tag{4}$$

Where $i_o(t)$ and $i_i(t)$ are the average output and input current respectively. From Eqs. (1) and (2), the following equation is obtained:

$$Dv_i(t) = L\frac{di_L(t)}{dt} + (1-D)v_o(t) \tag{5}$$

Substituting Eq. (3) in Eq. (5), yields:

$$\frac{D}{1-D}v_i(t) = \frac{L}{(1-D)^2}\frac{di_o(t)}{dt} + v_o(t) \tag{6}$$

Eq. (6) represents the steady-state equivalent circuit for the chopper type voltage regulator. The equivalent circuit is shown in **Fig.3**. At steady-state motor impedance including (R_o and X_o)

varies according to the load applied to the motor which is 175W single phase capacitor-run induction motor. From the equivalent circuit shown in **Fig.3**, the transfer function of the output voltage $V_o(s)$ with respect to the input voltage $V_i(s)$ is obtained as, appendix A, **Kamel, 2013**:

$$\frac{v_o(s)}{v_i(s)}=\frac{D(1-D)(R_o+sL_o)}{s^3LL_oC_o+s^2LC_oR_o+s[L+(1-D)^2L_o]+(1-D)^2R_o} \tag{7}$$

From Eq. (3) and Eq. (7), Eq. (8) is obtained

$$\frac{I_L(s)}{V_i(s)}=\frac{D[s^2L_oC_o+sC_oR_o+1]}{s^3LL_oC_o+s^2LC_oR_o+s[L+(1-D)^2L_o]+(1-D)^2R_o} \tag{8}$$

The source current $I_s(s)$ and source voltage $V_s(s)$ are obtained as

$$I_s(s)=DI_L(s)+I_{ci}(s)$$

$$=V_i(s)\cdot\left[\frac{D^2[s^2L_oC_o+sC_oR_o+1]}{s^3LL_oC_o+s^2LC_oR_o+s[L+(1-D)^2L_o]+(1-D)^2R_o}+sC_i\right] \tag{9}$$

$$\mathrm{v}_s(s)=sL_i\mathrm{I}_\mathrm{s}(\mathrm{s})+\mathrm{v}_\mathrm{i}(\mathrm{s})$$

$$=V_i(s)\cdot\left[\frac{sL_iD^2[s^2L_oC_o+sC_oR_o+1]}{s^3LL_oC_o+s^2LC_oR_o+s[L+(1-D)^2L_o]+(1-D)^2R_o}+s^2L_iC_i+1\right]$$
(10)

From Eq. (9) and Eq. (10), the following relation is obtained for simplicity:

$$\frac{Vs(s)}{Is(s)}=\frac{a_5s^5+a_4s^4+a_3s^3+a_2s^2+a_1s+a_0}{b_4s^4+b_3s^3+b_2s^2+b_1s+b_0} \tag{11}$$

Where: $a_5=C_iL_iLL_oC_o$, $a_4=LL_iC_oC_iR_o$, $a_3=[D_2L_iL_oC_o+L_iC_i[L+(1-D)^2L_o+LL_oC_o]$, $a_2=[D^2L_iC_oR_o+C_iL_i(1-D)^2R_o+LC_oR_o]$, $a_1=[L_iD^2+L+(1-D)^2L_o]$, $a_o=(1-D)^2R_o$, $b_4=C_iC_oLL_o$, $b_3=LC_oC_iR_o$, $b_2=[D^2L_oC_o+C_i[L+(1-D)^2L_o]]$, $b_1=[D^2C_oR_o+(1-D)^2C_iR_o]$, $b_o=D^2$

Under an appropriate selection of the parameters L, L_i, C_o and C_i satisfying a_5 a_4 a_3 a_2 b_4 b_3 b_2 b_1 0, Eq. (10) can be approximated as follows:

$$\frac{\mathrm{Vs(s)}}{\mathrm{Is(s)}}\approx\frac{s[L_iD^2+L+(1-D)^2L_o]+(1-D)^2R_o}{D^2}$$

[ ] (12)

From Eq. (12), the angle of the power factor is given by

$$\theta \approx \tan^{-1}\frac{\omega[L_i D^2 + L + (1-D)^2 L_o]}{(1-D)^2 R_o}$$

$$\frac{[\qquad\qquad]}{} \tag{13}$$

Where is the angular frequency of the source voltage.
Derivation of equations: (7, 8, 9, 10 and 12) are shown in appendix A, **Kamel, 2013**.

4. DESIGN OF INPUT AND OUTPUT FILTERS AND VOLTAGE CONTROLLER

For fast dynamic response the voltage controller, which uses the output peak-voltage as the feedback signal, is designed to keep the stability of the output voltage in case of input voltage fluctuation. The peak-voltage detector system is shown in **Fig.4**. Where v_o is the rms voltage across the load terminals, v_{od} is the sensed output of the proposed detector, k_d is the detection gain and V_o is the peak value of the output voltage. A fast detection technique is composed of a phase shifter, two multipliers, and an adder. The detection technique utilizes the simple trigonometric principle as follows, **Kown, et al., 1999** :

(14)

The sensed output v_{od} is:

(15)

When the disturbed input v_i , is applied to the system, the sensed output v_{od} (disturbed by the disturbance input) needs to be regulated to a desired constant reference V_r with no steady-state error where V_r is $k_d^2 V_{or}^2$ and V_{or} is the peak value of the desired output voltage. A good response is obtained by using a traditional PI controller. The integral part of the designed controller makes the steady-state output voltage error zero. The controller output is duty ratio D, **Nan, et al., 2009**:

$$\int \tag{16}$$

Where k_p and k_i are proper proportional and integral gains respectively. Δv is the controller input:

$$\Delta v = V_r - v_{od} \tag{17}$$

A filter must be added at the power input of a switching converter for improving power quality and interface issues. Low pass input LC filter needs to be damped at the corner frequency fc to prevent the gain of the filter to go to infinity otherwise, this rise would cause extreme current peaks which would make the system worse than if it was without filter. Taking into account only the dominant harmonic, the input current of the converter is represented with good approximation by, **Barbi, et al., 1991**:

(18)

Where I_{ip} is the peak value of the input current, thus,

(19)

The role of the input filter is to prevent the harmonic current i_h from circulating through inductor L_i . According to the harmonic equivalent circuit shown in **Fig.5**:

(20)

According to the usual specification, the total harmonic distortion (THD) of the input current i_i is ≤ 5%. Then reducing the value of i_{Lhp} (which is the maximum harmonic current circulating through inductor L_i) to 3% of input current, the THD ≤ 5% is ensured, **Barbi, et al., 1991**

=> , where

then using Eq. (20):

(21)

rad/s, where

f_s=25KHZ, Let L_i=0.5mH , then

F. A value of 3µF is chosen.

A damped filter made with a resistor R_d in series with a capacitor C_d as shown in **Fig.6**, all connected in parallel with the filter's capacitor C_i. The purpose of resistor R_d is to reduce the output peak impedance of the filter at the cutoff frequency. The choice of C_d ,that leads to the minimum peak output impedance, for a given value of R_d can be expressed as following:

For C_d =20µF, then

=> n=6.7 , the optimum damping resistance value R_d is equal to, **Erickson, 1999**:

≈ 6Ω (22)

The filter high-frequency attenuation is not affected by the choice of C_d and the high-frequency asymptote is identical to that of the original undamped filter, **Erickson, 1999**. The energy storage inductor L is used to store the energy from the source during the active mode of the chopper operation, then transfer it to the load during the discharging mode. During one switching period T_s, inductor must be satisfied such that, **Li, et al., 2011**:

(23)

With maximum value of duty ratio evaluated from, **Li, et al., 2011**:

$$(\quad) \qquad (24)$$

$$= 0.578$$

And for typical values of output current = 1.4A, **Kamel, 2013**, η (convertor efficiency)=90%, k_c (ripple coefficient of inductor current) ≤0.5, **Li, et al., 2011**. The boundary L_{min} =1mH, for $L \geq L_{min}$., the convertor operates in continuos conduction mode(CCM). A value of 1mH is chosen. Output filter capacitor is used to reduce the output voltage ripple and harmonics. During one T_s , to limit the output voltage ripple ,output filter capacitor C_o must satisfy the following, **Li, et al., 2011**:

With k_v (ripple coefficient of output voltage) ≤0.1, **Li, et al., 2011,** the boundary C_{omin} equals to 1.43μF, for C_o more than or equal to C_{omin} ($C_o \geq C_{omin}$); A value of 10 μF is chosen in the simulation to ensure output voltage without harmonics.

5. SIMULATION RESULTS

To show the feasibility of the proposed analysis method and control strategy, the simulation model of the proposed voltage regulator is implemented using Matlab/Simulink software. The induction motor whose its specifications shown in **Table 1** and its measured parameters listed in **Table 2** are used in the simulation, **Kamel, 2013**. THD values for current input to the chopper and motor input current and voltage are listed in **Table 3** (the values are obtained by using Matlab/Simulink).

5.1 Results for Sudden Change of Supply Voltage from (220V rms) Value to (160V rms) Value

At normal operation the supply produces rms voltage equals to the rated voltage (220V); if suddenly a disturbance occurred in the system leads to drop the voltage to (160V) rms value, then the voltage controller will detect it and the AC chopper will regulate the dropped voltage to be the same as the rated voltage needed by the motor.

5.1.1 No-load condition

Fig. 7 shows the simulated waveform of the supply voltage and load voltage at no-load and at source main frequency of 50HZ. In this figure it is shown that after (0.5sec), the load voltage dropped then increased gradually within (60msec) to reach its rated (rms value =220V) with low THD equals to (0.35%) even if the supply continues on the low level (160V). **Fig. 8** shows the simulated waveform of the supply current which has rms value equals to (1.76A), with (THD = 4.09%). **Fig. 9** shows the simulated waveform of the motor input current, the disturbance occured at (0.5sec), current decreased temporarily (since voltage across load terminals dropped temporarily) then gradually increased to reach (rms value = 0.56A). Motor speed is shown in **Fig. 10**, at no-load motor runs at (1500rpm), after the disturbance occurred, the motor speed dropped temporarily corresponding to the drop in load voltage, then the motor returns to run at no-load speed.

5.1.2 **Full-load condition**

The simulated waveforms of the supply voltage and load voltage at full-load are the same as those shown in **Fig.7**, since same drop in supply voltage occurred at (0.5sec). The load terminals still receive rated (220V) rms value, with low THD equals to (0.51%) even if the supply continues on the low level (160V). **Fig. 11** shows the simulated waveform of the supply current which has (rms value =2.40A) at steady state operation; then if the disturbane occurred at (0.5sec) and input voltage dropped to (160V) rms value, then current drawn from the supply equals to (2.68A) rms value, with (THD =4.47%). **Fig. 12** shows the simulated waveform of motor input current, the disturbance occured at (0.5sec), current decreased temporarily (since voltage across load terminals dropped temporarily), then increased gradually to reach rms value close to (1.40A). Motor speed is shown in **Fig. 13**, full-load motor runs at (1240rpm) after the disturbance occurred at (0.5sec) motor speed dropes temprorily then increased (corresponding to the load voltage variation) until motor returns to run at speed of (1240rpm).

5.2 Results for Sudden Increase of Supply Voltage from (220V rms) Value to (280V rms) Value

At normal operation the supply produces rms voltage equals to the rated voltage (220V); if suddenly a disturbance occurred in the system leads to increase the voltage to (280V) rms value, then the voltage controller will detect it and the AC chopper will regulate the voltage to be same the rated voltage needed by the motor.

5.2**.1 No-load condition**

Fig.14 shows the simulated waveform of the supply voltage and load voltage at no-load and at source main frequency of 50HZ. In this figure it is shown that after (0.5sec), the load voltage increased then dropped gradually within (40msec) to reach its rated rms value (220V) with THD (measured from Matlab/Simulink) equals to (0.40%) even if the supply continues on the high level (280V). **Fig.15** shows the simulated waveform of the supply current which has (rms value = 1.76A); at (0.5sec) the supply is disturbed and input voltage is increased to (280V) rms value, then current drawn from the supply equals to (2.12A) rms value. **Fig.16** shows the simulated waveform of the motor input current, the disturbance occured at (0.5sec), current increased temprorily then returned to the rms value (0.56A). Motor speed is shown in **Fig.17**, at no-load motor runs at (1500rpm), after disturbance occurred at (0.5sec) motor speed exceeds (1528rpm) temprorily, corresponding to the increase in load voltage.

5.2.2 **Full-load condition**

The simulated waveforms of supply voltage and load voltage at full-load are the same as those shown in **Fig.14** and at source main frequency of 50HZ. In this figure it is shown that after (0.5sec), the load voltage increased then decreased gradually to reach its rated rms value (220V) with low THD equals to (0.70%) even if the supply continues on the high level (280V). **Fig.18** shows the simulated waveform of the supply current which has rms value equals to (2.40A); at (0.5sec) the supply is disturbed and input voltage is increased to (280V) rms value, then current drawn from the supply equals to (2.68A) rms value, with (THD =4.24%). **Fig.19** shows the simulated waveform of the motor input current, at full-load motor draws rated (rms value =1.41A), when the disturbance occured at (0.5sec), current increased temprorily then returned to its rated value. Motor speed is shown in **Fig.20**, at full-load motor runs at (1240rpm), after disturbance occurred at (0.5sec) motor speed increased to (1320 rpm) temprorily, corresponding to the increase in load voltage, then the motor returns to run at its full-load speed again. Total harmonic distortion (THD) for input current, load current and voltage across the load terminals after disturbing input voltage at (0.5sec) are shown in **Table 3** (The values of (THD) are obtained by using Matlab/Simulink software); it is seen that the design of input filter ensures that (THDi < 5%), also load current and load voltage has a low value of (THD) since the output filter is well designed. **Table 4** illustrates how the input power (W) that is drawn from the source, varies with the line power factor which is measured by using Matlab/Simulink, depending on the equation: $p.f = P/(P^2+Q^2)^{1/2}$, where P and Q are active and reactive input powers respectively and *p.f* is the input power factor.

6. CONCLUSION

The analysis of Buck-Boost AC chopper circuit, that can regulate output voltage higher or lower steplessly is presented. The input current is sinusoidal waveform with low harmonic components. The output voltage control system is designed using PI control method and the peak-voltage detector. The simulation results show that the voltage controller has a good dynamic performance when input voltage swells or sags occur, since the output voltage returns to its normal value of (220V) rms value after no more than three cycles (60msec). The results show low total harmonic distortion factor for input current, load current and load voltage. The AC chopper achieves an acceptable line power factor at full load with low input voltage, since *(D*) will be increased, according to Eq. (13), the motor needs a power (175W) to run at full load, but the power drawn from the source is higher, the difference represents the losses since in the construction of the motor the resistances of its windings are very high, appendix B, **Kamel, 2013**.

REFERENCES

Barbi, Fagundes, J. *C.*, and Kassick, E. V., 1991, *A Compact AC/AC Voltage Regulator Based on An AC/AC High Frequency Flyback Converter*, IEEE Power Electronics Specialists Conference 22nd Annual, pp. 846-852.

Erickson, R.W., 1999, *Optimal Single Resistor Damping of Input Filters*, IEEE Applied Power Electronics Conference and Exposition, 14th Annual , Vol.2, pp.1073-1079.

Kamel, S. W., 2013, *Analysis of Buck-Boost AC Chopper Fed Capacitor Run Induction Motor*, A thesis submitted in fulfillment of requirements for award of the Master of engineering, Electrical Department, Engineering College, University of Baghdad.

Kim, J.H., Min, B. D., Kwon, B. H., and Won, S. C., 2011, *A PWM Buck-Boost AC Chopper Solving the Commutation Problem*, IEEE Trans. on Indust. Electronics, Vol.45, No. 5.

Kown, B. H., Youm, J. H., and Choi, J. H., 1999, *Automatic Votage Regulator with Fast Dynamic Speed*, IEEE Proc.-Elect., Power Appl.Vol. 146. No.2.

Kwon, B.-H., Min, B.-D., and Kim, J.-H., 1996, *Novel Topologies of AC Choppers*, IEEE proc. –Elect, Power Appl, Vol 143, No. 4.

Li, L., Yang, J., and Zhong, Q., 2011, *Novel Family of Single-Stage Three-Level AC Choppers*, IEEE Trans. on Power Electronics, Vol.26, No. 2.

Nan, J., Hou-jun, T., Wei, L. and Peng-sheng, Y., 2009, *Analysis and Control of Buck-Boost Chopper Type AC Voltage Regulator*, IEEE Power Electronics and Motion Control, 6th International Conference, pp.1019-1023.

NOMENCLATURE

C_b = snubber capacitor, μF.
C_d = damping capacitor, μF.
C_i = input capacitor, μF.
C_o = output capacitor, μF.
D = duty ratio.
f = main frequency, Hz.
f_c = corner frequency, Hz.
f_s = switching frequency, Hz.
i_1 = output capacitor current, A.
i_2 = load current, A.
i_{Ci} = input capacitor current, A.
i_h = harmonic current, A.
I_{hp}= peak harmonic current, A.
$i_i(t)$ = average input current during the switching period, A.
I_{ip} = peak converter input current, A.
$i_L(t)$= average inductor current during the switching period, A.
I_{Lhp}= peak harmonic current in input inductance, A.
$i_o(t)$ = average output current during the switching period, A.
i_s = source current, A.
k_c = ripple coefficient of inductor current.
k_d = detection gain of the output voltage.
k_p , k_i = proportional and integral gains respectively.
k_v = ripple coefficient of output voltage.
L = energy storage inductor, mH.
L_i = input inductor, mH.
R_d= damping resistance, Ω.
R_o= resistance of the load, Ω.
S_1= first unidirectional switch.
S_2= second unidirectional switch.
S_3= third unidirectional switch.
S_4= forth unidirectional switch.
T_s = one switching period, s.
$v_i(t)$= average input voltage, V.
$v_L(t)$= average inductor voltage, V.
$v_o(t)$= average output voltage, V.
v_{od} = detected output peak-voltag, V.
v_r = reference voltage, V.
v_s = source voltage, V.
v_t = switch-to-switch voltage across two bidirectional switches, V.
X_o =inductance of the load, Ω.
Z_o= output impedance, Ω.
η= conversion efficiency.
θ= input phase angle.

θ_o= output phase angle.
ξ= damping factor.
= angular frequency of the source voltage, rad/s.
$_s$= angular switching frequency, rad/s.

9 FIGURES AND TABLES

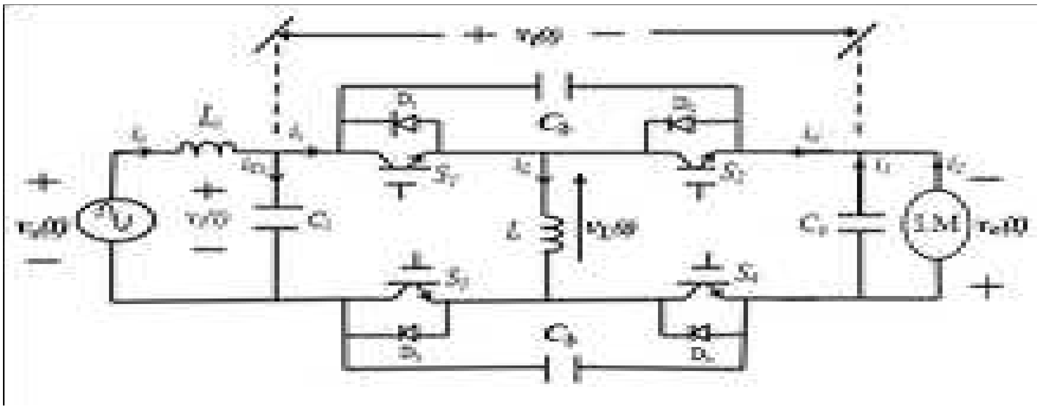

Figure1. Buck-boost AC chopper circuit configuration.

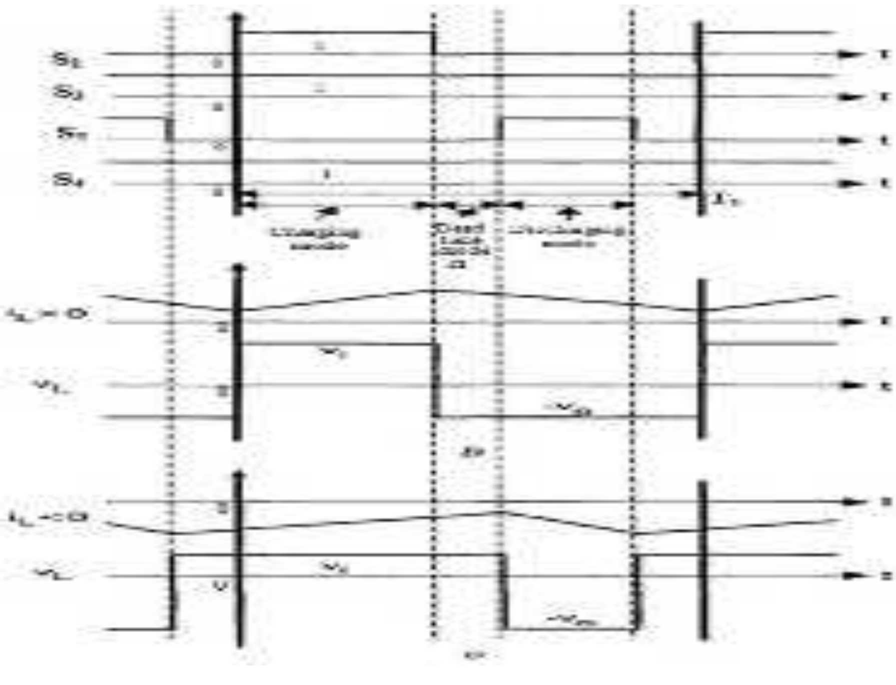

Figure 2. a.Gate signals, b. Inductor current and voltage waveforms for v_t>0, i_L>0 during one switching cycle,c. i_L and v_L for i_L<0.

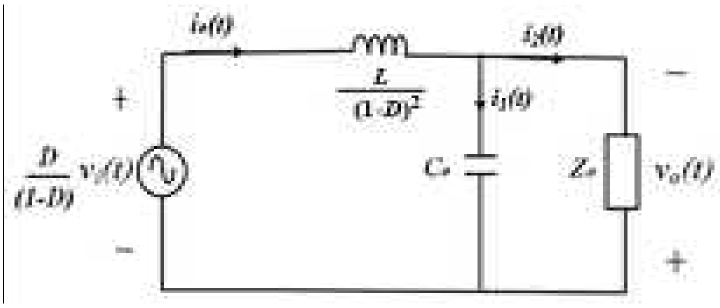

Figure 3. Steady state equivalent circuit of buck-boost AC chopper.

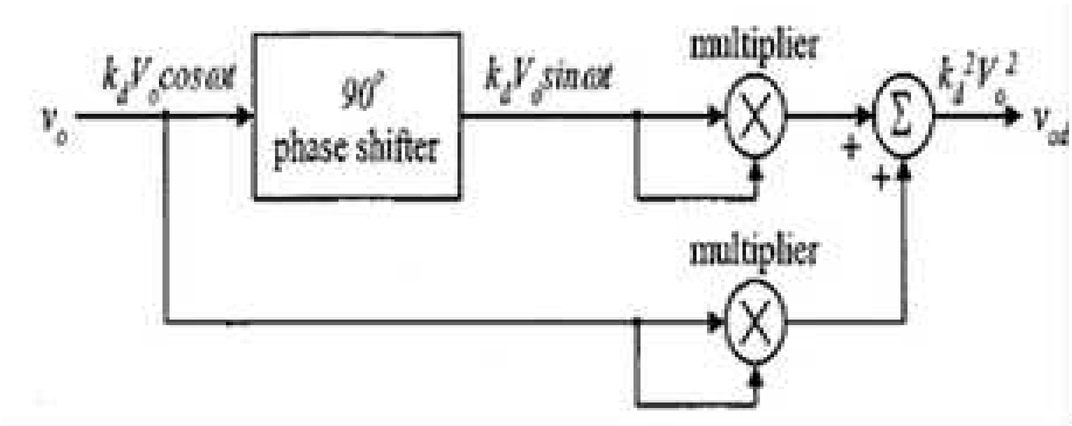

Figure 4. Fast peak voltage detector.

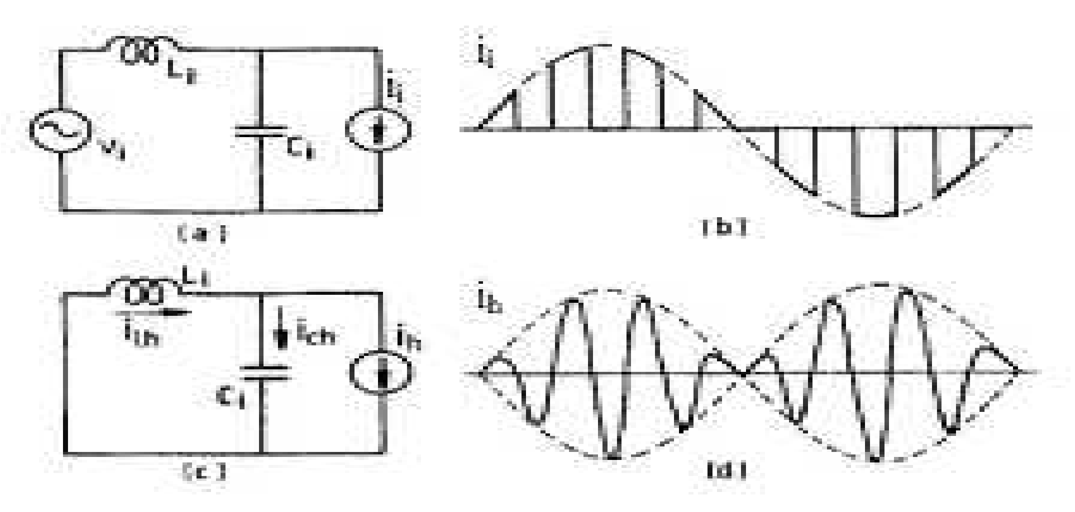

Figure 5. (a) Input filter:(b) input converter current; (c) harmonic equivalent circuit; (d) dominant harmonic current i_h

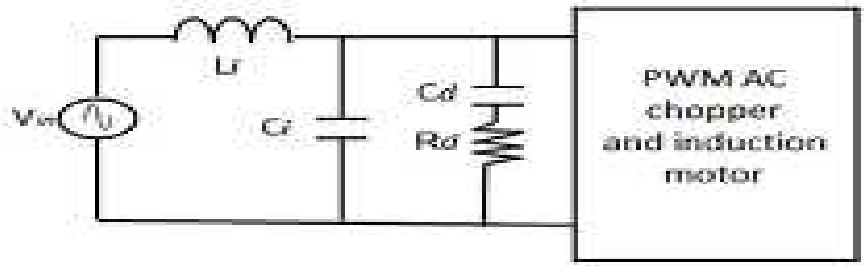

Figure 6. Structure of undamped and damped LC filter.

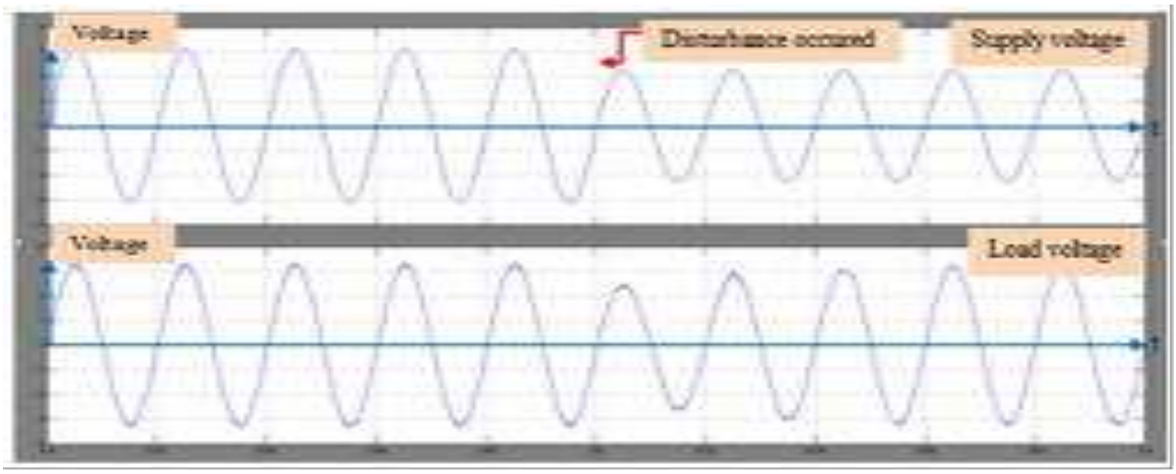

Figure 7. Steady state of supply voltage and load voltage waveforms at source main frequency HZ, (100V/div), time(20ms/div).

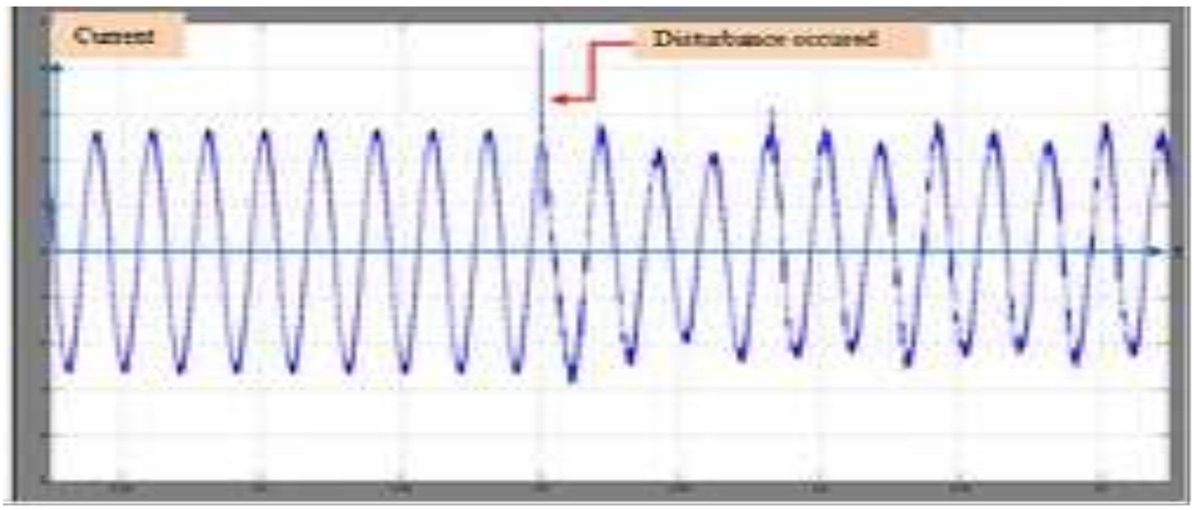

Figure 8. Steady state of supply current waveform, (1A/div), time(50ms/div).

.

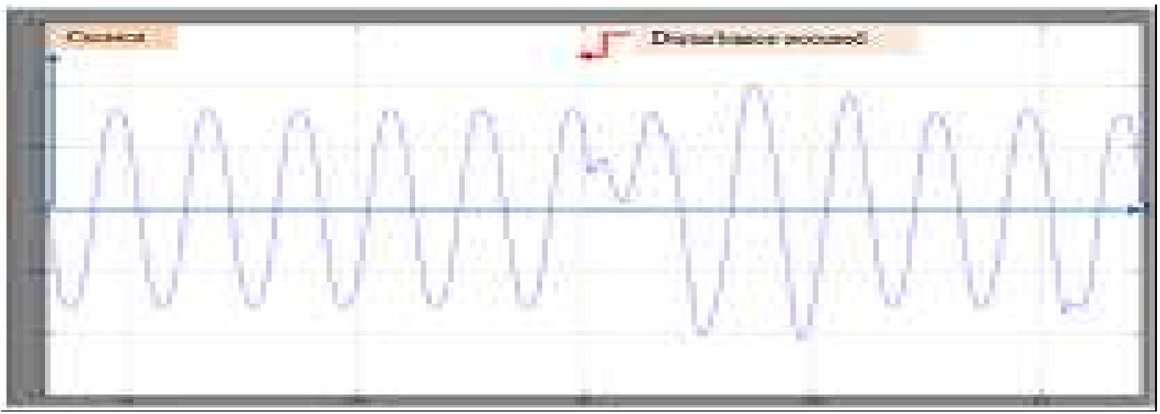

Figure 9. Steady state of motor input current waveform, (500mA/div), time(50ms/div).

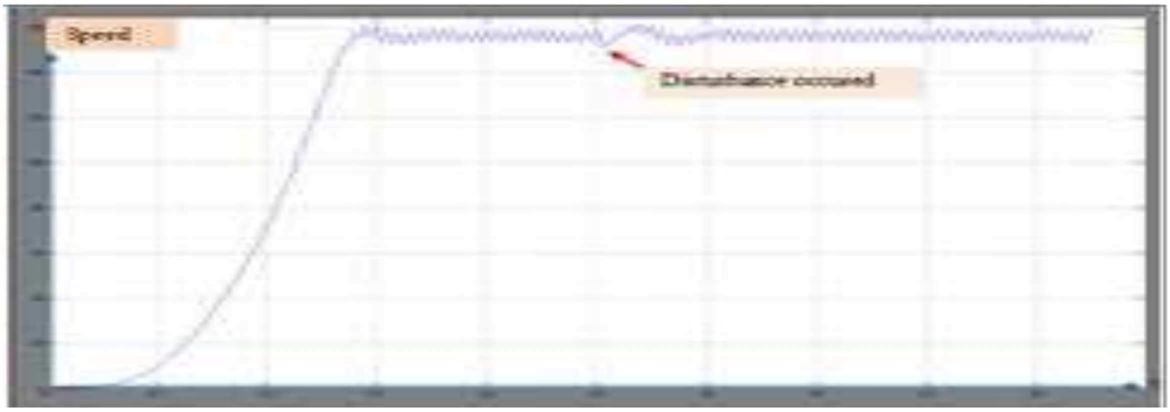

Figure 10. Steady state motor speed at source main frequency 50HZ, (20rad/s/div), time(s).

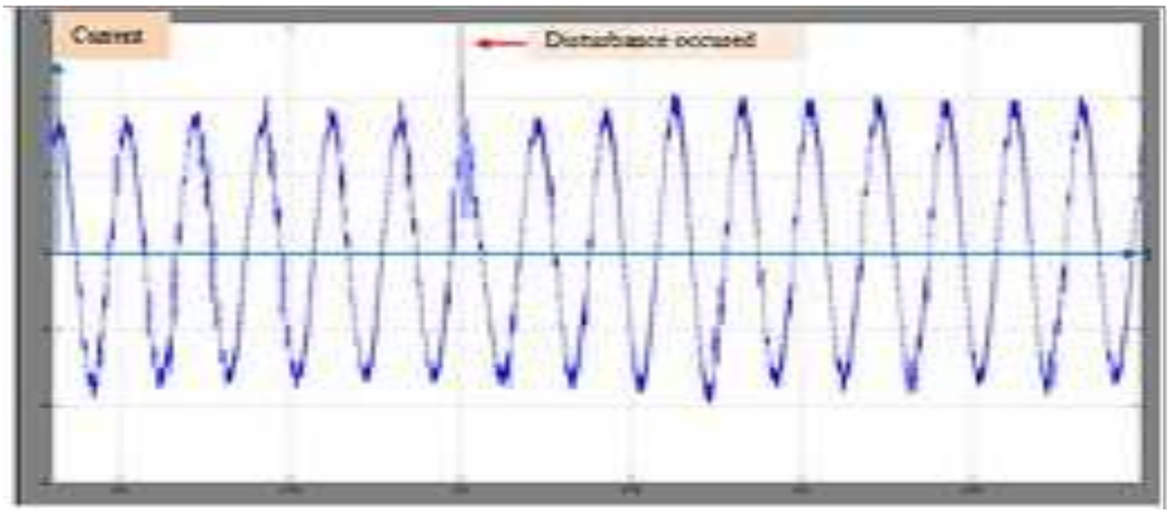

Figure 11. Steady state of supply current waveform, (2A/div), time(50ms/div).

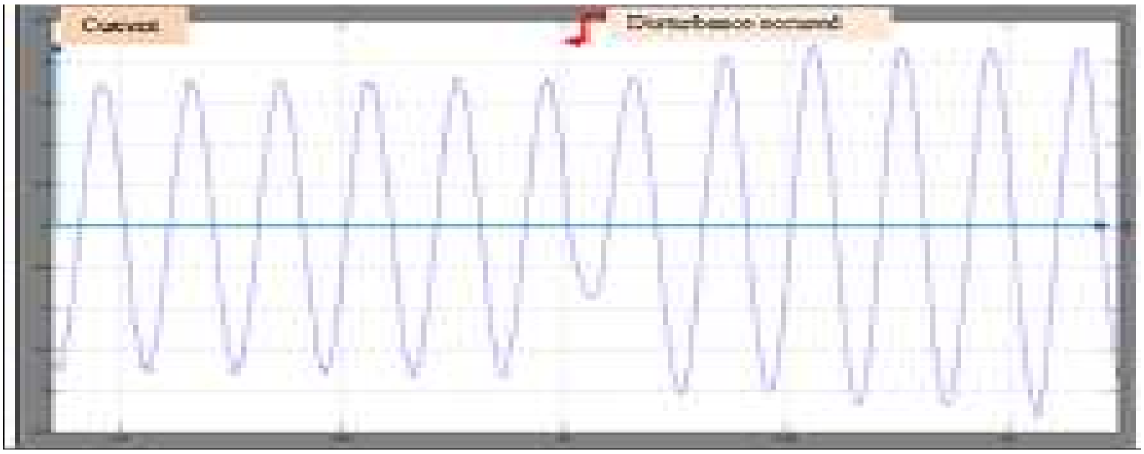

Figure 12. Steady state of motor input current waveform, (500mA/div), time(50ms/div).

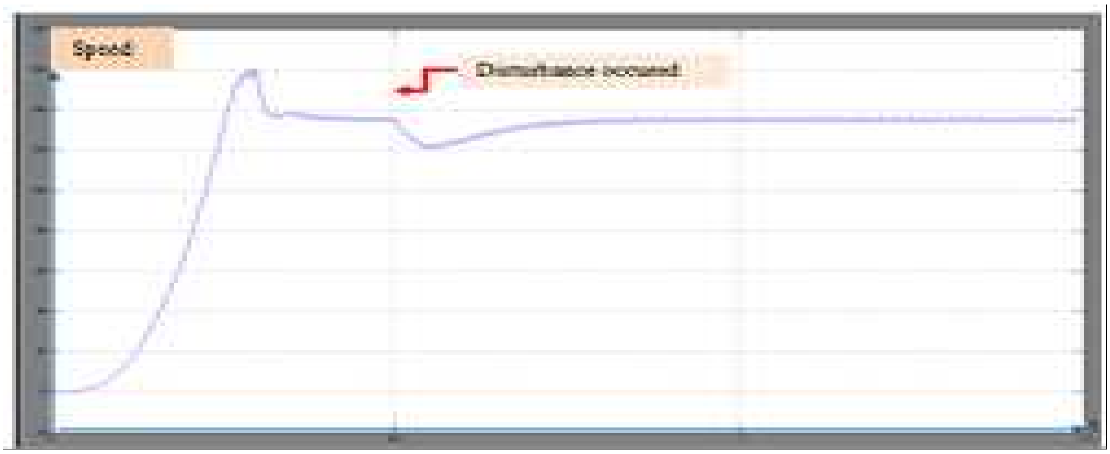

Figure 13. Steady state motor speed at source main frequency 50HZ, (20rad/s/div), time(s).

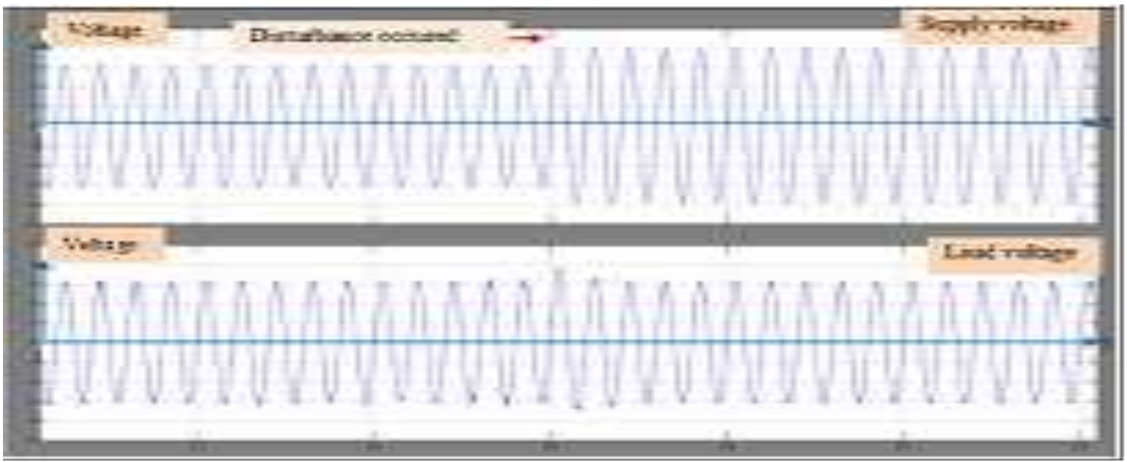

Figure 14. Steady state of supply voltage and load voltage waveforms at source main frequency 50HZ, (100V/div), time(100ms/div).

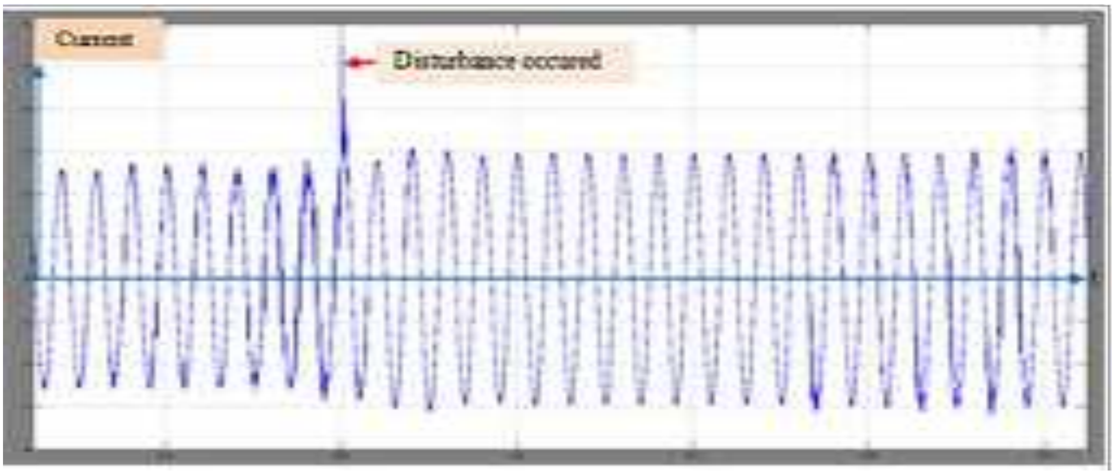

Figure 15. Steady state of supply current waveform, (1A/div), time(100ms/div).

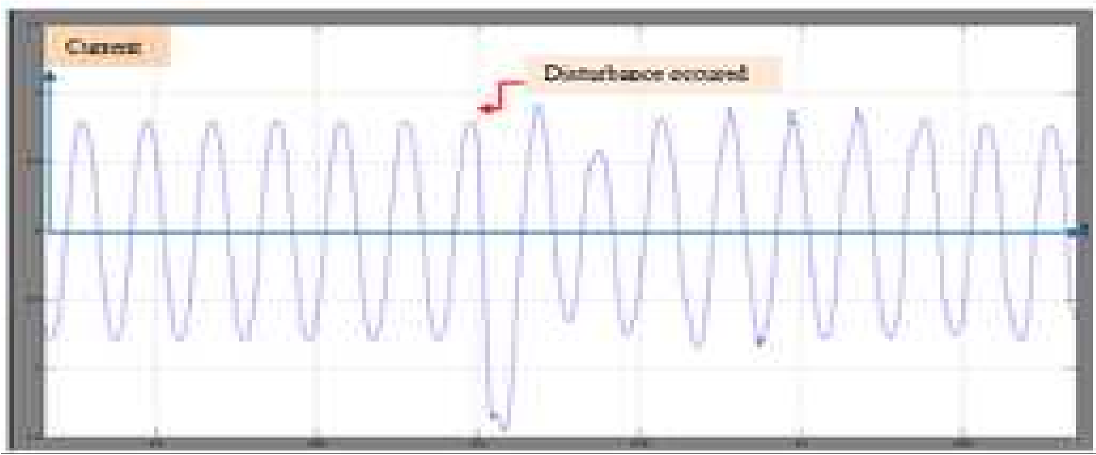

Figure 16. Steady state of motor input current waveform, (500mA/div), time(50ms/div).

Figure 17. Steady state motor speed at source main frequency 50HZ, (20rad/sec/div), time(s).

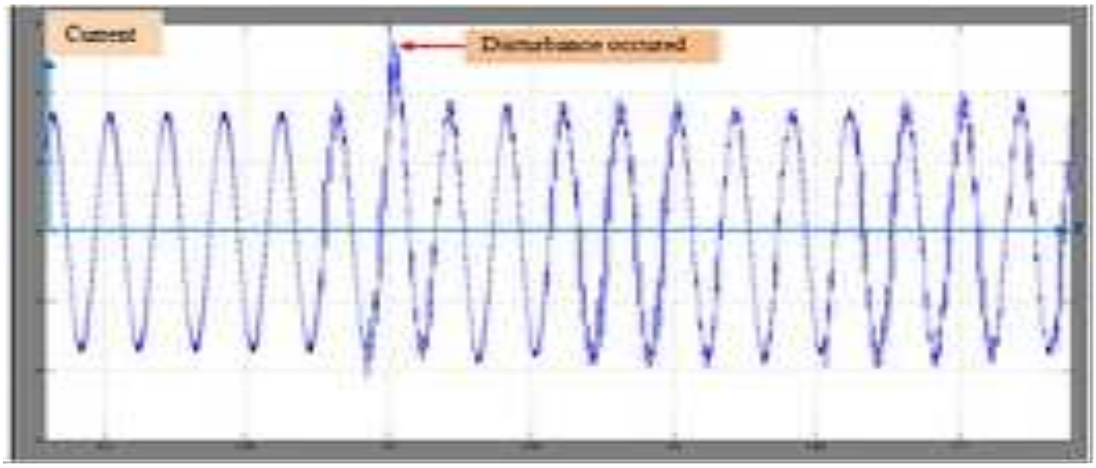

Figure 18. Steady state of supply current waveform, (1A/div), time(50ms/div).

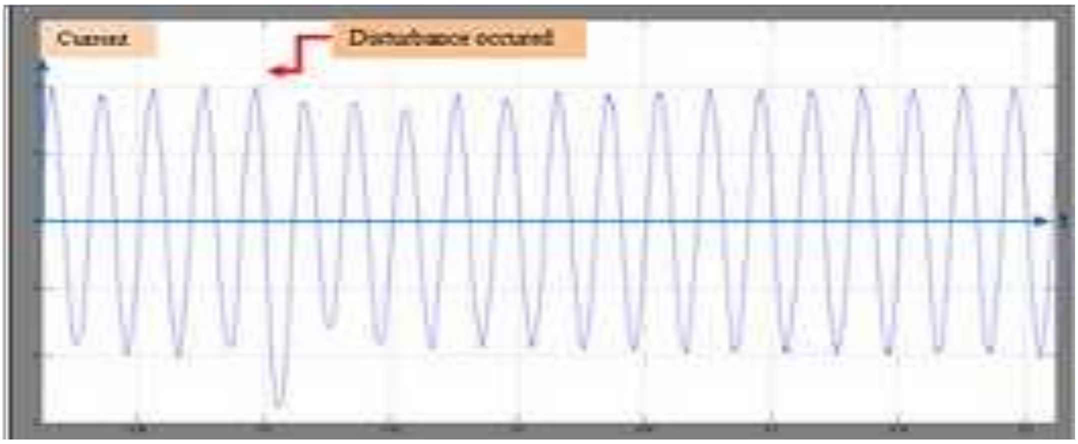

Figure 19. Steady state of motor input current waveform, (1A/div), time(50ms/div).

Figure 20. Steady state motor speed at source main frequency 50HZ, (20rad/sec/div), time(s).

Table 1. Name-plate data of the single phase capacitor run induction motor.

Induction motor	
Parameter	Value
Rated rms voltage	220 V
Rated frequency	50 HZ
Rated rms current	1.47 A
Number of poles	4
Capacitor	8 μ F ± 7%
Rated output	175 W
Rated speed	1140±40% rpm

Table 2. Motor parameters.

Parameter	value
Main winding stator resistance	43Ω
Main winding stator leakage reactance	34.05 Ω
Main winding rotor resistance	32.76 Ω
Main winding rotor leakage reactance	34.05 Ω
Main winding mutual reactance	466.60 Ω
Auxiliary winding stator resistance	23Ω
Auxiliary winding stator leakage reactance	40 Ω
turn ratio (aux/main)	1.1
Moment of inertia(J)	0.767x10^-3 Kg.m2
Friction coefficient	0.118x10 ^-3 N.m.s/rad

Table 3. Total harmonic distortion; for input current, load current and voltage across the load terminals when input voltage varied at (0.5sec).

Voltage variation	Load condition	THD_i	$THDi_L$	$THDv_o$
Rated rms input voltage dropped to(160V)	No-load	4.09%	3.80%	0.60%
	Half-full load	4.53%	1.97%	0.59%
	Full-load	4.47%	1.52%	0.51%
Rated rms input voltage increased to(280V)	No-load	3.29%	3.31%	0.40%
	Half-full load	3.44%	2.25%	0.46%
	Full-load	4.24%	1.32%	0.70%

Table 4. Input power (W) values according to line power factor variation at different supply voltage.

Input voltage (V)	Source Current (A)	Load applied on the motor (N.m)	Input power factor	Input capacity (VA)	Input power (W)
(160V)	1.76	0	0.355	281.6	99.9
	2.68	1.3	0.810	428.8	347.3
(220V)	1.76	0	0.250	387.2	96.8
	2.47	1.3	0.650	543.4	353.2
(280V)	2.12	0	0.170	593.6	100.9
	2.47	1.3	0.500	691.6	345.8

Numerical Study of Optimum Configuration of Unconventional Airfoil with Steps and Rotating Cylinder for Best Aerodynamics Performance

Dr. Najdat N. Abdulla
Professor
College of Engineering-University of Baghdad
Najdat_abdulla@yahoo.co.uk

Ahmed J. Hamoud
M.sc.
College of Engineering-University of Baghdad
ahmed_alzaidy80@yahoo.com

ABSTRACT

Numerical study of separation control on symmetrical airfoil, four digits (NACA 0012) by using rotating cylinder with double steps on its upper surface based on the computation of Reynolds-average Navier- Stokes equations was carried out to find the optimum configuration of unconventional airfoil for best aerodynamics performance. A model based on collocated Finite Volume Method was developed to solve the governing equations on a body-fitted coordinate system. A revised (k-w) model was proposed as a known turbulence model. This model was adapted to simulate the control effects of rotating cylinder. Numerical solutions were performed for flow around unconventional airfoil with cylinder to main stream velocities ratio in the range of 1 to 4 and for various positions of the steps on the airfoil from the leading edge, 0.1c, 0.2c, 0.3c, 0.4c, 0.5c for the first step and 0.5c, 0.6c, 0.7c, 0.8c for the second step with constant step depth and length of 0.03c and 0.125c respectively. Reynolds number of 700,000 which was based on the cord length (c), with angle of attacks 0, 5, 8, 10, 12, 15 degrees was considered for the assessment of the unconventional airfoil performance. The numerical investigation showed that the optimum configuration for the unconventional airfoil was found to be at velocities ratio (U/U∞=4) with the steps positions at 0.5c and 0.8c for best airfoil performance.

Keywords: unconventional airfoil, airfoil with rotating cylinder, airfoil with upper steps.

دراسة عددية للشكل الامثل لجناح غير تقليدي يحوي على عتبات واسطوانة دوارة لأفضل اداء ديناميكي هوائي

د.نجدت نشأت عبدالله
استاذ
كلية الهندسة- جامعة بغداد

احمد جميل حمود
ماجستير
كلية الهندسة- جامعة بغداد

الخلاصة

تضمن العمل دراسة عددية للسيطرة على انفصال جريان الهواء من على سطح جناح متناظر نوع NACA 0012) باستخدام اسطوانة دوارة في مقدمة الجناح واضافة عتبات اثنين على السطح العلوي للجناح, وهذا التحليل تم باستخدام معادلة متوسط رينولد- نافير ستوك) وذلك لايجاد افضل اداء ايروديناميكي للجناح بعد الاضافات. اعتمد هذا الموديل الرياضي على طريقة الحجوم المحددة لحل , وقد تم استخدام موديل رياضي للجريان الاضطرابي. أجري الحل العددي للتدفق حول الجناح غير التقليدية مع اسطوانة دوارة بنسبة السرعات من 1 الى 4 اضعاف سرعة التيار الهوائي الرئيسي ومع اختلاف اماكن العتبات على الجناح بمسافة مقاسة من الحافة الأمامية وقد كان عدد رينولدز من 077.777 مع زاوية من الهجمات 7، 5، 8، 17، 11، 15 درجة لتقييم الأداء الجناح غير تقليدية.

1. INTRODUCTION

In modern civil transport aircraft, the main objectives to be achieved are the needs of cruise conditions (low drag) with a particular attention on the economic, as well as aerodynamic efficiency because most of the flight time is spent during this phase of flight at transonic conditions. Hence, the shape of the wing must be able to minimize the strength of any shock waves present in order to reduce the wave drag. In addition, the wing must be able to satisfy the necessary requirements of take-off and landing. Therefore, complementary high-lift systems are usually employed by combat aircraft, not only for short take-off and landing, but also to enhance high-speed maneuverability by delaying the onset of high-speed stall. High-lift system mainly consists of mobile mechanical device capable of separating some parts of the wing and repositioning them in a suitable configuration in order to increase the chamber and effective area of the wing. The result of these arrangements is a new configuration, which allows a significant improvement in lifting capabilities compared to the clean wing of the cruise configuration. The first practical application of the moving surface for the boundary layer control was demonstrated by, **Favre, 1938**. He studied an airfoil with an upper surface formed by a belt moving over two rollers. The separation was delayed until the angle of attack reached to 55 degree, where the maximum lift coefficient of 3.5 was realized. **Cichy, et al., 1972**, studied the application of rotating cylinder to improve ship maneuverability. Extension force measurements and flow visualization experiments were conducted using a large circulating water channel. Three different configurations of rudder were used with the rotating cylinder; (1) in insulation, (2) the leading-edge of the rudder, and (3) combined with a flap-rudder where the cylinder being at the leading-edge of the flap. From the overall consideration of hydrodynamic performance and mechanical complexity, configuration number (2) was preferred as far as power consumption concerned. **Buckholtz, 1986**, observed the irregular shape of many insect wings as well as other studies indicating a higher lift on these wings. A flow visualization scheme was used to observe and photograph stream lines around two different wing sections. One of these, a sheet metal model with geometry matching that of a butterfly wing, was studied at a Reynolds number of 1500 and 80 based on corrugation depth. **Freymuth,et al, 1989**, worked on the airfoil with rotating cylinder at the nose to demonstrate concept of dynamic separation without dynamic stall. The airfoil was tested in the wind tunnel with uniform velocity of 61 cm/s and cylinder rotating speed of 3000 r.p.m. at a Re=4300 based on the chord length. They found that for a pitch angle of 20^o a speed ratio was 2.5, for 40^o the ratio was 4.2, and at 90^o it was 12. An increase in speed ratio beyond the minimum had no detrimental effect on stall control but resulted in a wall jet passing over the suction side of the airfoil which continued as a jet behind the trailing edge. These results were inferred from flow visualization and confirmed by speed profiles obtained with a hot-wire anemometer, after the final pitch position of the airfoil had been reached. **Al- Tornachi, and Abu- Tabikh, 1998**, developed a numerical method to analyze steady incompressible flow around airfoils with turbulent separation. The model used was a direct viscous- inviscid interaction scheme based on a vortex panel method. The overall method was relatively simple and allowed for predicting the complete wing characteristics. Some example calculations were discussed, and good agreement between calculations and experiment was obtained. **Al-Garni, et al., 2000**, worked on the experimental investigation of two –dimensional NACA 0024 airfoil equipped with a leading-edge rotating cylinder. The airfoil was stated for different angles, and they found that the leading-edge rotating cylinder increases the lift coefficient of a NACA 0024 airfoil from 0.85 at Uc/U=0 to 1.63 at Uc/U=4 and delay the stall angle of attack by about 160%. In the same year, Yeung, 2000, studied the flow visualization on a corrugated airfoil. He confirmed that the trapped vortices leaded to a modification of the effective wing shape and an increase in lift. He also, found that the leading-edge rotating cylinder effectively extend the lift curve of an airfoil without substantially affecting its slop. **Sahu, and Patnaik, 2010**, investigated the flow past NACA 0012 airfoil. The simulations were performed for different angles of attack varying from 0^o to 20^o in sub- critical Reynolds numbers range. The results observed that, stall occurred at $\alpha=12^o$ and Re=46400.Also, the stall angle was delayed by using the simple momentum injection technique with the help of one rotating element as an actuator disc on the leading edge of airfoil. **Lukas, et al., 2011**, studied the boundary layer separation, both stall and separation bubbles, related to the low-Reynolds number transition mechanism. Airfoil of three czech-designed sailplanes and their wing-fuselage interaction were subjected to study. Effect of passive flow control device-vortex generators was surveyed and counter- rotating vortex generators was applied. Separation suppression was reached and consequent drag coefficient reduction of test aircrafts was measured in flight. All above studies were neither considered the combine effects of leading edge rotating cylinder and the steps on the upper side of airfoil nor high Reynolds numbers flow.

The present work investigate the combine effect of the rotating cylinder of diameter 0.1c in leading edge and double steps at different locations with constant depths and length on the upper side of airfoil. Symmetrical airfoil four digits, (NACA 0012) with Reynolds number of 700000 were considered in this work. Upon the numerical results of all above considered cases, an optimum configuration of airfoil which is represented by lengths, depths and positions of each step in addition to the cylinder to mainstream velocities ratio were obtained for the best performance enhancement of unconventional airfoil.

2. MATHEMATICAL FORMULATION

2.1 Governing Partial Differential Equations

In the present work, the working fluid is air and flow was considered to be steady, two dimensional mean flows, fully turbulent, incompressible, and Newtonian fluid.

The governing equations were derived in Cartesian coordinate systems. Finite volume methods for solving differential equations require continuous physical space to be discretized into a uniform computational space. However, the applications of the boundary conditions require that the boundaries of the physical space fall on coordinate lines of the coordinate system.

In order to analyze the flow field around the airfoil with rotating cylinder and two steps, solution of two dimensional Navier-Stokes equations is required, due to the complexity of flow around airfoil configurations and the dominancy of viscosity effects.

The governing equations for the mean velocity and pressure are the mass and momentum equations, these are analyzed the averaged Navier- Stokes equations. A two- equation turbulence model (k-ω) is used for the system of the momentum equations.

2.2 Reynolds-averaged Navier- Stokes Equations

The basic governing fluid flow equations for, incompressible flows will be summarized. The derivation of these equations, details regarding the constitutive relations used and the various turbulence modeling assumptions employed can be found in several references, **White, 1991,and Ferziger and Peric, 1999.**

Employing indicial notation, the instantaneous form of continuity and momentum equations in Cartesian coordinates can be written as follows:

$$\frac{\partial}{\partial x_j}(u_j) = 0 \tag{1}$$

$$\frac{\partial}{\partial x_j}(\rho u_i u_j) = -\frac{\partial P}{\partial x_i} + \frac{\partial \tau_{ij}}{\partial x_j} \tag{2}$$

Where x_i is position vector, τ_{ij} is viscous stress tensor. The constitutive relation between stress and strain rate for a Newtonian fluid is used to relate the components of the stress tensor to velocity gradients:

$$\tau_{ij} = \mu\left(\frac{\partial u_i}{\partial x_j} + \frac{\partial u_j}{\partial x_i}\right) - \frac{2}{3}\mu\frac{\partial u_i}{\partial x_j}\cdot\delta_{ij} \tag{3}$$

Where μ represents the molecular viscosity and δ_{ij} is the Kronecker delta. The conservation equations above hold exactly for laminar flows. For turbulent flows, in the context of RANS methods, ensemble averaging will be resorted. The time- averaged form of the above equations for turbulent flows is obtained by mass- averaging. The various flow properties are decomposed into mean and fluctuating components, as follows:

$$u_i = \bar{u}_i + u_i' \tag{4}$$

$$\tau_{ij} = \bar{\tau}_{ij} + \tau_{ij}' \tag{5}$$

$$P = \bar{P} + P' \tag{6}$$

Note that Favre-averaging is used for u_i and τ_{ij} (bar and prime denote a Favre- averaging mean quantity and the fluctuation above this mean, respectively). Reynolds- averaging is used for P (bar and prime denote a Reynolds- Averaged mean quantity and the fluctuation above this mean, respectively). After mass- averaging, the mean- flow governing equations become:

$$\frac{\partial}{\partial x_j}(\bar{u}_j) = 0 \tag{7}$$

$$\frac{\partial}{\partial x_j}(\rho\bar{u}_j\bar{u}_i) = -\frac{\partial\bar{P}}{\partial x_i} + \frac{\partial}{\partial x_j}\left(\tilde{\tau}_{ij} - \rho\overline{u_i'u_j'}\right) \tag{8}$$

The double correlation between u_i' and itself, which appears in the term on the right hand side of equation , is the kinetic energy per unit volume (k) of the turbulent velocity fluctuations and can be defined as:

$$k = \frac{1}{2}\overline{u_i'u_j'} \tag{9}$$

The term $\rho\overline{u_i'u_j'}$ is called the Reynolds-stress tensor and can be shown by:

$$\bar{\rho}\sigma_{ij} = -\rho\overline{u_i'u_j'} \tag{10}$$

Or

$$\sigma_{ij} = -\overline{u_i'u_j'} \tag{11}$$

$$\sigma_{ij} = -\overline{u_i' u_j'} = \mu_t \left(\frac{\partial \bar{u}_i}{\partial x_j} + \frac{\partial \bar{u}_j}{\partial x_i} \right) - \frac{2}{3} \mu_t \frac{\partial \bar{u}_i}{\partial x_j} \cdot \delta_{ij} - \frac{2}{3} \rho k \cdot \delta_{ij} \tag{12}$$

Two major approaches are currently used to model these terms, namely:

(a) Eddy Viscosity Models (EVM)

(b) Reynolds- Stress Models (RSM)

The EVM employ Boussineq's eddy hypothesis, which relates the Reynolds stresses to the gradient of mean variables as follows:

Where μ_t is the turbulent (eddy) viscosity. In the most common models in this category, it is postulated that eddy viscosity is dependent on the kinetic energy of the turbulent velocity fluctuations (k) and its dissipation rate (ε) or some combination thereof (such as $\omega = \varepsilon/k$). These variables, in turn are computed by solving transport equations which employ some modeling assumption. On the other hand, the RSM, , estimate the Reynolds stresses by solving transport equations for σ_{ij}. Modeling assumption are required to close the transport equations for σ_{ij}; since the modeled terms are of a higher order than those in the EVM. The RSM are also called second-order closure or second-moment closure models. Incorporating the above modeling assumption, the governing equations for turbulent flow using EVM can be expressed as:

- Continuity equation:

$$\frac{\partial}{\partial x_j} (\bar{\rho} \bar{u}_j) = 0 \tag{13}$$

- Momentum equation:
- $$\frac{\partial}{\partial x_j} \left(\rho \bar{u}_j \bar{u}_i \right) = -\frac{\partial \bar{P}}{\partial x_i} + \frac{\partial}{\partial x_j} \left((\mu + \mu_t) \left(\frac{\partial \bar{u}_i}{\partial x_j} + \frac{\partial \bar{u}_j}{\partial x_i} \right) - \frac{2}{3} \mu_t \frac{\partial \bar{u}_i}{\partial x_j} \cdot \delta_{ij} \right) \tag{14}$$

2.3 Boundary Conditions

-Inlet boundary

At inlet, the velocity components (u and v), the static pressure, the turbulent kinetic energy (k) and its dissipation rate (ε) and ($\omega = \varepsilon/k$) are specified. The values of ($k, \varepsilon \ and \ \omega$) are approximated based on assumed turbulence intensity (Ti) typically between (1% and 6%) and length scale approximation. Approximate value of ($k, \varepsilon \ and \ \omega$) for internal flows can be obtained by means of the following simple assumed forms, **Versteeg and Malalasekera,1995**;

$$k_{in} = \frac{3}{2} (u_i . T_i)^2 \tag{15}$$

$$\varepsilon_{in} = C_\mu^{3/4} \frac{k^{3/2}}{l}, \quad l = 0.07L \tag{16}$$

Where; u_i: Inlet velocity.

T_i: Turbulence intensity.

L: Equivalent length.

C_μ : Universal constant, 0.09

l: Length scale of turbulence.

Moult, and Srivatsa, 1977, assumed that (k, ε and ω) are specified with (k) taken arbitrary as (3%) of the incoming specific kinetic energy and (ε) evaluated with assumed length scale (1) equals (3%) of the domain dimension.

- Outlet boundary

Usually the velocity is known only where the fluid enters the physical domain. At outlet, the velocity distribution is decided by what happens within the domain, **Moult, and Srivatsa, 1977 and Versteeg, and Malalasekera, 1995.** The velocity gradients normal to the outlet surface are assumed to be zero.

-Wall boundary

Wall functions are special formula for evaluating effective exchange coefficient at the wall (Γ_{wall}), **Versteeg, and Malalasekera,1995**, summarized the expressions for wall function for different dependent variables based on dimensionless quantities;

$$y^+ = \frac{\rho \kappa^{1/2} C_D^{1/4} \delta}{\mu_l} \tag{17}$$

$$u^+ = \frac{1}{\kappa} L_n(E.y^+) \tag{18}$$

Where (δ) is the distance to the wall from the nearby grid node. The constants (κ and E) can be obtained from the law of wall. Usually (K= 0.4107) and (E= 9.793) for smooth wall, **Moult,and Srivatsa, 1977**. In a region very close to the wall, kinetic energy of turbulence is set equal to zero. The value of (ε) is fixed at the near wall point with;

$$\varepsilon = \frac{C_\mu^{3/4} . k^{3/2}}{\kappa . \delta} \tag{19}$$

-Moving boundary

For viscous flow, velocity components normal to the moving boundary (Rotating cylinder) are set to zero while velocity components parallel to the moving boundary are specified as follows:

$$\vec{V} = \omega . r \tag{20}$$

3. NUMERICAL SOLUTION

Computational Fluid Dynamics, commonly known as CFD has becomes an important tool used for the design and analysis of thermal-fluid systems over the last several decades .Increases in computing power have permitted more detailed calculations to be undertaken in significantly less time leading to an expanded envelope for computational modeling. Ultimately, it is desirable to continue the development of newer and more accurate CFD algorithms while benchmarking current computational packages. A detailed summary of the CFD methodology and techniques employed during this study will be discussed in the following sections.

3.1 GAMBIT Software

Geometry and Mesh Building Intelligent Tolls (GAMBIT v2.4.6) mesh generation software is discretizing software used to mesh the turbine blade model. The control volumes in this analysis represent the flow domain on the airfoil with steps and front rotating cylinder. Discretization is the process of subdividing the surfaces that represent the fluid flow and solid regions into smaller areas called cells. In CFD, flow variables are solved from one of the cell to the next until the solution for the entire control volume is completed.

3.2 Geometry Definition

The geometry nodes was built by the developing a computer program to the airfoil equations in the Microsoft Excel program by using the equations of the airfoil boundaries for upper and lower parts and making several modifications to give the exact locations and dimensions of the steps that will be studied.

The testing airfoil and domain was built by the Gambit software with the domain dimensions 3c in from the airfoil original point which is at the leading edge and 4c back word of the airfoil trialing edge and 3c for both upper and lower surfaces of airfoil. The airfoil NACA 0012 cord length was 1m, the front rotating cylinder diameter was (0.1c) and the gap between the cylinder and the airfoil was 1mm.

By importing the vertices of the airfoil coordinates in the Gambit program and convert this nodes to surface and subtracting from the domain to mesh the domain according to the Reynold number value and by using the equations (32 to 33) and **Table 2** and **3**.were the mesh cell number calculated.

3.3 Turbulence Model ($k-\omega$)

Many models under the turbulence model ($k-\omega$) can be used in flow field depending on the type of the applications and the associated boundary conditions that work on it. In the present study, according to the boundary conditions which can work on the turbulence model ($k-\omega$), SST model had been built on a baseline model, namely, (BSL Model), which combines the **Wilcox,1993** ($k-\omega$) model near-wall region with the ($k-\varepsilon$) model in the outer part of the boundary layer, **Peng and Eliasson, 2007**.

In simulations of separating aerodynamic flow, indeed, the success reached with the SST model may largely be attributed to the SST assumption inherent in the modeling formulation. The baseline (BSL) model, on the other hand, enables an alleviation of free stream sensitively in the outer edge of the boundary layer due to the combined ($k-\varepsilon$)model. The shear stress transport equation is given by, **Peng and Eliasson, 2007**,as follows:

$$\frac{\partial \rho k}{\partial t}+\frac{\partial(\rho \overline{U_j} k)}{\partial x_j}=\tau_{ij}\frac{\partial \overline{U_i}}{\partial x_j}-C_k f_k \rho k \omega+\frac{\partial}{\partial x_j}\left[\left(\mu+\frac{\mu_t}{\sigma_k}\right)\frac{\partial k}{\partial x_j}\right] \quad (21)$$

$$\frac{\partial \rho \omega}{\partial t}+\frac{\partial(\rho \overline{U_j} \omega)}{\partial x_j}=C_{\omega 1} f_\omega \frac{\omega}{k}\tau_{ij}\frac{\partial \overline{U_i}}{\partial x_j}-C_{\omega 2}\rho\omega^2+\frac{\partial}{\partial x_j}\left[\left(\mu+\frac{\mu_t}{\sigma_\omega}\right)\frac{\partial \omega}{\partial x_j}\right]+C_\omega \frac{\mu_t}{k}\frac{\partial k}{\partial x_j}\frac{\partial \omega}{\partial x_j} \quad (22)$$

The first three terms on the right-hand side of **Eqs. 21** and **22** are subsequently the production term, the dissipation/destruction term and the diffusion term for (k) and(ω), respectively. The last term in the(ω) equation is the cross diffusion term. This term does not exist in the standard ($k-\omega$) model but appears in the SST model in the outer part of the wall layer.

Where τ_{ij} is the mass-averaged viscous stress tensor defined as:

$\tau_{ij} = -\rho\overline{u_i u_j}$ And can be calculated using the Boussinesq approximation, **Davidson, 2009**:

$$\tau_{ij} = \mu_t\left[\left(\frac{\partial \overline{U_i}}{\partial x_j}+\frac{\partial \overline{U_j}}{\partial x_i}\right)-\frac{2}{3}\frac{\partial \overline{U_k}}{\partial x_k}\delta_{ij}\right]-\frac{2}{3}\delta_{ij}k\rho \tag{23}$$

And turbulent eddy viscosity can be calculated from the equation. **Peng and Eliasson, 2007:**

$$\mu_t = \frac{a_1\rho k}{\max(a_1\omega/f_\mu, SF_2)} \tag{24}$$

The coefficients, f_μ, f_k,and f_ω, appearing in the transport equation are empirical function of the turbulent Reynolds number, $R_t = \mu_t/\mu$, being free of any wall parameters. These empirical functions take the following forms, **Peng. and Eliasson, 2007**.

$$f_\mu = 0.025+\left\{1-\exp\left[-\left(\frac{R_t}{10}\right)^{3/4}\right]\right\}\left\{0.975+\frac{0.001}{R_t}\exp\left[-\left(\frac{R_t}{200}\right)^2\right]\right\} \tag{25}$$

$$f_k = 1-0.722\exp\left[-\left(\frac{R_t}{10}\right)^4\right] \tag{26}$$

$$f_\omega = 1+4.3\exp\left[-\left(\frac{R_t}{1.5}\right)^{1/2}\right] \tag{27}$$

And thus:

$$F_2 = \tanh\left\{\left[\max\left(\frac{2\sqrt{k}}{C_k\omega y},\frac{500\mu}{\rho\omega y^2}\right)\right]^2\right\} \tag{28}$$

The model constants are **Jones,and Clark,2005** :

Table1. Constants used in the ($k-\omega$) equation.

C_k	$C_{\omega 1}$	$C_{\omega 2}$	C_ω	σ_k	σ_ω	a_1
0.09	0.42	0.075	0.75	0.8	1.35	0.31

The general form of the $(k-\omega)$ equation, **Fluent** is:

$$\frac{\partial}{\partial t}(\rho k)+\frac{\partial}{\partial x_i}\left(\rho k\bar{U}_j\right)=G_k+Y_k+\frac{\partial}{\partial x_j}\left(\Gamma_k\,\frac{\partial k}{\partial x_j}\right)+S_k \tag{29}$$

$$\frac{\partial}{\partial t}(\rho\omega)+\frac{\partial}{\partial x_i}\left(\rho\omega\bar{U}_j\right)=G_\omega+Y_\omega+\frac{\partial}{\partial x_j}\left(\Gamma_\omega\,\frac{\partial\omega}{\partial x_j}\right)+D_\omega+S_\omega \tag{30}$$

Where: G_k ,G_ω, Y_k , Y_ω, S_k ,S_ω , and D_ω represent, the generation of (k), generation of (ω), dissipation of (k), dissipation of (ω), source term of (k), source term of (ω) and the cross-diffusion term, respectively.

3.4 Mesh Generation

Standard CFD methods require a mesh that fits the boundaries of the computational domain. The generation of computational mesh that is suitable for the discretized solution of two dimensional Navier-Stokes equations has always been the subject of intensive researches. This kind of problem covers a wide range of engineering applications.

For a complex geometry, the generation of such a mesh is time consuming and often requires modifications to the model geometry. There are mainly two types of approaches in surface meshing, structured and unstructured meshing.

In structured mesh, the governing equations are transformed into the curvilinear coordinate system aligned with the surface. It is trivial for simple shapes, **Hanaa 2006 and Nbras, 2009**. However, it becomes extremely inefficient and time consuming for complex geometries. Therefore, it has been excluded in this study. In the unstructured approach, the integral form of governing equations is discretized and either a finite-volume or finite-element scheme is used. The information regarding the grid is directly incorporated into the discretization. Unstructured grids are in general successful for complex geometries, so it was used in present work.

3.5 Quality of Mesh

It is important to investigate mesh quality and check elements orientation. The importance of quality parameter is the face alignment; it is the parameter that calculates skew-ness of cells. Elements with high skew-ness should be avoided. The face skew-ness can be calculated as:

$$\text{Face skewness}=1-\frac{\text{length of shorted face diagonal}}{\text{length of longer face diagonal}} \tag{31}$$

This value is in the range of (0.2 to 0.5), FLUENT.

3.6 Grid Independent Test

The way of checking whether the solution is grid independent or not is to create a grid with more cells to compare the solutions of the two models. Grid refinement tests for drag coefficient indicated that a grad size of approximately (100,000 cell) provide sufficient accuracy and resolution to be adopted as the standard for airfoil surface. **Fig.1** shows the grid independency test performed for airfoil surface with steps and rotating cylinder.

3.7 Mesh Smoothness

The number of cells should be more near the viscosity affected regions like walls and smaller at non critical regions. Since the critical part of our domain is the region of airfoil near rotating cylinder surface, a finer mesh is generated there. But, how far the mesh should be refined near the wall prior to extract any result is depend on the value of y^+ near the surface and must be checked. It gives a measure of mesh resolution near the wall boundaries.

It has been shown in **Fig.2** that the averaged value of $y^+$for the surface is less than 100 which is within the range of (SSTk $-$ ω) turbulence model, Jones, and Clark, 2005.

3.8 Total Cell Count

The final point in a good mesh is the total number of cells generated. It is vital to have enough number of cells for a good resolution but memory requirements increase as the number of cells increase. For the present study, an average of (100,000) cell is used. **Fig.3** shown the mesh on the airfoil surfaces

The procedures for calculation the number of the nodes and discretization of the airfoil and flow domain following (Gambit 2.4.6) are:

Refinement Factor: Coarse, medium, and fine mesh types are available. Mesh density varies based upon the assigned refinement factor. The refinement factor values for the mesh densities are given in **Table 2**.

Table 2. Refinement factors.

Mesh density	Refinement factor
Fine	1
Medium	1.5
Coarse	2.25

Using the refinement factor, first cell height is calculated with the following formula, **Gambit 2.4.6:**

$$\text{First Cell Height} = \text{Refinement factor}\left[\frac{\text{Yplus} \times (\text{Characteristic Length}^{0.125} \times \text{Viscosity}^{0.875})}{0.199 \times \text{Velocity}^{0.875} \times \text{Density}^{0.875}}\right] \quad (32)$$

Reynolds number based upon chord length is used to determine Yplus. Yplus values for turbulent flow conditions are summarized in **Table 3**.

Table 3. Flow regime vs. Reynolds number.

Reynolds number	Flow regime	Yplus/Firstcell height
Re≤50000	Turbulent, enhanced wall treatment	Yplus < 10
Re>50000	Turbulent, standard wall functions	Yplus > 30

The number of intervals along each edge is determined by using geometric progression and the following equation, **Gambit 2.4.6.**

$$\text{Intervals} = \text{INT}\left[\frac{\text{Log}\left\{\dfrac{\text{Edge\_length} \times (\text{Growth ratio} - 1)}{\text{First Cell Height}} + 1.0\right\}}{\text{Log}(\text{Growth ratio})}\right] \qquad (33)$$

The edges are meshed using the first cell height and the calculated number of intervals. The entire domain is meshed using a map scheme.

4. METHOD OF SOLUTION

The method of analysis involves the numerical solution of flow field equations:
Continuity equation,
Momentum equation and
Transport equation of turbulence.

The solution algorithm implies modified version of SIMPLE method of **Patanakar, 1980**, which is an iterative sequence consists of two major parts: the SIMPLE procedure,

The SIMPLE algorithm developed by **Patanakar, 1980**, involves one predictor step and one corrector step. It links the solution of the momentum equation with the continuity equation through the pressure. This is accomplished by solving the momentum equation using the guessed pressure field or values from the previous iteration for the parameters appearing in the equation. This yields to new velocity fields.

Thus, the velocity field obtained satisfies the momentum equation but in general violates the conservation of mass principle. Hence, a correction is introduced into the velocity and pressure fields, after that the transport equation for turbulent is solved using the new velocity field.

This iteration sequence is repeated until the residual (error) levels fall below pre-determined maximum allowable limits indicating a converged solution has been achieved. The total maximum residual is taken to be (1*10-5).

Changing the angle of attack and Re number, and finding the separation points and stall conditions of the NACA0012, after that select the optimum locations and dimensions (i.e. depth and length of the step) to improve the pressure gradients and to move the separation points to the back and delaying the stall.

5. RESULTS

Improvement in performance of the conventional symmetrical airfoil, four digits (NACA 0012) with leading edge rotating cylinder and two steps on its upper side is investigated. The rotating cylinder velocity to main stream velocity ratio,($U/U\infty$) in the range of 1,2,3 and 4 and the change in the positions (0.1c,0.2c,0.3c,0.4c,0.5c) and (0.5c,0.6c,0.7c,0.8c) for first step and second steps respectively, were considered, while, the steps depth and length were kept constant, **Finaish & Stephen 1998.** Assessment of airfoil performance was tested for Reynolds number of 700,000 based on the cord length (c).The numerical results will discuss as follow:-

Fig.5 shows the airfoil lift to drag coefficients ratio for velocity ratio of ($U/U\infty=1$). The flow separation occurs at relatively high angle of attack. The upper surface flow remains attached to the airfoil up to a distance downstream of the leading edge then at it separates and leads to a large separation bubble, with reattached towards the trailing edge. The rotation of the leading edge cylinder results in increased suction over the nose and the smoothness of the transition from the cylinder to the airfoil surface. The same trend was obtained by **Modi, and Mokhtarian, 1988**. The maximum value of the aerodynamic characteristic ratio (lift/drag) reaches up to 34 for the airfoil with steps position at (0.5c and 0.8c).

From **Fig.6** illustrates the increases in momentum injection into the boundary layer as velocity of rotation increase ($U/U\infty=4$) and, delays the flow separation (stall) from the upper airfoil surface and consequently, resulting in a high (Cl_{max}). Different flow patterns can be recognized. It was also noticed that the existence of critical speed is also evident beyond which momentum injection through a moving surface appears to have relatively less effects and the maximum value of the aerodynamic characteristics ratio reach to 38 for the airfoil with steps position at (0.5 and 0.8) at($U/U\infty=2$).

The aerodynamic characteristic ratio (lift/drag) slightly increases between the angle of attack (11^o up to 15^o) as shown in the **Fig.7** for the steps positions at 0.5 c and 0.8 c. For the velocity ration ($U/U\infty=3$) a considerable increases was observed for the same flow conditions (Re=700,000 and $\alpha=15$) and reaches up to 43.

A significant increases in the ratio of lift/drag for combined effect of step positions and velocities ratio, ($U/U\infty=4$) was observed as shown in **Fig.8.** They cause to delay the separation and increase in lift/drag ratio. The maximum ratio was found at the airfoil with the step position at 0.5c and 0.8c which reached up to 47. The flow developments on the upper side of this airfoil configuration were expected. The separation of the airfoil trailing edge and of a primary vortex that separates from the step leading edge induced a secondary vortex in the vicinity of the step. During events of the flow development, these induced vortices may interact with each other in a complicated manner; comprise flow reattachments over the airfoil surface. These flow developments produce large change in the overall lift and drag coefficients.

Fig.9 shows an increase in the lift coefficient with increasing angle of attack for unconventional airfoil due to the effect of the rotating cylinder and steps position compared with normal airfoil, NACA 0012. Also, an increase of 31% in lift coefficient for unconventional airfoil with optimum configuration is obtained when compared with normal airfoil. A same trend for lift coefficient is obtained with the normal airfoil lift coefficient as shown in **Figs.9, 10 and 11**.

A decrease in drag coefficient is noticed for all values of the velocities ratios as the angle of attack are increasing. A reduction of 26% in drag coefficient for unconventional airfoil with optimum configuration is obtained when compared with normal airfoil at the same angle of attack.as shown in **Fig.10.** The trend of drag coefficient for unconventional airfoil is similar to drag coefficient.

The optimum configuration for the unconventional airfoil is found to be at velocities ratio (U/U∞=4) with the steps position at 0.5c and 0.8c as shown in **Fig.11**. A high ratio of lift to drag was observed compared with the same airfoil without leading edge rotating cylinder and steps on the its upper side.

6. CONCLUSIONS

- The rotating cylinder considered to be the best and effective flow control device which was controlling the stall of airfoil flow. The large separation region on stalled airfoil can be reduced significantly by using the rotating cylinder and two upper steps.
- The stalled airfoil flow is sensitive to rotating cylinder speed ratio (U/U∞).
- The lift coefficient of the airfoil is also increased with increase of angle of the attack.
- The rotating cylinder and upper steps causes a decrease in drag and more increase in lift.
- Lift to drag coefficient values of 34,38,43 and 47 are obtained for velocity ratios (U/U∞) 1,2,3 and 4 respectively
- The optimum configuration for the unconventional airfoil is found to be at velocities ratio (U/U∞=4) with the steps positions at 0.5c and 0.8c for best airfoil performance.
- Normal airfoil separates at angle of attack 12^o, while unconventional airfoil with optimum configuration separates at angle of attack 15^o.
- An increase of 31% in lift coefficient for unconventional airfoil with optimum configuration is obtained compared with normal airfoil.
- A reduction of 26% in drag coefficient for unconventional airfoil with optimum configuration is obtained compared with normal airfoil at the same angle of attack.

NOMENCLATURE:

C : cord (m)

CL: lift coefficient

DL: drag coefficient

P: pressure (N/m^2)

Re: Reynolds number

U∞: uniform flow velocity (m/s)

Uc: velocity of the rotational cylinder (m/s)

α: angle of attack (Degree)

μ: viscosity (kg/m.s)

$u_{i,}u_j$: velocity in tenser notation (m/s)

x_i: position vector in tensor notation (m)

δ_{ij}: Kronecker delta

ρ: density (kg/m^3)

τ_{ij}: shear stress (N/m^2)

REFERENCES

- Al- Tornachi, S.J. and Abu- Tabikh, M.I., 1998, *Computation of the Flow Around Airfoils and Wings under High Lift Separated Flow Condition*, Dept. of Mechanical Engineer, University of Technology, Iraq, Journal Eng & technology Vol. 17, No.9.

- Al-Garni, A. Z.,Al-Garni,AM; Ahmed, SA; Sahin, AZ. 2000, *Flow Control for an Airfoil with Leading-Edge Rotation: an Experimental Study*, AMER INST AERONAUT ASTRONAUT, JORNAL OF AIRCRAFT; pp: 617-622; Vol: 37.

- Buckholtz, R.H.,1986, *The Functional Role of Wing Corrugations in Living System*, Department of Mechanical Engineering, Columbia University, New Yourk, NY 10027.

- Cichy, D. R., Harris, J. W., and MacKay, J. K., 1972, *Flight Tests of a Rotating Cylinder Flap on a North American Rockwell Yov-10A Aircraft*, NASA CR-2135.

- Davidson, L., 2009, *An Introduction To Turbulence Models*, http://www.tfd.chalmers.se, 16.

- Fathi Finaish and Stephen Witherspoon., 1998, *Aerodynamic Performance of an Airfoil with Step-induced Vortex for Lift Augmentation.* Dept. of Mechanical and Aerospace, University of Missouri, Rolla, MO 65401.

- Favre, A., 1938, *Contribution of an Experimental Studies of Three-dimensional Hydrodynamic*, Ph.D Thesis presented to the University of Paris.

- Ferziger, J. H. and Peric, M., 1999, *Computational Methods for Fluid Dynamics*, 2nd Edition Springer, Berlin.

- Freymuth, P., Jackson, S., and Bank, W., 1989, *Toward Dynamic Separation without Dynamic Stall*. Dept. of Aerospace Engineering Sciences, University of Colorado, Boulder, CO 80309, USA. Experiments in Fluids. Springer-Verlag,

- Hanaa, A. H., 2006, *Numerical and Experimental Investigation on the Effect of Restriction Shape on Characteristics of Airflow in a Square Duct*, Ph.D. thesis, Mech. Eng. Dept., Univ. of Technology.

- Jones, D.A., and Clark, D.B., June 2005. *Simulation of a Wing-body Junction Experiment using the Fluent Code*, Commonwealth of Australia AR-013-426.

- Modi, V.J. and Mokhtarian, F., 1988, *Effect of Moving Surfaces on the Airfoil Boundary-Layer Control*, Aircraft J., Vol.27, No.1, pp.42-50,

- Moult, A. and Srivatsa, S. K., 1977, *Kora-2 A Computer Code for Axi-symetrical Combustion Chambers*, Chan computer code 201, London, England.

- Nbras, H., 2009, *Effect of Riblet Geometry on Drag Reduction and its Application on Airfoil*, Ph.D. thesis, Mech. Eng. Dept., Univ. of Technology.

- Patanakar, S. V., 1980, *Numerical Heat Transfer and Fluid Flow,* Series in computational methods in mechanics and thermal sciences. Hemisphere Publ. Corp., McGraw-Hill.

- Peng, S. H. and Eliasson, P., 2007, *Examination of the Shear Stress Transport Assumption with a Low -Reynolds Number* $(k-\omega)$ *Model for Aerodynamic Flow*, American Institute of Aeronautics and Astronautics.

- Popelka Lukas, Simurda David, Matejka Milan, Souckova Natalie, 2011,*Boundary Layer Transition, Separation and Flow Control on Airfoils and Bodies in CFD, Wind-tunnel and in-Flight Studies*, proceeding of the 27th International Congress of the Aeronautical Sciences, Prague.

- Sahu, R.D. and Patnaik, B.S.V., 2010, *Momentum Injection Control of Flow Past an Aerofoil,* Proceedings of the 37th National & 4th International Conference on Fluid Mechanics and Fluid Power December 16-18, IIT Madras, Chennai, India.

- Versteeg, H. K., and Malalasekera, W., 1995, *An introduction to Computational Fluid Dynamics, the Ffinite Volume Method*, Longman Scientific and technical.

- White, F. W., 1991, *Viscous Fluid Flow, 2nd Ed.*, McGraw-Hill, New York.

- Wilcox, D. C., 1993, *Turbulence Modeling for CFD*, DCW Industries Inc., La Canada, California.
- Yeung, W.W.H., 2006. *Lift Enhancement on Unconventional Airfoils*, Journal Mekanikal December, No. 22, 17-25.

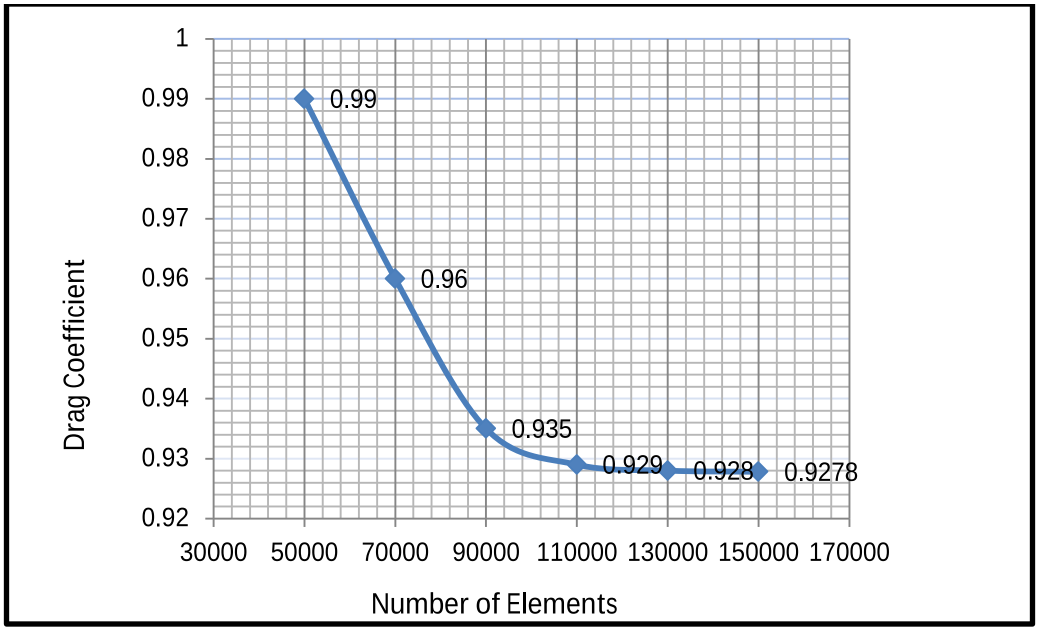

Figure1. Mesh independency test for airfoil with steps and rotating cylinder.

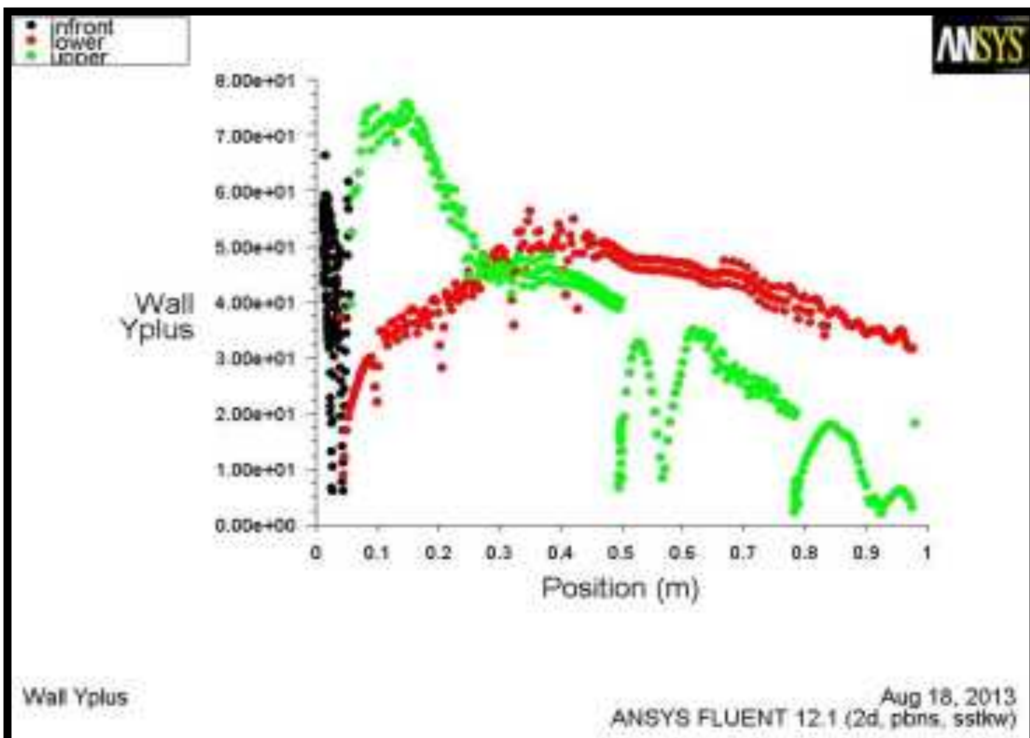

Figure 2. Wall (y^+) variation along the airfoil with steps and rotating cylinder.

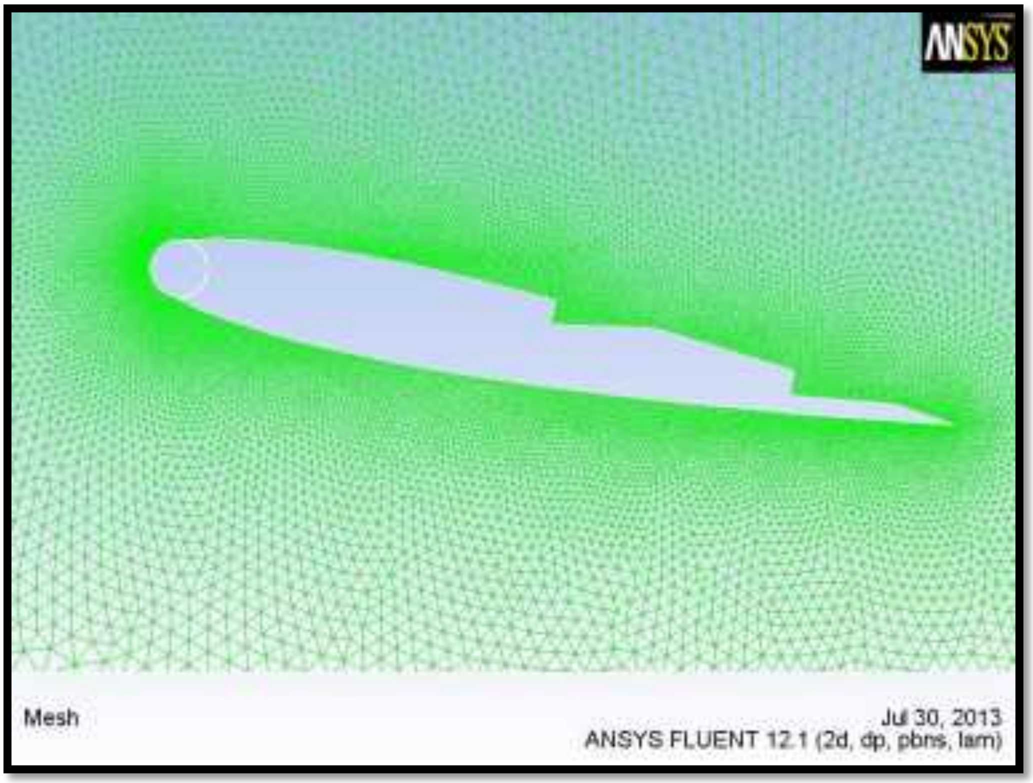

Figure3. Mesh on the airfoil surfaces.

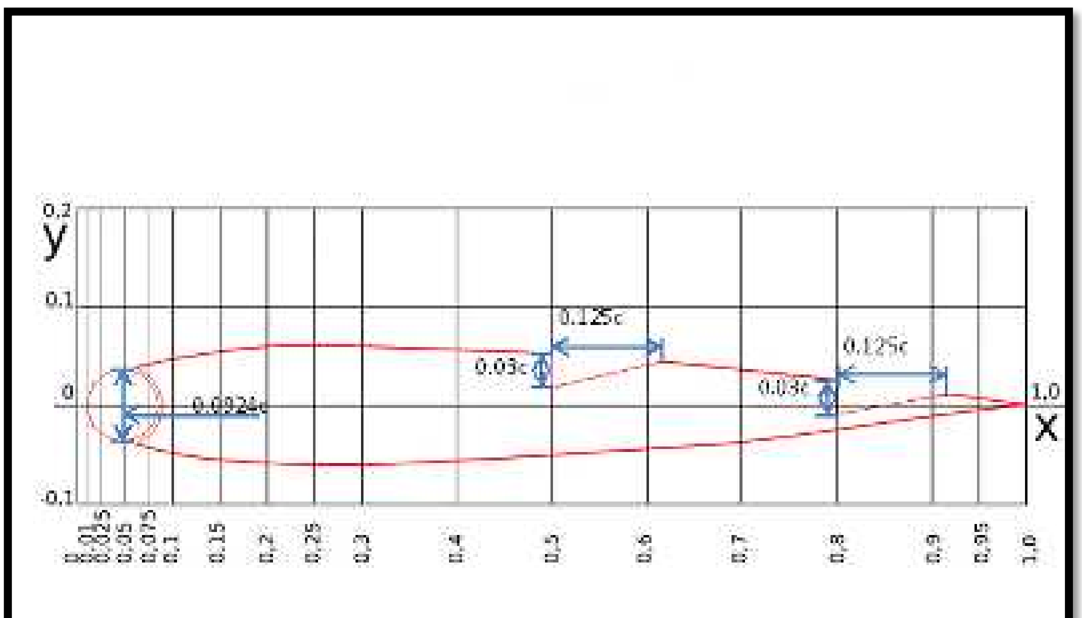

Figure4. Geometry and coordinates of the unconventional airfoil consists of front rotating cylinder and double steps on its upper surface.

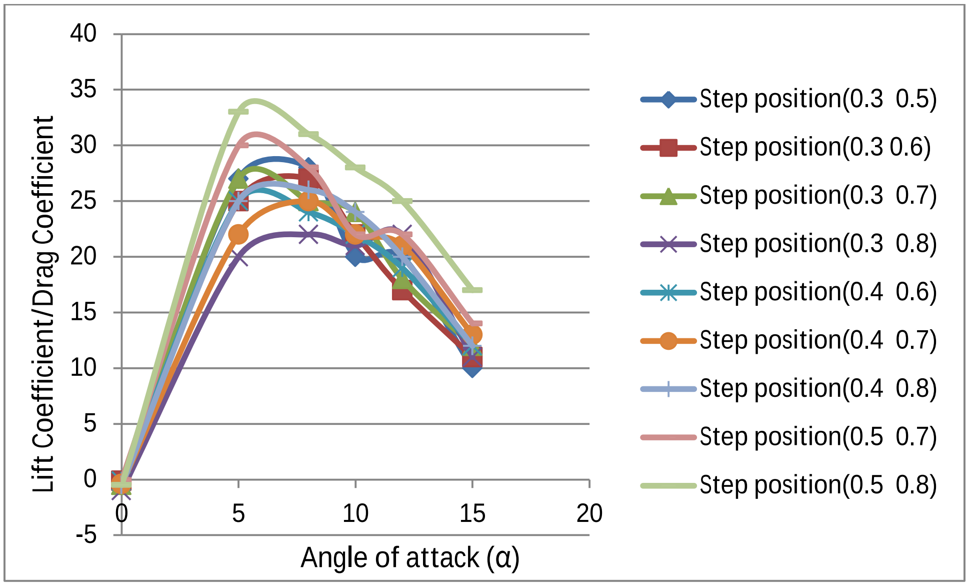

Figure 5. Lift to drag coefficient ratio with various angles of attack (α) at velocity ratio (U/U∞=1).

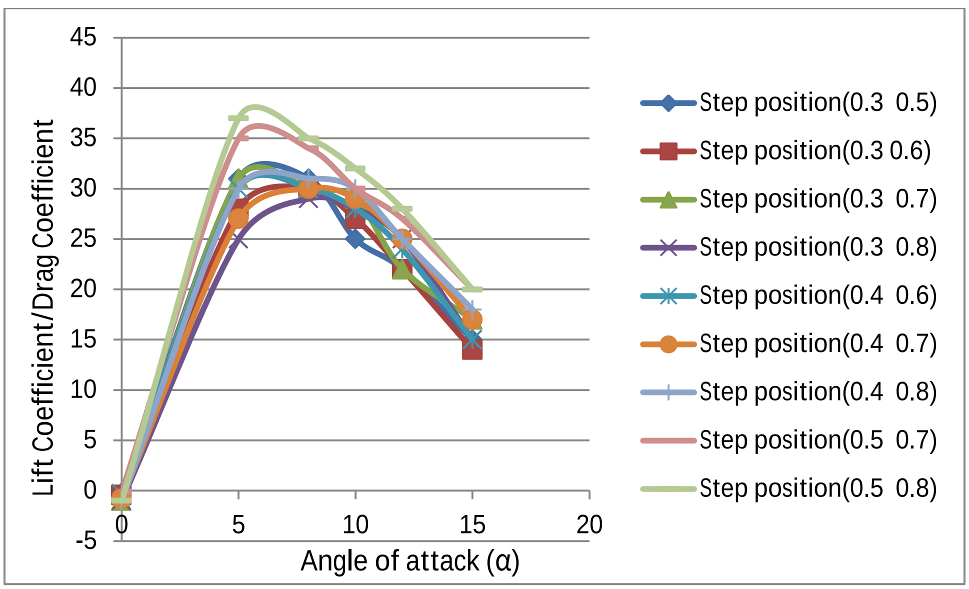

Figure 6. Lift to drag coefficient ratio with various angles of attack (α) at velocity ratio (U/U∞=2).

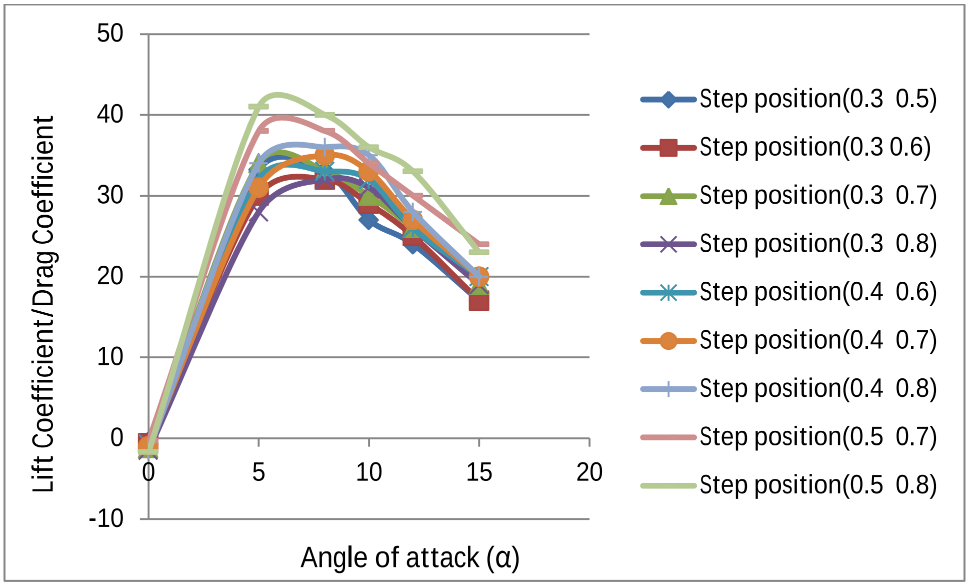

Figure 7. Lift to drag coefficient ratio with various angles of attack (α) at velocity ratio (U/U∞=3).

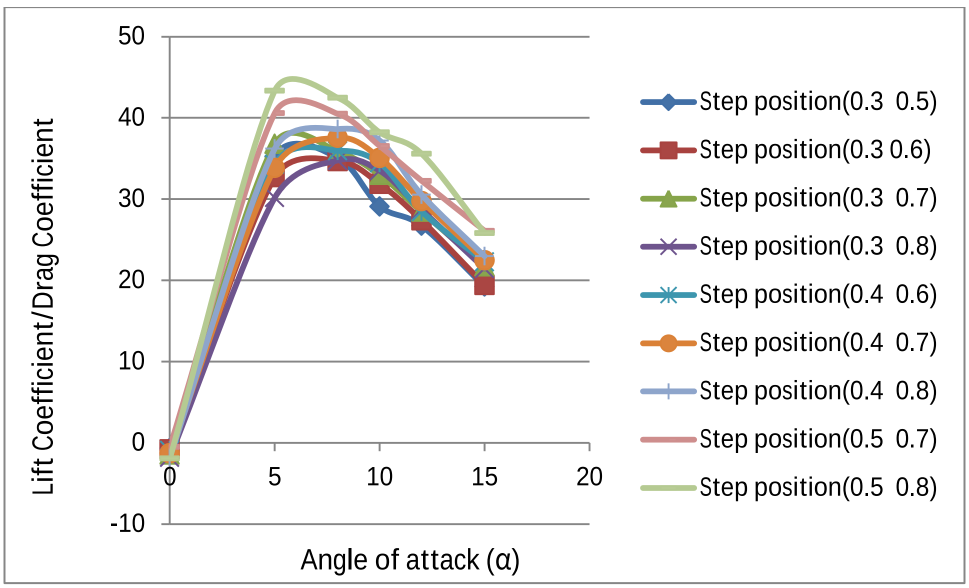

Figure 8. Lift to drag coefficient ratio with various angles of attack (α) at velocity ratio (U/U∞=4).

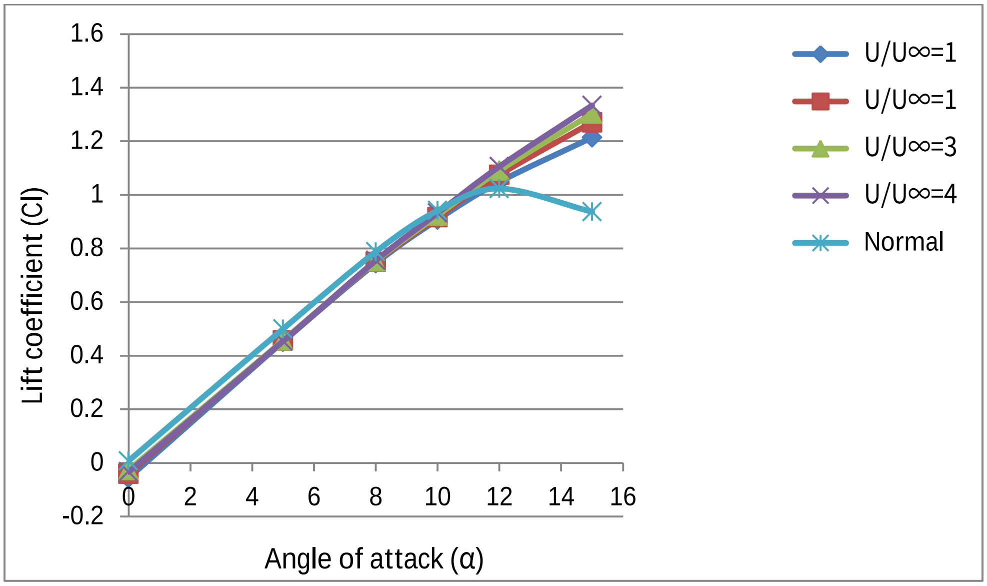

Figure 9. Lift coefficient with various angles of attack at steps positions 0.5c and 0.8c.

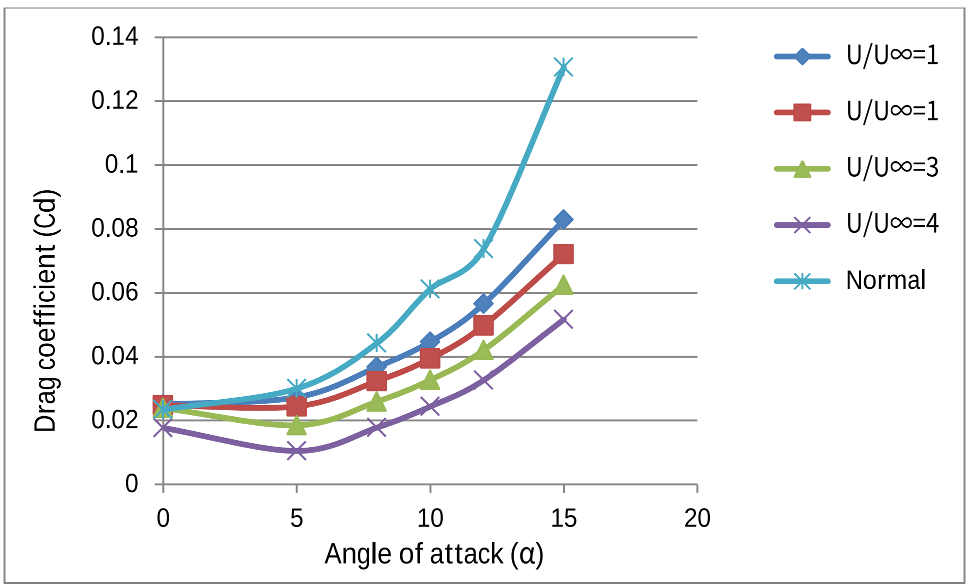

Figure 10. Drag coefficient with various angles of attack at steps positions 0.5c and 0.8c.

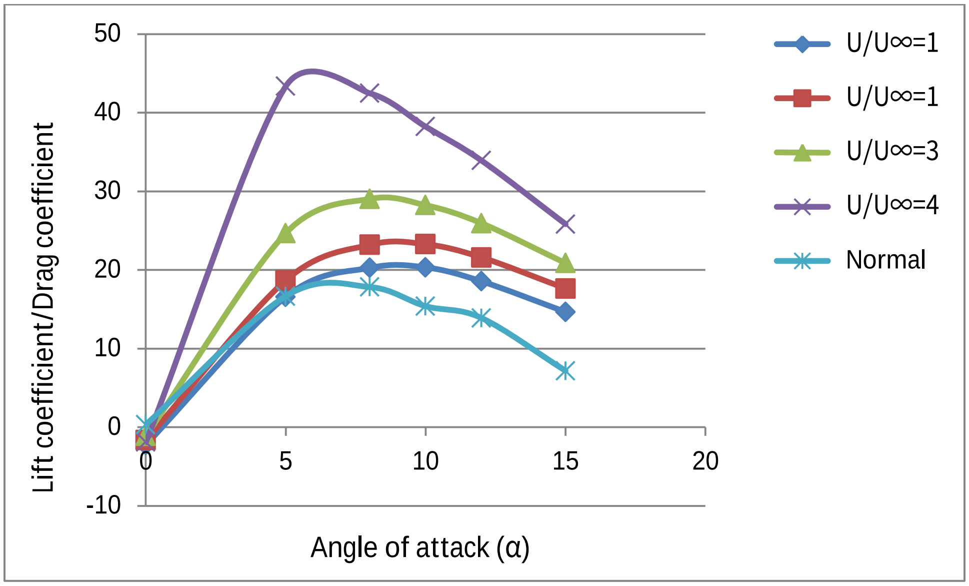

Figure 11. Lift to drag coefficient ratio with various angles of attack for steps positions at 0.5c and 0.8c.